Kumar Hemant Singh
Ritesh Mohan Joshi *Editors*

Petro-physics and Rock Physics of Carbonate Reservoirs

Likely Elucidations and Way Forward

Springer

Petro-physics and Rock Physics of Carbonate Reservoirs

Kumar Hemant Singh · Ritesh Mohan Joshi
Editors

Petro-physics and Rock Physics of Carbonate Reservoirs

Likely Elucidations and Way Forward

Springer

Editors
Kumar Hemant Singh
Department of Earth Sciences
Indian Institute of Technology Bombay
Mumbai, Maharashtra, India

Ritesh Mohan Joshi
Department of Earth Sciences
Indian Institute of Technology Bombay
Mumbai, Maharashtra, India

ISBN 978-981-13-1210-6 ISBN 978-981-13-1211-3 (eBook)
https://doi.org/10.1007/978-981-13-1211-3

This Springer imprint is published by the registered company Springer Nature Singapore Pte Ltd.
The registered company address is: 152 Beach Road, #21-01/04 Gateway East, Singapore 189721, Singapore

Preface

Carbonate reservoirs hold 60% of the world's hydrocarbon reserves. In order to obtain a reliable estimate of reserves in a given reservoir and also to prepare a development plan for optimum production of hydrocarbons from the reservoir, a quantitative assessment of the petrophysical parameters of the reservoir is essential. However, petrophysical properties of carbonates are not easy to predict because of the post-depositional processes like dissolution, re-crystallization and re-precipitation, which alter the properties of the carbonate reservoirs and make them extremely heterogeneous and, hence, bear a profound effect on the productivity and flow dynamics in the reservoir. However, we lack an adequate understanding of how to dynamically model these post-depositional processes. The evolution of porosity through dissolution channels, solution vugs, fractures, etc., is all post-depositional processes. For realistic modelling of the reservoir, we need to understand the dynamics of the fluid flow through the complex network of the carbonate matrix. This calls for proper integration of various geophysical, geological, petrophysical, core data and dynamic data such as MDT, PLT, well test analysis.

Although the challenges in the study of carbonate rocks have led to the development of many techniques, these technologies largely have been patented and, therefore, are not accessible to all workers in this field. With an objective of sharing whatever sharable information is available in the industry and academia in India, a workshop was organized at IIT Bombay in November–December 2017. This volume is an outcome of the deliberations in the workshop.

The volume has been divided into various sections based on the review of the geo-scientific data by different workers in this field in order to understand the various aspects of carbonate reservoirs which make them different from a clastic reservoir. The first section discusses the geological processes in carbonates from a perspective of distribution of porosity and permeability and fluid flow properties of the reservoir. This includes historical review and latest trends on different rock characterization techniques that are being employed by the researchers globally.

Due to the diversity and inherent heterogeneity of carbonates, various laboratory-based results are classified among various empirical models derived for carbonates. This comprises the second section of the proceedings. The laboratory

experiments combined with the log data including high-resolution data acquired by the oil and gas industries are used to develop petrophysical and rock physics models of reservoirs which comprise the next section of the volume. Integrated with seismic data, the existing and new trends in providing solutions to seismic reservoir characterization form the subsequent section of the volume. Characterization of clastic reservoirs and challenges to the wellbore instability problems is addressed in the final section. It is hoped that these proceedings will provide a useful reference for the researchers and practitioners in this field. Your feedback will be valuable for organizing workshops in this field in future.

Mumbai, India

Kumar Hemant Singh
Ritesh Mohan Joshi

Acknowledgements

First and foremost, the editors would like to thank their sponsors, Society of Petrophysics and Well Log Analyst-India Chapter (Mr. R. V. Rao, GGM-Chief Logging Services), for sponsoring the Carbonate Reservoir Workshop held at the Indian Institute of Technology Bombay, and Oil and Natural Gas Corporation Limited (Mr. U. S. D. Pandey, Executive Director, ONGC, and Mr. A. Bhardwaj Executive Director—HOI Geopic, ONGC) for sponsoring a total of seven delegates fee towards the workshop. Humble thanks to both the institutions for entrusting us, having confidence in us and considering us capable enough to conduct the workshop.

We are indebted to Indian Institute of Technology Bombay, Department of Earth Sciences, and especially to the then Head of the Department Prof. T. N. Singh for their guidance, support and logistics during the workshop and throughout the making of this publication.

This book would not have taken shape without the support of all the contributing authors belonging to geologically and geographically diverse places and institutions. The editors from bottom of their heart are indebted to all of them for the time they took to pen down their finding and research so that it can be disseminated with a larger audience. Special mention is for a highly talented and experienced industry professional Mr. U. S. D. Pandey (for keynote address), Mr. P. P. Deo, Mr. K. Vasudevan and Mr. A. Dave all from ONGC, India, for their respective talks and astound academician Dr. Ravi Sharma, Professor from IIT Roorkee, for revising the content and themes related to carbonate reservoir workshop besides contributing to the papers in the book.

We would like to express our deepest appreciation to Dr. C. H. Mehta (Ex-Executive Director and Head, Geopic, ONGC), Dr. Sandip Kumar Roy (Consulting Geologist) and Mr. Asit Kumar (Consulting Geophysicist) for their timely contribution in critically reviewing the papers, editing the articles and making the content easier to understand for the readers.

This book would not have been a reality without the typesetting work and continuous support of Indian Institute of Technology Bombay research students Mr. Anil Kumar, Mr. Anup Shahi and Ms. Arpita Adhikary. They have been the

backbone of the entire process. From organizing the workshop, till the finalization of papers for publishing, their effort has been noteworthy. A big thank you to all.

Literary contributions to the workshop especially by the students from IIT Roorkee, IIT Bombay, VNIT Nagpur and IIT-ISM Dhanbad should not go in vain without being acknowledged. A big thanks to all of you as well.

Last but not least, to the efforts of all those behind the scene and whose names are not captured here, we would like to take a bow to show our gratitude towards you.

Contents

Part I
Geological Processes and Rock Characterization Techniques

Chapter 1
Carbonate Reservoirs: Recent Large to Giant Carbonate Discoveries Around the World and How They Are Shaping the Carbonate Reservoir Landscape

Ritesh Mohan Joshi and Kumar Hemant Singh

Abstract Carbonates are very heterogeneous when compared to clastic reservoirs in terms of reservoir properties. Yet, some of the biggest discoveries in recent times have come from carbonates alone. In 10 years, between 2006 and 2015, there have been four major discoveries and some of them have the potential of being called giants and supergiant. First, it was Tupi discovery renamed as Lula in the pre-salt which opened a new play in the deep-waters of Santos basin. A few more discoveries followed in the same play but then the next big discovery, even bigger than Lula, came in the year 2011 with the discovery of another Oil pool Libra in the same basin. Till 2006, Santos basin was underexplored as it was considered a frontier basin and all the focus was in the neighbouring Campos basin where there were many pre-salt and post-salt discoveries. Post-2006, with a couple of discoveries, the Lower Cretaceous carbonate reservoirs have come up as a new play in the upper Synrift and post-rift sequences. Looking at the tectonic reconstruction of the plate, 140 million years ago (Early Cretaceous) the conjugate margins of Brazil and Angola were juxtaposed before the opening of south Atlantic. This also tells us that Santos and Campos basin of Brazil was located adjacent to Benguela and Kwanza basin of Angola. It is common wisdom that two basins with similar geological history should have similar hydrocarbon prospects. So, the question was whether the pre-salt success of Brazil would recur in Angola where pre-salt drilling was nearly absent before 2011. The answer came with the discovery of Azul by Maersk, which proved a working petroleum system and later Cameia discovery by Cobalt in 2012. With reserves to the tune of 30 TCF (5.5 billion BOE) housed in a 100 km^2 of carbonate mound, it has a potential to become one of the largest gas discoveries of the world. It is already the biggest in Egypt and the Mediterranean. These discoveries and many more are changing the carbonate reservoir landscape. Once upon a time when talking about Carbonates, the reservoir of Middle East basins used to come to mind, not any more. In the age of globalization, it appears that carbonates and large to giant carbonate discoveries have also globalized.

Keywords Carbonate discoveries · Santos Basin · Lula · Cameia · Libra

R. M. Joshi · K. H. Singh (✉)
Indian Institute of Technology Bombay, Mumbai, India
e-mail: kumar.h.singh@iitb.ac.in

K. H. Singh and R. M. Joshi (eds.), *Petro-physics and Rock Physics of Carbonate Reservoirs*, https://doi.org/10.1007/978-981-13-1211-3_1

1 Introduction

Carbonates and Clastics are the main two reservoir rocks considered in hydrocarbon exploration and production. Globally, more than 60% of the oil is hosted in carbonate reservoirs (Roehl and Choquette 1985). 62% of the world's proven conventional oil reserves are in Gulf Countries. 70% of these oil reserves are contained in carbonate reservoirs. Carbonates can be formed by both biochemical as well as inorganic processes. However, it is observed that the deposition of most of the carbonates in the world is controlled by biological activities (Moore 1989). Carbonate deposition needs very specific environmental conditions in reference to light, temperature, salinity and the availability of nutrients. Therefore, most carbonates are formed in tropical, shallow marine depositional environment. These rocks are prone to significant diagenetic changes as they are highly susceptible to chemical alteration, re-crystallization and dissolution processes (Major and Holtz 1997). Giant hydrocarbon fields are discovered and being exploited in the Middle East, Russia, Kazakhstan and Libya. The world's largest conventional oil field in Saudi Arabia is Ghawar which contains multi-billion barrels of oil reserves in the Jurassic carbonate. 54.5% of the newly discovered significant hydrocarbon reserves have been found in marine carbonate and 12% in the lacustrine carbonates during 2000–2012 (Bai and Xu 2014).

A number of significant oil and gas discoveries have been made in carbonate reservoirs around the world in the last decade. Tupi and Libra oil discovery in Brazil by Petrobras in 2006 and 2011, respectively, Cameia discovery in Angola by Cobalt International Energy in 2012 and Zohr gas discovery in Egypt by ENI in 2015 (Eni 2015) are real game-changers. New play types in carbonate have opened up through these big hydrocarbon findings. Giant oil discoveries have been made in Pre-salt carbonate reservoirs in Santos Basin in Brazil and Pre-Caspian salt basin in Kazakhstan (discovered in 2000).

2 Petroleum System

The generation and entrapment of hydrocarbon in the above mentioned giant discoveries are well related to the tectonic evolution of the basins. Large scale intraplate rifting between South America and Africa during the final breakup of western Gondwana in Late Jurassic—Early Cretaceous resulted in South Atlantic rift basins (Heine et al. 2013). The Santos basin in Brazil and Benguela basin in Angola were formed during the last stage of the breakup of the conjugate margin at around 113 Ma (Heine et al. 2013). Microbialite and coquina are the main carbonate rocks identified as hydrocarbon-bearing reservoirs within these rift basins on both sides of the margin. These carbonate rocks are sealed by evaporates which were deposited in shallow marine condition during the first marine transgression in Aptian. The origin of these carbonates is quite controversial. One school of thought is that the carbonates are

associated with reefs and other buildups (stromatolites) formed during various stages of sea-level rise. However, the other model suggests chemical precipitation of carbonates in travertine condition with secondary biogenic growth (Mohriak 2015). This Barremian/Aptian pre-salt carbonate play in upper rift/sag phase in Brazil offshore is proven to be prolific in terms of hydrocarbon reserves after the discovery in 2006. Lula oil field estimating around 5–8 billion barrels, Lara estimating about 3–4 billion barrels, Libra oil field of around 8 billion barrels, are but a few giant discoveries in pre-salt carbonates in Brazil. Libra oil field has an approximate area of 1500 km^2.

The conjugate margin Campos basin in Brazil is the Kwanza basin in Angola on the other end of Atlantic. Microbialite and coquina are reported in the Syn-rift Lower Cretaceous play in Kwanza basin, Angola, similar to that of Campos Basin in Brazil. The carbonate Syn-rift is capped by Aptian salt in Kwanza basin which also witnessed many significant oil and gas discoveries in 2012. Benguela and Namibe basins in West Africa are the conjugate margin of Santos basin of Brazil. However, this part of the West African margin is affected by Valanginian volcanics (Teboul et al. 2017). High concentration of Carbon dioxide in the present-day deep-water of the Lower Cretaceous Syn-rift play associated with deep-seated faults is also reported in Kwanza basin.

The recent discoveries have changed the landscape of the Carbonate reservoirs. Here we discuss only a few major discoveries during the 10-year span from 2006 to 2015. These discoveries have made a significant change in the way we look at the carbonate reservoirs. Some are deep to very deep, some are extensive, while some are in places, which, a few years back, were not possible to even map (shadow zone). We discuss these interesting discoveries in the subsequent sections.

3 2006—Tupi (Now Named Lula) Oil Discovery—Brazil—Petrobras

The discovery of the Tupi oil field (Renamed as Lula) in Brazil (Fig. 1) was a historic event. Petrobras drilled Lula in deep-water of Santos basin (Petrobras 2010). In 2100 m of water depth, the well was drilled about 5200 m from mudline. So, a total well depth of 7300 m was quite deep and resulted in a high cost of over $200 Million.

Despite its very high drill cost, the well proved rewarding. The 2 km of thick salt bed is underlain by 6 billion barrels of Oil in HPHT condition.

Coming to the petroleum system, the organic-rich lake shale is the main oil source. Lacustrine beach sands, porous limestones and dolomites (Microbialites) are the reservoirs and impervious salt acts as a seal. Figure 2 shows a seismic line passing through Lula (Tupi) discovery with the massive evaporates acting as a seal, which can be seen in magenta above the Microbialites reservoir.

The carbonate rocks (limestones and dolomites) that are associated with growths of algae known as stromatolites are referred to as Microbialites. These kinds of stromatolites can be seen in present-day Shark Bay, Australia. The reservoir in which

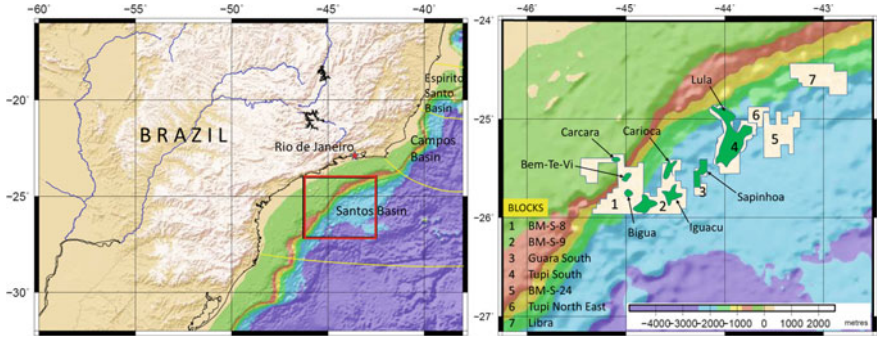

Fig. 1 Location map of Lula and Libra discovery (reproduced with permission from Koning 2015)

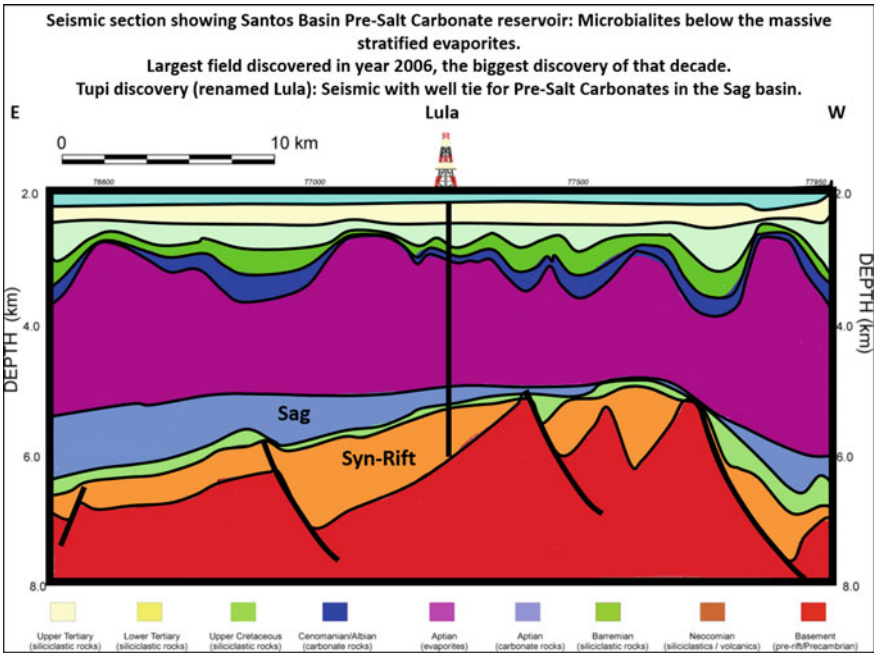

Fig. 2 Geological cross-section showing the location of Tupi (Lula) discovery well. (https://www.aapg.org/publications/copyright, Modified after Mohriak 2015)

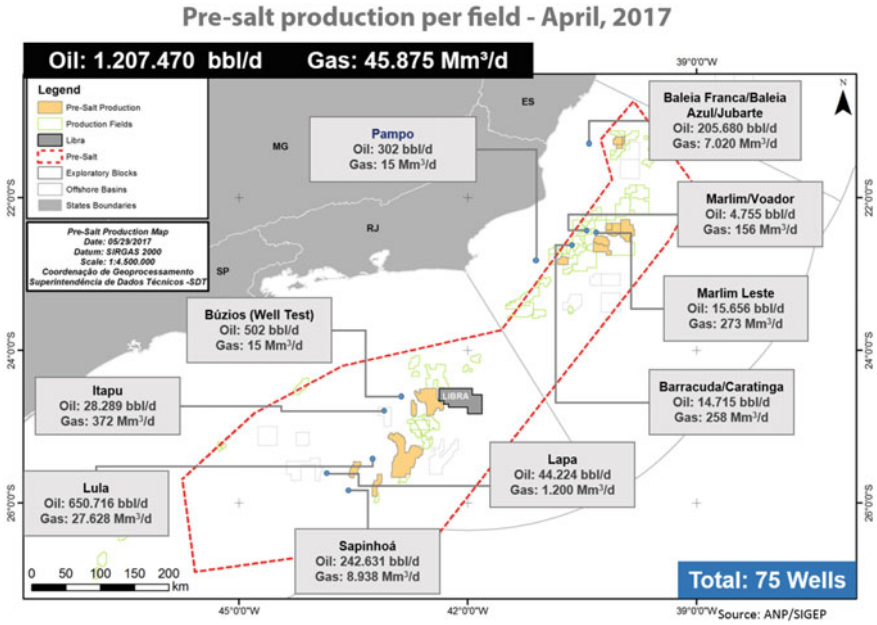

Fig. 3 Field wise production per day from pre-salt reservoirs (reproduced with permission from Oddone et al. 2017)

top section is Microbial carbonates in the sag sequence and the lower section is Coquinas of the Syn-rift sequence mostly have typical vuggy porosity with 9–12% range and permeability pegged at 100 mD.

As per Offshore Technology (Petrobras Dec 30, 2010), today the recoverable volume in the Lula Field is 6.5 billion BOE with 28° API, while the recoverable volume in the Iracema area, Cernambi Field is 1.8 billion, with 30° API. The total recoverable volume amounts to 8.3 billion BOE.

As per the latest numbers shared by ANP 2017–2019 bidding rounds document, the Lula is producing 650,716 bbl/d of oil and 27,628 Mm^3/d of gas. Referring to Fig. 3 which is taken from ANP document from June 2017 "Oil and Gas Opportunities in Brazil; 2017–2019 Bidding Rounds", it is clear that around 75 wells in the Pre-Salt reservoirs are producing a total of ~1.2 million bbl/d of oil and ~46,000 Mm^3/d of gas as of May 2017, which is suggestive of an extremely good production. This is without the contribution of Libra production.

4 2011—Libra Discovery—Brazil—Petrobras

Lula was a game-changer, and it changed the game rapidly not only in the deep-water of Santos basin but also nearby Campos basin. Since Lula, many more pre-

salt discoveries (Carioca-Sugar Loaf, Jubarte, Lara and also gas giant Jupiter) have taken place and the number of recoverable hydrocarbons is increasing steeply. As an estimate by private agencies, the pre-salt oil reserves could be 20–30 billion barrels whereas as per ANP: National Agency of Petroleum, Natural Gas and Biofuels, the number stands at somewhere 50 billion barrels.

Around 230 km off the coast of Rio de Janeiro in the Santos basin and north of giant Lula field (Fig. 1) lies an ultra–deep-water oil field named Libra which was discovered in May 2010. Libra covers an area of 1550 km^2 and the reservoir is below 2000 m of water and approximately 5000 m of sand, rock and shifting salt layer. Figure 4 shows the Geological section through the Libra discovery where the thick salt is marked in magenta colour and the reservoir is in faded sky blue just below it. The oil–water contact is clearly brought out in the seismic section (not shown here).

As reported in Total's website which was last updated in September 2016 (Total 2016) an article in World oil, one of the world's largest offshore oil and gas accumulations is Libra field where the recoverable reserves are estimated to be 8–12 billion BOE. This makes the earlier discovery of the decade (Lula) looks smaller and had to settle for the next largest discovery in ten years after Kazakhstan's 17.2 billion bbl Kashagan Field.

In a presentation made by Bruno Moczydlower of Petrobras (Moczydlower 2014), who is also Libra Reservoir Manager and SPE Brazil Section Chairman, outlines the

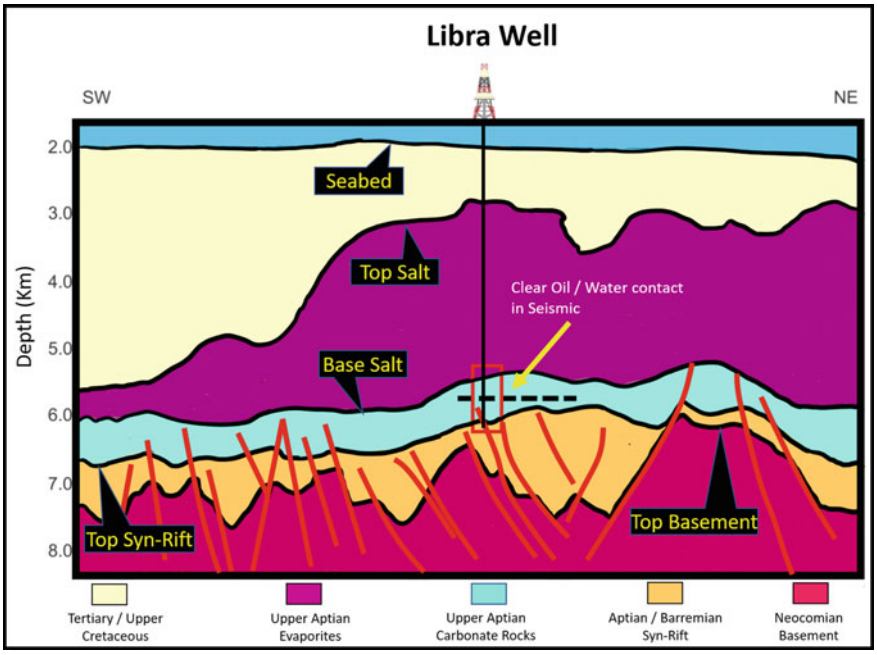

Fig. 4 Geological cross-section showing the location of Libra discovery well (https://www.aapg.org/publications/copyright, modified after Mohriak 2015)

main characteristics of the reservoir. He mentions that the Libra reservoir is a very thick pre-salt reservoir with good reservoir quality in terms of permeability and porosity. The oil is light of around 27 API with low H_2S and high GOR (440 m^3/m^3) but the CO_2 content is slightly higher of about 44%. From the structural map of the base of salt (top of the reservoir) there are a few numbers worth noting for structure Libra2 C1. Referring to Libra Base of Salt Structure Map, Moczydlower (2014) shows that the spill point is at around 5700 m, the area above the oil-water contact is 578 km^2, the reservoir top is at 4750 m and the maximum gross pay is around 950 m. Similarly, from the well log of well 2-ANP-2A-RJS (Moczydlower 2014), the reservoir parameters look impressive. The gross pay is around 329 m, with net pay of around 278 m which gives an N/G ratio of ~85%. The poro-perm is calculated to be 14% and 13%, respectively.

5 2012—Cameia Discovery—Angola—Cobalt International Energy

The first month of the year 2012 and Maersk was happy to announce its first well Azul-1 to penetrate pre-salt reservoir in the deep water of Angola block #23. The total depth drilled by the well was 5330 m out of which the water column was 920 m. Among the many firsts, this was the first deep-water well in the Kwanza basin that targeted the pre-salt reservoirs (Fig. 5).

The second month of the year 2012, and this time Cobalt International Energy (CIE) was happy to announce the results of its well Cameia-1. This was drilled in slightly deeper water (i.e. 1680 m of water) in deep-water Block #21 (Fig. 6). A 360 m of gross Oil column with 75% N/G was penetrated in the Pre-Salt target reservoir.

In the absence of any clear gas–oil or oil–water contact on wireline logs an extended DST was performed. The production of the well was at 5010 bopd of 44° API oil and 14.3 million cubic feet per day of gas which approximately amounts to a total of 7400 bopd.

The well result actually surprised and surpassed all expectations. The reservoir had 365-m-thick oil column and 275-m-thick gas column with over 75% *N*/*G* ratio (Fig. 7). The reservoir is highly permeable and fractured carbonates. The area is between 20 and 101 km^2.

6 Angola's Petroleum Systems

The Azul and Cameia well discoveries in the Kwanza basin confirmed a working pre-salt petroleum system similar to their conjugate margin in Brazil. It helped to de-risk the play.

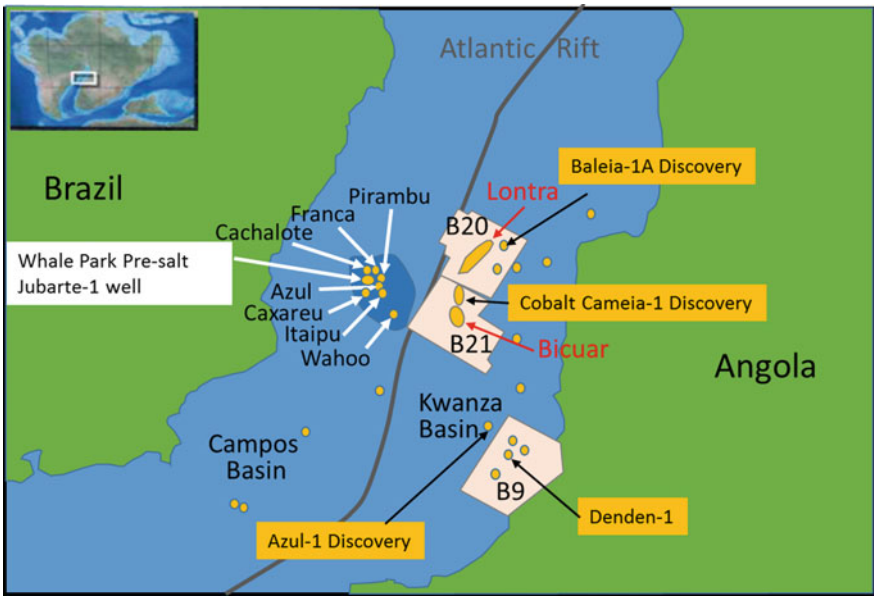

Fig. 5 Location map of the Kwanza basin showing major discoveries including Azul-1 and Cameia-1 (Cobalt 2012)

Angola's hydrocarbon-bearing basins are namely Kwanza, Congo and Namibe. So far only Kwanza and Congo have discovered oil in commercial quantities while Namibe Basin remains underexplored.

A very strong Lower Cretaceous and Tertiary petroleum system is the reason behind the success of Cameia discovery. Continental breakup during Early Cretaceous (Fig. 8) developed lacustrine rift basins and Bucomazi formation, an organic-rich shale became the main source rock for the pre-salt traps in the Kwanza basin.

7 2015—Zohr Gas Discovery—Egypt—ENI

The mother of all discoveries, however, was Zohr discovery, offshore Egypt (Eni 2015). No wonder when someone exclaimed! "The truth? I have never seen 600 m of gas permeated rock with pressure point so aligned". Let's have a look at why this is known as a supergiant.

With over 850 billion cubic meters (30 TCF) of lean gas resources, or 5.5 billion BOE housed in a 100 km^2 field is undoubtedly the largest discovery of Egypt and in the Mediterranean Sea which has a potential of becoming one of the world's largest natural gas field. Located in the deep-water of Egypt' Shorouk block at a water depth of 1450 m the field was announced on August 30th, 2015. A total depth of approx.

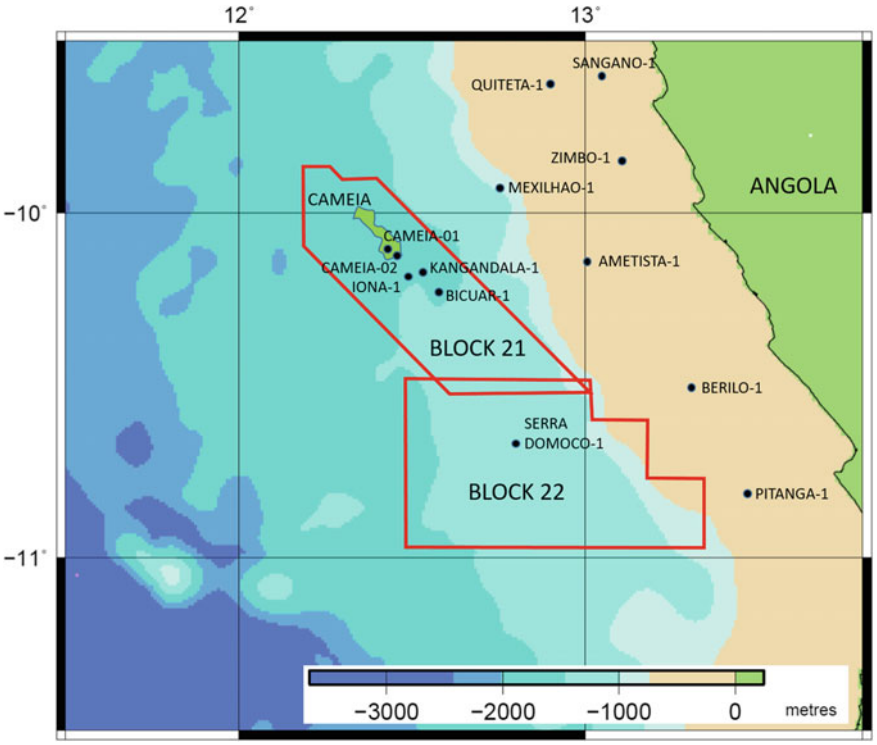

Fig. 6 Block location map of the Kwanza basin showing block #21 and discovery well Cameia-01 (reproduced with permission from Duval et al. 2015)

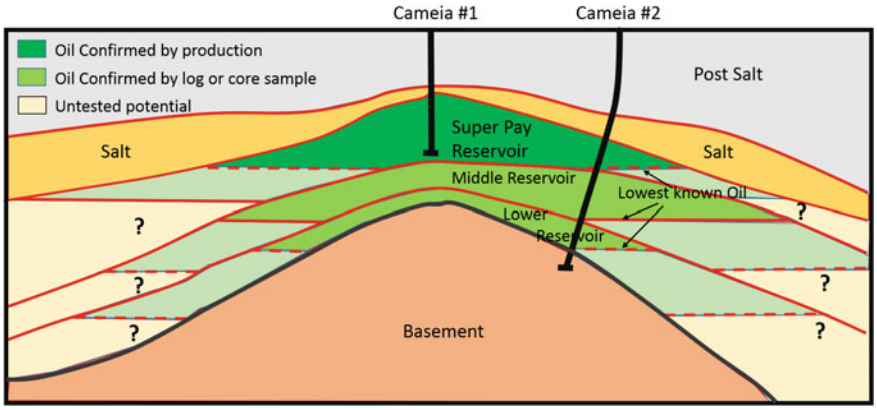

Fig. 7 Geological cross-section of the discovery well Cameia-1 and also Cameia-2 well (modified after Koning 2014)

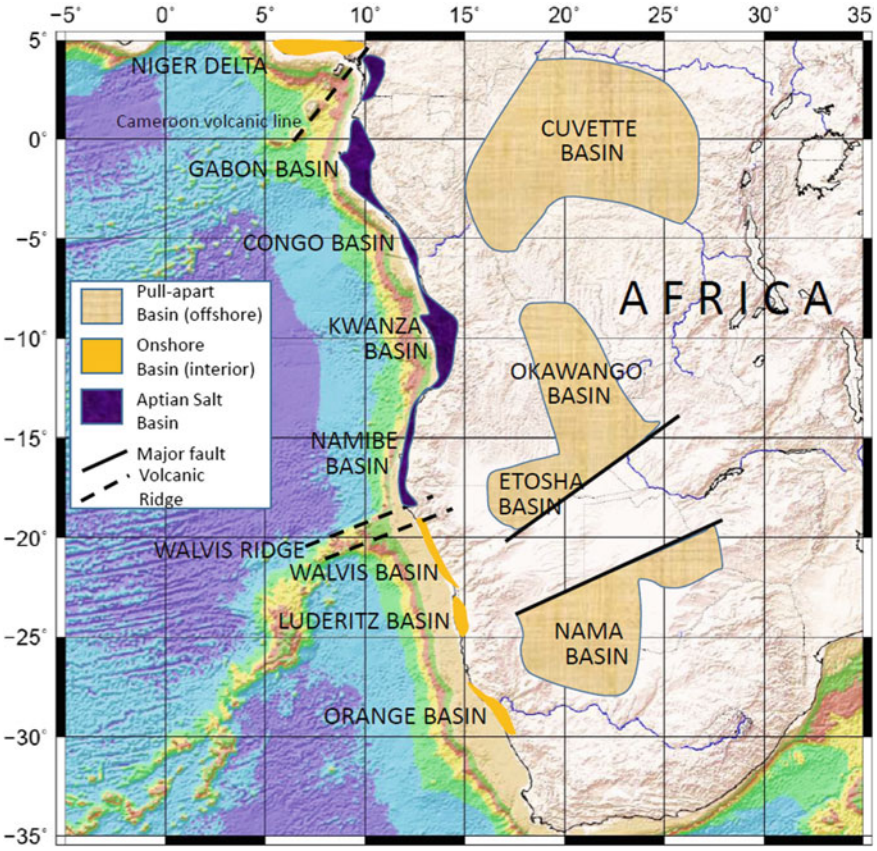

Fig. 8 Structural elements map of the West Africa basins

4131 m was drilled for Zohr 1X NFW and had around 630 m of hydrocarbon column out of which 410 m were the net pay (Nikolaou 2016). The reservoir is Miocene age carbonate Reef and has very good reservoir parameters. Digging deep into a bit of geology, it was understood that the geological evolution and tectonic history of Eratosthenes carbonate platform, is the main reason for the existence of Zohr field. As per press release of ENI, "The *discovery, after its full development, will be able to ensure satisfying Egypt's natural gas demand for decades*". As of Dec 20th, 2017; the first gas started flowing from the supergiant Zohr field in record time. No wonder that the Zohr discovery was a game-changer for the region and it indeed opened up a new play (Fig. 9).

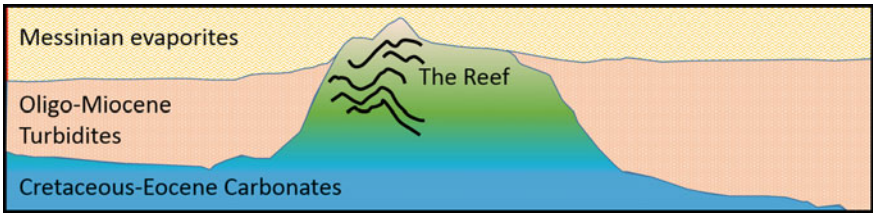

Fig. 9 Geological section of the Zohr discovery

8 Conclusions

Lula (Tupi) pre-salt oil field was discovered because with the advancement of technology it is now possible to see beneath salt in the seismic data. And also, because the geologists were able to understand the depositional environment. And also, because the reservoir engineers were able to understand the reservoir properties of Microbialite reservoirs. It has never been possible to work in silos and come up with an astounding result. Always a cooperative approach and integration of data have done wonders. So it did in Lula, Libra, Cameia and Zohr. Given the pace of advancement of technology and geoscientist's understanding of their respective domain, the day is not too far when the Lula, the Libra, the Cameia and the Zohr's will appear dwarfs on the worlds carbonate discovery map.

Acknowledgements The authors hereby acknowledge the efforts made by Mr. Sumangal Dasgupta of IIT-ISM Dhanbad for his significant contribution to the Introduction section of the paper and modification of some figures. His insights into the carbonate reservoirs are exceptional and the immense experience which he has gained over the years by working on a different dataset from the basin around the world was immensely useful in critical assessment, writing material and in producing the final manuscript of this paper. The authors of this paper will be immensely indebted to the valuable critical contribution he made to this paper despite his busy schedule.

References

Bai G, Xu Y (2014) Giant fields retain dominance in reserves growth. http://digital.ogj.com/ogjournal/20140203?pg=46#pg46.. Accessed 16 March 2019

Cobalt IE (2012) Update on West Africa and Gulf of Mexico Drilling Programs. http://phx.corporateir.net/External.File?item=UGFyZW50SUQ9NDUxOTQ0fENoaWxkSUQ9NDc3MTMzfFR5cGU9MQ==&t=1. Accessed 16 Mar 2019

Duval G, Mann J, Houston L (2015) Angola, Kwanza Basin: exploring further and deeper. GeoExPro 10(6). https://www.geoexpro.com/articles/2015/03/angola-kwanza-basin-exploring-further-and-deeper. Accessed 16 Mar 2019

Eni (2015) Eni discovers a supergiant gas field in the Egyptian offshore, the largest ever found in the Mediterranean Sea. https://www.eni.com/en_IT/media/2015/08/eni-discovers-a-supergiant-gas-

field-in-the-egyptian-offshore-the-largest-ever-found-in-the-mediterranean-sea. Accessed 16 Mar 2019

Heine C, Zoethout J, Mueller RD (2013) Kinematics of the South Atlantic rift. Solid Earth 4:215–253

Koning T (2014) Brazil's deepwater pre-salt oil play as a model for pre-salt oil exploration in deepwater West Africa. http://www.cspg.org/cspg/documents/Technical/Division%20Talks/International/05212014Koning.pdf. Accessed 16 Mar 2019

Koning T (2015) Is Brazil's prolific pre-salt petroleum geology a template for oil & gas exploration in West Africa? In: GeoConvention 2015: new horizons, Calgary, Canada. https://www.geoconvention.com/archives/2015/116_GC2015_Is_Brazils_Prolific_Pre-Salt_Petroleum_Geology_a_Template.pdf. Accessed 16 Mar 2019

Major RP, Holtz MH (1997) Predicting reservoir quality at the development scale: methods for quantifying remaining hydrocarbon resource in diagenetically complex carbonate reservoirs. In: Kupecz JA, Gluyas J, Bloch S (eds) Reservoir quality prediction in sandstones and carbonates. AAPG, Memoirs, Tulsa, OK, 69, pp 231–248

Moczydlower B (2014) Brazilian pre-salt & Libra: overview, initial results & remaining challenges. https://www.kivi.nl/uploads/media/565f1082c89da/Pre-Salt_Presentation_to_KIVI_Oct14_R2.pdf. Accessed 16 Mar 2019

Mohriak W (2015) Pre-salt carbonate reservoirs in the South Atlantic and world-wide analogs. AAPG Search Discov. Artic. #51086 http://www.searchanddiscovery.com/pdfz/documents/2015/51086mohriak/ndx_mohriak.pdf.html. Accessed 16 Mar 2019

Moore CH (1989) Carbonate diagenesis and porosity, 1st edn. Developments in sedimentology, vol 46. Elsevier, Amsterdam, The Netherlands, pp 75–117

Nikolaou KA (2016) The discovery of Zohr gas field in Egypt '… a game changer…' impacts—opportunities. http://www.iene.eu/microsites/9thseeed/articlefiles/PDF-Session-VIII-part-II/Final-K-NIKOLAOU-IENE-Thessaloniki-June-29–30.pdf. Accessed 16 Mar 2019

Oddone D, Amaral A, Kury F, Barroso W (2017) "Oil and gas opportunities in Brazil" 2017–2019 bidding rounds. ANP—National Agency of Petroleum, Natural Gas and Biofuels. http://sciencedocbox.com/Geology/68865381-Anp-national-agency-of-petroleum-natural-gas-and-biofuels-oil-and-gas-opportunities-in-brazil-bidding-rounds.html. Accessed 16 Mar 2019

Petrobras (2010) Petrobras Announces Commerciality of Tupi and Iracema Offshore Brazil. https://www.offshoreenergytoday.com/petrobras-announces-commerciality-of-tupi-and-iracema-offshore-brazil. Accessed 16 Mar 2019

Roehl PO, Choquette PW (1985) Carbonate petroleum reservoirs. Springer, New York, pp 1–18

Teboul PA, Kluska JM, Marty NCM, Debure M, Durlet C, Virgone A, Gaucher EC (2017) Volcanic rock alterations of the Kwanza Basin, offshore Angola—insights from an integrated petrological, geochemical and numerical approach. Mar Pet Geol 80:394–411

Total (2016) Drilling begins on the Libra field in Brazil. https://www.total.com/en/media/news/news/drilling-begins-libra-field-brazil. Accessed 16 Mar 2019

Chapter 2
Conquering Carbonate Complexities: Understanding Geological Processes that Control Poro-Perm Relationships

K. Vasudevan

Abstract Carbonate reservoirs, although contain the lion's share of discovered In Place hydrocarbons globally, present the most complex challenges in reservoir characterization, accurate estimation of hydrocarbon volume and consequently in optimal field development planning and exploitation. The main causative of such complexities is the multi-scale heterogeneity in carbonate rocks that affect the rock fabric right from nanoscale to seismic scale, which renders any realistic modelling in spatio-temporal domain an arduous task. It has been observed that the porosity-permeability (poro-perm) relationship in carbonates does not exhibit any direct linear relationship contrary to siliciclastic reservoirs. Although it has been empirically demonstrated that reservoirs that have high depositional porosity (high energy carbonates) tend to have higher effective permeability, the complex diagenetic history, the natural compaction-induced fracturing at reservoir scale and tectonic-induced fracturing at the field scale, result in a very complex poro-perm relationship in most carbonate reservoirs. Added to this is the phenomenon of dual porosity-dual permeability reservoirs encountered in many carbonate reservoirs, makes the task even more challenging. The pore throat geometry and hence, the aspect ratio of pores in carbonates is very complex due to primary depositional control, various intrinsic and extrinsic factors, thermodynamic constraints, diagenetic potential and history and kinetic factors. The influence of Green House/Icehouse periods and the Milankovitch cycles on carbonate deposition imparts different sequence architecture and frequency of individual cycles resulting in large scale heterogeneities in the distribution of primary porosities. The diagenetic overprint on the primary rock fabric further renders the reservoir more complex. Thus, the poro-perm preservation, enhancement or reduction can be understood by unravelling the depositional cyclicity and the diagenetic overprint. Wherever well-preserved cores are available, this task can be accomplished relatively easily, but in cases where the data set are sparse as is often the case, the Gamma-ray and effective porosity logs can be used to decipher both the primary depositional cyclicity and the diagenetic cycles by using the detrending method. The analysis of Eocene, Oligocene and Miocene carbonates of several hydrocarbon fields of Mumbai Offshore basin has lucidly brought out the differing nature of Milankovitch cycles,

K. Vasudevan (✉)
GEOPIC, ONGC, KDMIPE Campus, Kaulagarh Road, Dehradun, India
e-mail: vasudevan_k@ongc.co.in

K. H. Singh and R. M. Joshi (eds.), *Petro-physics and Rock Physics of Carbonate Reservoirs*, https://doi.org/10.1007/978-981-13-1211-3_2

the depositional versus diagenetic cyclicity and the impact on the poro-perm relationships in the spatial and temporal domain. It has been observed that carbonates deposited during Paleocene Eocene Thermal Maxima (PETM) exhibit relatively thick, high-amplitude–low-frequency carbonate cycles with low clay volume (often <20%) with diagenetic enhancement of porosity at the top of the cycles corresponding to the long exposure surfaces with destruction of porosity in the lower part of the cycles. The poro-perm relationship in these reservoirs exhibits a relatively direct linear relationship although moderate scatter is observed. In contrast, the Oligocene and Miocene carbonates have high-frequency low amplitude cycles with frequent thin shale layers followed by shallowing up Mudstone to Grainstone cycles often capped by uranium-rich high Gamma high resistivity carbonates representing exposure hard grounds. The Poro-perm relationship in these carbonates is much more complex resulting in a higher degree of heterogeneity in the distribution of speed zones, baffles and seals.

Keywords Poro-Perm relationship · Milankovitch cycles · Oligocene · Miocene carbonates · Mumbai Offshore

1 Introduction

Approximately 40% of present global hydrocarbon production comes from carbonate reservoirs and are expected to continue in future years also mainly owing to numerous giant fields of Middle-East. Therefore, understanding the carbonate reservoirs and produce them effectively is the prime challenge to global E&P industries. Deciphering the enigma of carbonate rock's complex pore space, permeability barrier and conduits behaviour are the key challenges that geoscientists face.

Extremity is the common feature of carbonates. Carbonate reservoirs can be gigantic though the majority of the pores being microscopic. In such a case, matrix permeability would be immensely low while the fractures would act like highway allowing fluid to flow through them. This makes carbonate rocks significantly different from siliciclastic reservoirs due to different depositional process, depositional environments and complex diagenetic history (Anselmetti and Eberli 1993; Lucia 1995, 1999). Shallow and deep marine areas, evaporitic basins, lakes, etc. are the places of carbonate deposits. Majority of the ancient carbonates formed in a marginal marine environment while the modern carbonates are widespread in the deep marine settings. Carbonates being chemically less stable, undergo intense cementation, dissolution, dolomitization, etc., as a consequence of a change in water depth, burial depth, temperature and pressure (Brie et al. 1985). Often, intense diagenetic alteration completely obliterates mineralogy and texture of the original framework, causing carbonates to exhibit varied porosity types, such as interparticle, intraframe, moldic, vuggy and micro-cracks or fractures. The prime hurdle of quantitative carbonate reservoir characterization is the identification of producible economic reserves and to distinguish it from non-recoverable reserves. The producibility can be better understood

from the permeability estimation which in turn is related to the complexity of the pore structures mentioned above (Anselmetti and Eberli 1993; Lucia 1995, 1999; Baechle et al. 2005; Baechle et al. 2007). Therefore, for the purpose of delineation of the sweet zone and flow properties determination, prediction of pore throat architecture from seismic and well log is utmost essential. Presence of varied types of pore structures in carbonates makes characterization a very complex process to accomplish. The modified response of rock physics parameters due to diagenetic effects and the presence of different clay minerals within pores escalate the complexity to a greater degree.

2 Factors Controlling Carbonate Deposition

Biological control over the carbonate deposition is overwhelming. Over 90% of deposited carbonate is of biological origin. Distribution and species assemblage of carbonate-secreting organisms have changed significantly through geological time. Since the character of carbonate rock depends heavily on its parental organisms, therefore, the character of carbonates also changes significantly through geological time.

Carbonate deposition is controlled by various factors like Bathymetry, Eustatic Sea Level Change, Turbulence of water, Ocean circulation, Nutrients, Climate belts, Global Atmosphere, Tectonic setting, Biological community, etc. Deviation from the normality of in any single factor leads to the cessation of deposition.

Water Temperature: Temperatures between 25 and 30 °C are optimum for carbonate deposition. Temperatures above 35 °C kill carbonate-secreting organisms. Since more than 30 °C temperature is rare in the open ocean, so the main influencing factor is the absence of cold water.

Water Depth: The depth to which carbonate-secreting organisms can thrive is a function of light penetration. Therefore, water depth coupled with light penetration governs the carbonate deposition. In exceptionally clear water this limit can be extended up to 100 m but for normal cases, it ranges between 70 and 80 m.

Turbulence in water: Organisms don't flourish in turbid waters. Turbidity impedes the light penetration thereby restricts the carbonate deposition.

Nutrients: Carbonate-secreting organisms need continuous nutrient supply. The abundance of planktons is governed by the open ocean current that carries nutrients in solution. Currents are thus favourable to carbonate deposition.

Salinity: Normal salinity is required for carbonate growth. Organisms live within the salinity range 27–40%. Carbonate deposition is stopped by great floods of fresh water sweeping over them from land killing the organisms.

3 Carbonate Uniqueness

Carbonates and siliciclastic rocks are diametrically opposite to each other. Compositionally siliciclastic rocks are polymineralic, silica being the primary constituent, whereas carbonates are mono-mineralic or bi-mineralic (mineral composition is restricted to calcite/aragonite, dolomite, gypsum and evaporite minerals/anhydrite) only. Majority of carbonates rocks are in situ and having biological origin whereas siliciclastic rocks are having a mechanical origin and may have travelled thousands of kilometres from source before deposition. Mono-mineralic carbonates are vested with the complexity of multiple order starting from scale-dependent to petrographic to petrophysical. Key challenges associated with carbonates are complex multi-scale heterogeneity, low porosity-permeability correlation, complex sonic velocity, V_p/V_s, porosity relationship-pore size and types, wettability related issues, fracture compartmentalization impact, etc.

Unlike siliciclastics, pore architecture in carbonates are very complex and often shows polymodal pore systems. Presence of polymodal pore systems makes the petrophysical evaluation very difficult. It is often found that there exists no relationship between porosity and permeability which cumulated to give rise big difference between storage and flow capacity. Moreover, non-correlation in both numerical and spatial domain makes the job of model preparation a real nightmare.

Diagenesis plays havoc in case of carbonate. This is the single most significant difference between siliciclastic and carbonate systems. Almost all the carbonate rocks undergo diagenetic changes but the impact of diagenesis may be variable. Diagenesis can invert primary depositional texture and completely reorganize the pore network system. The impact of diagenesis on petrophysical properties and dynamic flow properties is still uncertain and poorly understood. The petrophysical response of two identical rocks but with different diagenetic episode can be extremely different. Two identical oolitic grains of sand subjected to two opposite diagenetic episode, e.g. early compaction followed by cementation and on the other hand, early cementation followed by compaction will have totally different contact architecture and hence have a differing response to P-wave velocity (Brigaud et al. 2010). The rock which has undergone early compaction will have grain to grain contact even after cementation. Therefore, P-wave velocity will be higher in this case. On the other hand, the rock which underwent early cementation will have cement between the two grains in all cases even after cementation. Cement acts as a cushion during the P-wave propagation and dampens its velocity. Therefore, P-wave velocity will be lower in this case.

The porosity-permeability relationship in carbonate is very complex. Different facies can have similar petrophysical, hydrodynamic properties while similar facies can have widely different properties. For a given porosity, a wide range of permeability is possible. High porous carbonates (>30%) often have negligible permeability (<1 mD) since micropores or disconnected moldic/vuggy porosity form a dominant porous network. Moderate porosity carbonates (15–20%) often have excellent permeability (>100 mD) because of well-connected pore network, e.g. via secondary

pores and fractures. Extremely low porous (2–4%) carbonates may have good permeability because of well-connected fractures (Karst breccia).

Carbonates have low sonic/density contrast between the reservoir and sealing unit. Velocity in carbonate is a function of the dominant pore types and total porosity. There exists Inverse porosity velocity relationship but significantly deviated due to dolomitization and presence of various pore types. Frame forming pore types such as moldic/vuggy porosity have significantly higher velocity at equal porosities compared to interparticle/micro/fracture porosity (Xu and Payne 2009). The validity of Gassmann fluid substitution in carbonates is uncertain owing to the complex presence of different pore system and multi-scale heterogeneity.

4 Porosity-Permeability Relationship

Porosity-Permeability distribution is a very critical factor in reservoir characterization. This distribution plays a significant role in determining completion strategies for the implementation of water flooding program, construction of simulation model (Shirer et al. 1978; Chopra et al. 1989). Each microfacies as per Dunham classification clearly demonstrate a different poro-perm relationship (Dunham 1962).

Matrix-supported facies such as mudstone, wackestone shows little correlation of porosity with permeability. Grain supported facies shows linear poro-perm relationship but subjected to diagenetic changes. Diagenesis acts in both ways. It can both increase or decrease the poro-perm relationship. Progressive compaction and cementation destroy both storage and flow capacity but leaching and fracturing works in the opposite way. Grain leaching increases the porosity but cement leaching and fracturing increase the permeability. Dolomitization can affect the poro-perm relation in a great way. A global study of limestone and dolostone indicates that (Ehrenberg et al. 2006), in deep-buried platforms average porosity in limestone is much lower than associated dolostones, but average permeability hardly differs for given porosity. But in shallow buried platforms the scenarios is totally reversed. Average porosity does not differ much for limestone and dolostone but there is a huge difference in average permeability, dolostones being more permeable. With an increase in burial depth, there is hardly any reduction of porosity in carbonates but in clastics the reduction is considerable.

Classically permeability is determined from porosity using Eq. (1)

$$\ln k = a\varphi + b \tag{1}$$

where k is permeability, φ is the porosity, a and b are arbitrary constants.

However, this equation is often based on statistically insignificant data sets and lacks theoretical background. A linear relationship between logarithms of porosity and permeability is assumed because it appears that permeability is log-normally distributed over the space but the correlation between two parameters may not show any relationship. Theoretically, porosity is independent of grain size but permeability

is strongly inversely proportional to grain size. The plot of porosity versus log permeability may indicate linear relationship but there remains very high and very low permeability zone within the same porosity level. The plot of porosity and permeability of all data contained from the routine core analysis of the cores retrieved from the NBP field of ONGC (Fig. 1) elucidates this complex poro-perm relationship. The present context exhibited clearly in the plot. If we take 10% porosity value, the variation of permeability ranges from 0.01 to 100 md.

Therefore, the estimation of accurate permeability from porosity data cannot be made from the traditional approach. There exist various alternative models for porosity-permeability transform, proposed by several authors (Timur 1968; Dubrule and Haldorsen 1986; Stiles and Hutfilz 1992; Dorfman et al. 1990) but lack theoretical background. Hence for any given rock type, the different relationships estimated for porosity and permeability are suggestive of the manifestation of different hydraulic units (Hearn et al. 1984; Slatt and Hopkins 1990).

Hydraulic Unit (HU) is the characteristic part of the reservoir facies within which the geological and petrophysical properties that influence the fluid movement are consistent within but different from the other rock facies while comparing on similar properties. Therefore, hydraulic flow unit (HU) is a part of the reservoir that has both lateral and vertical extension and with similar flow and geologic characteristics (Hearn et al. 1984). As already discussed pore geometry is the prime influencer of fluid flow through porous media. Pore throat attribute, in turn, is dependent on mineralogy (type, abundance, location) and texture (grain size, grain shape, sorting

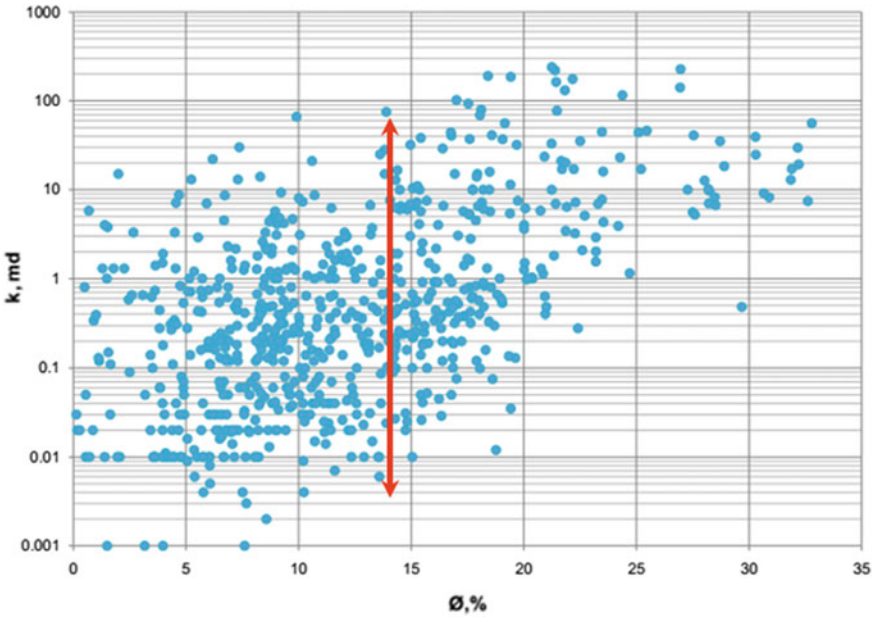

Fig. 1 Poro-perm relationship from cores of NBP field of ONGC

and packing). Various permutation and the combination of these petrophysical and geological properties could lead to the determination of distinct flow units that will have similar fluid transport properties (Abbaszadeh et al. 1996). The basis of HU classification is grouping of rocks that follow from fundamental flow attributes.

5 Rhythmic Sedimentation and Milankovitch Cycle

Depositional cyclicity in carbonates is influenced largely by Milankovitch Cycles viz. Obliquity, Eccentricity and Precession. Eccentricity is Earth's orbit shape around Sun. Orbital shape changes from more elliptical to less elliptical (0–5% ellipticity) with a cycle of 100,000 years. These oscillations, from more elliptic to less elliptic, are of prime importance for season change and glaciations. As a consequence, the distance between sun and earth changes and subsequently solar radiation received at the Earth's surface get reduced or increased in different seasons. Obliquity or Axial tilt is the inclination of the Earth's axis. Axial tilt oscillates from 21.5° to 24.5° with a periodicity of 41,000 years. Precession is the slow wobbling of Earth as it spins on its axis. It has a periodicity of 23,000 years. During half of the time North Pole points towards Polaris and another half of time, it points towards Vega. These perturbations due to orbital variations force climate changes which in turn triggers the progression and retreat of ice caps causing high-frequency eustatic cycles. As Ahr (2008) points out in his paper—"The amplitude of relative sea-level change in these cycles may range from 100 to 10 m depending on whether the sea level change happened during "icehouse" (extensive continental glaciation) or "greenhouse" (limited continental glaciation) times". The thickness of polar icecaps increases to its maximum during icehouse periods. Increase and decrease of ice sheets of the size of continents are controlled by Milankovitch cycles and the subsequent sea-level changes are huge, often beyond 100 m. The magnitudes of the changes due to the glacio-eustatic sea-level generally exceed the background sea-level variation. These sequences which are high-frequencies are greater than the high-frequency counterparts caused by greenhouse effect. There exist differences in porosity evolution and diagenetic trends between greenhouse and icehouse conditions. The high-amplitude sea-level changes in icehouse condition associated with high-frequency sequences under humid climatic conditions lead to the formation of deep, intense and overlapping karst. During lowstands, hydrologic head in open meteoric aquifers will create rapid meteoric water flux and intensely modifies the primary porosity. The entire platform will be exposed during arid conditions at high-amplitude low stands resulting in massive low stand evaporite deposition in adjacent basins. Under greenhouse conditions in a humid climate, surfacial karst will develop at the top of sequences. Sequence-bounding unconformities will be the place for the development of open gravity-driven aquifer systems. Because of lower water flux, the modification of porosity during icehouse times will be more intense than greenhouse periods.

To understand the cyclicity as observed in the logs, detrending approach has been followed. Detrended logs were generated using the operation stated in Eq. (2):

$$x_{\mathrm{d}} = x_i - \overline{x} \tag{2}$$

where,

x_{d} Detrended log value
x_i Recorded log value t particular depth point i
$\overline{x}$ Mean value of recorded log in the particular section.

The detrending approach brings out the cyclicity very clearly. Different detrended logs provide different information, e.g. detrended Gr log indicates the cleanliness of the facies and in turn infers about the depositional energy and when coupled with detrended effective porosity logs the diagenetic alteration cycles can be inferred.

Using this approach, the cyclicality pattern of carbonate formations from Eocene to Miocene age of Mumbai Offshore basin is analyzed. Carbonate of Middle to Late Eocene age shows very broad cyclicity (Fig. 2) on detrended GR log indicating greenhouse period. When this detrended GR log is interpreted along with detrended effective porosity logs it brought out that upper part is heavily karstified as its showing both dirty and facies with huge porosity. This is the sign of secondary porosity enhancement through diagenesis. On the contrary, the middle part is bone tight in both clean and dirty facies indicating porosity destruction through diagenesis.

Early Oligocene formation shows an increase of cyclicity as a number of cycles in both GR and Effective porosity logs increase (Fig. 3). This is the initiation of the Ice house period. Ice house period prevails in overlying Late Oligocene Formation

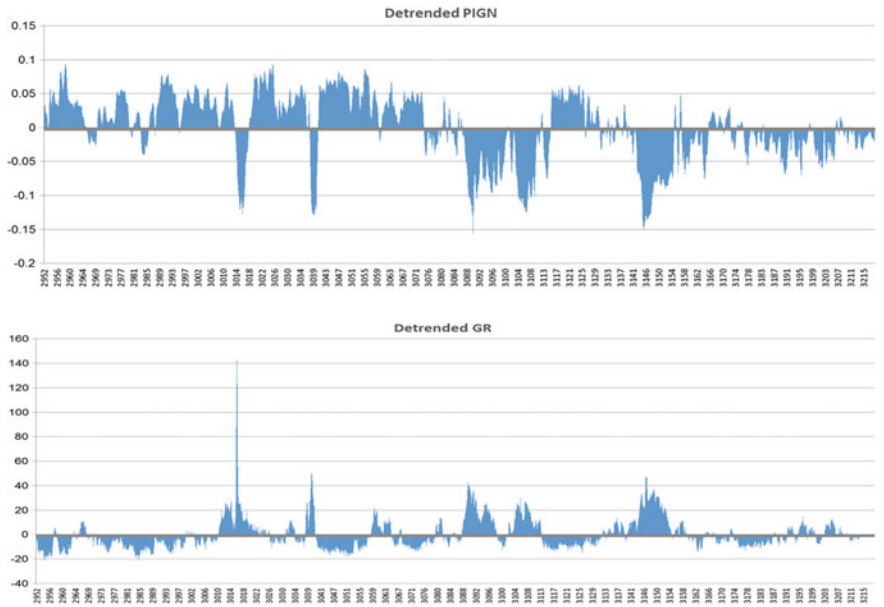

Fig. 2 Detrended GR and effective porosity logs eocene carbonate

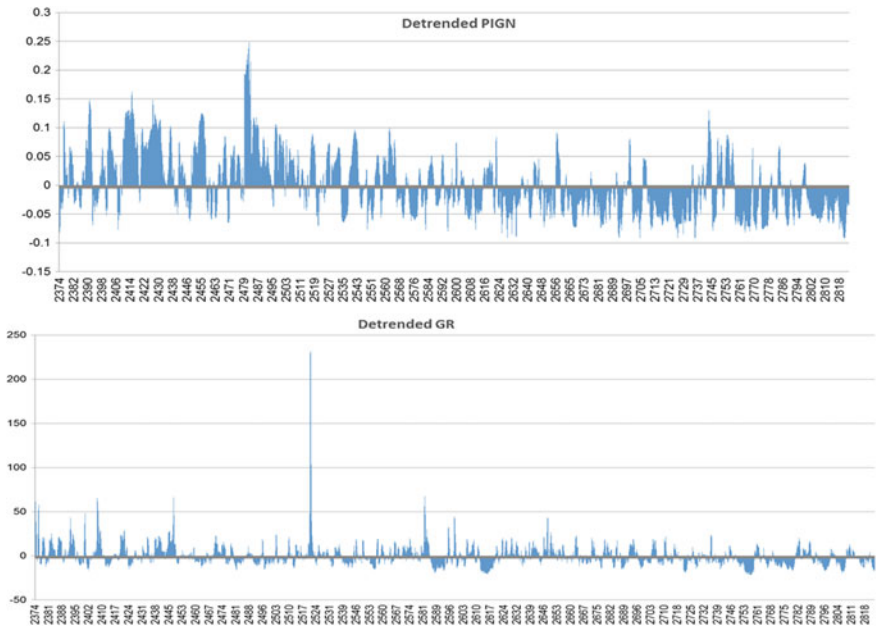

Fig. 3 Detrended GR and effective porosity logs early oligocene carbonate

(Fig. 4) of Late Oligocene age and Bombay Formation of Miocene age. Bombay Formation shows a very high frequency of oscillations indicating the smaller amplitude of sea-level fluctuation (Fig. 5).

To quantify the periodicity of the cycles observed in the logs, Fourier Transform was applied to change amplitude domain to the frequency domain. Before applying the transform, a depth log was converted to time log using the standardized markers' age. One conspicuous peak at ~400 k.y. after the fundamental frequency is observed for all the formations indicating the role of seasonal fluctuations associated with Eccentricity (Fig. 6). Change in the amplitude and frequency is also observed from Eocene to Miocene Carbonates through Oligocene. Fourier Transform high-amplitude and low-frequency signal mostly dominated in the Eocene carbonate. High-frequency signals started to appear in Oligocene carbonate and in Miocene high-frequency signals are most prevalent. High-amplitude–low-frequency signals are the signature of greenhouse period and icehouse period is marked by abundant high-frequency signals.

6 Conclusion

- Carbonate reservoirs present most complex challenges in reservoir characterization, In Place Volume estimation and in planning effective exploitation strategy.

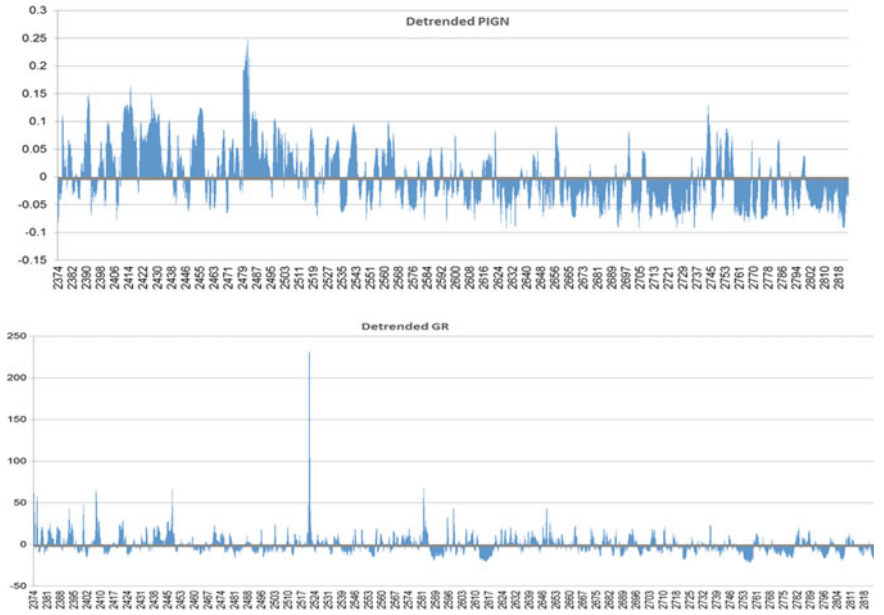

Fig. 4 Detrended GR and effective porosity logs late oligocene carbonate

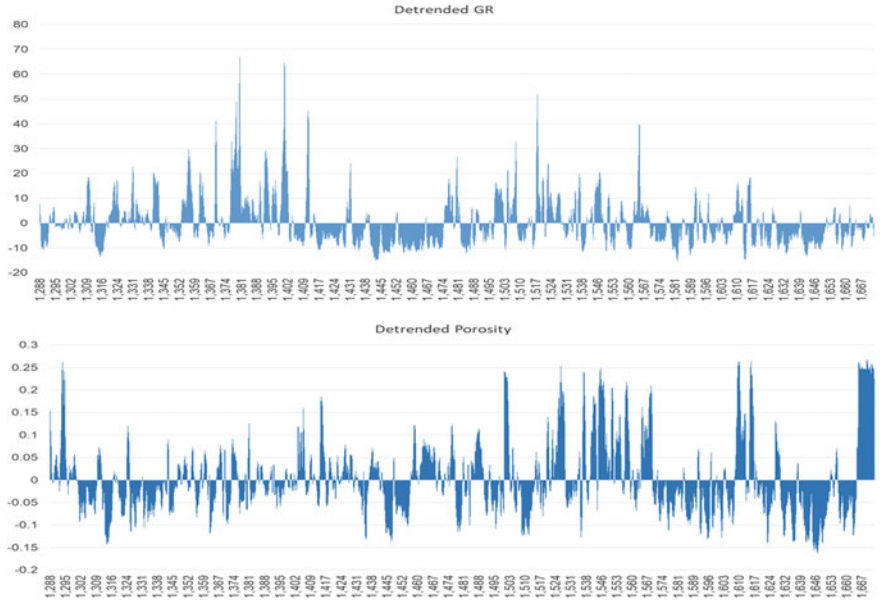

Fig. 5 Detrended GR and effective porosity logs miocene carbonate

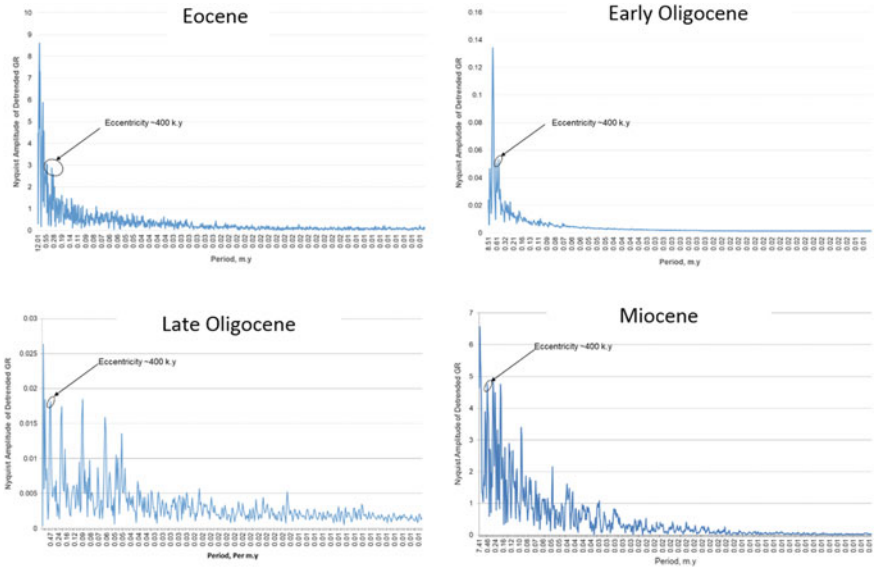

Fig. 6 Spectral density plot of carbonates of all ages

- In-depth understanding of the geological processes that control and influence the deposition and diagenesis of carbonates aids in the effective characterization of these complex reservoirs.
- The main causative of such complexities is the multi-scale heterogeneity in carbonate rocks that affect the rock fabric right from nanoscale to seismic scale.
- Contrary to siliciclastic reservoirs, Porosity—permeability (poro-perm) relationship in carbonates do not exhibit any direct linear relationship.
- Key challenges associated with carbonates are complex multi-scale heterogeneity, low porosity-permeability correlation, complex sonic velocity, V_p/V_s, porosity relationship-pore size and types, wettability related issues, fracture compartmentalization impact, etc.
- The porosity–permeability (poro-perm) relationship in carbonates do not exhibit any direct linear relationship.
- Although it has been empirically demonstrated that reservoirs that have high depositional porosity (high energy carbonates) tend to have higher effective permeability, the complex diagenetic history, the natural compaction-induced fracturing at reservoir scale and tectonic-induced fracturing at the field scale, result in a very complex poro-perm relationship in most carbonate reservoirs.
- The influence of Green House/Ice house periods and the Milankovitch cycles on carbonate deposition imparts different sequence architecture and frequency of individual cycles resulting in large scale heterogeneities in the distribution of primary porosities.

- The poro-perm preservation, enhancement or reduction can be understood by unravelling the depositional cyclicity and the diagenetic overprint.
- The gamma-ray and effective porosity logs can be used to decipher both the primary depositional cyclicity and the diagenetic cycles by using the detrending method.
- The analysis of Eocene, Oligocene and Miocene carbonates of several hydrocarbon fields of Mumbai Offshore basin has brought out that carbonates deposited during Paleocene Eocene Thermal Maxima (PETM) exhibit relatively thick, high-amplitude–low frequency carbonate cycles with low clay volume (often <20%) with diagenetic enhancement of porosity at the top of the cycles and the Oligocene and Miocene carbonates have high-frequency low-amplitude cycles with frequent thin shale layers followed by shallowing up Mudstone to Grainstone cycles often capped by uranium-rich high Gamma high resistivity carbonates representing exposure hard grounds.
- The poro-perm relationship in Middle to late Eocene carbonate reservoirs exhibit a relatively direct linear relationship although moderate scatter is observed whereas in Oligo-Miocene carbonates it is much more complex, resulting in higher degree of heterogeneity in the distribution of speed zones, baffles and seals.

References

Abbaszadeh M, Fujii H, Fujimoto F (1996) Permeability prediction by hydraulic flow units—theory and applications. Soc Pet Eng. https://doi.org/10.2118/30158-PA

Ahr WM (2008) Geology of carbonate reservoirs: the identification, description and characterization of hydrocarbon reservoirs in carbonate rocks. Wiley, Hoboken, NJ, USA

Anselmetti FS, Eberli GP (1993) Controls on sonic velocity in carbonate rocks. Pure Appl Geophys 141(2):287–323

Baechle GT, Weger R, Eberli GP (2005) Changes of shear moduli in carbonate rocks: implication for Gassmann applicability. Lead Edge 24(5):507–510

Baechle GT, Colpaert A, Eberli GP, Weger RJ (2007) Modeling velocity in carbonates using a dual porosity DEM model. SEG Tech Program Expand Abstr 26(1):1589–1593. https://doi.org/10.1190/1.2792799

Brie A, Johnson DL, Nurmi RD (1985) Effect of spherical pores on sonic and resistivity measurements. Society of Petrophysicists and Well Log Analysts, 26th annual logging symposium, June, Paper W:11

Brigaud B, Vincent B, Durlet C, Deconinck J-F, Blanc P, Trouiller A (2010) Acoustic properties of ancient shallow-marine carbonates: effects of depositional environments and diagenetic processes (Middle Jurassic, Paris Basin, France). J Sediment Res 80:791–807

Chopra AK, Stein MH, Ader JC (1989) Development of reservoir descriptions to aid in design of EOR projects. Soc Pet Eng. https://doi.org/10.2118/16370-MS

Dorfman MH, Newey JJ, Coates GR (1990) New techniques in lithofacies determination and permeability prediction in carbonates using well logs. Geol Soc Lond Spec Publ 48(1):113–120

Dubrule O, Haldorsen HH (1986) Geostatistics for permeability estimation. In: Lake LW, Carroll HBJr (eds) Reservoir characterization. Academic Press, Inc., Orlando, FL, USA, pp 223

Dunham RJ (1962) Classification of carbonate rocks according to depositional texture. In: Ham WE (ed) Classification of carbonate rocks. Am Assoc Pet Geol Mem 1:108–121

Ehrenberg SN, Eberli GP, Keramati M, Moallemi SA (2006) Porosity-permeability relationships in interlayered limestone-dolostone reservoirs. AAPG Bull 90(1):91–114

Hearn CL, Ebanks WJ, Tye RS, Ranganathan V (1984) Geological factors influencing reservoir performance of the Hartzog Draw field. Society of Petroleum Engineers, Wyoming. https://doi.org/10.2118/12016-PA

Lucia FJ (1995) Rock-fabric/petrophysical classification of carbonate pore space for reservoir characterization. Am Asso Petrol Geol Bull 79:1275–1300

Lucia FJ (1999) Carbonate reservoir characterization. Springer, New York, USA

Shirer JA, Langston EP, Strong RB (1978) Application of field-wide conventional coring in the Jay-Little Escambia Creek Unit. Society of Petroleum Engineers. https://doi.org/10.2118/7048-pa

Slatt RM, Hopkins GL (1990) Scaling geologic reservoir description to engineering needs. Soc Pet Eng. https://doi.org/10.2118/18136-PA

Stiles JH, Hutfilz JM (1992) The use of routine and special core analysis in characterizing Brent Group Reservoirs, U.K. North Sea. Society of Petroleum Engineers. https://doi.org/10.2118/18386-pa

Timur A (1968) An investigation of permeability, porosity, and residual water saturation relationships. Soc Petrophys Well-Log Anal Log Anal 9(4):8–17

Xu S, Payne MA (2009) Modeling elastic properties in carbonate rocks. Lead Edge 28:66–74. https://doi.org/10.1190/1.3064148

Chapter 3
Understanding Clastic-Carbonate Interplay in Distal Part of Tapti-Daman Sector of the Mumbai Offshore Basin and Its Implications on Hydrocarbon Prospectivity

Debakanta Biswal, Nasimudeen Nedeer, Subrata Banerjee and Kumar Hemant Singh

Abstract The prolific gas prone Tapti-Daman Block of the Mumbai Offshore Basin is one of the thrust areas for exploration and development along the west coast of India. Hydrocarbon accumulations generally occur in clastic and carbonate reservoirs of Early Oligocene Mahuva Formation and Late Oligocene Daman Formation. During Early Oligocene, the basin experienced the maximum subsidence that led to the deposition of Mahuva Formation. In the proximal part, the Mahuva Formation comprises of thick under-compacted claystone relating to the prograding delta from the northeast which has also resulted in the formation being overpressure in many instances. However, towards the distal part, the clastic influence diminishes and carbonates become more predominant. The close of Early Oligocene is marked by a minor period of non-deposition in Tapti-Daman area. During Late Oligocene, Tapti-Daman Block witnessed reduced subsidence resulting in a regressive coastline. During this period, a fluvial system with distributary channels, coastal bars, tidal deltas and other transitional environments encased in marginal silty and carbonaceous shale known as Daman Formation formed in the proximal part. The depositional regime changes from clastic to carbonate in the distal part particularly towards the southern and western part of the B9 area. Sea-level changes due to regional-tectonic and climatic parameters during Oligocene formed a major controlling factor for sediment deposition. The westerly tilt of the basin created additional accommodation space. The sediment supply during this period in the proximal part was controlled by increasing input of clastic material from northeast. However, in the distal part, a thick carbonate succession was formed due to low sediment supply, adequate rate of subsidence and conducive climatic conditions. As a result, the carbonate factory in the subsiding distal part of the basin was influenced by this interplay which further complicates the understanding of the distribution of reservoir facies. However,

D. Biswal (✉) · N. Nedeer · S. Banerjee
Adani Welspun Exploration Ltd., Welspun House, 3rd Floor, Lower Parel, 400013 Mumbai, India
e-mail: debakanta.biswal@adani.com

D. Biswal · K. H. Singh
Indian Institute of Technology Bombay, 400076 Powai, Mumbai, India

K. H. Singh and R. M. Joshi (eds.), *Petro-physics and Rock Physics of Carbonate Reservoirs*, https://doi.org/10.1007/978-981-13-1211-3_3

in the proximal part, the carbonate build-up was restricted by increasing input of silici-clastics and eventually led to the termination of the carbonate factory during Late Oligocene. The formation of a potential reservoir for hydrocarbon accumulation and seal was significantly influenced by this interplay, particularly along the clastic-carbonate transition areas in the distal part of the basin. Through this study, an attempt has been made to understand:

1. The basic litho-facies deposition, their disposition in time and space and the physical properties associated with these litho-facies that can aid in the prediction of reservoir distribution and in the refinement of geologic models.
2. Its implication on hydrocarbon accumulation through the integrated interpretation of seismic and well data and previous studies in the area.

About 20 wells from proximal to distal set-up along B12 and B9 areas have been analysed to develop an understanding of the distribution of potential reservoir rocks and thickness variation. Well correlation is carried out and a number of geological sections were prepared to understand the interplay between the clastic and carbonate litho-facies and its implications on hydrocarbon accumulation. An attempt has been made to delineate the sand, shale and carbonate litho-facies through integrated interpretation of 3D seismic data. Key seismic attributes have been generated to understand the limit of clastic input and carbonate distribution patterns.

Keywords Tapti-Daman · Clastic-carbonate · Mahuva formation · Potential reservoir rocks · Litho-facies

1 Introduction

The mixed carbonate-siliciclastic Daman formation depositional systems occurring in the distal part of Tapti-Daman block in Mumbai offshore basin consist of terrigenous clastic deposits from the Tapti-Daman delta system, marginally marine silty and carbonaceous shale and shelfal carbonates formed in shallow marine conditions. Many discoveries have been made in this deltaic facies consisting of sand bodies. These facies comprise of sand bodies deposited under various geological environments like coastal bars, distributary channels, tidal deltas and other transitional environments. Hydrocarbon is mainly being produced from Daman formation; the reservoirs facies are from delta front distributary channel sand and mouth bar silty sand. The extensive post-Miocene shale acts as a regional caprock in the basin. The local shale inter-beds within limestones act as a local cap rock for different pay zones (Goswami et al. 2007).

The study area is located in the western and southwestern part of Tapti-Daman block (Figs. 1 and 2). Being situated in the distal part of the basin, the development of reservoir grade sand is restricted due to increase in bathymetry and decrease in clastic influx. Towards further west and southwest, these sandstones are shaled out and grade into shelfal carbonates with shale intercalation. Carbonates are chalky and mixed type varying from mudstone, wackestone to packstone. At places, the growth of

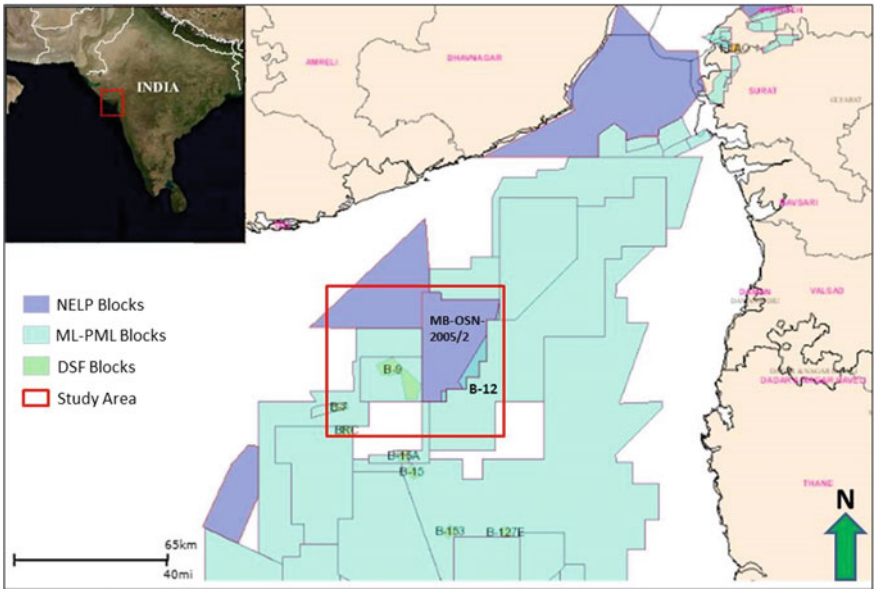

Fig. 1 Location of study area

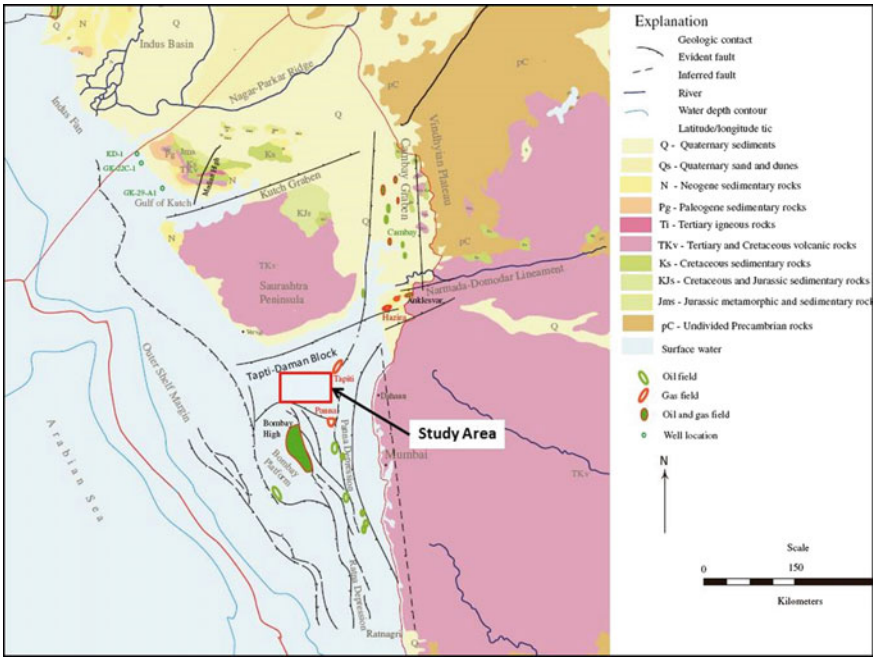

Fig. 2 Geological map of Mumbai Offshore Basin (https://pubs.usgs.gov/bul/2208/F/b2208-f.pdf, Wandrey 2004)

these limestones has been subdued due to increased clastic supply and vice versa. This has resulted in inter-fingering of clastic and carbonates lithology and significantly influenced the distribution and quality of reservoir facies and their hydrocarbon accumulation potential particularly along the clastic-carbonate transition areas in the distal part of the basin.

Through this study, an attempt has been made to delineate the sand, shale and carbonate litho-facies through well log correlation, integrated interpretation of 3D seismic data and key seismic attribute study.

2 Geological Setting

Tapti-Daman tectonic block is located in the shallow shelf region of Mumbai offshore basin on the Western Continental margin of India. The water depth varies from 25 to 30 m (Fig. 2). The area is marked by presence of vast thickness of sedimentary rocks ranging from Palaeocene to Recent. Figure 3 depicts the general stratigraphy of the area. It is based on well information which also indicates age relationships, lithostratigraphy and depositional environments.

The Palaeocene to Lower Eocene Panna formation is deposited under fluvial to shallow marine conditions. The Panna formation acts as the major source rock in the area. Panna formation is overlain by Middle Eocene Belapur formation. It comprises of mostly calcareous shale. Middle to Upper Eocene Diu formation overlies the Belapur formation. It consists of silty shales. Lower Oligocene Mahuva formation overlies the Diu formation. It comprises of mostly shales with thin bands of carbonates. The environment of deposition is estuarine to shallow open marine. Mahuva formation is unconformably overlain by Daman formation belonging to Upper Oligocene age. Potential sandstone reservoir rocks are abundant in Daman formation. These reservoir rocks are deposited under fluvial/estuarine regime with tidal influence. The Mahim formation belonging to Middle Miocene age overlies the Daman formation and is dominated shale lithology. This paper is mainly focused on Upper Oligocene Daman formation.

3 Deposition of Daman Formation

The Upper Oligocene in the distal part of Tapti-Daman is characterised by a rapid decrease in the sea level. During this period, there was reduced subsidence in Surat Depression. This has given rise to a regressive coastline (Source: http://www.dghindia.gov.in/assets/downloads/56cfd7ae55eb2Mumbai_Offshore_basin.pdf). An increase in clastic influx from north resulted in the deposition of thick clastics in an overall prograding deltaic regime. This has resulted in the deposition of a package of sediments comprising of sand bodies deposited in distributary channels, coastal bars, tidal deltas and other transitional environments. These

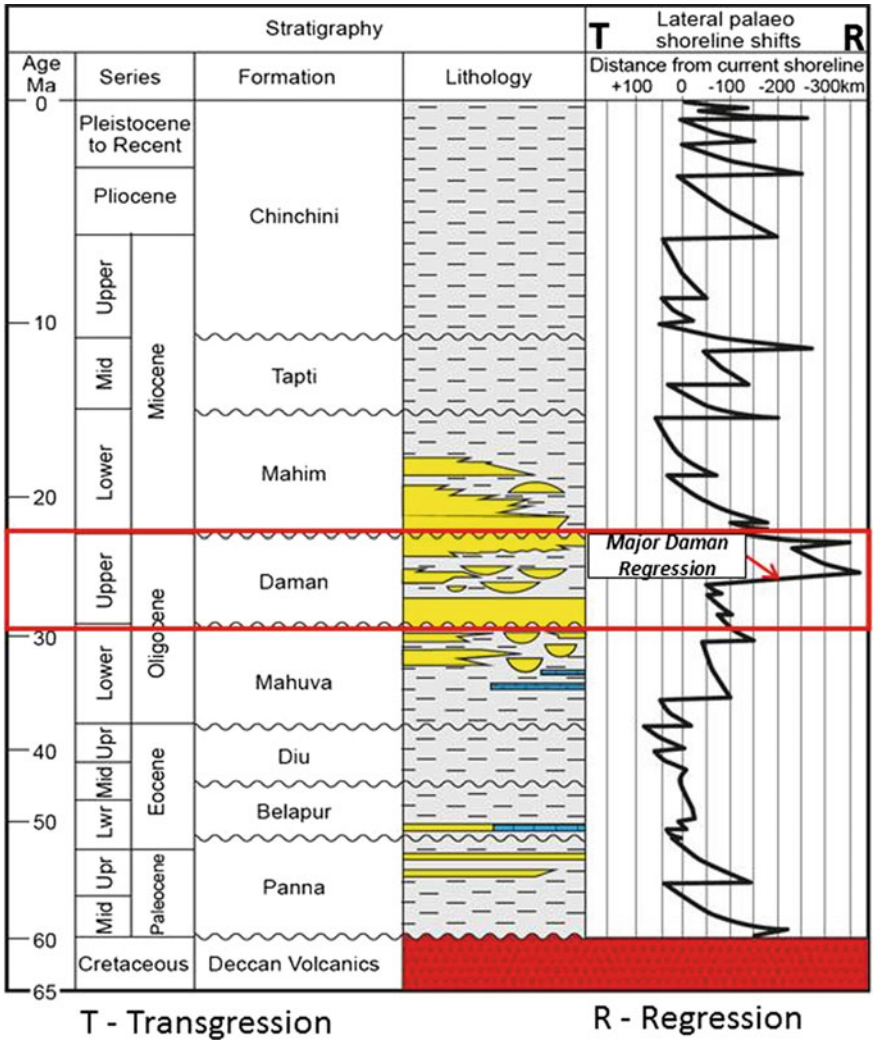

Fig. 3 Stratigraphy column of Tapti-Daman block (reproduced with permission from Huggett et al. 2015)

sand bodies are enclosed within normally pressured silty and carbonaceous shale deposited under marginal marine condition. The present area of study represents the southwestern limit of these prograding clastics. The litho-facies is represented by sub-aqueous prodelta thick clastics with very thin inter-beds of carbonates and shales in the distal part transitioning into off shelfal carbonates formed in shallow marine conditions towards further SW which is away from the influence of the delta deposits. Litho-biostratigraphic studies suggest that these sediments represent deposition in an intertidal (foreshore) set-up with periodic tidal influence.

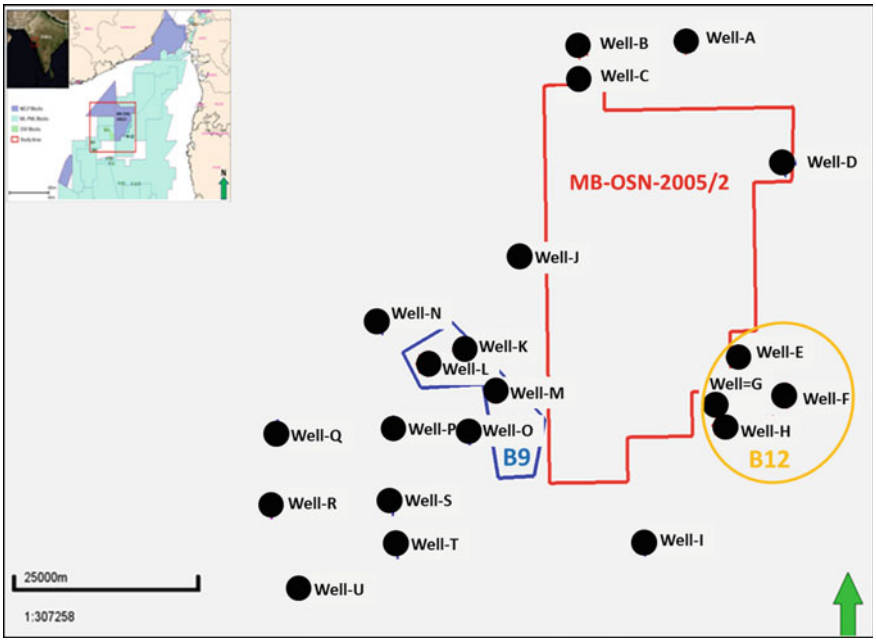

Fig. 4 Location of wells considered for this study

4 Daman Lithology

The Late Oligocene succession in the study area is represented by mixed clastic and carbonate rocks. The coarser clastic sediments dominating in the north-eastern part of the area in wells viz., Well-E, Well-J, Well-K, Well-M, gradually decrease towards southwest with an increase in carbonates (Fig. 4). In southwestern wells Well-Q and Well-P, dominantly limestone with finer clastics have been observed. Further, shale-carbonate inter-beds are prominent in the lower part and dominantly clastics (sand, silt and shale) in the upper part. Three wells situated in different parts of basin i.e. well Well-J in the proximal part, well Well-P in the distal part and well Well-M in proximal-distal transition are selected for detailed study and to develop a greater understanding of change in litho-facies in Daman as one move from proximal to the distal part of the basin.

5 Well-J

The sedimentary succession in well Well-J comprises of intercalations of limestone and Shale in the lower part of Daman formation and mainly intercalation of siltstone and shale with few limestone bands (Fig. 5). Limestone is off white, dirty white,

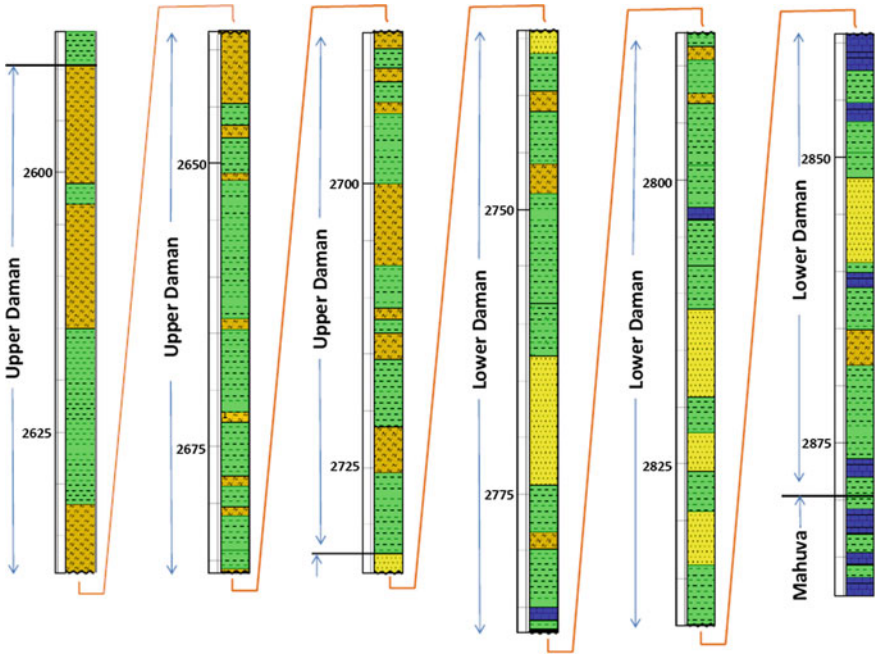

Fig. 5 Lithostratigraphy along Daman section in Well-J well

moderately hard, dense and comprises of bio-clasts, chalky at places. The upper part of Daman formation is dominated by sandstone, siltstone and shale. Sandstone is grey, moderately hard and compact, coarse to fine-grained, subangular to sub-rounded, poorly sorted and non-calcareous. Matrix is argillaceous. Siltstone is grey to dark grey, moderately hard, ferruginous, carbonaceous and non-calcareous with the argillaceous matrix. Shale is grey, brownish, fissile, thinly laminated and at places turning to claystone.

6 Well-M

The Lower Daman in well Well-M is mainly composed of shale with limestone inter-beds with the dominance of sandstone beds in the Upper Daman (Fig. 6). Sandstone and Sandy siltstones are fine to very fine grained, subangular to subrounded with occasional sand-size quartz grains at places, floating in the argillaceous matrix and have moderate microporosity. These are essentially delta front sands representing the farthest part of deltaic lobes. Shale is light to dark grey, moderately hard to hard, fissile, lenticular bedded, feebly calcareous, trending to sideritic siltstone at places. Limestone is found to be wackestone and packstone. Wackestones is light to dark grey, very hard, compact occasionally pyritic with poor porosity. Packstones is light

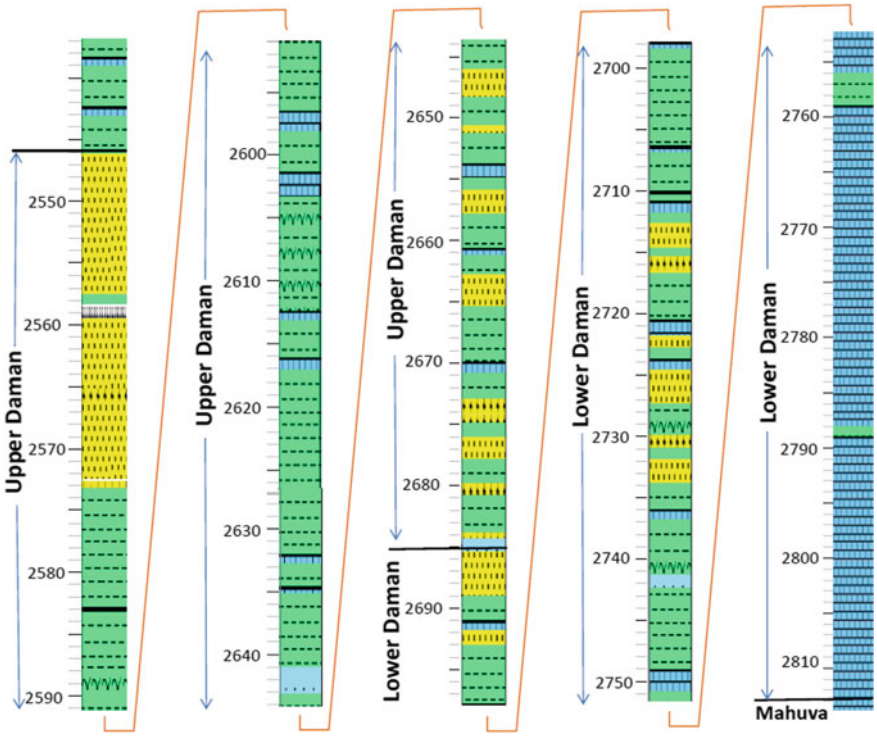

Fig. 6 Lithostratigraphy along Daman section in Well-M well

grey; off white, brownish, friable to moderately hard, compact, skeletal grains are common.

7 Well-P

Lower Daman section in Well-P well consists mainly of limestone with minor shale intercalations and upper part consists of mainly shale with minor limestone intercalations (Fig. 7). The limestones (foraminiferal wackestone) are dirty white to light grey to light brown at places, moderately hard, micritic, pyrite specks, and black specks, algal matter, small and larger foraminifera. Presence of grey clayey lenses is observed. Some foraminifera are ferruginised. Owing to low porosity, these limestones are poor reservoir rock. Shales are mostly grey, moderately hard and soft, silty, feebly calcareous. Siltstones are grey to brownish grey, hard, feebly calcareous with black ferruginous material. At places calcareous, greenish clay patches are seen. Pyritic nodules are also present.

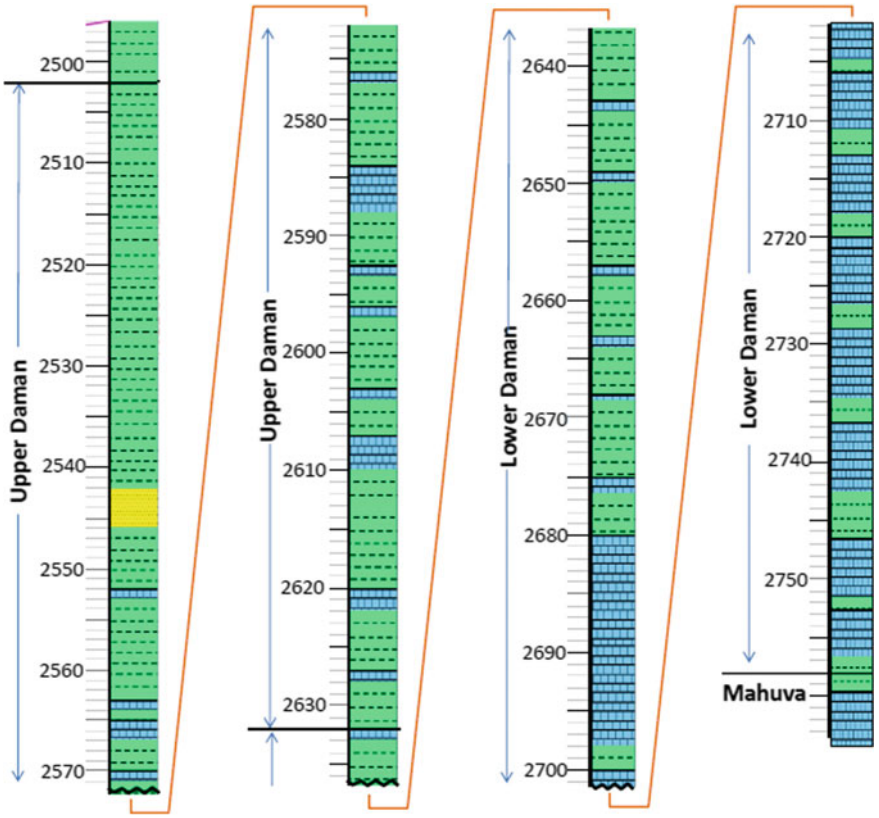

Fig. 7 Lithostratigraphy along Daman section in Well-P well

8 Log Correlation

To understand the facies variation across the study area, a number of well sections are prepared by carefully selecting the wells encompassing proximal to distal set-up (Figs. 8 and 9). Within the Daman Mega sequence, two sub-units are identified on the basis of log signature and litho-facies association. The gamma-ray values are lowest at the bottom, highest in middle and moderate on top.

Lower Daman: The lower sub-unit (Lower Daman) comprises of limestone with inter-bedded shale. A gradual change in litho-facies from shale in the northeast to limestone with an increase in thickness towards southwest has been observed (Fig. 8). These sediments were deposited in a shallow inner shelf set-up ranging from water depth 10 to 20 m. Two distinct depositional regimes are observed in this sub-unit. While the finer clastics dominate the area northeast of Well-M, the carbonates are the major litho-facies in wells Well-Q and Well-P in the area southwest of Well-M. In well Well-P, limestones are mainly sandy wackestone and chalky limestone

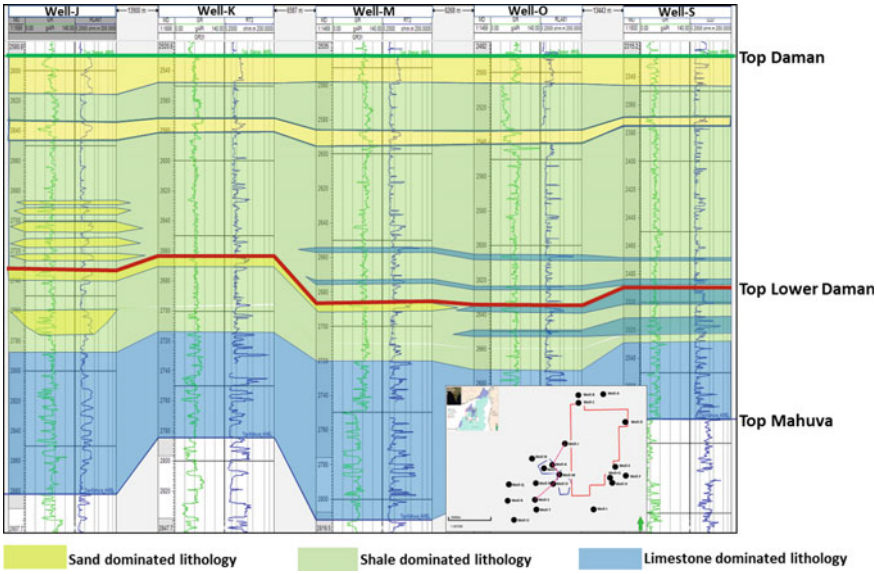

Fig. 8 Well correlation along wells J, K, M, O and S

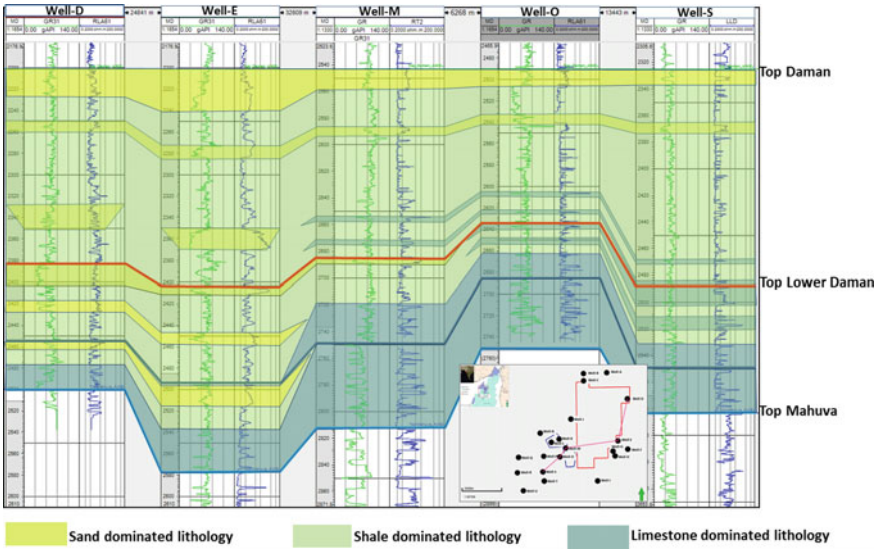

Fig. 9 Well correlation along wells D, E, M, O and S

with no appreciable porosity. Similar facies with no appreciable porosity have also been observed in mud supported wackestones of well Well-P and Well-K. These limestones in the lower part have shown an indication of gas. As stated above, the facies of this unit becomes more argillaceous in northeast across the Well-M well. Thin carbonates in wells Well-L, Well-M and Well-J are represented by compact, dense wackestones in the lower part and foraminiferal packstone in the upper part. In general, the porosity is moderate to poor and dominantly intra-granular in nature. Towards the north-eastern part where the facies is dominantly shaly, the thin inter-bedded mudstones show very poor vuggy porosity.

Upper Daman: The overlying sub-unit (Upper Daman) is characterised by thick shales with thin inter-beds of limestone in the southwest area of Well-Q and Well-P. In the area around the wells Well-L and Well-M and east of it, a gradual increase in sand, silt and shale have been observed. Limestones are either absent or present as very thin streaks. Sedimentological studies suggest that the sands are medium to fine and coarse to very coarse-grained, poorly sorted and associated with kaolinitic clay, carbonaceous matter, pyrite nodules and shell fragments. The sedimentary structures observed are massive bedding with floating clay clasts, bioturbated and lenticular bedding in finer clastics.

9 Facies Association

A wide range of facies is recognised in this mixed carbonate-siliciclastic environment that shows substantial variations both laterally and vertically. Three major facies association are identified representing proximal to distal transition from fluvial channel sand in the proximal part to intertidal to subtidal distal delta front grading into carbonate platform in the distal part.

Fluvial channel sand: The microfacies in sandstone are quartz arenite/quartz wacke with moderate to good inter-granular porosity. Further, quartz over-growth and argillaceous matrix have reduced the primary porosity. Siltstone is observed with good microporosity. These sands are gas-bearing in wells Well-A, Well-F, Well-E and Well-H. In the upper part of Late Oligocene in well Well-E, a thick channel fill has been observed. The sands of this channel fill are medium to coarse-grained, bioturbated with clay clasts. Further southwest up to the Well-M well, the channel character diminishes with a decrease in grain size and thickness of homotaxial sands.

Intertidal to subtidal distal delta: This indicates a transition of the environment from intertidal (in Well-E) to subtidal (equivalent to distal delta front) in wells Well-K and Well-L and Well-M with deterioration in reservoir quality towards the southwest. The southwestern limit of sand influx is observed up to northern and north-eastern part of B-9 area. Further southwest towards Well-O, Well-P and Well-Q, prodelta regime appeared to be prevalent which is marked by the complete absence of sands and dominance of shale in the area. They grade into an alternate with fluvial channel sand facies in the proximal direction and the carbonate in the distal direction (Figs. 8

and 9). This creates an inter-fingering pattern of clastics and carbonates in the distal delta front area which diminishes the abundance and quality of reservoir sand with the increased supply of carbonates from the down-dip.

Carbonate platform: Biostratigraphic studies carried out in some of the wells; suggest that at the commencement of Late Oligocene, sedimentation took place in a stable shallow shelf set-up with an active carbonate platform towards south and southwest of Well-O well thus restricting the sand influx up to north and north-eastern part of B-9 area. These carbonates are thick in the lower part. In the upper part, they are thin and are in alternation with thin inter-beds of silt and sand. In the southwestern part of the study area, these carbonates are mainly sandy wackestone and chalky limestone with no appreciable porosity. Further northeast in wells Well-L, Well-M and Well-J, the carbonates streaks are thin and represented by compact, dense wackestones in the lower part and foraminiferal packstone in the upper part. The limestones in the lower part have shown an indication of gas. In general, the porosity is moderate to poor.

10 Seismic Attribute Analysis

The sum of positive amplitude surface attribute on top of Lower Daman reflector shows low amplitude in the north-eastern part indicating very extensive clastic reservoir sand deposition that appears to be in the form of sheet sand distributed along Well-K, Well-L and Well-M area (Figs. 10 and 11). Sum of positive amplitudes increases from northeast to southwest. The reflection pattern in the seismic changes from low amplitude discontinuous reflection to high amplitude continuous reflection as we go SW towards Well-O.

While the area around Well-O well shows moderate amplitude values indicating non-reservoir facies and is dominated by shale inter-bedded with limestone, further southwest, high amplitude anomaly is observed due to significant impedance contrast indicating limestone as dominant lithology. Thus, seismic attribute analysis further supports the prodelta clastic dominance in the proximal part (north-eastern part of the study area) and grading into shale and limestone in the distal part.

11 Implication on Hydrocarbon Accumulation

The Daman formation is a progradational sequence, during which, a major delta system existed at north and north-eastern part of Tapti-Daman block. Most of the clastic deposited during this period were maximum limited to north and northeast to B-12 and B-9 areas. The coarser clastic sediments dominating in the north-eastern part of the area in wells viz., Well-E, Well-J, Well-M, Well-L, gradually decrease towards the southwest with an increase in carbonates. In southwestern wells Well-Q

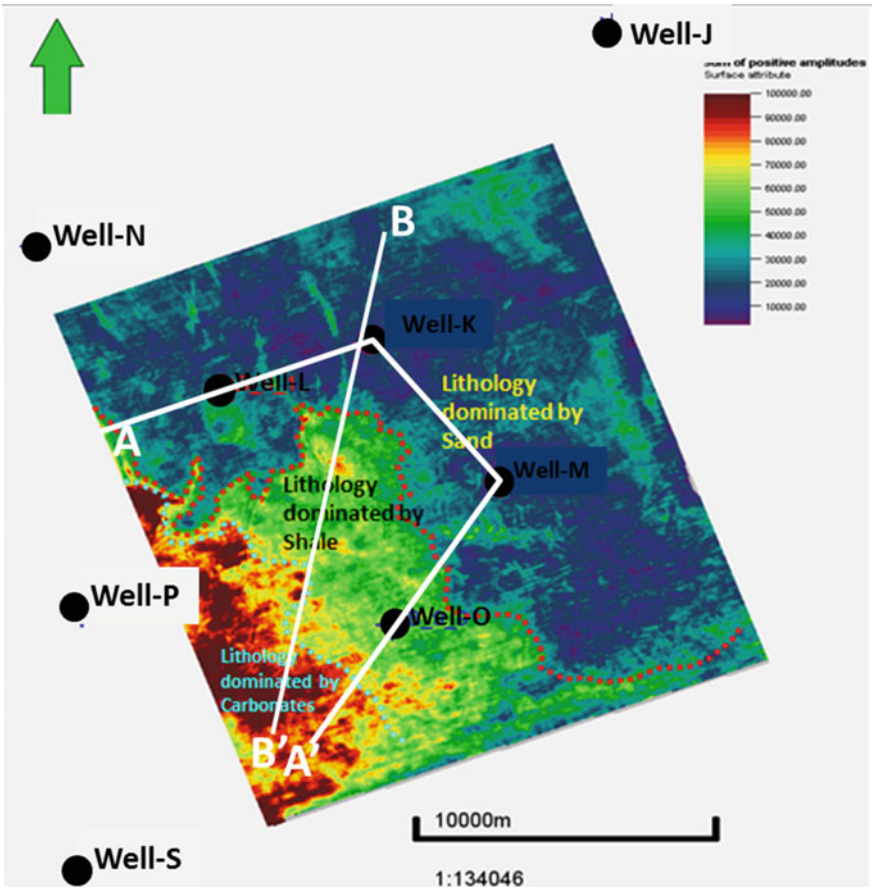

Fig. 10 Sum of positive amplitude on top of Lower Daman

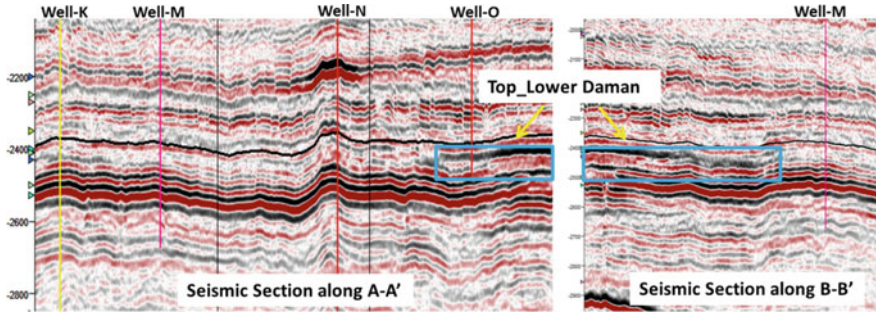

Fig. 11 Seismic sections across wells Well-K, Well-L, Well-M, Well-O indicating increase in sum of positive amplitude from NE to SW as highlighted in blue

and Well-P, Daman lithology is dominantly limestone with finer clastics has been observed. Further, shale-carbonate inter-beds are prominent in the Lower Daman and dominantly clastics (sand, silt and shale) in Upper Daman. However, during periods of major influx, finer sands were carried down to B-12 and B-9 areas, through delta front channels and canyons, and deposited as sheet sand, by tidal action. Though few channel signatures are observed in some wells like Well-E and Well-J, the wide spread areal extent of the sand and limited thickness as observed across all the wells, clearly indicate the sheet nature of sands. Thus, reservoir rocks in the study area are expected as sandstones from the upper part of Daman formation and limestone inter-bedded with shale from Lower Daman.

The reservoir in Lower Daman: In the southwestern part, Lower Daman formation is dominated by limestones that are mainly sandy wackestone and chalky limestone with no appreciable porosity. These are basically mud supported wackestones in wells Well-P and Well-S. Though the limestones in the lower part have shown indication of gas during drilling, these limestones are tight in nature with no appreciable porosity and therefore poor reservoir. The facies of this unit becomes more argillaceous towards northeast. Thin carbonates in wells Well-L, Well-M and Well-J are represented by compact, dense wackestones in the lower part and packstone in the upper part. In general, the porosity is low indicating poor quality of reservoir.
Reservoir in Upper Daman: In the north-eastern part, towards Well-K and Well-E, the Upper Daman is dominantly clastics with reduced influence of carbonates. These clastics have shown the presence of hydrocarbons on testing. Geological analysis suggests that these clastics represent the distal part of prograding Late Oligocene delta from Tapti – Daman area and deposition in an intertidal regime with tidal influence towards the northeast. The quality of these clastic reservoirs deteriorates in wells Well-O, Well-P and Well-Q. The significant feature of these hydrocarbon-bearing reservoir sands towards the northeast part of the study area is the presence of inter-granular porosity in the medium to fine-grained sands. Therefore, these reservoirs have good potential to hold a significant amount of hydrocarbon.

12 Conclusions

Hydrocarbon discoveries in the distal part of Tapti-Daman block in Mumbai offshore basin are largely restricted to the deltaic facies of Daman formation. These facies comprise of sand bodies deposited under various geological environments like coastal bars, distributary channels, tidal deltas and other transitional environments. Good quality medium to coarse-grained reservoir sands with moderate to good inter-granular porosity are prevalent in the north-eastern part of the study area.

The southwestern part of the study area is represented by a transitional environment from intertidal to subtidal (equivalent to distal delta front) with deterioration in reservoir quality. Further southwest a prodelta regime appeared to be prevalent which is marked by the complete absence of sands and dominance of shale and limestone

in the area. This creates an inter-fingering pattern of clastics and carbonates in the distal delta front area which diminishes the abundance and quality of reservoir sand with the increased supply of carbonates from the down-dip. These carbonates are thick in the lower part of Daman formation and thin and are in alternation with thin inter-beds of silt and sand in the upper part. Though the limestones in the lower part have shown indication of gas, the porosity, in general, is low indicating poor quality of the reservoir.

Analysis of seismic data and well data also suggests the prodelta clastic dominance in the proximal part (north-eastern part of the study area) and grading into shale and limestone in the distal part. Therefore, a proper understanding of the clastic-carbonate interplay and their delineation in space and time across Daman lithology will add significant value to the future exploration programme that will further enhance the chances of success.

Acknowledgements Authors are thankful to the management of Adani Welspun Exploration Limited for giving permission to publish the paper.

References

Goswami BG, Singh H, Bhatnagar AK, Sinha AK, Singh RR (2007) Petroleum systems of the Mumbai Offshore Basin, India. In: Proceedings of the AAPG annual convention, Long Beach, California, Apr 1–4, AAPG Search and Discovery Article 10154

Huggett JM, Burley SD, Longstaffe FJ, Saha S, Oates MJ (2015) The nature and origin of authigenic chlorite and related cements in oligo-miocene reservoir sandstones, Tapti gas fields, Surat depression, offshore western India. J Pet Geol 38(4):383–410

Pandey JP, Singh KRK, Singh M, Kalaiarasan T, Mukherjee RN, Marathe UG (2013) Late oligocene sandstone reservoirs of Saurashtra offshore, significance of their deposition—an integrated study resulting in regional clastic model. In: SPG 10th Biennial international conference & exposition held in Kochi, India. http://www.spgindia.org/expanded-abstracts-Kochi-2013. Accessed 17 Mar 2019

Wandrey C (2004) Bombay geologic province eocene to miocene composite total petroleum system, India. U.S. Geological Survey Bulletin 2208-F. https://pubs.usgs.gov/bul/2208/F/b2208-f.pdf. Accessed 17 Mar 2019

Chapter 4
Accelerated Weathering of Limestone for CO_2 Mitigation

Moulishree Joshi

Abstract Rock weathering is a natural phenomenon which brings about several changes on the Earth's landscape but it has one more useful function. It controls the CO_2 concentration in the atmosphere by precipitating the magnesium and calcium carbonates. The process is slow and takes place over a long period of time. However, if this process is accelerated, the atmospheric CO_2 can be removed in sufficient volumes at a faster rate and converted to bicarbonates thus mitigating the greenhouse effect. A geochemistry-based capture and sequestration process that reacts CO_2 with water to produce a carbonic acid solution is one of the methods to understand this phenomenon. This carbonic acid solution is then reacted with carbonate rocks to precipitate bicarbonates. The rate of reaction depends upon the temperature, flow rate and particle size. In the present study, the accelerated weathering of limestone was carried out using different sizes of limestone cuttings (4 mm, 500, 250, 100 and 50 μm) under different flow rates of carbonic acid (0.5, 1.0 and 1.5 L/min) for a duration of 2 h at a constant temperature of 80 °C. SEM and elemental analysis were done before and after the experiment. Results from the experiment showed that the highest flow rate (1.5 L/min) exhibits the greatest weight loss. This weight loss is brought about by the dissolution of calcium to release bicarbonate and carbonate ions. EDX analysis shows a reduction in both calcite and dolomite indicating dissolution of these two minerals. Acid attack on the samples forms dissolution patterns which are visible in SEM images. The principle mode of sequestration in limestone formation is ionic trapping. CO_2 trapped in this way in the form of bicarbonate solution can be safely discharged in a water body or reservoir for storage.

Keywords Carbon dioxide · Global warming · Accelerated weathering · Limestone

M. Joshi (✉)
Faculty of Chemical and Energy Engineering, Universiti Teknologi Malaysia, Johor Bahru, Malaysia
e-mail: moulishreej@yahoo.com

Present Address:
164, Amit Niketan, Nainital, Uttarakhand, India

K. H. Singh and R. M. Joshi (eds.), *Petro-physics and Rock Physics of Carbonate Reservoirs*, https://doi.org/10.1007/978-981-13-1211-3_4

1 Introduction

Global warming caused by increasing industrial and fossil fuel emissions is the biggest challenge being faced by the world in the twenty-first century (Lackner 2003; Pacala and Socolow 2004). Increasing CO_2 concentration has increased the global temperature significantly. By the year 2100, it has been predicted that the rise in the global temperature could be up to 4 °C due to the possible increase in the atmospheric CO_2 concentration by 540–970 ppm (Solomon et al. 2007; Houghton 2001). Sequestration of atmospheric CO_2 in geological formations and oceans has come up as one of the remedies of this problem (Metz et al. 2005). Among some of the proposed techniques for sequestering CO_2, injection into deep geological formations, particularly in saline aquifers, seems to be the most promising alternatives (Bachu et al. 1994; Holloway 2001; Metz et al. 2005). This technique is favoured as it offers substantial storage capacity for large volumes of CO_2. However, the success of this option is questionable as geological formations are susceptible to fracturing and thereby leaking the stored CO_2 back to the atmosphere which could prove hazardous (Hawkins 2004; Rochelle et al. 2004).

Another method includes a geochemistry-based capture and sequestration process in which initially CO_2 is captured which then reacts with water to form a carbonic acid solution (Rau and Caldeira 1999; Caldeira and Rau 2000). The solution then reacts and neutralizes with limestone, thereby converting the original CO_2 gas to calcium bicarbonate in solution. The chemical process can be summarized as follows:

$$CO_2 + CaCO_3 + H_2O => Ca_2^+ + 2HCO_3 \quad (1)$$

The dissolved calcium bicarbonate produced as a result of this process gets mixed and is diluted in the ocean. The concentration of calcium bicarbonate would add only meagerly to the large pool of these ions already present in seawater. This process is similar to the weathering phenomenon that is an ongoing continuous process on the earth surface which can naturally consume the anthropogenic CO_2 but the process is slow and takes place over thousands of years and hence is ignored as a potential technique in CO_2 mitigation. Venus, a planet close to the earth in terms of distance and size has a much higher concentration of CO_2 due to the fact that on the earth the runoff water from the incessant rains removes the topsoil and weathered rock which exposes the fresh rock from within, while Venus is devoid of such weathering process. The earth is believed to have a similar CO_2 budget as Venus, but instead of the substantial part of it is in the form of gas, it largely exists as carbonate rocks which are produced from chemical weathering of silicates (Holland 1984).

Accelerated Weathering of Limestone or AWL has been known to effectively convert CO_2 emissions to benign carbonates (Caldiera and Wickett 2005) without any environmental impact at a low cost. The present work was carried out to explore the feasibility of AWL technique in CO_2 mitigation using different sizes of limestone cuttings and different flow rates of carbonated water.

2 Experimental Procedure

Limestone samples were collected from a limestone outcrop at Pahang region of Peninsular Malaysia. The samples were ground and sieved to obtain different sizes (4 mm, 500, 250, 100, 50 μm). High purity CO_2 was injected into deionized water and stirred at the rate of 100 RPM to obtain carbonated water. The rock samples were injected with carbonated water at different flowrates (0.5, 1, and 1.5 L/min) for 2 h in a glass reactor after which the reactor was sealed for 2 weeks. After 2 weeks SEM and EDX were performed on the rock samples to analyze the effect of CO_2 and mineralogical changes as a result of carbonation.

The effect of the CO_2 flow rate on the dissolution of limestone is investigated from fifteen sets of experiments under atmospheric pressure and controlled temperature (80 °C) conditions. A glass reactor of volume 300 ml was used to prepare all solutions. In the experiment, the glass reactor was enclosed by an open water bath maintained at a constant temperature through heating filament (Fig. 1) (Jalilavi et al. 2014). The evaporation losses were reduced by cooling the reactor through a condenser cooled with tap water. The temperature and pH of the solution were measured at the beginning of the experiment. CO_2 was injected through the solution at different flow rates with the help of a gas bottle connected through a pressure regulator and a flow meter. Crushed rock samples of 4.0 mm particle size weighing 10 g were poured into a glass reactor containing 300 ml of carbonate water. CO_2 bubbled through the slurry at a flow rate of 0.5 L/min. The flow of the carbon dioxide was stopped after two

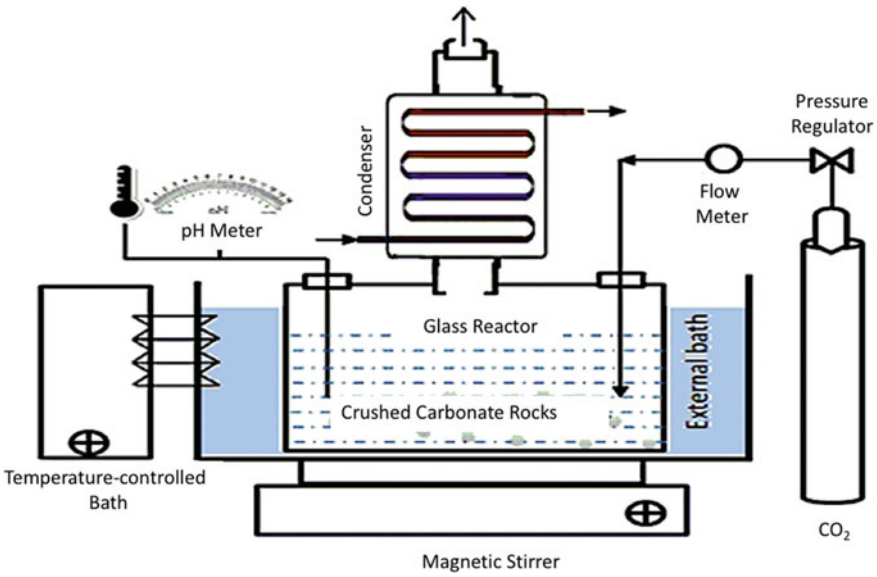

Fig. 1 The experimental setup to investigate the effect of the CO_2 flow rate on the dissolution of limestone (reproduced with permission from Jalilavi et al. 2014)

hours. A Whatman 45 μm filter paper was used to filter the solution immediately, and the filtered solution was sealed for four weeks for sample ageing or weathering to take place. The same procedure was repeated with 1.0 L/min and 1.5 L/min flow rate of CO_2 respectively. The filtered debris and rocks were washed using deionized water and dried at 120 °C overnight then weighed and prepared for the next set of experiments. The reactor glass was washed at the end of each experiment. The rock samples (4 mm) subjected to 1.5 L/min were analyzed with SEM and EDX before and after the experiment.

3 SEM Analysis

In order to study the effect of accelerated weathering on limestone, SEM investigation was conducted. Figure 2 show SEM microphotographs of limestone surface textures after the experiment. The surface abnormality and etching effects can be clearly seen in the SEM images.

4 Discussion

Behaviour of calcium carbonate (limestone) is governed primarily by equilibrium reaction:

$$CaCO_3 + H_2CO_3 = Ca^{+2} + 2HCO^{-3} \tag{2}$$

where $CaCO_3$ is the solid calcite while HCO_3 is the weak carbonic acid.

The reaction is reversible and the process continues until equilibrium is reached. Any process that increases the amount of CO_2 in a calcite system will promote the production of H_2CO_3. In this case, it is has been observed that the equilibrium shifts to consuming the increased CO_2. The increased H_2CO_3 leads to the reaction to shift to the right causing the dissolution of $CaCO_3$ in the system.

In the present work, it was observed that as the flow rate of CO_2 was increased from 0.5 to 1.5 L/min there was an increase in the rate of limestone dissolution. Since calcium is more reactive than magnesium, a significant reduction in the wt% of calcium was observed while there was the very little dissolution of magnesium. Dissolution of calcite is initiated because of the reduction in pH due to the increase in acidity. However, after ageing the limestone samples in the acidic environment resulting in the dissolution of calcium carbonate, the pH is seen to become higher indicating the increasing concentration of calcium carbonate.

The experiment was carried out at 80 °C. Further increase in temperature would disturb the equilibrium and move the reaction towards left and consequently more carbonic acid would be produced thereby precipitating calcium. CO_2 dissolution

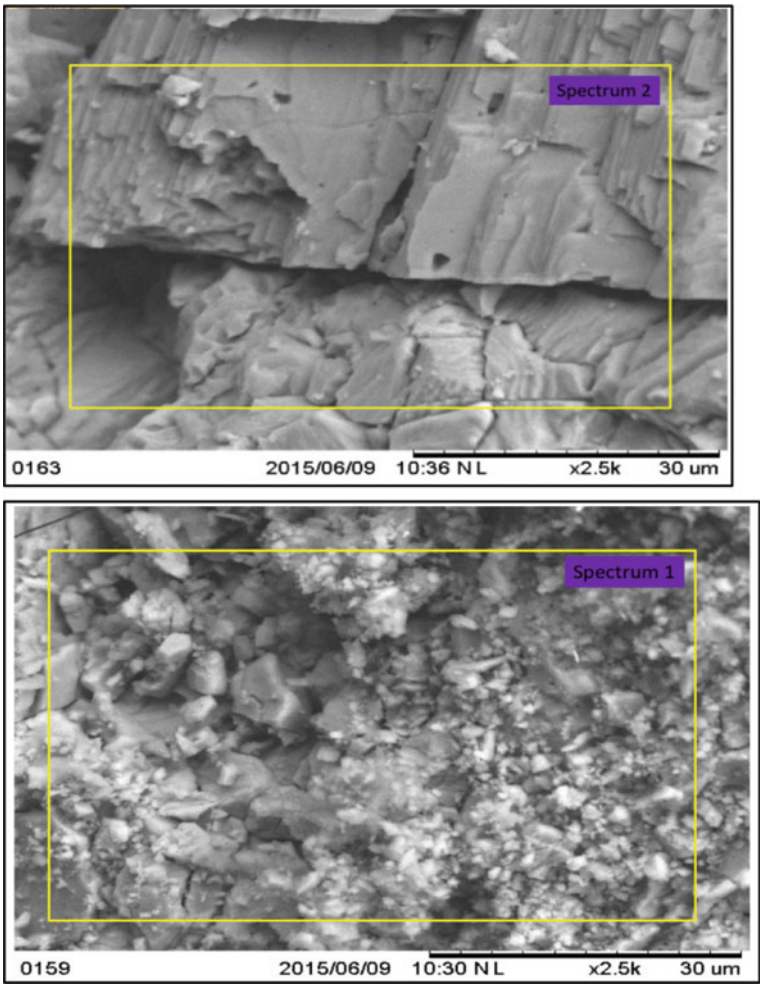

Fig. 2 SEM micrographs showing the effect of dissolution caused by accelerated weathering of limestone

in water is temperature-sensitive. In this work, the effect of temperature was not monitored.

As pH decreases, the number of hydrogen ions increases in solution. Carbonates go into solution as the pH is lowered releasing calcium carbonate in solution. When the limestone samples are left in the CO_2 solution for ageing, with an increase in the concentration of calcium ions in solution the pH of the solution swings towards basic thereby precipitating calcite.

Accelerated weathering of limestone can be used as a feasible solution for CO_2 mitigation as the overall procedure is very simple. The natural procedure of weathering can be enhanced by increasing the rate of reaction of CO_2 with the carbonate

rocks. The smaller the grain size the better is the rate of reaction so it may be assumed that fine-grained limestones are better candidates for this procedure than the coarse-grained varieties. The process is seen to hasten with an increase in the flow rate. The required experimental setup and the chemicals are inexpensive. Carbonate rocks required for the neutralization of carbonic acid are abundantly found on the earth's crust. The storage of CO_2 in this method is effective and long term. The end products of the reaction are environmentally benign.

For a suitable setting, for CO_2 mitigation AWL seems to be conducive and an attractive option since the required reactants are relatively inexpensive, environment-friendly and abundant. The technology is relatively modest and affordable and the storage is effective and long-term. The AWL process accelerates the CO_2 mitigation mechanism, the carbonate weathering.

Acknowledgements The support of Faculty of Chemical and Energy Engineering, Faculty of Mechanical Engineering, Faculty of Bioscience and Medical Engineering and Centre for Sustainable Nanomaterials is gratefully acknowledged.

References

Bachu S, Gunter WD, Perkins EH (1994) Aquifer disposal of CO_2: hydrodynamic and mineral trapping. Energy Convers Manage 35(4):269–279

Caldeira K, Rau GH (2000) Accelerating carbonate dissolution to sequester carbon dioxide in the ocean: geochemical implications. Geophys Res Let 27:225–228

Caldeira K, Wickett ME (2005) Ocean model predictions of chemistry changes from carbon dioxide emissions to the atmosphere and ocean. J Geophys Res Oceans 110(C09S04). https://doi.org/10.1029/2004JC002671

Hawkins DG (2004) No exit: thinking about leakage from geologic carbon storage sites. Energy 29:1571–1578

Holland HD (1984) The chemical evolution of the atmosphere and oceans. Princeton University Press, Princeton, NJ, USA

Holloway S (2001) Storage of fossil fuel-derived carbon dioxide beneath the surface of the earth. Annu Rev Energy Environ 26:145–166

Houghton JT, Ding Y, Griggs DJ et al (2001) Climate change: the scientific basis. Intergovernmental Panel on Climate Change (IPCC), Cambridge University Press, Cambridge, 881 p

Jalilavi M, Zoveidavianpoor M, Attarhamed F, Junin R, Mohsin R (2014) Artificial weathering as a function of CO_2 injection in pahang sandstone Malaysia: investigation of dissolution rate in surficial condition. Sci R 4:3645. https://doi.org/10.1038/srep03645

Lackner KS (2003) Climate change: a guide to CO_2 sequestration. Science 300:1677–1678

Metz B, Davidson O, de Coninck H, Loos M, Meyer L (2005) IPCC special report on carbon dioxide capture and storage. Cambridge University Press, New York, p 442

Pacala SW, Socolow RH (2004) Stabilization wedges: solving the climate problem for the next 50 years with current technologies. Science 305(5686):968–972

Rau GH, Caldeira K (1999) Enhancing carbonate dissolution: a means of sequestering waste CO_2 as ocean bicarbonate. Energy Convers Manag 40:1803–1813

Rochelle CA, Czernichowski-Lauriol I, Milodowski AE (2004) The impact of chemical reactions on CO_2 storage in geological formations: a brief review. Geol Soc London Spec Publ 233:87–106

Solomon S, Qin D, Manning M, Chen Z, Marquis M, Averyt KB, Tignor M, Miller HL (2007) Climate change 2007: the physical science basis. The contribution of working group 1 to the fourth assessment report of the intergovernmental panel on climate change. Cambridge University Press, Cambridge, UK

Part II
Empirical Models in Carbonate Reservoirs

Chapter 5
Petrophysical Modelling of Carbonate Reservoir from Bombay Offshore Basin

Monesh Sharma, Kumar Hemant Singh, Sanjay Pandit, Anil Kumar and Ashok Soni

Abstract The integration of well logs with laboratory measurements derived from core to analyse the reservoir characteristics of WELL P, of Bombay Offshore Basin, India. The reservoir properties such as permeability (k), Porosity (ϕ), shale volume (V_{sh}), lithology, water saturation (S_w), net pay thickness and other parameters were determined from well logs. The petrophysical model was derived from depth X150 m to X400 m. But the main focus of analysis were four pay zones named as Zone A (X195 m to X212 m), Zone B (X226 m to X282 m), Zone C (X299 m to X310 m) and Zone D (X338 m to X374 m). The logs used for analysis were CGR, NPHI, RHOB, LLD, DTCO and DTSM. Fluid types were identified by NPHI versus RHOB crossplot, VP, VS (vp/vs) versus DTCO crossplot and neutron/density log signatures which indicate the absence of gas and the presence of oil and water in the given well. The signatures of DTCO and DTSM followed each other indicating the absence of gas in the pay zones. Wet resistivity quick look technique was applied to locate the hydrocarbon-bearing zones of interest and any crossovers on density and neutron logs as indicators of the presence of oil zones. Saturation cross plots (Pickett plot) was used to determine the saturation exponent (n), cementation factor (m), tortuosity factor (a), and formation water resistivity (R_w), a prerequisite to their use in the determination of water saturation from Archie's equation. The main lithology in the region of the study was limestone (calcite) and shale (illite). Shale although present but was in a very small amount. The final volume fractions obtained of each mineral mainly calcite and dolomite from the petrophysical model were compared with those obtained from X-ray Diffraction (XRD). The average porosities of four zones were found to vary from 14.1 to 16.9% which indicated good porosity for a carbonate reservoir. The average water saturations of zones varied from 0.631 to 0.667. The results of the study indicate that the zones where the porosity is good, the measured permeability turns out to be poor (less than 5 mD) which suggests that the pores perhaps are not interconnected. This could be true for carbonates. Thus, the measured values need to be compared with the porosity and permeability values

M. Sharma · K. H. Singh (✉) · S. Pandit · A. Kumar
Indian Institute of Technology Bombay, Mumbai 400076, India
e-mail: kumar.h.singh@iitb.ac.in

A. Soni
GEOPIC, ONGC, KDMIPE Campus, Kaulagarh Road, Dehradun 248195, India

K. H. Singh and R. M. Joshi (eds.), *Petro-physics and Rock Physics of Carbonate Reservoirs*, https://doi.org/10.1007/978-981-13-1211-3_5

obtained from other laboratory measurements like Routine Core Analysis (RCA) and MicroCT scan to study the connectedness and non-connectedness of the pore-system in the cores.

Keywords Petrophysical model · Well logs · RCA · XRD

1 Introduction

Carbonates hold up to 60% of the world's hydrocarbon reserves and hence plays a major role in fulfilling the hydrocarbon demand of the coming generations. However, carbonates display strong heterogeneity in terms of porosity distribution and their permeability primarily due to the post-depositional processes like dissolution, recrystallization, precipitation, collectively known as diagenesis, which affects and alter the properties of the carbonate reservoirs entirely (Ahr 2008).

Porosity is defined as the ratio of pore volume to the total volume in a given rock sample. However, the porosity in Carbonates is completely in contrast to clastics (except in some cases). The genesis of the carbonate porosity lies in 'post-depositional chemical dissolution', and as a result the secondary porosity takes dominance (Akbar 2001) in the form of fracturing or dissolution channels or vugs. Normally the carbonate is made up of two items: (a) Finer grained matrix material which is very fine, sub-crystalline texture and interstitial material called Micrite. They could also be found as fine textured, coarsely crystalline called Sparite. (b) Allochems are Fossils, Molds, Oolites or Intraclasts.

One of the major challenges of petrophysical evaluation of carbonate reservoirs is to estimate important properties of reservoirs such as porosity, permeability, water and hydrocarbon saturations and mineralogy as accurately as possible. Unlike sandstone with well-established porosity, permeability, saturation, etc. the heterogeneous pore-system of carbonates defy routine petrophysical analysis since most of the relationships were developed for the clastic depositional environment (Lucia 1995; Marzouk et al. 1995).

An accurate prediction of the petrophysical parameters can be achieved by using log data along with the integration of core data obtained from the same well. The paper presents the preliminary results from Well P of the Bombay offshore region for all pay zones as inferred from the log data and Well Completion Report. The X-ray Diffraction (XRD) experiments and Routine Core Analysis (RCA) were performed on core samples to identify minerals present in the core samples which is then used to constrain the petrophysical models derived from log data analysis.

2 The Study Area

2.1 Geology and Stratigraphy

The Bombay offshore basin is a divergent passive continental margin basin which is situated on the continental shelf off the west coast of India. The basin is confined to the bounds of the western coastline of India, Bombay Offshore is a pericratonic rift basin located on the western continental shelf of India (USGS 2000). In the Northwest, it is bounded by Saurashtra peninsula, north by Diu arch, East by Indian craton and south by Vengurla arch which divides the Mumbai offshore with Kerala-Konkan basin. There are five structural provinces viz. Surat Depression in the north, Panna-Bassein-Heera Block in the east-central part, Ratnagiri in the southern part, Mumbai High-/Platform-Deep Continental Shelf (DCS) in the mid-west and Shelf Margin adjoining DCS and the Ratnagiri Shelf.

According to the DGH (2019), this is a category-I basin which has a proven commercial productivity and it covers an area ~116,000 km^2 for up to 200 m bathymetry. Bombay high field in the western offshore region of India is a giant carbonate field. The field was discovered in 1974 by Indian National Oil Company ONGC is producing since 1976 and now is in its mature phase. The field covers an area of 1200 km^2 with over 600 drilled well. The field produces from Miocene L-III limestone reservoir. It has around 10 separate hydrocarbon-bearing layers with very less vertical communication. The current study is from one such reservoir in a well of one such field in Bombay offshore basin in western offshore of India.

2.2 Well Log and Core Data

In our study area, Bombay High-DCS and Ratnagiri Block of Mumbai Offshore Basin has reservoir rock of carbonates of Lower Miocene period. The logs used for analysis were CGR, NPHI, RHOB, LLD, DTCO and DTSM. Core samples from carbonates were made available for research work in the laboratory (Fig. 1). The aim of this work is to integrate the laboratory measurements like RCA and XRD with traditional logs to derive the most accurate estimates of the petrophysical parameters of the reservoir (for instance lithology, hydrocarbon volume in place, porosity, water saturation, and permeability).

Data from one well (Well P) was made available for the study with a suite of logs, including caliper, spontaneous potential (SP), gamma-ray (GR), density (RHOB), neutron and density porosity (PHIN and PHID), PEF and shallow and deep resistivity (LLD, LLS) (Fig. 1). P- and S-wave sonic logs are also available for detailed analysis. The well is located in the South-West region of the Bombay Offshore Basin. The mentioned suite of well logs is used in evaluating petrophysical properties such as Porosity (phi), Hydrocarbon saturation (Sh), Water Saturation (S_w), Permeability

Fig. 1 Core samples for Well P collected from Regional Geological Laboratory, Panvel, Maharashtra, India

and Water Resistivity (R_w) and hence the Hydrocarbon potential of the region can be assessed.

2.3 Petrophysical Modelling

The log analysis begins with the identification of the zones of interest and demarcate the clean and shale baselines on the logs. Certain quick look methods such as density and neutron porosity crossover, wet resistivity method can be used which provide indicators that point to certain hydrocarbon zones requiring further investigation (Tiab and Donaldson 1996; Schlumberger 2008).

2.3.1 Lithology Determination

Lithology is best determined using Neutron-Density crossplot. The natural radiation of the formation is measured through Gamma log which are indicative of litho units in the subsurface in the vicinity of wells. On the crossplot, the clustering of data can be studied on the lithology line. This could indicate the dominant lithology present

in the area. The crossplots between Vp/Vs and DTCO could also be used to identify the lithology. These crossplots are also routinely used to identify the gas zones and shale zones (Mheluka and Mulibo 2018).

2.3.2 Wet Resistivity (Ro) Quick Look Technique

The quick look technique is applied to identify the hydrocarbon-bearing zones. In this method, Ro from the porosity and an estimate of formation water resistivity (R_w) is calculated. Ro is then plotted as an overlay on the deep resistivity curve. In water-bearing zones, Ro and the deep resistivity should overlay seamlessly while in hydrocarbon-bearing zones, the deep resistivity should be higher than Ro, with the separation increasing with increasing hydrocarbon saturation. The basic formulation of the technique is (Archie 1952):

$$\mathrm{Ro} = F \times R_w = (a \times R_w)/\emptyset^m \tag{1}$$

where Ro is the resistivity of the formation saturated with water, R_w is the Formation water resistivity, $\emptyset$ is the Porosity, and a is the tortuosity factor.

2.3.3 Shale Volume Estimation Using Gamma-Ray Log

The volume of shale can be estimated using non-linear and linear equation functions. A linear response is used because age information of lithounits is generally unavailable. The non-linear responses have been formulated by Steiber, Larionov (for older strata), Larionov (Tertiary) and Clavier. This method does not work well in areas where radioactivity is not primarily associated with the clays, such as in feldspathic sands. Linear Scaling method is used in this study for estimation of the volume of shale.

The volume of shale and Gamma-ray index are related as:

$$V_{sh} = I_{GR} = \left(\mathrm{GR}_{log} - \mathrm{GR}_{min}\right)(\mathrm{GR}_{max} - \mathrm{GR}_{min}) \tag{2}$$

where V_{sh} is the shale volume fraction calculated using the GR_{log} response, I_{GR} is the gamma-ray index, GR_{min} is the minimum gamma-ray from the log, GR_{log} is the gamma-ray reading from the log, and GR_{max} denotes the maximum gamma-ray from the log.

2.3.4 Porosity Estimation

The estimation of porosity is done using density and neutron logs. Porosity parameter is determined from the density logs by taking the bulk density readings obtained from the formation density log within each reservoir and then applying the value to Eq. (3)

for calculating the porosity. The porosity can be calculated from the density log as follows:

$$\varnothing_{\mathrm{D}} = (\rho_{\mathrm{ma}} - \rho_{\mathrm{b}})/(\rho_{\mathrm{ma}} - \rho_{\mathrm{f}}) \tag{3}$$

where $\varnothing_{\mathrm{D}}$ is the porosity calculated though the density log, ρ_{ma} is the matrix density, ρ_{b} is the bulk density as obtained from the log and ρ_{f} is the fluid density. The total porosity is the average of the two measurements obtained from Density ($\varnothing_{\mathrm{D}}$) and Neutron ($\varnothing_{\mathrm{N}}$):

$$\varnothing_{\mathrm{T}} = (\varnothing_{\mathrm{D}} + \varnothing_{\mathrm{N}})/2 \tag{4}$$

The effective porosity $\varnothing_{\mathrm{E}}$ is the actual porosity needed in determining water saturation and reserve estimation. The effective porosity is determined from the total porosity ($\varnothing_{\mathrm{T}}$) after eliminating the effect of shale using the following relationship:

$$\varnothing_{\mathrm{E}} = \varnothing_{\mathrm{T}}(1 - V_{\mathrm{sh}}) \tag{5}$$

2.3.5 Saturation Crossplot (Pickett Plot)

The water-bearing zones are equally important as hydrocarbon-bearing zones, hence they both need to be determined. The Pickett plot is one such technique which is used for their estimation. The Pickett plot provides information about the parameters Archie's constants like a, m, n and R_{w} which is crucial for determining the water saturation from Archie's equation.

$$\log(\phi) = -\frac{1}{m}\log(R_{\mathrm{t}}) + \frac{1}{m}(\log(a x R_{\mathrm{w}}) - n\log(S_{\mathrm{w}})) \tag{6}$$

2.3.6 Water Saturation Estimation

After calculating the effective porosity, water saturation is determined from Archie's equation. The Archie equation for calculating water saturation in clean, porous rocks is given by:

$$S_{\mathrm{w}}^{n} = \frac{a R_{\mathrm{w}}}{\phi^{m} \times R_{\mathrm{t}}} \tag{7}$$

$$S_{\mathrm{h}} = 1 - S_{\mathrm{w}} \tag{8}$$

where R_t is the Formation Resistivity, S_w is the water Saturation, ϕ is the Total Porosity, m is the cementation exponent, a is the Tortuosity Factor, R_w is the Water Resistivity and R_{sh} is the Resistivity of Pure Shale.

2.3.7 Permeability Estimation

Permeability is a measure of the ability of a porous media to transmit fluid (Tiab and Donaldson 1996). Permeability can be computed from empirical models like Wylie and Rose (Eqs. 9 and 10), Timur (Eq. 11) based on grain size, pore dimensions, mineralogy and surface area, or water saturation. The details of these methods can be found in Tiab and Donaldson (1996). Typically, the log derived permeabilities are valid only for estimating permeability in formations at irreducible water saturation. So before using the equations for determining permeability, whether the formation is at irreducible water saturation or not, must be determined.

$$K = \left(250 \times \frac{\phi^3}{S_{wirr}}\right)^2 \tag{9}$$

$$K = \left(79 \times \frac{\phi^3}{S_{wirr}}\right)^2 \tag{10}$$

$$K = \left(93 \times \frac{\phi^{2.2}}{S_{wirr}}\right)^2 \tag{11}$$

where K is permeability, ϕ is porosity and S_{wirr} is irreducible water saturation.

2.3.8 Core Sample Analysis

Core data can be used as a reference to study the parameters interpreted with wireline logs. Routine Core Analysis data points can be plotted on the log analysis depth plots for comparison. The volume fraction of minerals obtained from petrophysical models can be compared with those obtained from the XRD analysis for available for cores at respective depths. The XRD data points can also be plotted on the log analysis depth plots for comparison.

2.3.9 Net Pay

The porosity cut-off of 5% was used for the analysis while shale volume cut-off of 50% was defined for the quality of the reservoir rock. Water saturation, S_w, cut-off value of 70% was used to define pay. The reservoirs were defined by the porosity greater than 5% and less than 40% and shale volume less than 50%. For the net pay, if

the water saturation within the reservoir is less than 70%, it is considered to contain hydrocarbon.

2.3.10 Quanti-Elan

The petrophysical was created using the Quanti-Elan module of Techlog software provided by Schlumberger. The module follows the principle of inversion of the data. Linear equations in Quanti-Elan has a general form as:

$$L_1 = C_{11}V_1 + C_{12}V_2 + \cdots + C_{1n}V_n, \tag{12}$$

where V_n's are the volumetric components and C_n's are endpoints values for L_n equation at 100% of n component in the rock. A response equation is a mathematical description of how a given measurement varies with respect to each formation component. The simplest linear response equation can be expressed as:

$$\text{measurement} = \sum_{i=1}^{\text{fc}} V_i \times R_i \tag{13}$$

where, V_i is the volume of formation component i, R_i is the response parameter for ith formation component fc. Although some linear equations include additional terms, and the non-linear equations are more complex, the concept displayed by Eq. (12) remains the same. Hence, the total measurement observed is determined by the volume of each formation component and how the tool reacts to that formation component?

3 Results

The methodology described above is basically applied to create a Petrophysical model from X150 m to X400 m. There are four zones of interest in the WELL P which are described as pay zones A to D (reservoir zones) (Fig. 2). The depths ranges of pay zones are mentioned in Table 1.

3.1 Lithology Determination and Gas Indication Using

NPHI versus RHOB Crossplot

The crossplot calculated for NPHI versus RHOB is shown in Fig. 3. The depth between X150 m to X400 m shows most of the data points to cluster along the limestone and dolomite lines. The data points away from the dolomite line indicate

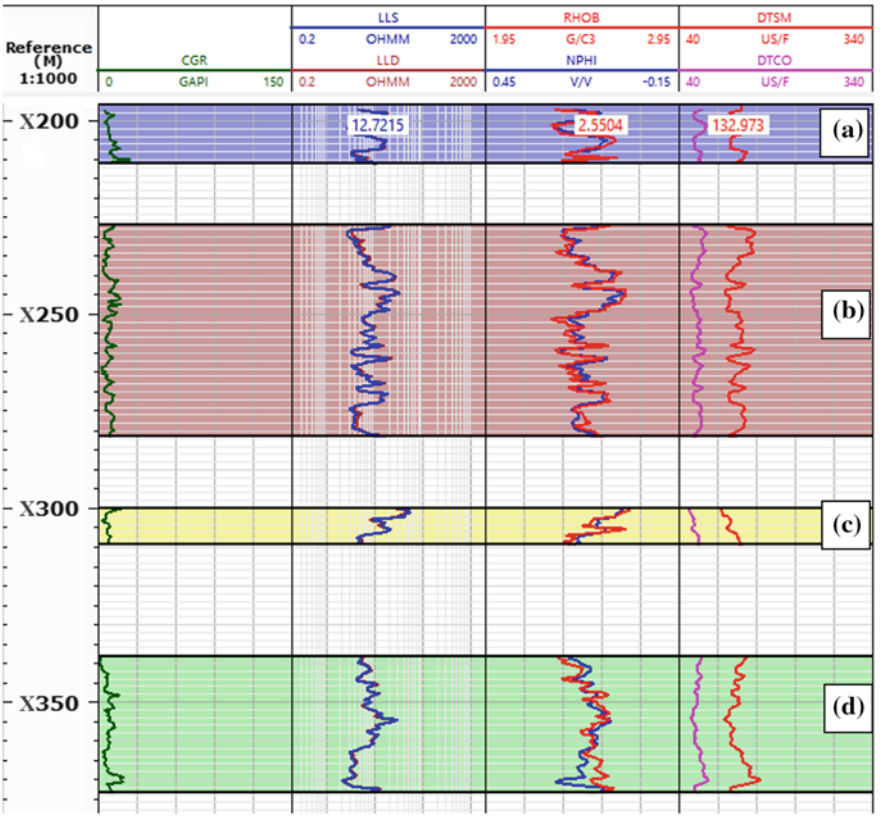

Fig. 2 Depth ranges of pay zones (A–D) highlighted on well log data of Well P

Table 1 Depth range of pay zones (A–D) in Well P

Pay zone	Top (m)	Bottom (m)
Zone A	X195	X212
Zone B	X226	X282
Zone C	X299	X310
Zone D	X338	X374

shale zones. There are no points towards low bulk density values which indicate that there are no gas zones present in the given data. Thus the dominant lithology in the reservoir is limestone.

Vp/Vs versus DTCO crossplot

The result highlighted in Fig. 3 is also confirmed from the Vp/Vs versus DTCO crossplot. If gas is present in the formation the compressional wave becomes slower, while the shear wave is not affected. The Vp/Vs versus DTCO in gas sand will, therefore, be different from a water-saturated sand. Thus, if DTCO becomes slower

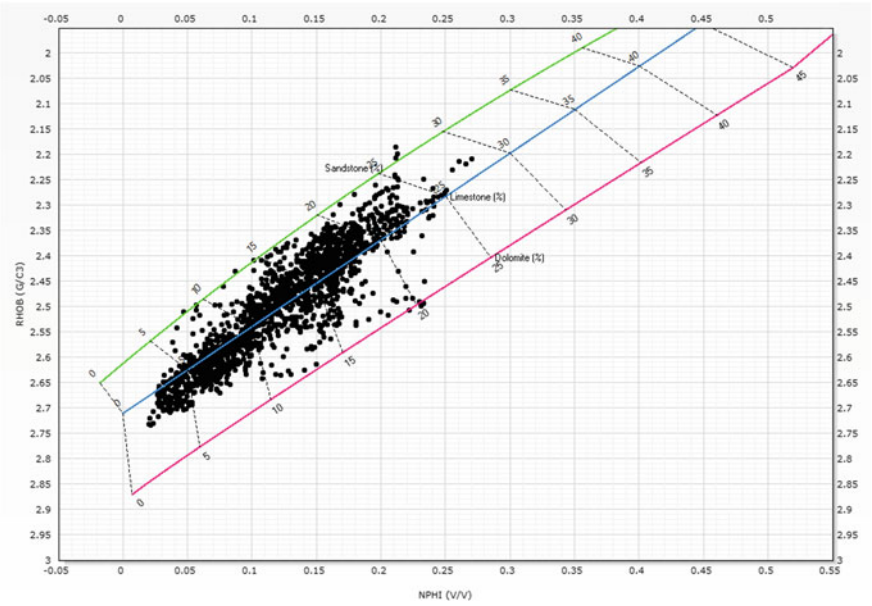

Fig. 3 NPHI (*Y*-axis) versus RHOB (*X*–axis) crossplot for WELL P from depths X150 m to X400 m

while shear stays constant (thus a lower VP/VS) then this can be interpreted as a qualitative indication that gas is present. It is only an indication of gas (or light oil), but it does not help quantify the exact amount of gas present. All the lines on the plot are theoretical lines based research on a few data sets, and not all formations follow the standard. Figure 4 shows most data points to cluster on the limestone line indicating that the prominent lithology is limestone and shale.

Saturation Crossplot

The Pickett plot shown in Fig. 5 provides the relationship between the porosity values and resistivity for the entire depth range of the reservoir for all four zones. The estimated values are $a = 1$, $m = n = 2$ and R_w to be 0.11 Ω m.

3.2 Depth of Interests from Wet Resistivity Quick Look Method

To illustrate the methodology, zone B is shown in Fig. 6 for the depth range X226 m to X282 m. At depths where LLD (Deep resistivity) exceeds Ro (Resistivity of formation water), the presence of hydrocarbon is indicated and is confirmed from the crossovers seen in RHOB and NPHI curves for corresponding depths.

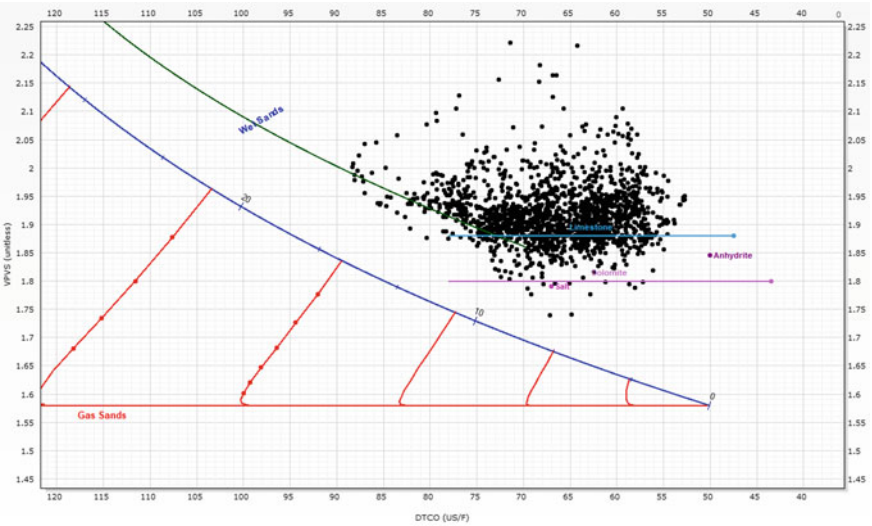

Fig. 4 Vp/Vs (*Y*-axis) versus DTCO (*X*-axis) crossplot for WELL P from depths X150 m to X400 m

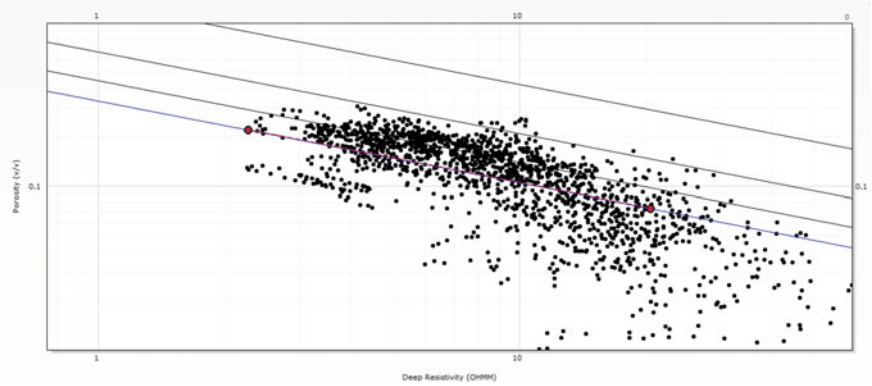

Fig. 5 Pickett plot of Porosity (*Y*-axis) versus Deep Resistivity (LLD) (*X*-axis) crossplot for WELL P from depths X150 m to X400 m

3.3 Petrophysical Model

4 Summary and Conclusions

The petrophysical well logs were used to derive petrophysical properties for the hydrocarbon-bearing zones. The resultant properties were then calibrated using the RCA and XRD from the core samples. The result of calibration can be summarised as follows (Figs. 7 and 8)

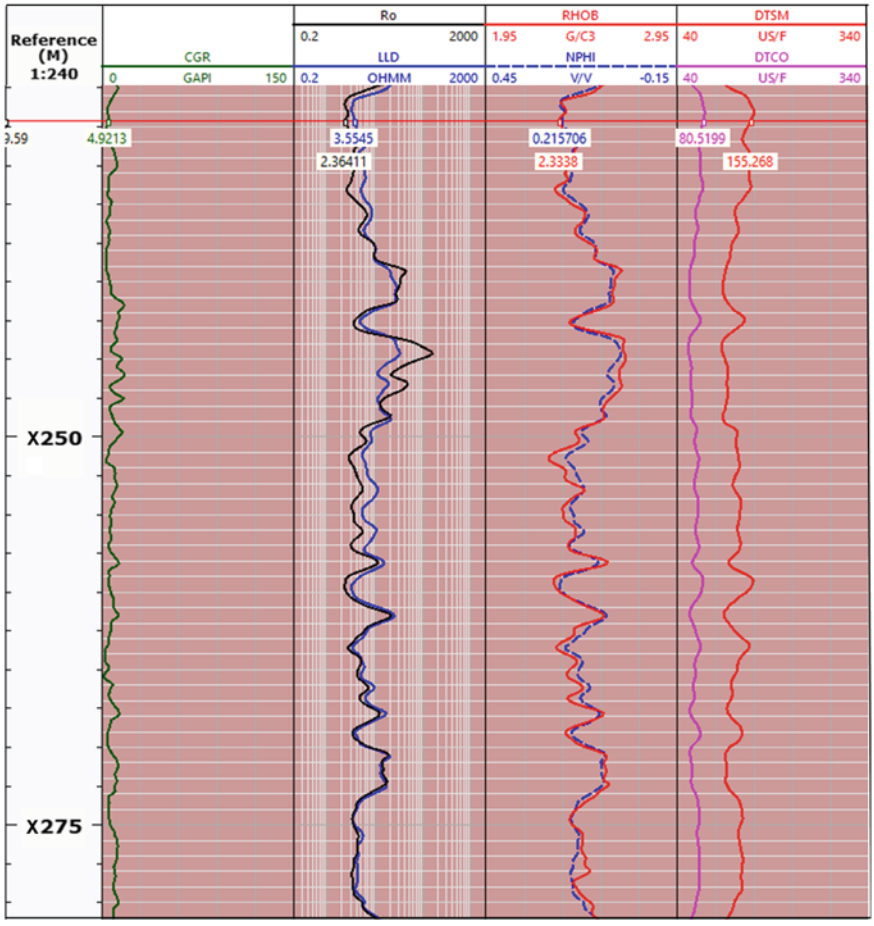

Fig. 6 Quick look Technique has shown for WELL P shown for zone B in the second track

1. The calculated petrophysical properties such as dry mineral volume fractions from well logs agree well with the volume fractions obtained from XRD.
2. The grain density and porosity calculated from well logs matches well with the grain density and porosity obtained from core samples.
3. The above properties obtained from well logs matches well with the core equivalent with the margin of error in the estimation of depth for core samples.

The resultant petrophysical properties such as average porosity, average saturation and average shale volume along with Net Pay and Net to Gross ratio has been presented in Table 2. The lithology is mainly calcite dominated with a small fraction of dolomite at a few intervals. The shale volume in the studied zone is negligible. The average porosity in the analysed zones is from 14 to 17% with an oil saturation

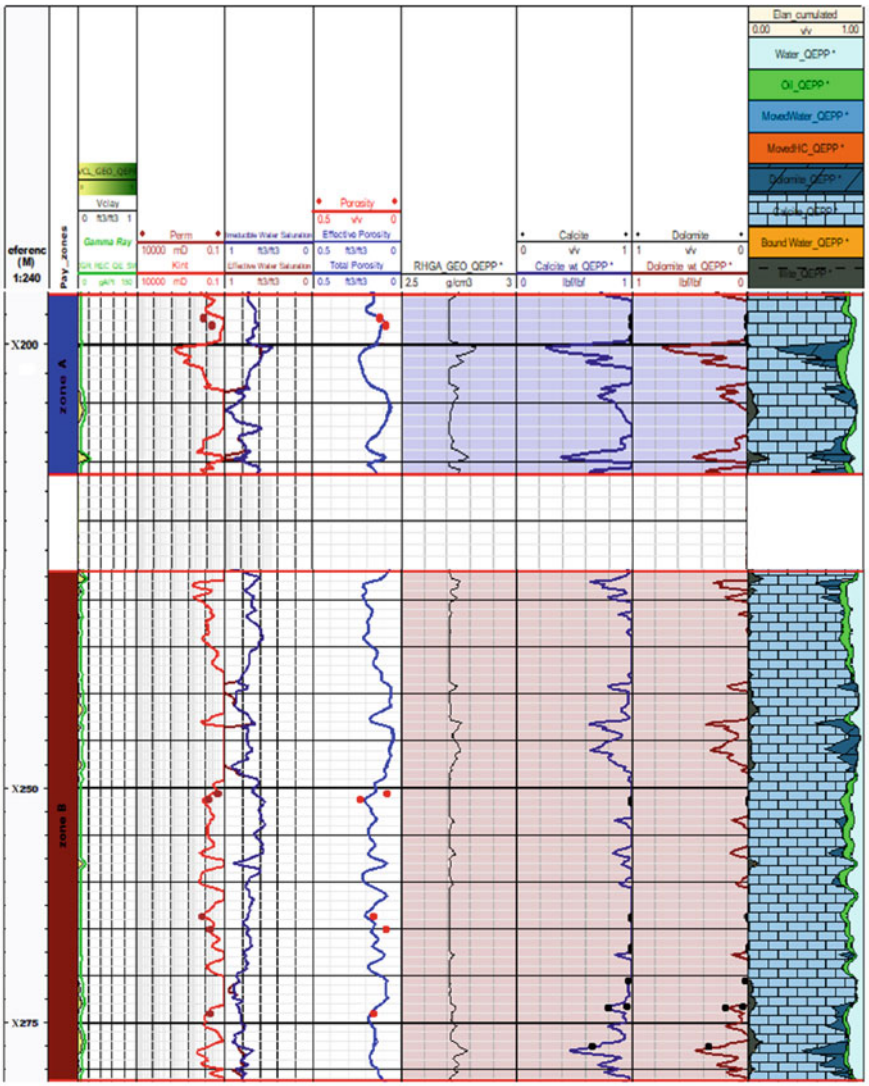

Fig. 7 Final Petrophysical Model for WELL P (from depth X195 m to X282 m). The shaded portions are Zone A and B. From left shale volume (first track), permeability (second track), water saturation (third track), porosity (fourth track), calcite volume fraction (fifth track), dolomite volume fraction (sixth track). Points in the second (permeability) and fourth (porosity) track indicate core data whereas in fifth (calcite volume fraction) and sixth (dolomite volume fraction) indicate XRD data

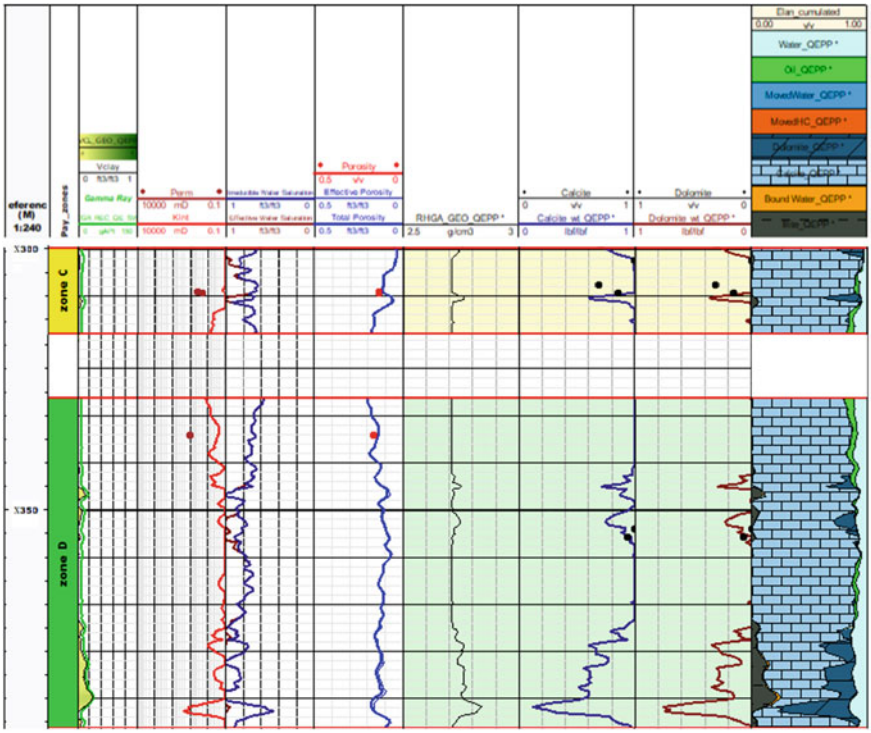

Fig. 8 Final petrophysical model for WELL P (from depth X299 m to X374 m). Zone C and D are highlighted

Table 2 Petrophysical model of Well P for all pay zones

Pay zone	Top (m)	Bottom (m)	Net/Gross (fraction)	Net pay (m)	Gross (m)	Avg. Por.	Avg. Sat (S_w)	Avg. Shale Volume
Zone A	X195	X212	0.388	5.893	15.187	0.161	0.649	0.026
Zone B	X226	X282	0.295	16.002	54.292	0.169	0.631	0.011
Zone C	X299	X310	0.283	2.602	9.208	0.141	0.667	0.000
Zone D	X338	X374	0.134	4.724	35.190	0.158	0.650	0.006

of ~35%. The permeability obtained from RCA suggests that the above zones have 1–10 mD.

References

Ahr WM (2008) Geology of carbonate rocks. A John Wiley & Sons Inc., Publication

Akbar M (2001) A snapshot of carbonate reservoir evaluation. Oilfield Review, winter edition, pp 20–41

Archie GE (1952) Classification of carbonate reservoir rocks and petrophysical considerations. Bull Am Assoc Pet Geol 36(2):278–298

DGH (2019) http://dghindia.gov.in//assets/downloads/56cef5d421448Sedimentary_Basins_Link_6.pdf Accessed on 20 May 2019

Lucia JF (1995) Rock-fabric/petrophysical classification of carbonate pore space for reservoir characterization. AAPG Bull 79(9):1275–1300

Marzouk I, Takezaki H, Suzuki M (1995) New classification of carbonate rocks for reservoir characterization. Soc Pet Eng 49475:178–187

Mheluka J, Mulibo G (2018) Petrophysical analysis of the Mpera well in the exploration block 7, Offshore Tanzania: implication on hydrocarbon reservoir rock potential. Op J Geol 8:803–818. https://doi.org/10.4236/ojg.2018.88047

Schlumberger (2008) Carbonate advisor—Quantitative producibility and textural analysis for carbonate reservoirs, brochure. https://www.slb.com/services/characterization/petrophysics/. wireline/legacy_services/carbonate_advisor.aspx Accessed on May 20, 2019

Tiab D, Donaldson EC (1996) Petrophysics: theory and practice of measuring reservoir rock and fluid transport properties. Gulf Publishing Co., Houston, Texas, p 706

Chapter 6
Foam for CO_2 EOR in a Carbonate Reservoir: Scale-up from Lab to Field

M. Sharma, Z. P. Alcorn, S. B. Fredriksen, M. A. Fernø and A. Graue

Abstract Carbon dioxide has been used for more than five decades in fields for tertiary oil recovery; and because of commercial and environmental reasons, it has received lot of attention in the last few years. Based on the experience with large-scale CO_2 flooding, it is well understood that even with a high local displacement efficiency, the process suffers from poor volumetric sweep due to reservoir heterogeneity, viscous instability and gravity override. Based on laboratory studies, foam has been found to address these limitations at small-scale, however understanding of CO_2-Foam flow at field-scale is limited within industry. Field pilots performed so far have shown technical success especially near well, but there exist a gap to establish a methodology to scale-up the CO_2-Foam technology to large-scale. A research program was established to run CO_2-Foam field trial in a field with heterogeneous carbonate reservoir onshore in west Texas, USA to guide technology scale-up. The research aims at implementing a modelling and monitoring approach as part of the roadmap. The static model created by integrating geologic framework, well logs and core data, and dynamic model created based on analysis of reservoir engineering data, including relative permeability, fluid phase behaviour and EOR coreflood studies forms the basis for reservoir simulation study for the pilot area. In this paper, we provide an overview of various elements of the three-dimensional numerical model. We demonstrate the application of a systematic approach to incorporate the uncertainties associated with model inputs, which is used to guide decision making for the baseline survey. The success will be validated via an appropriate monitoring plan in the ongoing pilot program.

Keywords CO_2 · Foam · Mobility control · Field pilot · Uncertainty

M. Sharma (✉)
The National IOR Centre of Norway, University of Stavanger, Stavanger, Norway
e-mail: mohan.sharma@uis.no

Z. P. Alcorn · S. B. Fredriksen · M. A. Fernø · A. Graue
Department of Physics and Technology, University of Bergen, Bergen, Norway

K. H. Singh and R. M. Joshi (eds.), *Petro-physics and Rock Physics of Carbonate Reservoirs*, https://doi.org/10.1007/978-981-13-1211-3_6

Nomenclature

BOPD	Barrels of oil per day
BWPD	Barrels of water per day
CCE	Constant composition expansion
CCUS	Carbon capture utilization and storage
EoS	Equation of state
epcap	Foam model parameter in F_{shear}
epdry	Foam model parameter in F_{water}
epsurf	Foam model parameter in F_{surf}
fmcap	Foam model parameter in F_{shear}
fmdry	Foam model parameter in F_{water}
FM	Mobility reduction factor
fmmob	Maximum gas mobility reduction factor
fmsurf	Foam model parameter in F_{surf}
KPI	Key performance indicator
MMscfd	Million standard cubic feet per day
MPZ	Main pay zone
OIIP	Oil initially in place
PR	Peng-robinson
ROZ	Residual oil zone
SAG	Surfactant-alternating-gas
Sorw	Residual oil saturation for water
UP	Uncertainty parameter
USBM	U.S. bureau of mines
WAG	Water-alternating-gas (CO_2)

1 Introduction

CO_2 injection has proven to be an attractive technique for improving oil recovery in mature fields, which have been waterflooded for several years (Jarrell et al. 2002). Although CO_2 has properties making it favourable compared to other solvents, it also suffers from phenomena like gravity segregation, viscous fingering and channelling, eventually leading to poor volumetric sweep. Previous studies (Heller 1994; Kibodeaux and Rossen 1997; Turta and Singhal 1998; Fernø et al. 2015a) confirm the effectiveness of foam for mobility control at the core-scale. Figure 1 (Haugen et al. 2014) shows that for oil-wet fractured core plugs, use of foam can significantly improve tertiary recovery and sweep efficiency, especially under miscible conditions. Based on these studies, it is well understood that foam can improve conformance for solvent-based EOR by reducing gas mobility away from the injectors and selectively isolating high permeability zones within the reservoir.

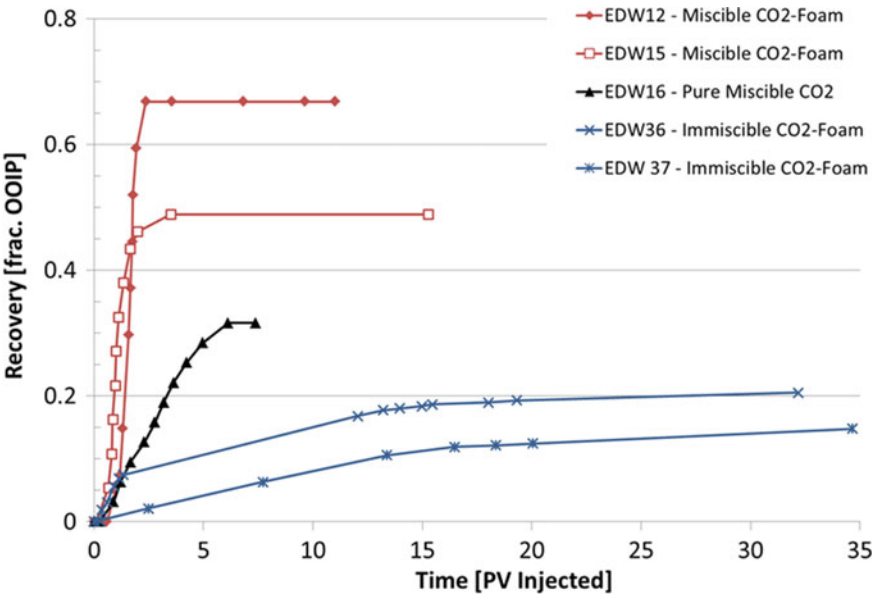

Fig. 1 Comparison of oil recovery (in % OOIP) for pure CO_2 injection and CO_2-foam injection in oil-wet core plugs (Edwards Limestone). Mobility control by foam injection increased both rate of recovery and ultimate recovery significantly. Miscible foam injections produce more oil than immiscible foam injections

The challenge is to ensure the scalability of displacement mechanisms to a larger scale, and development of a fit-for-purpose approach that will assist in advancing CO_2 foam technology to high risk and high-cost environment. So, a field pilot research program has been initiated which aims at integrating traditional laboratory studies with data acquired from field pilot studies to get insights into fluid dynamics at multiple scales.

A few field pilots have been run in the past with varying extent of success. One of the earliest field pilot for foam-assisted CO_2 EOR was performed in the Wilmington field, located in southern California in 1984, which achieved the primary objectives (Holm and Garrison 1988). Since then field tests have been performed in Rock Creek, Virginia (Heller et al. 1985), Rangley Weber Sand Unit, Colorado (Jonas et al. 1990), North Ward/Estes, Texas (Chou et al. 1992), Slaughter, west Texas and Greater Areth, southeast Utah (Hoefner and Evans 1995), East Vacuum Grayburg/San Andres Unit, New Mexico (Harpole and Hallenbeck 1996), SACROC, Texas (Sanders et al. 2012) and Salt Creek (Mukherjee et al. 2014, 2016) with success to varying extent. Due to low oil prices and technical challenges involved in the process, foam has not been tested since the mid-90s. However, a continued decline in conventional production and growing concern about climate change associated with emission of greenhouse gases has renewed interest over recent past in use of foam for mobility control as part of Carbon Capture, Utilization and Storage (CCUS).

This research works aims at scaling up CO_2 foam EOR from laboratory to field. In order to accomplish the objective, a heterogeneous carbonate reservoir has been identified onshore in west Texas, USA. Various stages of the project have been initiated, and the paper aims at providing an overview of different elements involved in this multidisciplinary research. Given the fact that there is limited data available for detailed reservoir characterization, a probabilistic approach has been applied to understand the impact of individual uncertainty parameter on key performance indicators. This has been used to transition the project through the 'Concept Select' and 'Define' phases to 'Execute' phase. As an outcome, an appropriate data acquisition strategy has been decided and agreed with the operator, to improve the baseline model, which will be used as a vehicle to obtain an injection strategy subject to the reduced level of uncertainties.

2 Methodology

2.1 Field Overview

The Unit-A of the field selected for pilot study, which is located in the Permian basin, west Texas (Fig. 2), was developed throughout the 1940s and produced 12%

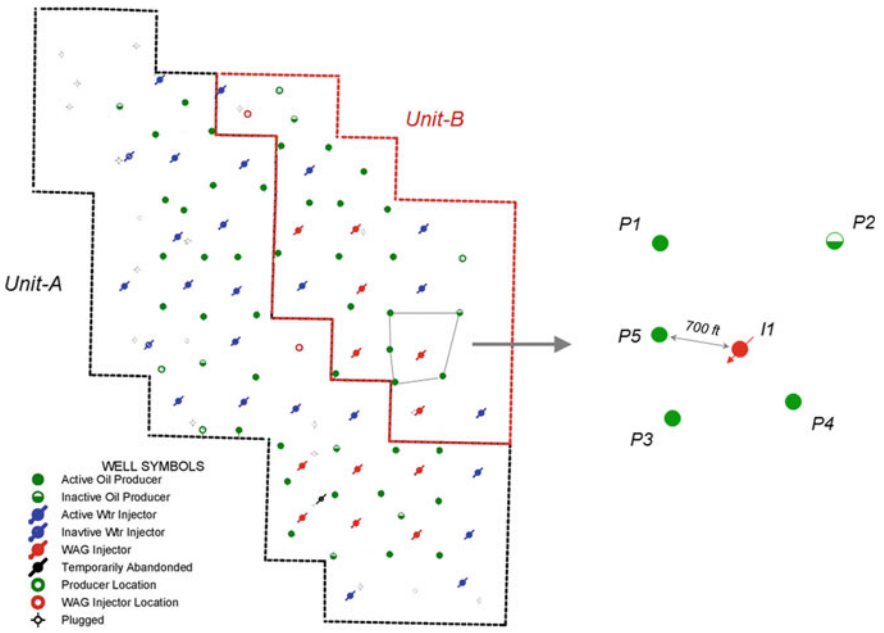

Fig. 2 Field layout and location of selected pilot area

Fig. 3 Effect of tilting on initial hydrocarbon distribution

of mapped oil initially in place until late 1960s. Waterflood began in the early 1970s with infill drilling to establish 40-acre peripheral waterflood patterns. The Unit-B was developed throughout the early 1980s. However, with a low primary plus secondary recovery of only 22% of OIIP by the late 1980s, the operator realized the need to reduce pattern size. An infill program was run to develop both the units on a 20-acre five-spot pattern. The infill drilling yielded excellent results with an increase in production from 400 to 1200 BOPD. However, a steep decline in production and high remaining oil saturations after waterflood indicated the potential for tertiary oil recovery.

It has been well identified from the regional data that the reservoir consists of two zones (Fig. 3): Main Pay Zone (MPZ), and Residual Oil Zone (ROZ). MPZ has produced by primary depletion and water flooded for over 50 years. ROZ is thought to be formed by structural tilting or seal breach events and has been naturally waterflooded over the geologic time. ROZ has significant immobile oil (20–40% of OOIP), which cannot be technically drained by primary or secondary mechanisms.

Tertiary CO_2 injection for EOR started in south-eastern part of the Unit-B in Oct-2013 to target remaining oil, both in MPZ and ROZ with commingled production and injection. This resulted in an increased production rate from 10 to 15 BOPD. However, the peripheral producers of the pattern have already experienced CO_2 breakthrough, with the breakthrough occurring as early as within 4 months from the start of CO_2 injection. The reservoir heterogeneity and unfavourable mobility of CO_2 thus makes the reservoir a good candidate to improve sweep and reduce CO_2 recycling by foam injection.

Aligned with the operator's plans for field development, and to minimize the amount of time required to gather data, an injector-producer well pair was selected for the first foam injection trial. The selection of a well pair is advantageous for the use of CO_2 foam as interwell distances are greatly reduced, and reservoir response to foam can be seen at a much shorter time intervals. After a careful analysis of possible well pairs in the south-eastern portion of the Unit-B, a well pair consisting of injector I1 and producer P5 was identified. Some of the criteria governing the choice of the pilot area included continuity of reservoir flow zones, well injectivity, gas breakthrough time, well arrangement and well workover requirements.

3 Laboratory Studies

A range of surfactants including cationic, non-ionic and zwitterionic were evaluated to identify a formulation that will satisfy the requirements for CO_2 foams in carbonate reservoirs (Nguyen et al. 2015). Foam generation, texture and stability was examined as a function of the surfactant structure and formulation variables such as pressure, temperature, surfactant concentration, water salinity and oil concentration. The partitioning of surfactants between CO_2 and water, as well as oil and water was evaluated along with adsorption to develop the injection strategy for field-scale application. A non-ionic water-soluble surfactant from Huntsman—Surfonic L24-22 was selected for the field pilot based on surfactant screening studies for the reservoir (Jian et al. 2016). Surfonic L24-22 is a linear alcohol ethoxylate, which is produced by the addition of ethylene oxide (EO) to linear, primary alcohols. It is a 22-mole ethoxylate of linear, primary 12–14 carbon number alcohol.

Because of material unavailability from the field (i.e. reservoir core and crude oil), limestone core from an analogous reservoir was used to obtain parameters for foam modelling. The cores were 100% saturated with synthetic reservoir brine made from analytical grade chemicals. A surfactant solution was made by adding 1 wt% Surfonic L24-22 to the reservoir brine. The core-scale system was made up of two 2" limestone cores stacked vertically providing a total length of ~25 cm. The cores were pre-flushed with surfactant solution prior to foam injection to reduce adsorption effects. To investigate the stability and generation of foam, gas and surfactant solution were co-injected at a total rate of 50 ml/h (~2 ft/day) starting at a foam quality of 0.9 (i.e. CO_2 and surfactant solution was simultaneously injected at a ratio of 9:1). The pressure differential was measured across the cores as foam was generated in situ. When differential pressure reached steady-state, the foam quality was reduced in steps of 0.1 to obtain a foam quality scan (Osterloh and Jante 1992; Xu and Rossen 2004; Kim et al. 2005). The process was repeated until a foam quality of 0.1 was achieved. The experiment was performed at supercritical conditions of 85 bar and 60 °C.

There are two general approaches available to model foam transport. The first, explicit-texture population-balance model (Falls et al. 1988; Rossen et al. 1999), allows direct simulation of foam creation, propagation, and coalescence effects that can be observed in laboratory core experiments (Fernø et al. 2016). The second approach, an implicit-texture local-equilibrium model (Cheng et al. 2000; Alvarez et al. 2001), uses an empirical relation to capture the effect of surfactant concentration, water saturation, oil saturation (Law et al. 1992; Farajzadeh et al. 2012), shear-thinning due to flow velocity on foam mobility. The gas permeability in the presence of foam (k_{rg}^{f}) is modified by multiplying the gas relative permeability without foam (k_{rg}^{nf}) at a specific water saturation with a mobility reduction factor (FM), which is a function of aforementioned factors. The water permeability in the presence of foam remains unchanged.

$$k_{\mathrm{rg}}^{f} = k_{\mathrm{rg}}^{nf} \times \mathrm{FM} \tag{1}$$

Because of complex foam dynamics and challenges associated with extracting model parameters from them coreflood experiments for the mechanistic population-balance approach, the second approach was found more appropriate for foam scoping studies at field pilot scale. We studied the effect of water saturation, shear rate and surfactant concentration on mobility reduction factor in numerical modelling, given by the expression:

$$\mathrm{FM} = \frac{1}{1 + \mathrm{fmmmob} \times F_{\mathrm{water}} \times F_{\mathrm{shear}} \times F_{\mathrm{surf}}} \tag{2}$$

fmmmob refers to the maximum gas mobility reduction that can be achieved. F_{water}, F_{shear} and F_{surf} with expressions below capture the water saturation, shear rate and surfactant concentration dependence, with all lying in the range of 0–1. The capillary number N_{ca} represents the relative effect of viscous and capillary forces.

$$F_{\mathrm{water}} = 0.5 + \frac{\arctan\left[\mathrm{epdry}(S_w - \mathrm{fmdry})\right]}{\pi} \tag{3}$$

$$F_{\mathrm{shear}} = \begin{cases} \left(\frac{\mathrm{fmcap}}{N_{\mathrm{ca}}}\right)^{\mathrm{epcap}} & \text{if } N_{\mathrm{ca}} > \mathrm{fmcap} \\ 1 & \text{otherwise} \end{cases} \tag{4}$$

$$F_{\mathrm{surf}} = \left(\frac{\text{Surfactant concentration}}{\mathrm{fmsurf}}\right)^{\mathrm{epsurf}} \tag{5}$$

The apparent foam viscosity was calculated at a steady state based on the data generated from the laboratory coreflood experiments. Regression was performed to obtain values for fmmob, fmdry and epdry (Ma et al. 2012), and an acceptable match to measured data was obtained at values of 180, 0.4 and 10,000 for these parameters respectively (Fig. 4). The values for fmcap and epcap were based on previous studies. The critical saturation at which foam collapses was considered as 0.475 for this study. fmsurf, which corresponds to reference concentration for transition from weak to

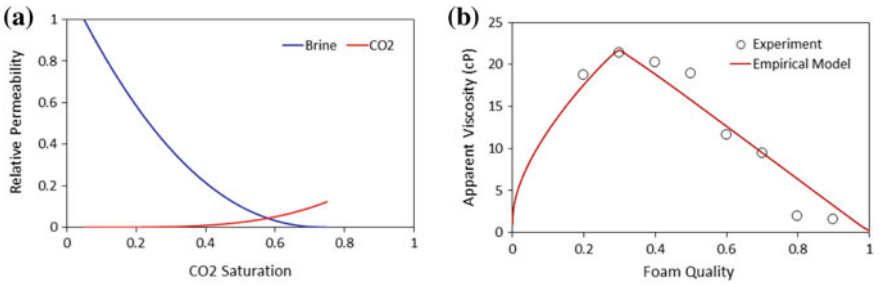

Fig. 4 **a** CO_2-brine relative permeability for analogous limestone. **b** Foam quality scan data fit to empirical model

strong foam was assumed to be ten times the critical micellar concentration (0.01 wt%) measured in the laboratory. epsurf was assumed to be 1.

4 Geologic Model

The field produces from the San Andres reservoir, a heterogeneous carbonate formation consisting of subtidal to supratidal deposits. The formation was deposited during a regression of Guadalupian seas with minor rises in sea level creating a cyclical sequence of subtidal and intertidal deposits, interbedded with shaley mudstone layers. Mudstone layers act to limit vertical communication throughout the reservoir and can be thought of as barriers to flow. Subtidal dolostone facies make up the bulk of the reservoir rock, which are typically located deeper within the overall pay section. Reservoir rocks have well-developed intercrystalline porosity, which has later been enhanced through leaching and subsequent dedolomitization (Wang et al. 1998).

To assist the pilot design, a sector model for the selected well pair and peripheral producers was setup. The reservoir heterogeneity makes investigation of the continuity of reservoir flow zones in interwell region challenging. Identification of rock units with appreciable reservoir characteristics was based on the analysis of available petrophysical logs and well core. The information was used to establish a geologic framework for the pilot area (Alcorn et al. 2016).

Drill core and well log data were correlated in the pilot area. Gamma-ray, neutron, density, and resistivity logs were used to tie the core analysis to log data and define flow units. Porosity was calculated from the neutron and density logs; lithology and saturation was determined from gamma-ray and resistivity logs, respectively. The porosity for reservoir zones range between 0.12 and 0.15, whereas permeability varies between 1 and 300 mD with an average of 15 mD. Four and two flow zones were identified in MPZ and ROZ, respectively, each separated by impermeable units.

A three-dimensional reservoir model was built for the pilot area using the structural and geocellular modelling capabilities of Petrel (Schlumberger 2015, 1). The tops of the reservoir flow zones and impermeable zones were mapped, which were used to build the geologic framework. The grid has dimensions of $63 \times 61 \times 46$ with approximately 120,000 active cells. The grid cells are 50×50 ft areally, and layer thickness varies from 1 to 10 feet depending upon mapped stratigraphic units. The facies model was prepared based on the hard data (cores and logs) available from the wells. Porosity, permeability, and water saturation available for each well provided values for grid cells penetrated by those wells. Since limited information is available to characterize the reservoir, the modelling workflow began with a framework obtained deterministically, and moved towards a stochastic approach to obtain interwell property distribution. Static properties were extended to interwell regions through the calibration of individual petrophysical well data to the modelled facies distribution. Stochastic simulation of petrophysical properties was used with strati-

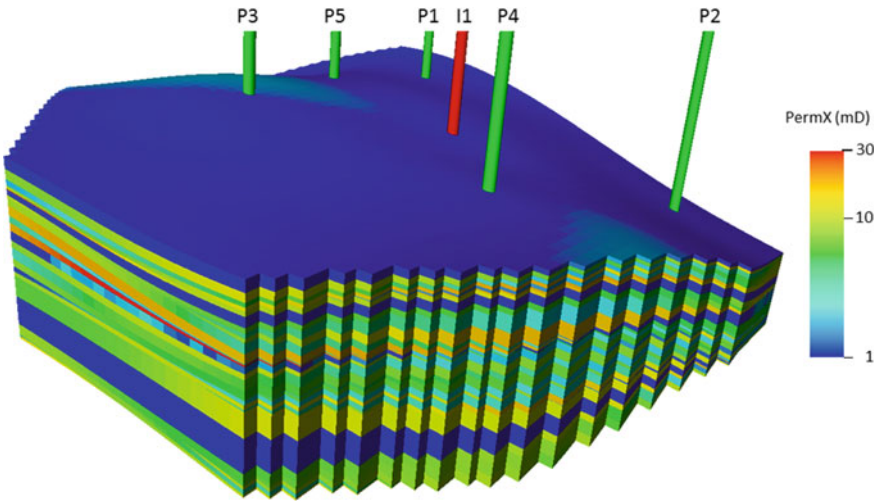

Fig. 5 Permeability distribution in base geologic model

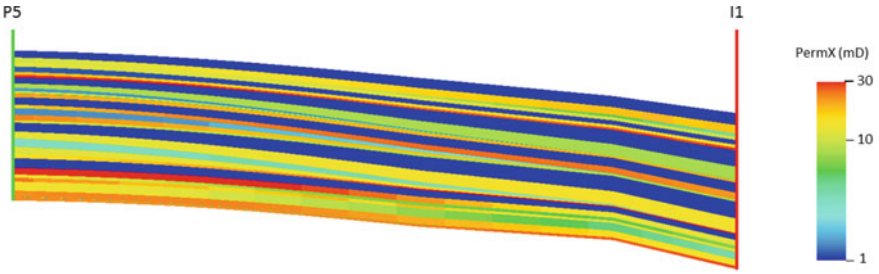

Fig. 6 Cross-section (permeability) across I1 and P5

graphic constraints to populate grid cell properties in interwell regions as shown in Figs. 5 and 6.

5 Simulation Model

A conventional finite-difference compositional model (ECLIPSE, Schlumberger 2015, 1) was setup using the tuned EoS model (Islam and Farouq-Ali 1990; Rossen 2013; Masoudi et al. 2015). In ECLIPSE, aqueous phase is traditionally modelled using a single component. We introduced a second component to model the surfactant component for the foam model. Foam adsorption and desorption were modelled using reversible chemical reaction. A component to model surfactant adsorbed to the rock was introduced. The effect of solid deposition on pore volume (or permeability)

reduction was not included in the modelling. Foam decay was also modelled using a chemical reaction to convert the surfactant component to water. Other foam model parameters were specified as obtained from laboratory studies. Grid cells with permeability less than 5 mD were identified as a region property, and were assigned an fmmob of 0. All other grid cells were assigned the value obtained from laboratory study, which was varied during uncertainty study as explained in the next section. The mathematical details of the foam model and chemical reaction model are available in the ECLIPSE Technical Description, and are not discussed here.

Fluid and rock characterization is important for reservoir performance prediction. Available data, including well surveys, was analyzed to prepare inputs for an integrated baseline model. The composition for an oil sample from MPZ was measured in the laboratory (Honarpour et al. 2010). Because oil in ROZ is immobile and significant quantity of oil could not be collected, the operator used a recombined sample of stock tank oil from MPZ and synthetic gas (adjusted for gas composition from ROZ) for PVT studies (Table 1). Data for routine tests and swelling experiment was available for oil sample from MPZ, which was used to tune Peng-Robinson (PR) equation of state (EoS) model.

The Minimum Miscibility Pressure was measured using Slimtube test as 1500 psi. An 8-component model, which included 4 C7 + components, was setup. The lighter components were lumped as CO_2, N_2 + C1, H_2S + C2 + C3, C4 + C5 + C6. The C7 + fraction from the reported composition was split using Gamma distribution, followed by Gaussian quadrature based lumping and critical property estimation using Lee-Kesler. Pc, Tc and volume shift for 4 C7 + components; and binary interaction coefficients for CO_2 and hydrocarbons were tuned to get a match on routine PVT and swelling test data. The tuned EoS was then used to match the

Table 1 MPZ and ROZ fluid composition

Component	Fluid composition (mol%)	
	MPZ	ROZ
N_2	0.51	0.04
CO_2	2.47	0.02
H_2S	1.96	0
C1	24.65	20.1
C2	9.1	9.07
C3	7.57	6.95
iC4	1.41	0.04
nC4	4.03	3.9
iC5	1.76	0.04
nC5	2.03	2.49
C6	3.54	2.69
C7+	40.97	54.66

oil viscosity data using Pedersen model. Previously mentioned parameters were excluded from the regression while tuning viscosity.

Figures 7 and 8 show the fluid model fit to available experiment data from differential liberation, swelling and constant composition expansion tests (test data as circles and tuned model as line). The cores recovered using pressure-retaining coring in an infill well for ROZ were used to measure oil and water saturation, mainly using Dean Stark extraction. Remaining Oil Saturation (ROS) ranged between 10 and 40% with an average of 31.7%, and did not show any significant correlation with rock properties like porosity, permeability or square root of the ratio of permeability to porosity. ROS measured on cores recovered using Sponge coring on four wells ranged from 10-38% with an average of 29.8%. This was in good agreement with data on pressure-retained cores. The observed water saturation in the ROZ is much higher than the Swirr from the primary drainage capillary pressure due to natural water flooding that occurred during geological times. The water-oil relative permeability curve (Fig. 9) has been obtained by tuning the parameters for Corey-type model to available laboratory coreflood data. Straight-line relative permeability function has been used for miscible oil displacement by CO_2 in numerical modelling.

Due to availability of limited production data, information derived from petrophysical logs and well surveys that were run prior to start of CO_2 injection, coupled with base geology model, forms the basis for reservoir simulation studies. The reservoir pressure for I1 was recently measured to be 3714 psia at 5300 ft. This depth is slightly above the topmost reservoir horizon for the pilot area, and was considered

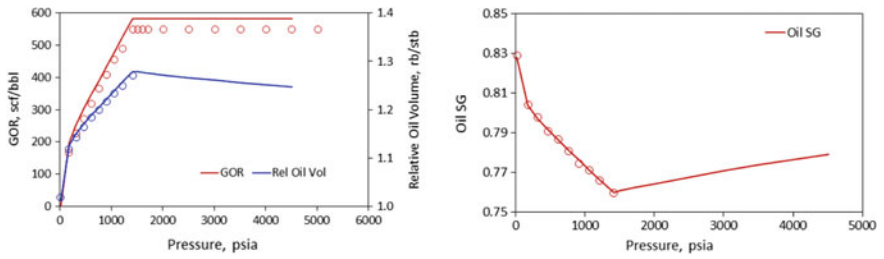

Fig. 7 Fluid model fit to PVT data: Differential Liberation

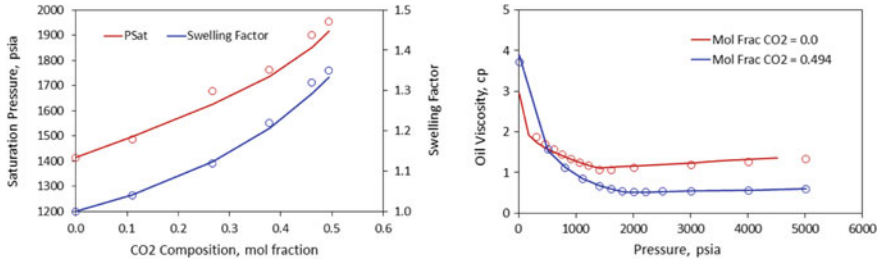

Fig. 8 Fluid model fit to PVT data: Swelling and CCE/Viscosity (Oil + CO_2)

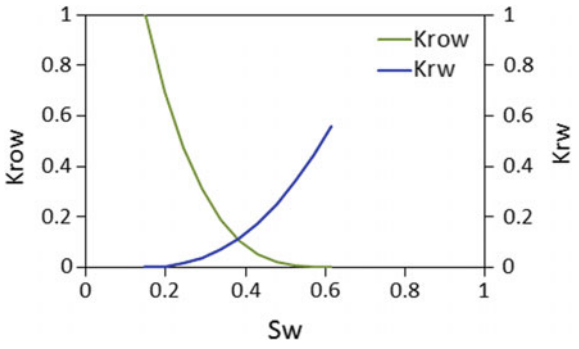

Fig. 9 Water-Oil imbibition relative permeability

reference for simulation studies. The pressure recorded was higher than hydrostatic (2300 psi at reference depth), which increased during CO_2 injection over the past 4 years. The operator is considering depressurizing the reservoir by completing a disposal well in a separate reservoir zone. Injection profiling was done for the reservoir zone in I1 under flowing conditions with CO_2 injection at 1.2 MMscfd with approximately 300 psi pressure drop across perforations, suggesting good injectivity in MPZ and ROZ. The profile was used to tune the well model. Base CO_2 injection rate of 2 MMscfd and base water injection rate of 1000 BWPD has been used as well control for I1, in-line with current field observation. The wellhead injection pressure is constrained to keep bottom-hole pressure 250 psi below the formation fracture pressure.

Capturing the well injectivity is critical for designing the injection strategy because the injection of a low-mobility fluid-like foam will increase the operating bottom-hole pressure to maintain set injection rate, and eventually a reduction in injection rate when bottom-hole pressure reaches a set upper constraint. The issues that complicate the prediction of well injectivity is the shear-thinning behaviour of foam, which can lead to an underestimation of injectivity with the use of Peacemen equation in the injection well grid block (Leeftink et al. 2015). Specifically during SAG, foam dries out below a critical water saturation near-wellbore during the gas cycle. The abrupt collapse increases gas mobility and injectivity significantly in the near well region. We addressed this issue by grid refinement around the injector at the cost of increased runtime.

To stay aligned with the operator's philosophy of reservoir management, SAG injection was planned for pilot study to avoid any corrosion problems in surface facilities. We studied a scenario consisting of three alternate slugs of surfactant and CO_2 injection with one-month frequency, each at a similar voidage rate. A pre-flush slug of water precedes the surfactant-alternating-CO_2 injection. The water injected in this stage will be compatible with subsequent chemical water injection, and will contain a sacrificial agent to minimize surfactant losses from the surfactant slugs. The last CO_2 cycle is followed by chase water injection for two months, which will be continued to completion of the pilot during subsequent modelling work and field operations.

6 Pilot Simulation Study

It is well understood within the integrated reservoir modelling domain that forecasting has to take into account the existence of a wide range of uncertainties that are caused by the complexity and access to limited information about subsurface systems. As a result, even the most carefully constructed models do not exactly represent reality, and their fundamental equations do not exactly describe the actual physical behaviour. To recognize the effect of all sources of uncertainty, we implemented a probabilistic forecasting workflow (Fig. 10). The model-based forecast is accompanied with an estimate of the uncertainty in the forecast, which can be made using an ensemble of forecasts.

It is then implicitly assumed that a (tuned) set of values for model parameters would describe (imprecise) observations of past and future behaviour. With the availability of well pressure and production data, the workflow typically involves using post-history match probability distributions for the uncertain parameters (Fernø et al. 2015b). For our study, we found it sufficient to construct a set of equiprobable forecasts using the agreed range for uncertainty parameters (UPs). The workflow requires identifying the Key Performance Indicators (KPIs) for the prediction phase during the uncertainty framing session. For the pilot, these included incremental fluid volume production at the end of the pilot, injection pressure and breakthrough time for

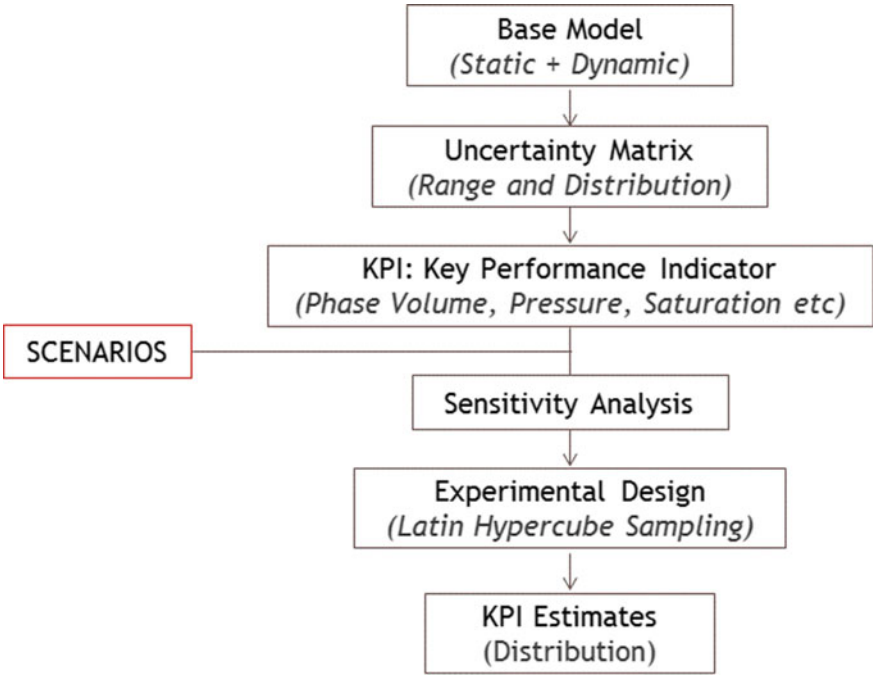

Fig. 10 Workflow for forecasting under uncertainty

surfactant. There is limited information available for characterizing reservoir, rock behaviour and foam model parameters. Therefore, parameters available for ROZ were used for MPZ, where applicable; and an uncertainty matrix (Table 2) was setup after discussion with stakeholders.

7 Results

7.1 Sensitivity Analysis

Sensitivity analysis was run to evaluate how uncertainties in the model inputs affect the model outputs. This involves generating simulations by varying one UP at a time from base value to low and high values. Tornado diagrams for KPIs were inspected after performing sensitivity analysis, where *x*-axis of such a diagram shows the relative change in the value of the selected KPI from the base case. Each UP in the model has its own bar, where red and blue bars correspond to low and high values of that UP, respectively. The width of each bar shows how much impact that UP can have on a selected KPI when varied through a range. The diagram is essentially a ranked list of UPs that was considered for designing surface operation plan and data acquisition program.

Based on the discussion with the operator, the bottom-hole pressure for injector was found to be an important KPI because of flowing bottom-hole pressure close to fracture pressure. Foam generation is expected to reduce injectivity, and the rates will have to be constrained while maintaining injection pressure during the pilot. Figure 11a shows the tornado diagram for bottom-hole pressure for injector at the start of surfactant injection. As shown in the figure, the bottom-hole pressure for injector at the start of surfactant injection is more sensitive to permeability, water injection rate and initial fluid saturation compared to others. Figure 11b shows that the bottom-hole pressure for injector during the first CO_2 slug injection (post surfactant slug) is also sensitive to foam model parameters, especially those controlling shear-thinning.

Various other KPIs were also identified like incremental oil production, amount of surfactant required, volumes of water and CO_2 required, drop in gas–oil ratio, etc., out of which the first two were of more importance to the operator. Figure 12a shows the tornado diagram for the cumulative oil production for pilot phase, which suggests that even though foam model parameters influence the additional recovery, the uncertainty in oil saturation for MPZ has the highest influence on it. The data acquisition program should, therefore, aim to reduce the uncertainty range in remaining oil saturation in the MPZ before the start of the pilot. Figure 12b shows that the amount of surfactant required depends relatively more on permeability, water injection rate and initial oil saturation than other uncertain parameters.

Table 2 Uncertainty matrix for pilot simulation study

Parameter	Description	Low	Base	High	Unit	Distribution
Static model						
POROMULT	Pore volume multiplier	0.9	1	1.1		Uniform
PERMMULT	Horizontal permeability multiplier	0.75	1	1.25		Uniform
KVKH	Vertical to Horizontal permeability ratio	0.05	1	0.2		Uniform
Foam model						
FMMOB	Reference foam mobility reduction factor	160	180	200		Uniform
FMDRY	Water saturation dependence parameter	0.397	0.4	0.403		Uniform
EPDRY	Water saturation dependence parameter	1000	10,000	50,000		Uniform
FMCAP	Shear-rate dependence parameter	1e-09	1e-08	1e-07		Uniform
EPCAP	Shear-rate dependence parameter	0.1	0.5	2		Uniform
Initialization						
SWIMPZ	Water saturation @ Start of Sim—MPZ	0.5	0.55	0.6		Uniform
SWIROZ	Water saturation @ Start of Sim—ROZ	0.62	0.68	0.75		Uniform
Well model						
WATINJRATE	Injection rate—Water slug	800	1000	1200	BWPD	Uniform
GASINJRATE	Injection rate—Gas slug	1.6	2	2.4	MMscfd	Uniform
MAXINJPRES	Maximum injection pressure	4800	5000	5200	psia	Uniform
PIMULTWATINJ	Injectivity multiplier—Water slug	0.8	1	1.2		Uniform

(continued)

Table 2 (continued)

Parameter	Description	Low	Base	High	Unit	Distribution
PIMULTGASINJ	Injectivity multiplier—Gas slug	0.8	1	1.2		Uniform

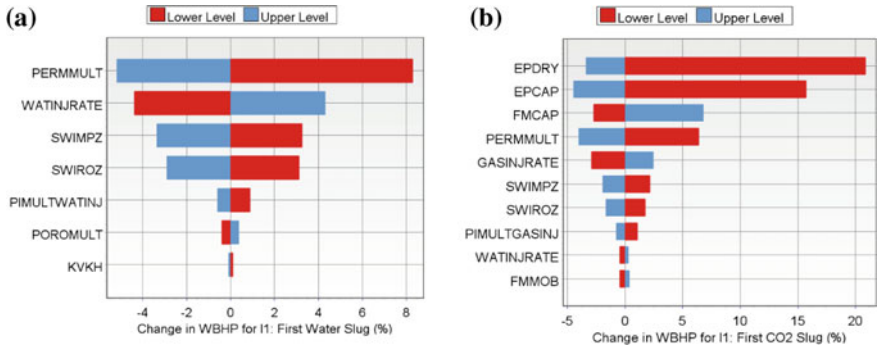

Fig. 11 Sensitivity analysis capturing the key uncertainty parameters influencing bottom-hole pressure for injector under. **a** Surfactant injection. **b** CO_2 injection

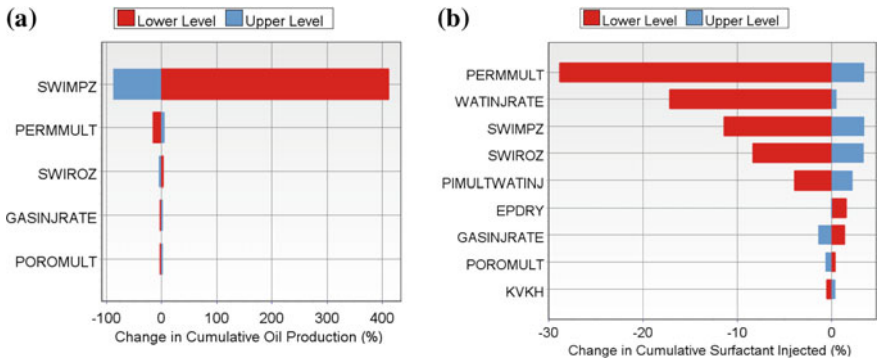

Fig. 12 Sensitivity analysis capturing the key uncertainty parameters influencing. **a** Cumulative oil production. **b** Cumulative surfactant injection for pilot

7.2 Experimental Design

Sensitivity analysis was followed by experimental design study to evaluate uncertainty in predictions. Some of the UPs could be removed as most of the KPIs did not show much sensitivity to variation in them, however, we carried all the UPs for further analysis as simulations could be run within available time. Moreover, there is

the possibility that some parameters may have an influence on the simulation model in conjunction with other parameters, which gets captured in this step.

The UP ranges were sampled again using the Latin Hypercube technique to generate approximately 10 times the 'number of UPs' simulation cases. Latin Hypercube takes the cumulative distribution function and splits the cumulative probability into equally large compartments. The number of compartments, and as a result the extent of detail, is determined by the number of simulations created. Each forecast used the same unique set of uncertainty parameter values for sampling to ensure that the entire parameter space is represented in the design matrix. After creating production profiles, discrete P90, P50 & P10 cases can be selected.

The preliminary study focussed on estimating the volume requirements for injectant fluid (water, CO_2) and surfactant. Figure 13 shows the cumulative water injection for the pilot duration, including pre-flush and chase period. The mean of all the forecasts obtained from simulation, or the ensemble mean, provides good information on the most likely amount of water required during the pilot, subject to known unknowns. Similarly, Fig. 14 shows the volume of CO_2 required during the pilot phase. The amount of surfactant required for the pilot subject to various combination of UPs is shown in Fig. 15, which suggests that 275,000 to 425,000 lb (lbs) of surfactant will be required for the pilot. The spread of the ensemble forecast indicates the confidence we can have in the predictions, where a large spread here indicates more uncertainty in predictions.

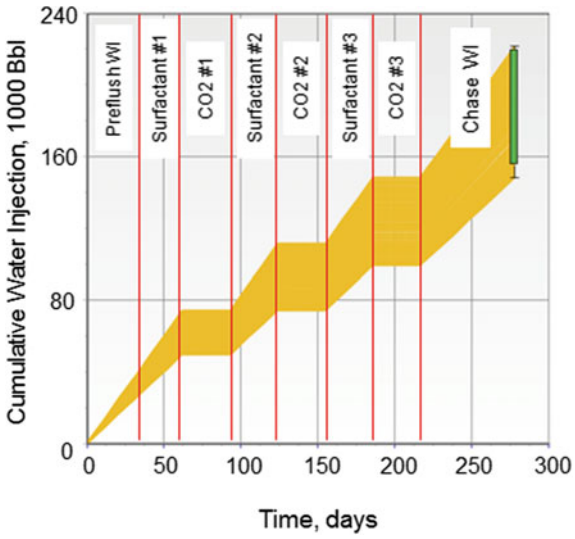

Fig. 13 Uncertainty in volume of water required for pilot duration

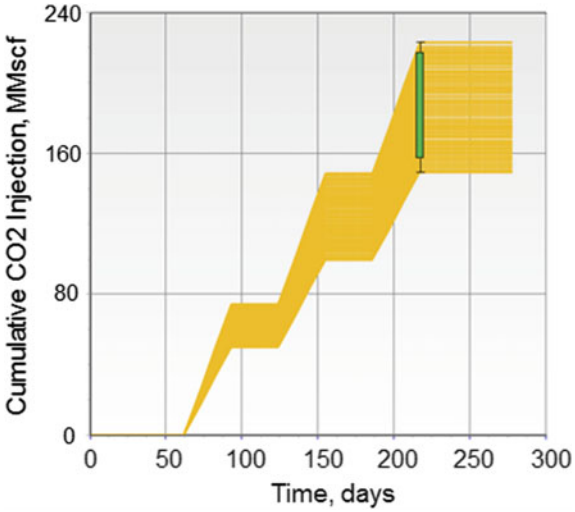

Fig. 14 Uncertainty in volume of CO_2 required for pilot duration

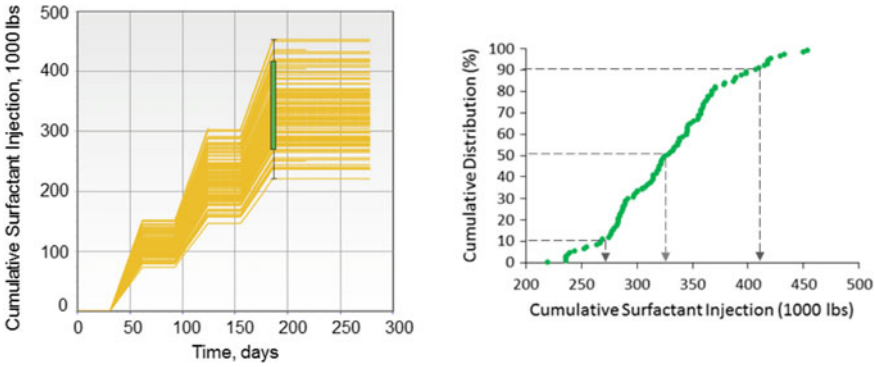

Fig. 15 Uncertainty in amount of surfactant required for pilot duration

8 Discussion

The results from the pilot simulation study were discussed with the operator, to agree on field operations' plan including data acquisition. The operator measured the water injectivity for the proposed injector for pilot phase, which was a producer until 2013, and was on continuous CO_2 injection since then. The water injectivity was found to be around 600 bbl/d which is lower than the range (800–1000–1200), including the injectivity index multiplier (0.8–1–1.2), that was considered for this study. Given the fact that surfactant cost will be a significant share of the overall pilot cost, it

was agreed to keep the total amount of surfactant to 200,000 lbs, and optimize the injection strategy in the next phase of pilot design.

Because of limited margin on increasing injection pressure, the operator will drill a disposal well in a separate deeper reservoir to facilitate reservoir depressurization before initiating the pilot. However, because of availability of the core from previous wells and understanding of vertical communication, no coring and vertical pressure profiling has been planned for this well. One of the CO_2 injectors in a similar pattern, further south of the pilot area, will be converted form continuous CO_2 injector to Water-alternating- CO_2 (WAG) injector, with 2:1 water-gas slug size ratio. It has bene planned to use the change in injectivity during multiple WAG cycles and additional recovery as a baseline to the proposed SAG pilot.

The data acquisition program has been designed to reduce uncertainty on some of the heavy-hitters like interwell connectivity and fluid saturation. In addition to surface monitoring, the plan for data acquisition, based on this study, includes injection profiling, tracer study and cross-well seismic. An interwell gas tracer study will be performed to understand the baseline volumetric sweep pattern for each producer with respect to the proposed injector I1. The petrophysical logs that are available for the wells will be reprocessed to estimate the remaining oil saturation post waterflood based on information from similar reservoirs in west Texas. Measuring saturation by running new petrophysical log or performing partitioning interwell tracer study was found to be expensive. The numerical model will be initialized using these saturation and calibrated for historical CO_2 injection, before simulating foam injection. The planned surveys will thus help reduce the uncertainty in performance prediction.

Foam model parameters based either on experiments performed with a limestone core from an analogous reservoir or on assumptions were also found to impact the KPIs. It was decided to perform experiments with reservoir core and fluids under representative conditions to obtain a more reliable foam model.

9 Conclusions

The design and performance prediction for the field pilot relies heavily on the numerical model generated by integrating multidisciplinary inputs. Given the fact that a limited data is available for reservoir characterization, the uncertainty analysis produces a basis for pilot performance expectations prior to start of field operations. We presented the analysis for one specific scenario with three SAG cycles. The results of this analysis were used to design the data acquisition program, within available resources, to assist in improved reservoir characterization. Laboratory work is currently ongoing to investigate mobility control during CO_2 injection and foam stability using selected surfactant at reservoir pressure and temperature using core material from the formation. Additional baseline surveys will shed more light on interwell connectivity and fluid distribution. The reservoir model is thus expected to grow in complexity over time as more data becomes available, which will be used as a basis to derive an optimal injection strategy.

Acknowledgements The authors acknowledge the Research Council of Norway CLIMIT program for financial support under grant number 249742—*CO_2 Storage from Lab to On-Shore Field Pilots Using CO_2-Foam for Mobility Control in CCUS* and industry partners; TOTAL E&P, Shell E&P and Statoil Petroleum AS. The authors acknowledge the Research Council of Norway and the industry partners; ConocoPhillips Skandinavia AS, Aker BP ASA, Eni Norge AS, Maersk Oil Norway AS, DONG Energy A/S, Denmark, Statoil Petroleum AS, ENGIE E&P NORGE AS, Lundin Norway AS, Halliburton AS, Schlumberger Norge AS, Wintershall Norge AS of The National IOR Centre of Norway for support.

References

Alcorn ZP, Fernø M, Graue A (2016) Workflow for optimal injection of CO_2 to enhance oil recovery in mature oil fields: a preliminary study for a field pilot program. In: Society of petroleum engineers, SPE-180029-MS. https://doi.org/10.2118/180029-ms

Alvarez JM, Rivas H, Rossen WR (2001) A unified model for steady-state foam behavior at high and low foam qualities. SPE J 6(03):325–333

Cheng L, Reme AB, Shan D, Coombe DA, Rossen WR (2000) Simulating foam processes at high and low foam qualities. In: Society of petroleum engineers, SPE-59287-MS. https://doi.org/10.2118/59287-ms

Chou SI, Vasicek SL, Pisio DL, Jasek DE, Goodgame JA (1992) CO_2 foam field trial at north ward-estes. In: Society of petroleum engineers, SPE-24643-MS. https://doi.org/10.2118/24643-ms

Falls AH, Hirasaki GJ, Patzek TW, Gauglitz DA, Miller DD, Ratulowski J (1988) Development of a mechanistic foam simulator: the population balance and generation by snap-off. SPE Res Eng 3(3):884–892

Farajzadeh R, Andrianov A, Krastev R, Hirasaki GJ, Rossen WR (2012) Foam-oil interaction in porous media: implications for foam assisted enhanced oil recovery. Adv Colloid Interface Sci 183–184:1–13

Fernø MA, Eide Ø, Steinsbø M, Langlo SAW, Christophersen A, Skibenes A, Ydstebø T, Graue A (2015a) Mobility control during CO_2 EOR in fractured carbonates using foam: laboratory evaluation and numerical simulations. J Petrol Sci Eng 135:442–451

Fernø MA, Steinsbø M, Eide Ø, Ahmed A, Ahmed K, Graue A (2015b) Parametric study of oil recovery during CO_2 injections in fractured chalk: influence of fracture permeability, diffusion length and water saturation. J Nat Gas Sci Eng 27(2):1063–1073

Fernø MA, Gauteplass J, Pancharoen M, Haugen Å, Graue A, Kovscek AR, Hirasaki G (2016) Experimental study of foam generation, sweep efficiency, and flow in a fracture network. SPE J 21(4):1140–1150

Harpole KJ, Hallenbeck LD (1996) East Vacuum Grayburg San Andres Unit CO_2 flood ten year performance review: evolution of a reservoir management strategy and results of WAG optimization. In: Society of petroleum engineers, SPE-175000-MS. https://doi.org/10.2118/175000-ms

Haugen A, Mani N, Svenningsen S, Brattekås B, Graue A, Ersland G, Fernø MA (2014) Miscible and immiscible foam injection for mobility control and EOR in fractured oil-wet carbonate rocks. Trans Por Med 104:109–131

Heller JP (1994) CO_2 foams in enhanced oil recovery. In: Schramm LL (ed) Foams: fundamentals and applications in the petroleum industry, advances in chemistry series. American Chemical Society, Washington DC, 242:201–234

Heller JP, Boone DA, Watts RJ (1985) Field test of CO_2 mobility control at rock creek. In: Society of petroleum engineers, SPE-14395-MS. https://doi.org/10.2118/14395-ms

Hoefner ML, Evans EM (1995) CO_2 foam: results from four developmental field trials. SPE Res Eng 10(4):273–281

Holm LW, Garrison WH (1988) CO_2 diversion with foam in an immiscible CO_2 field project. SPE Res Eng 3(1):112–118

Honarpour MM, Nagarajan NR, Grijalba Cuenca A, Valle M, Adesoye K (2010) Rock-fluid characterization for miscible CO_2 injection: residual oil zone, seminole field, permian basin. In: Society of petroleum engineers, SPE-133089-MS. https://doi.org/10.2118/133089-ms

Islam MR, Farouq-Ali SM (1990) Numerical simulation of foam flow in porous media. J Can Pet Tech 29(4):47–51

Jarrell PM, Fox CE, Stein MH, Webb SL (2002) Practical aspects of CO_2 flooding. society of petroleum engineers, SPE Monograph Series, vol. 22

Jian G, Puerto MC, Wehowsky A, Dong P, Johnston KP, Hirasaki GJ (2016) Static adsorption of an ethoxylated nonionic surfactant on carbonate minerals. Langmuir 32(40):10244–10252

Jonas TM, Chou SI, Vasicek SL (1990) Evaluation of a CO_2 foam field trial: Rangely weber sand unit. In: Society of petroleum engineers, SPE-20468-MS. https://doi.org/10.2118/20468-ms

Kibodeaux KR, Rossen WR (1997) Coreflood study of surfactant-alternating-gas foam processes: implications for field design. In: Society of petroleum engineers, SPE-38318-MS. https://doi.org/10.2118/38318-ms

Kim JS, Dong Y, Rossen WR (2005) Steady-state flow behavior of CO_2 foam. SPE J 10:405–415

Law DHS, Yang ZM, Stone TW (1992) Effect of presence of oil on foam performance: a field simulation study. SPE Res Eng 7(2):228–236. SPE-18421-PA. http://dx.doi.org/10.2118/18421-PA

Leeftink TN, Latooij CA, Rossen WR (2015) Injectivity errors in simulation of foam EOR. J Petrol Sci Eng 126:26–34

Ma K, Biswal SL, Hirasaki GJ (2012) Experimental and simulation studies of foam in porous media at steady state. AIChE Spring Meeting, Houston, TX, pp 1–5

Masoudi R, Giddins MA, Karkooti H, Jalan S, Gil AAV (2015) Foam simulation from coreflood to field scale. In: Presented at the SPE Asia Pacific enhanced oil recovery conference. Kuala Lumpur, Malaysia, 11–13 Aug

Mukherjee J, Norris SO, Nguyen QP, Scherlin JM, Vanderwal PG, Abbas S (2014) CO_2 foam pilot in Salt Creek Field, Natrona County, WY: phase I: Laboratory Work, reservoir simulation, and initial design. In: Society of petroleum engineers, SPE-169166. https://doi.org/10.2118/169166-ms

Mukherjee J, Nguyen QP, Scherlin JM, Vanderwal PG, Rozowski P (2016) CO_2 Foam pilot in Salt Creek field, Natrona County, Wyoming: phase III: analysis of pilot performance. In: Society of petroleum engineers, SPE-179635. https://doi.org/10.2118/179635-ms

Nguyen QP, Hirasaki GJ, Johnston KP (2015) Novel CO_2 foam concepts and injection schemes for improving CO_2 sweep efficiency in sandstone and carbonate hydrocarbon formations. Technical Report, U.S. Department of Energy, Award No. DE-FE0005902. https://www.osti.gov/servlets/purl/1178538

Osterloh WT, Jante MJ (1992) Effects of gas and liquid velocity on steady-state foam flow at high temperature. In: Society of petroleum engineers, SPE-24179-MS. https://doi.org/10.2118/24179-ms

Rossen WR (2013) Numerical challenges in foam simulation: a review. In: Society of petroleum engineers, SPE-166232. https://doi.org/10.2118/166232-ms

Rossen WR, Zeilinger SC, Shi JX, Lim MT (1999) Simplified mechanistic simulation of foam processes in porous media. SPE J 4:279–287

Sanders A, Jones RM, Linroth MA, Nguyen QP (2012) Implementation of a CO_2 foam pilot study in the SACROC field: performance evaluation. In: Society of petroleum engineers, SPE-160016. https://doi.org/10.2118/160016-ms

Schlumberger (2015) Technical description. ECLIPSE Reservoir Simulation Software

Turta AT, Singhal AK (1998) Field foam applications in enhanced oil recovery projects: screening and design aspects. In: Society of petroleum engineers, SPE-48895. https://doi.org/10.2118/48895-ms

Wang FP, Lucia JF, Kerans C (1998) Integrated reservoir characterization study of a carbonate ramp reservoir: Seminole San Andres Unit, Gaines County, Texas. SPE Res Eval Eng 1(2):105–113
Xu Q, Rossen WR (2004) Experimental study of gas injection in surfactant-alternating-gas foam process. SPE Res Eval Eng 7:438–448

Chapter 7
Integrated Reservoir Characterization Using Petrophysical and Petrographical Analysis

Archit Gupta and Gaurav S. Gairola

Abstract A sizeable chunk of spending in an exploration and production activity is expended to characterize a potential hydrocarbon reservoir. Despite the spectacular advances in reservoir characterization techniques and in 3D and 4D modelling, the risks involved in the exploration of new, deeper or diagenetically complex prospects remain large. However, diversity of reservoir rocks and inherent heterogeneity, methods for reservoir characterization, oil field-dependent pore structural model and varying petrophysical flow units pose a great challenge. There is an emerging trend of integration of petrophysical and petrographical analysis to tackle the challenges in reservoirs. Research shows that more than 60% of world's oil and 40% of world's gas reserves are held in carbonates. So, the characterization of carbonate reservoirs becomes a major concern. But producing oil and gas from carbonate reservoir is a challenging task. Since carbonate reservoirs are often naturally fractured that show varying wettability characteristics and complex porosities which significantly affects their multi-phase flow properties, production from such reservoirs pose a challenge. In carbonate reservoirs with time, rocks containing water and oil turns initially water-wet rocks into mixed-wet or even oil-wet rocks which is not the case with a sandstone reservoirs which are mostly water-wet. Therefore, characterization of wettability and its effect on fluid flow for a heterogenous reservoir would be crucial in computing the producible reserves. This paper deals with the analysis of conventional core samples from the Vindhyan Basin of India for reservoir characterization. It is envisaged that the work will provide a model which can be sued to determine the reservoir architecture, establish the fluid flow trend and identify growth potential of a reservoir. Here, the work focuses on reservoir characterization using petrophysical and petrographical analysis. Porosity studies in reservoirs require accurate mineralogical characterization. This is achieved by a petrophysical analysis which involves X-Ray

A. Gupta · G. S. Gairola (✉)
Department of Petroleum Engineering and Earth Sciences,
University of Petroleum and Energy Studies, Dehradun 248007, India
e-mail: gsgairola@ddn.upes.ac.in

K. H. Singh and R. M. Joshi (eds.), *Petro-physics and Rock Physics of Carbonate Reservoirs*, https://doi.org/10.1007/978-981-13-1211-3_7

Diffraction (XRD) analysis which will help in determining the properties of reservoir like porosity, permeability, lithology, water saturation and density. The petrographical analysis involves the preparation of samples for the thin section that are then observed under the microscope. These thin sections reveal the detailed description of rocks that provides information about depositional facies, diagenetic history and porosity system. The integrated approach and structured methodology developed in this study will result in developing a good simulation model with adequate resolution of data that simulate the production history with sufficient realism.

Keywords Reservoir characterization · Heterogeneity · Wettability · Petrophysical · Petrographical · Thin sections · XRD

1 Introduction

In recent years, the demand for oil and gas has surged. Sustaining global oil and gas demands requires proper advanced techniques for the characterization of potential reservoirs. Appropriate technology for reservoir characterization should be able to get adequate information about the reservoir properties, geology and quantify the uncertainties associated with the reservoir. The characterization of a reservoir is an integral part of reservoir management that can optimize the decision making and economics for the hydrocarbon field development.

Reservoirs are fundamentally divided into Carbonate and Sandstone Reservoirs. Both siliciclastic and carbonate sediments are nearly different in every aspect: origin, deposition, diagenesis, oil filling and evaluation. Siliciclastic rocks can be evaluated and characterized by the traditional approach but for carbonate reservoir, it gives erratic measurements. The global market says that 60% of the world's oil and 40% of the world's gas reserves are held in carbonate reservoirs (Schlumberger 2007). However, it is found that the carbonate reservoirs are far more complex than the sandstone reservoirs as deposition of sandstone is allochthonous while carbonates are autochthonous that makes it more prone to the chemical and physical processes that alter the fundamental characteristics of the rock such as porosity and permeability. At the time of deposition, carbonate reservoirs have very high porosities but it gets reduced sharply as the diagenesis proceeds. As a result, carbonate reservoirs possess heterogeneity that may exist at all scale in the pores of the grains and textures. The complexities associated with carbonate reservoir challenges the reliability and production performance of the well. The challenges of these reservoirs require adapted production strategies to enhance oil and gas production.

In this paper, the primary focus is on certain efficient techniques like thin section analysis (Petrographical) and XRD analysis (Petrophysical) for carbonate reservoirs that provides accurate measurements of the reservoir to co-relate our finding with the older findings for the efficient characterization of the reservoir. The thin sections provide the detailed information of rocks that can help us assess the depositional facies, diagenetic history and porosity system whereas the XRD analysis provides complete mineralogical characterization that can help us in determining the reservoir properties like lithology, porosity and permeability. The integration of petrophysical and petrographical analysis can help maximize the production, identifying the uncertainties and reduce the risks related to carbonate reservoir.

2 The Study Area

In this study, the conventional core sample is taken from Rohtas formation of Lower Vindhyan basin which is an intracontinental basin (Biswas et al. 1993) which also happens to be the largest among all the 'Purana Basins' and also the next biggest among all the Proterozoic basins (Chakraborty 2006). The exact location of the well is confidential therefore the coordinates are not mentioned here (Fig. 1). The succession

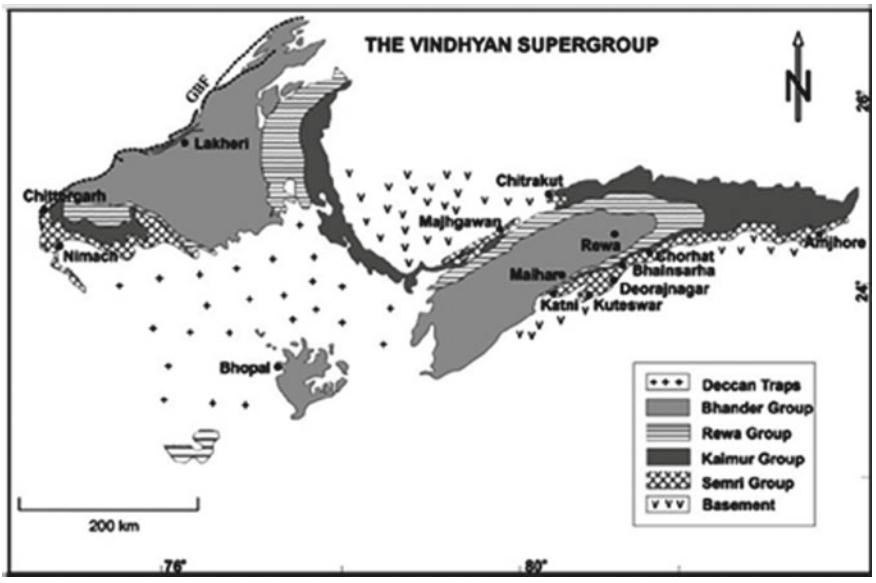

Fig. 1 Geological map of the Vindhyan Supergroup

delineates a thick sedimentary pile, about 6000 m belonging to Meso-Neoproterozoic age.

The Vindhyan succession is formed of various depositional systems which are marked by: braid delta, fan delta, alluvial fan, braidplain, tidal flat (carbonate as well as siliciclastic), eolian sand sheet, homoclinal carbonate ramp, storm-dominated shelf, shoreface (tide and storm-dominated), and epeiric peritidal flat (siliciclastic) and distally steepened carbonate ramp. The Palaeo- to Neoproterozoic Vindhyan Supergroup are exposed as repeated transitions between non-marine deposits and platform-type shallow marine (Bose and Chakraborty 1994; Bose et al. 2001; Chakraborty 2006). The former is dominated by calcareous and argillaceous with volcaniclastics which are known as Semri or Lower Vindhyan. The younger cycle predominated by siliciclastic sediments known as Upper Vindhyan which includes Kaimur, Rewah and Bhandar subgroups. The report from DGH (2019) about the paleocurrent directions of the depositional systems in the Son valley shows it to be northerly which indicates that the source lies towards the south.

The lower Vindhyan or Semri group is the oldest of the Vindhyan supergroup. In Son Valley, it rests unconformably on various primitive rocks like metamorphics and granites. In Bundelkhand region, the group blankets the Bundelkhand Granite gnessis and Bijawar group of metamorphics (DGH 2019). Semri series is sub-divided into four subgroups as the Basal stage, Porcellanite stage, Kheinjua stage and the Rohtas stage (Chakraborty et al. 2012; Ray et al. 2002; Rasmussen et al. 2002).

Gas discovery in Nohta-B from Rohtas Limestone has opened up a new spectrum for the prospectivity of Son Valley sector of Vindhyan Basin (Prasad 1984). So, the selected region has the potential tight gas resource which contains good quality of thermogenic gas (methane: 83–92%, calorific value 865–970 BTU/cubic feet) within Meso-Proterozoic Rohtas Limestone. According to the previous research, these tight gas formations are found to be thick and regionally extensive, commercial production of gas is daunting in view of low matrix porosities (2–4%) and permeabilities. So, the hydrocarbon present in the Vindhyan basin needs an unconventional approach for its characterization (Mukherjee et al. 2015).

3 Methodology

3.1 Thin Section Analysis

1. Start by cutting 8–10 mm piece from the main sample using a cutter. Grind the glass slide to make its surface rough to fix the sample onto the slide. Rub the sample's flat surface with Silicone carbide + water to make its surface rough.

2. Fix the sample to the glass slide using Araldite then the samples can be placed in the heater to assist in bonding the sample to the glass slide under pressure.
3. Then start grinding the sample surface with the grinding machine from 2.0 mm to 80 μm.
4. The slides are now ready for polishing on the machine.
5. Change the diamond cutter plate to the polishing plate.
6. Remove the samples and clean the plate.
7. The slides are now ready for analysis.
8. Finally, the photograph of the thin sections is taken through a microscope.

4 XRD Analysis

The carbonate-rich samples were selected from the Vindhyan basin core samples. Samples were powdered and sieved with a 63 μm mesh sieve to ensure a uniform size and sifted onto a vaseline coated zero background plate to reduce preferred orientation of grains. Then the prepared samples were sent for XRD.

1. Import the XRD data into the software for manipulation.
2. Set the manual ranges and the background.
3. Use the "search peaks" option and allow the software to display the distinct peaks.
4. Fit every peak to the profile.
5. Strip the Kα2 peak and replace it.
6. Using the "search match" and allow the software to display the probability of the minerals present.
7. Compare the peaks with standard XRD mineral chart present and manually decide the minerals present in the sample.

5 Results

The thin section analyses for the samples 1–18 obtained from various depths mentioned in Table 1 are shown in Figs. 2, 3 and 4.

Table 1 XRD analyses of samples 1–18 and the dominant estimated minerals

S. No.	Depth (ft)	Kaolinite (%)	Calcite (%)	Dolomite (%)	Quartz (%)	Hematite (%)	Aragonite (%)
1	12	4.01	52.62	1.60	14.90	2.56	6.16
2	16	7.21	49.39	6.32	14.43	2.89	13.17
3	17	1.70	89.80	0.63	6.63	0.22	0.26
4	19	7.19	56.31	4.65	12.01	2.80	10.25
5	23	5.50	64.08	3.92	11.77	2.03	7.62
6	25	5.77	49.52	6.40	18.65	2.50	8.20
7	28	6.94	39.16	12.50	21.54	3.39	10.15
8	33	7.50	40.05	8.05	22.16	3.76	11.43
9	36	6.59	42.58	7.08	18.86	3.39	9.83
10	41	7.29	37.27	8.10	22.91	6.61	5.23
11	45	7.00	48.05	6.80	18.15	3.35	10.30
12	46	8.19	17.14	15.51	37.32	4.80	4.50
13	51	1.76	68.33	5.25	60.62	0.25	0.587
14	52	7.31	12.50	22.36	30.91	4.60	11.57
15	53	6.23	28.28	12.76	25.44	3.40	10.13
16	55	6.98	49.09	6.55	13.08	3.16	9.98
17	56	7.50	12.17	21.28	31.35	4.22	12.24
18	57	6.80	55.20	15.70	12.30	2.60	2.00

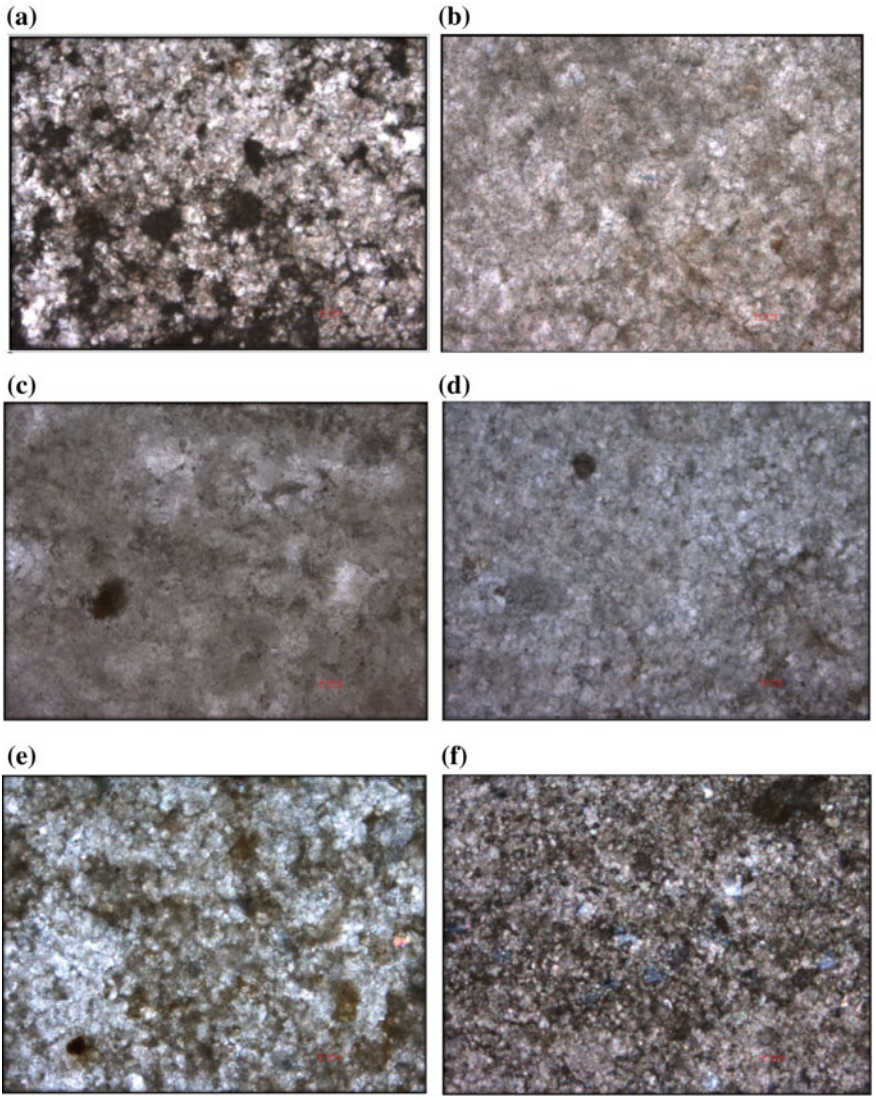

Fig. 2 Thin sections for samples 1–6 are shown in (**a**), (**b**), (**c**), (**d**), (**e**) and (**f**), respectively. The dominant minerals and their relative percentages are shown in Table 1

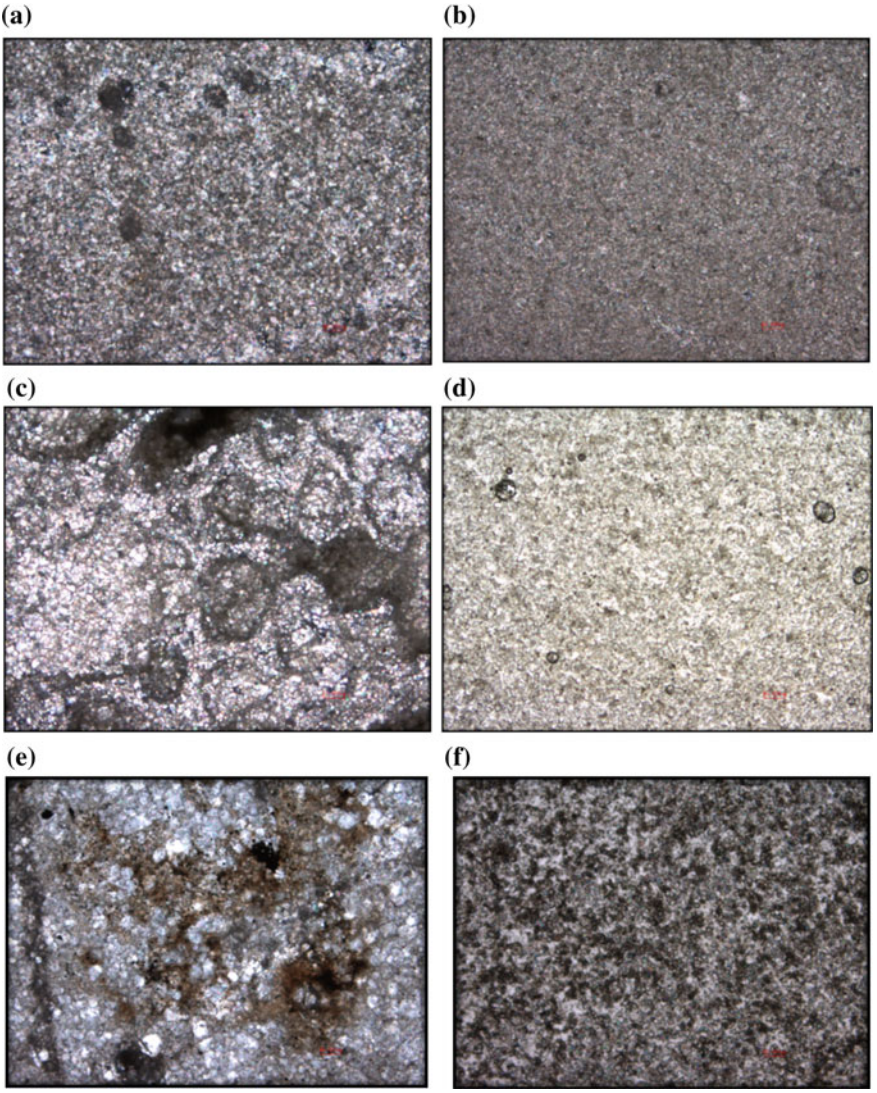

Fig. 3 Thin sections for samples 7–12 are shown in (**a**), (**b**), (**c**), (**d**), (**e**) and (**f**), respectively. The dominant minerals and their relative percentages are shown in Table 1

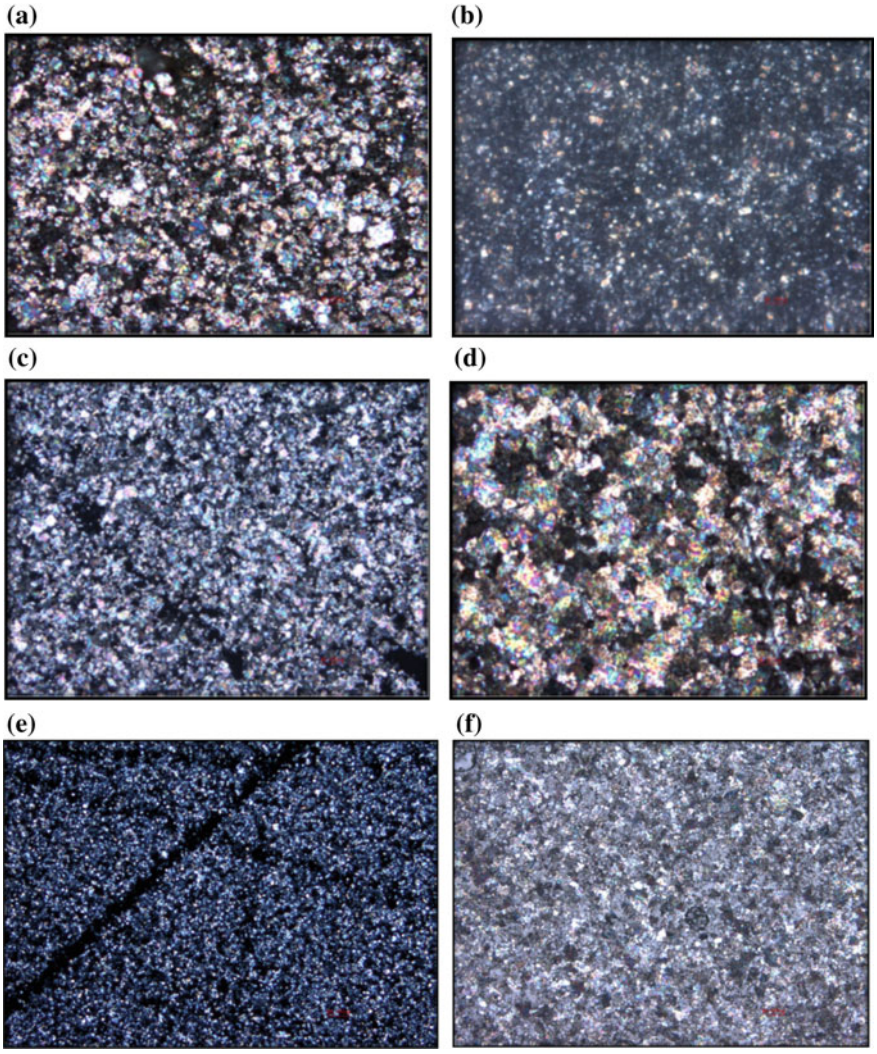

Fig. 4 Thin sections for samples 13–18 are shown in (**a**), (**b**), (**c**), (**d**), (**e**) and (**f**), respectively. The dominant minerals and their relative percentages are shown in Table 1

6 Conclusions

The conclusions mentioned below are only valid for a particular depth of Rohtas formation as the availability of data is limited. These conclusions can help in further characterization of this formation on the proper availability of data in future.

(1) In Sample Nos. 1, 3, 4, 6, 7, 9 black spots are clearly visible which possibly could be organic matter. Due to the presence of organic matter and kaolinite in

thin section and XRD, we can infer that sequence is punctuated by thin shale beds.

(2) XRD analysis of the sample indicates the dominance of calcite over dolomite with quartz.

(3) Overall the calcite is decreasing and dolomite is increasing with depth which indicates that calcite is converting to secondary dolomite. The increase in dolomite concentration with depth is indicative of secondary porosity. Sometimes the precipitation of secondary dolomite greatly reduces the fracture and Vuggy porosity which indicate tight limestone formation (Al-Awadi et al. 2009).

(4) Microfacies analysis of the limestone through petrographical method shows that samples are dominantly mudstone and micritic.

(5) From XRD results, it can be inferred that calcite and aragonite are converted to dolomite so the formation is selectively dolomitized therefore it shows varied effects of Replacement Neomorphism.

(6) In sample Nos. 2, 12 and 18 some brown alterations can be seen which could possibly be hematite as confirmed from XRD results. The presence of hematite is maybe due to either chemical weathering or oxidizing environment.

(7) The abundance of quartz detritus in Rohtas Limestone indicates the initiation of the siliciclastic input along with the carbonate precipitation at Semri–Kaimur boundary.

References

Al-Awadi M, Clark WJ, Moore WR, Herron M, Zhang T, Zhao W, Hurley N, Kho D, Montaron B, Sadooni F (2009) Dolomite: perspectives on perplexing minerals. Oilfield Rev 21(3):32–45

Biswas SK, Bhasin AL, Ram J (1993) Classification of the Indian sedimentary basins in the framework of plate tectonics: In: Biswas SK, Pandey J, Dave A, Maithani A, Thomas NJ (eds) Proceedings second seminar on petroliferous basins of India, vol 1. Indian Petroleum Publishers, Dehradun, India, pp 1–46

Bose PK, Chakraborty PP (1994) Marine to fluvial transition: Proterozoic Upper Rewa Sandstone, Maihar, India. Sediment Geol 89:285–302

Bose PK, Sarkar S, Chakraborty S, Banerjee S (2001) Overview of the Meso- to Neoproterozoic evolution of the Vindhyan basin, central India. Sediment Geol 141(2):395–419

Chakraborty C (2006) Proterozoic intracratonic basin: the Vindhyan example. J Earth Sys Sci 115:3–22

Chakraborty PP, Sarkar S, Patranabis-Deb S (2012) Tectonics and sedimentation of Proterozoic basins of Peninsular India. Proc Indian Natn Sci Acad 78(3):393–400

DGH (2019) The Vindhyan basin. Directorate general of hydrocarbon, ministry of petroleum & natural gas, India. http://dghindia.gov.in/assets/downloads/56ceb71d719c7 The_Vindhyan_basin-_22.pdf Accessed on 20 March 2019

Mukherjee S, Srivastava DK, Ram JN (2015) Exploration and exploitation of Tight gas reservoirs in Proterozoic Rohtas Limestone, Vindhyan Basin, India: major challenges and road ahead. Society of Petroleum Geophysicists. http://www.spgindia.org/11_biennial_form/exploration-and-exploitation-of-tight-gas-reservoirs-in-proterozoic-rohtas-limestone-vindhyan-basin-india-major-challenges-and-road-ahead-jaipur-2015.pdf Accessed on 20 Mar 2019

Prasad B (1984) Geology, sedimentation and paleogeography of the Vindhyan Supergroup, SE Rajasthan. Mem Geol Surv India 116(1):148

Rasmussen B, Bose P K, Sarkar S, Banerjee S, Fletcher I R, McNaughton NJ (2002) 1.6 Ga U–Pb zircon age for the Chorhat Sandstone, Lower Vindhyan, India: possible implications for early evolution of animals. Geology 30:103–106

Ray JS, Martin MW, Veizer J, Bowring SA (2002) U-Pb zircon dating and Sr isotope systematics of the Vindhyan Supergroup, India. Geology 30:131–134

Schlumberger (2007) Carbonate reservoirs: meeting unique challenges to maximise recovery. https://www.slb.com/~/media/Files/industry_challenges/carbonates/brochures/cb_carbonate_reservoirs_07os003.pdf Accessed on 20 March 2019

Chapter 8
Lithology Identification Using Lithology Impedance in Mumbai Offshore

Amrita Roy and Rima Chatterjee

Abstract The study area belongs to the marine geological setup of Surat depression of Mumbai Offshore Basin, India. The lithology of three wells in Mumbai offshore is analyzed using Gamma-Ray (GR) log, Density (ρ) log, Resistivity (Rt) log and Neutron Porosity (Φ) log. This analysis makes the identification of the lithology difficult. DSI log is recorded only for wells W-1 but for W-2, W-3 shear wave velocity data is not available. Major lithologies found in this area are sandstone, siltstone, shale, limestone and mixed lithologies of sand, silt, shale. This study aims to construct a lithology indicator parameter which is better in the identification of lithologies. This lithology indicator parameter is named as Lithology Impedance (LI). This parameter is calculated using density, P wave (V_p) and S wave (V_s) velocity. This indicator shows a better contrast for different lithology and also follows a specific range. To estimate the LI log value for W-2 and W-2, the Vp-Vs relation from W-1 is used, as Vs is not available in W-2 and W-3. To prove its validity Regression Method and Multilayered Feed forward Neural Network (MLFN) methods are used. Using Regressing method the relation of LI log values are established in relationship with the GR, V_p, Rt, ρ and Φ. Validation of Regression method shows the Regression model predicted LI shows poor fit $R^2 = 0.67$ with the Estimated LI value while the MLFN model predicted LI indicates satisfactory to good R^2 values 0.95 with the estimated LI value. This study successfully shows that the adopted method provides a good understanding of lithofacies distribution and their quality.

Keywords Surat depression · Lithology impedance · Multilayered feed forward neural network · Well log · Regression

1 Introduction

Estimation of subsurface reservoir quality, continuity and distribution is an important aspect for the optimization of hydrocarbon production. The range of velocity, density and resistivity of formation lithology varies greatly, which makes it difficult for inter-

A. Roy (✉) · R. Chatterjee
Department of Applied Geophysics, IIT (ISM), Dhanbad 826004, India
e-mail: roy.amrita23@gmail.com

K. H. Singh and R. M. Joshi (eds.), *Petro-physics and Rock Physics of Carbonate Reservoirs*, https://doi.org/10.1007/978-981-13-1211-3_8

preters to decide the type of lithology. In this paper, the basin modelling/analyses based on lithology over a part of the western offshore has been attempted. However, if we can incorporate several other parameters like velocity, density, formation resistivity and gamma-ray values, then we can generate such an attribute that can be helpful in identification of lithology. The study area belongs to the marine geological setup of Surat depression of Mumbai Offshore Basin. This has remained an active clastic 'depocentre' for a major period during Tertiary, accommodating a huge pile of sediments brought by Narmada-Tapti fluvial systems. The approach adopts cross plot analysis; namely V_p/V_s versus acoustic impedance, gamma-ray versus resistivity that helps us in deciding our input parameters. The lithology impedance is a function of the log parameters: gamma-ray, resistivity, density, porosity and acoustic impedance. It is a rock physical attribute that is generated using regression modelling taking conventional log data as independent input variables. Using Multilayered Feed forward Neural Network (MLFN) the results have been verified. The lithology impedance is able to identify sand, shale, limestone and basaltic trap from three wells namely W-1, W-2, W-3. From drilling report, it is found that these three wells show hydrocarbon prospects and some show presence of coal in the lithostratigraphic section. In the well W-1 data set is taken within a depth interval of 1430–2230 m, for W-2 and W-3 data is taken from 1400 to 1750 m and from 1600 to 2000 m. In W-1 gas shows were observed during drilling at different intervals in the depth range 2140–2150 m.

2 Lithology Impedance

Quakenbush et al. (2006), Zhou and Hilterman (2010), and Sharma and Chopra (2013) gave an idea about the combinations of Acoustic (AI) and Shear Impedances (SI). This combination can be used as a successful tool to predict lithofacies and fluid types in siliciclastic sediments. Such a parameter is named as Lithology Impedance (LI). Mathematically, lithology impedance is given as

$$\mathrm{LI} = \mathrm{AI} - \mathrm{C}^{*}\mathrm{SI} + \text{Intercept value} \tag{1}$$

$$= \mathrm{AI(t)} - \left[(\mathrm{AI/SI})_{\mathrm{wet}}\right]_{\mathrm{avg}}\mathrm{SI(t)} + \text{Intercept} \tag{2}$$

where AI(t) = Acoustic Impedance trace, (ft/s)*(g/cc), SI (t) = Shear Impedance trace, (ft/s)*(g/cc), C or $[(\mathrm{AI/SI})_{\mathrm{wet}}]_{\mathrm{avg}}$ = Rotation Optimization Factor.

Intercept value is estimated from cross plot between AI (along the *x*-axis) and SI (along the *y*-axis) which is shown in Fig. 1b. It is found that AI-SI relation from the cross plot has a good fit over the whole log with an $R^2 = 0.90$ and the relation is found to be,

$$\mathrm{SI} = 0.56 * \mathrm{AI} - 310.15 \tag{3}$$

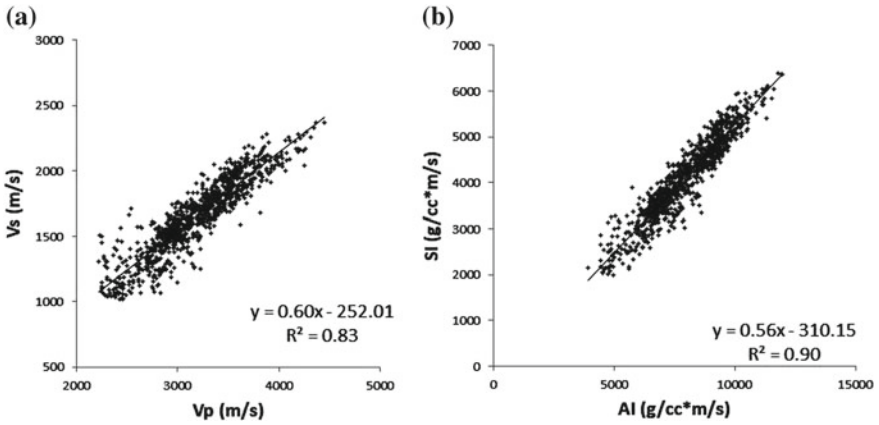

Fig. 1 Plots for V_p versus V_s in (**a**) and AI versus SI for W-1 in (**b**)

The whole study is based on this Eq. (2). The V_p-V_s relation, obtained from W-1 well log data is used to estimate V_s value (Greenberg and Castagna 1992; Castagna et al. 1985) of W-2 and W-3 as W-2 and W-3 well data don't have V_s log values. The relation which is obtained from W-1 well is given by,

$$V_s = 0.60 * V_p - 252.01 \tag{4}$$

This equation has a good linear fitting of data with an $R^2 = 0.83$ as shown in Fig. 1. LI log for W-1, W-2 and W-3 are shown in Figs. 2, 3 and 4.

Figures 2, 3 and 4 show the GR, Rt, Density and LI log responses of W-1, W-2 and W-3 respectively. We can qualitatively identify lithology characterized by low GR value and high GR values. But lithology cannot be quantitatively identified. This is the same for electrical resistivity and density logs. But LI log response shows a specific range of values for sandstone, shale, limestone and basaltic trap with an identifiable contrast of range.

3 Prediction of Lithology Impedance Through Regression Model

Geophysical logging has been extensively used to measure physical properties of rock-like density, transit time of compressional and transverse waves, Natural radioactivity, Neutron and density porosity, electrical resistivity of the formation among many other properties (Gelman 2005; Koch and Link 1970; Omudu et al. 2007; Chang et al. 2006). In this study, GR, V_p, Rt, $(\rho/\Phi)^2$ are used as independent variables for the computation of Lithology Impedance (LI). In this study, a Multiple Linear Regression Model is proposed for the study of LI, which makes the use of

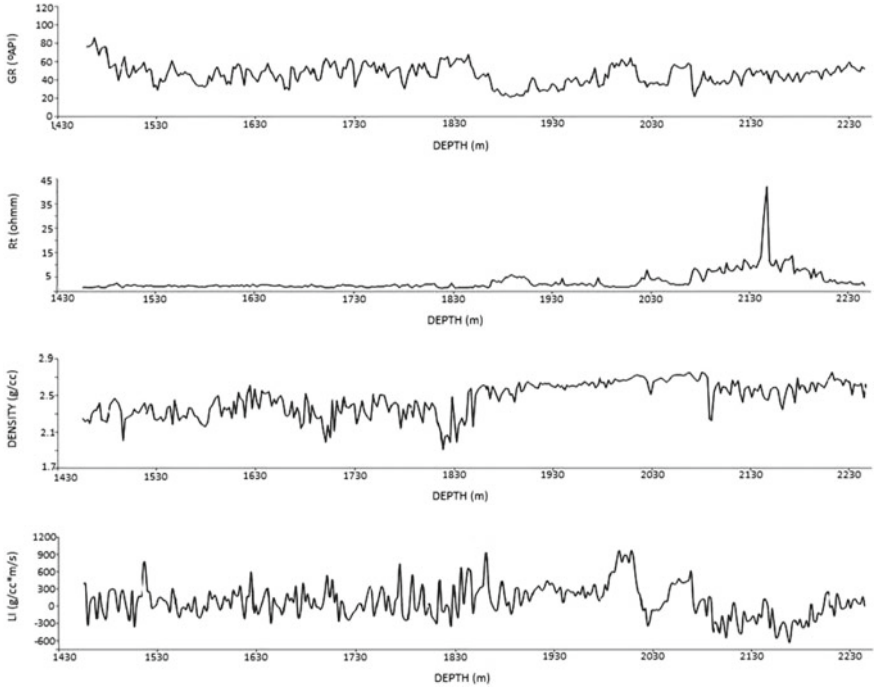

Fig. 2 GR, Rt, Density and LI log responses for W-1

four independent variables (previously mentioned) from two wells: W-1 and W-2 in the Mumbai offshore. An IBM SPSS statistical software is used for establishing the relationship between four independent variables and the dependent variable LI. It seems that the ANOVA model is perhaps the most widely used linear statistical model with independent variables. Table 1 shows the number of samples used for training and validation processes during regression method. Table 2 shows the good fit achieved by the said method. Table 3 gives the Regression Model that is used as the linear relationship between LI, GR, V_p, Rt and $(\rho/\Phi)^2$.

The linear relationship between LI, GR, V_p, Rt and $(\rho/\Phi)^2$ form the Multiple Linear Regression Method is given by,

$$\text{LI} = 0.13 * V_p + 11.14\, D2 * \text{GR} + 0.37 * \text{Rt} + 0.04(\rho/\phi)^2 - 482.97 \qquad (5)$$

Here, the constant coefficient is a simple mean of group means of independent variables. Standardized coefficient gives the idea about the influence of each predictor and the beta and p values are significance (sig.) for each predictor (Table 3). The beta value measures the influence of each predictor variable on the dependent variable. A high beta value is indicative of the greater influence of the predictor variable on the dependent variable.

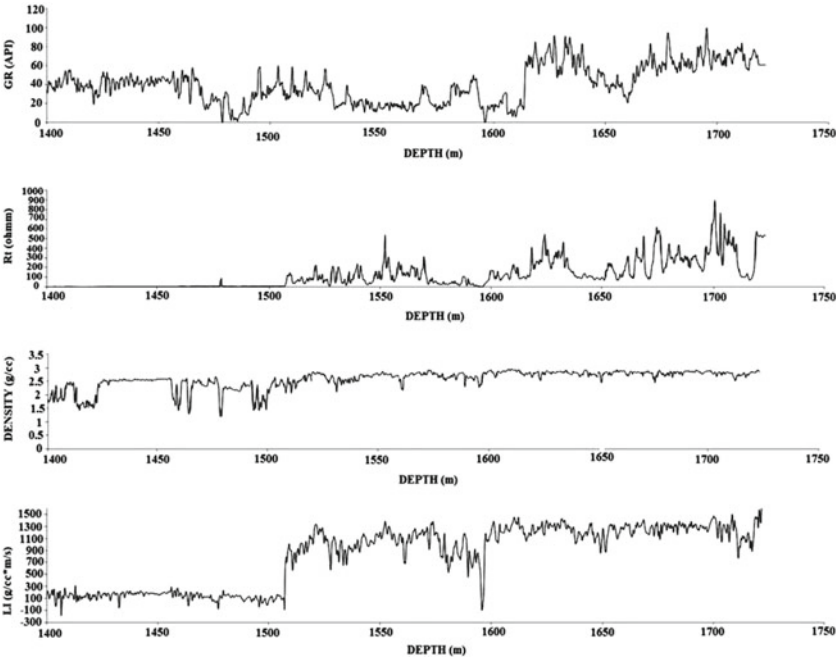

Fig. 3 GR, Rt, Density and LI log responses for W-2

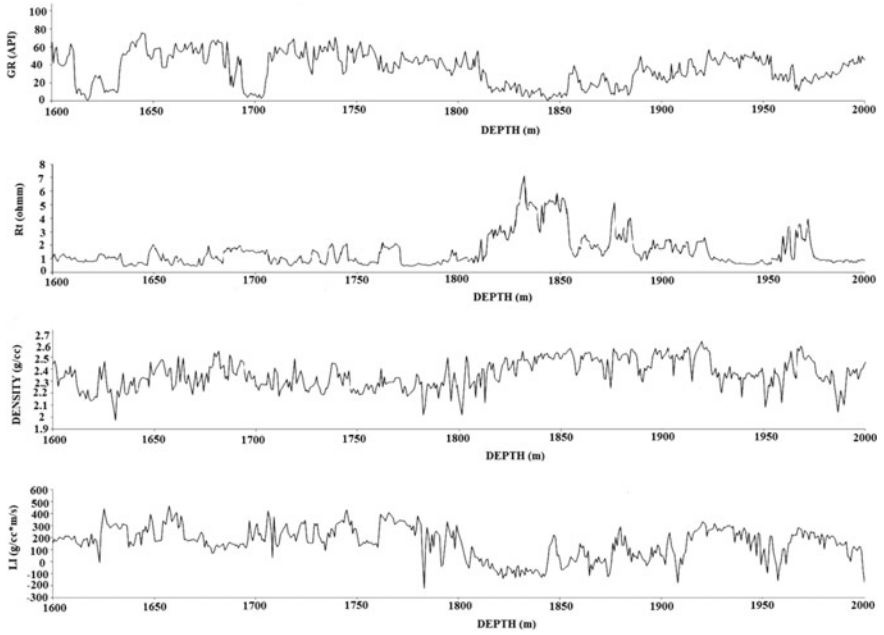

Fig. 4 GR, Rt, Density and LI log responses for W-3

Table 1 Number of samples used for training and validation process during regression method

S. no.	Independent variables	No. of samples	
		Training	Testing
1	V_p	30	225
2	GR	30	225
3	Rt	30	225
4	$(\rho/\Phi)^2$	30	225

Table 2 Error estimation obtained from the use of regression method

Model	R	R^2	Adj. R^2	Std. error
1	0.797	0.635	0.615	14.37842

Table 3 Regression model applied to LI, GR, V_p, Rt and $(\rho/\Phi)^2$ to seek linear relationship among the parameters

Model	Unconstrained coefficients		Standardized coefficients	t	Sig.
	B	Std. error	Beta		
(Constant)	−482.967	11.7393		−4.114	0.000
V_p	0.128	0.033	0.354	3.896	0.001
GR	11.144	1.273	0.609	8.753	0.000
Rt	0.371	0.243	0.141	1.529	0.141
$(\rho/\Phi)^2$	0.040	0.071	0.041	0.555	0.584

4 Prediction of LI Through Multilayered Feedforward Neural Network (MLFN) Model

In heterogeneous formation estimation of LI from logs becomes difficult to solve and does not provide good result using the linear regression method. Artificial neural network tool is now considered to be a very successful tool for estimating the petrophysical and rock physics model by integrating core and log data through an effective modelling strategy (Lim et al. 2009; Singha et al. 2014; Chatterjee et al. 2016; Ghosh et al. 2016; Dayoff 1990). A Multilayered Feedforward Neural Network (MLFN) model is derived from input parameters such as V_p, GR, Rt, ρ, Φ obtained from log data and LI as output parameter. The model consists of a single hidden layer containing 8 hidden nodes with 100 epochs. The training data consists of 30 data points taken from wells W-1 and W-2 involving input parameters: *P* wave velocity, deep resistivity, gamma-ray, density and neutron porosity for sandstone, shale, limestone, and basaltic trap lithologies. The desired output, LI was taken from wells W-1, W-2, W-3 for total 275 data points.

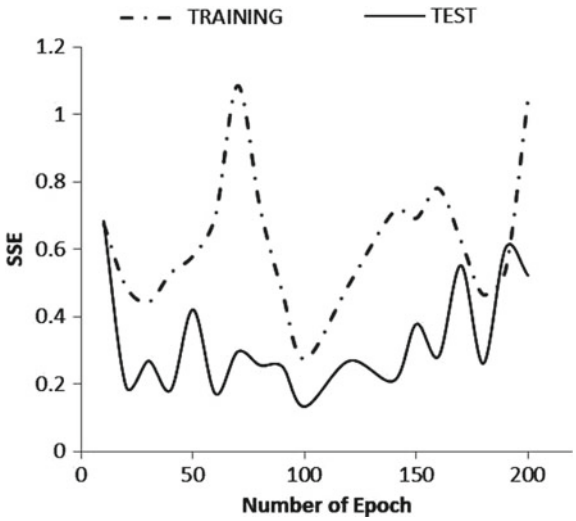

Fig. 5 Selection of optimum Epoch for the MLFN Method

The MLFN model consists of three layers—the input layer, the hidden layer and the output layer (Paul S et al. 2017; Masters 1994). These operators are chosen in such a way to ensures minimum sum-squared error (SSE) between the estimated LI from log data and the predicted LI. One hidden layer is taken for study. The hidden layer weights are selected for minimum SSE by doing trial models. SSE values for training and validation are recorded for 10–220 epochs with 2–22 nodes in the hidden layer. The IBM SPSS software used 70% of the total available data to train the network while 20% was utilized for validation and the remaining 10% was used for testing. As shown in Fig. 5 it is found that 100 epoch and 8 nodes are an optimum weight for the network analysis. During training 4 clusters of 4 known lithologies (namely sandstone, shale, limestone and basaltic trap) are considered, where the total no. of training sample data is 30. Network training gives a good fit ($R^2 = 0.95$) between estimated LI from log data and predicted LI from network training (Fig. 6). Once the data set is trained for a few known lithologies this network is then used to test 225 testing data points. Figure 6b displays a better fit of $R^2 = 0.86$ between estimated LI from log data and predicted LI from MLFN model for total 275 sample data of W-1, W-2, W-3.

5 Results

Table 4 shows the range of several conventional log values for different lithology encountered by W-1 and W-2. This also shows the contrast in LI log values is quite prominent.

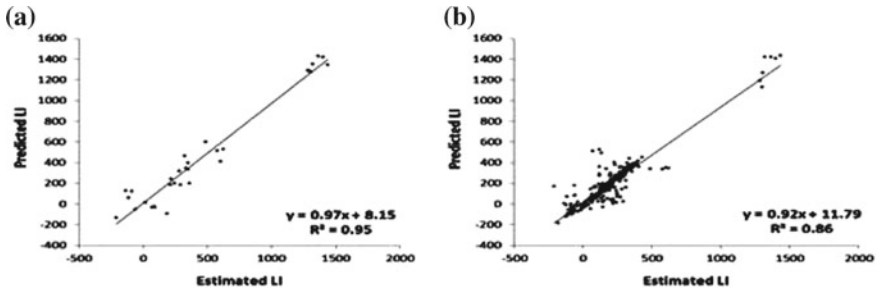

Fig. 6 Result of training for W-1 and W-2 in (**a**) and of testing for W-1, W-2, W-3 using MLFN method in (**b**)

Table 4 Log values for various lithologies observed in W-1 and W-2 wells

Lithology	Range of V_p log value (m/s)	Range of GR log value (^{O}API)	Range of Rt log value (Ω-m)	Range of ρ log value (g/cc)	Range of Φ log value (%)	Range of LI log value (g/cc*m/s)
Sandstone	2500.00–3500.00	20.30–30.76	0.89–3.18	2.15–2.69	25–36	(−210.08)–186.95
Shale	2020.95–2540.23	40.57–68.23	0.53–0.92	1.92–2.47	47–56	323.38–625.16
Limestone	3811.53–4193.36	2.60–13.29	3.50–5.35	2.51–2.66	14–22	211.90–291.21
Basaltic trap	5596.09–5979.40	72.53–95.70	157.29–835.45	2.81–2.89	6–18	1286.67–1436.85

6 Conclusion

Due to a large range of conventional log values, it is difficult to identify lithology quantitatively in the absence of core data. Lithology Impedance being a combination of gamma-ray, electrical resistivity, density, porosity and P wave velocity is proven to be a very good lithology indicator. Linear Regression Method is useful in case of clean lithology but as in nature we mostly encounter complex or mixed lithology hence linear relationship will not work properly. In that case, the Artificial Neural Network tool becomes very useful. It gives a nonlinear relationship among physical properties of the rock.

Acknowledgements The authors gratefully acknowledge the Gujarat State Petroleum Corporation (GSPC) for providing data for this research work and also thankful to Department of Applied Geophysics, IIT(ISM), Dhanbad for providing required technical support to carry out this research work successfully.

References

Castagna JP, Batzle ML, Eastwood RL (1985) Relationships between compressional-wave and shear-wave velocity in clastic silicate rocks. Geophysics 50(4):571–581

Chang C, Zoback MD, Khaksar A (2006) Empirical relations between rock strength and physical properties in sedimentary rocks. J Petrol Sci Eng 51:223–237

Chatterjee R, Singha D, Ojha M, Sen M, Sain K (2016) Porosity estimation from pre-stack seismic data in gas-hydrate bearing sediments, Krishna–Godavari basin, India. J Nat Gas Sci Eng 33:562–572

Dayoff JE (1990) Neural network architectures: an introduction. Van Nostrand Reinhold, New York, p 259

Gelman A (2005) Analysis of variance-why it is more important than ever. Ann Stat 33:1–53

Ghosh S, Chatterjee R, Shanker P (2016) Estimation of ash, moisture content and detection of coal lithofacies from well logs using regression and artificial neural network modeling. Fuel 177:279–287

Greenberg ML, Castagna JP (1992) Shear-wave velocity estimation in porous rocks: theoretical formulation, preliminary verification and applications. Geophys Prosp 40:195–209

Koch GS Jr, Link RF (1970) Statistical analysis of geological data, vol 1. Wiley, New York, NY, USA, pp 1–375

Lim TK, Ahmed A, Taslim G, Gibrata MA (2009) Combining wireline and LWD borehole seismic data for drilling HPHT well: a novel approach. In: International Petroleum Technology Conference, Doha, Qatar, December 7–9, IPTC 13083

Masters T (1994) Signal and image processing with neural networks: a C++ sourcebook. Wiley, New York, NY, USA

Omudu LM, Ebeniro JO, Xynogalas M, Adesanya O, Osayande N (2007) Beyond acoustic impedance: an onshore niger delta experience. In: SEG/San Antonio Annual Meeting, pp 412–415

Paul S, Ali M, Chatterjee R (2017) Prediction of compressional wave velocity using regression and neural network modeling and estimation of stress orientation in bokaro coalfield, India. Pure Appl Geophys 175(1):375–388. https://doi.org/10.1007/s00024-017-1672-1

Quakenbush M, Shang B, Tuttle C (2006) Poisson impedance. Lead Edge 25(2):128–138

Sharma RK, Chopra S (2013) Poisson impedance inversion for characterization of sandstone reservoirs. In: SEG/Houston Annual Meeting, pp 2549–2553. http://dx.doi.org/10.1190/segam2013-0181.1

Singha DK, Chatterjee R (2014) Detection of overpressure zones and a statistical model for pore pressure estimation from well logs in the Krishna–Godavari Basin, India. Geochem Geophys Geosyst 15(4):1009–1020

Singha DK, Chatterjee R, Sen MK, Sain K (2014) Pore pressure prediction in gas-hydrate bearing sediments of Krishna Godavari Basin in India. Mar Geol 357:1–11

Zhou Z, Hilterman FJ (2010) A comparison between methods that discriminate fluid content in unconsolidated sandstone reservoirs. Geophysics 75(1): B47–B58

Chapter 9
A Review on Influence of Mineralogy and Diagenesis on Spectral Induced Polarization Measurements in Carbonate Rocks

Neha Panwar and Ravi Sharma

Abstract Due to the heterogeneity of the carbonate reservoirs, it becomes very difficult to determine the correct mineralogy or lithology of the formation. Before any petrophysical analysis, it seems imperative to determine the mineralogy. Different Lithologies and facies vary in different ways and require different methods for further interpretation. Spectral-induced polarization is one of the geophysical methods that is sensitive to the fluid-grain interface and hence very beneficial in delineation of geological material. Using this method, we measure complex conductivity. The basic principle is that a sinusoidal current is injected into the rock and the resulting voltage is calculated. The capacitive nature of the rocks introduces a phase difference between the injected current and the measured voltage waveform between the potential electrodes. In this paper, we will discuss previous published data on the impact of various rock types (Skarn ore, Skarn rock, Carbonate rocks) on the SIP response by obtaining the chargeability and relaxation time. SIP is a compelling approach to study and characterize sandstone, shale rocks, volcanic rocks, etc. Although, little work is done in exploration of carbonate rocks using SIP till now.

Keywords Induced polarization (IP) · Spectral-induced polarization (SIP) · Time domain induced polarization (TDIP)

1 Introduction

The ohmic and capacitive electrical processes and its frequency dependence of a rock material can be understood through electrical measurements over the Earth's surface or in the laboratory via controlled experiments. The resulting amplitude and the phase shift for the conductive material can be determined in the low-frequency range. This technique involves measurements of complex conductivity at a very large number of frequencies ranging from 1 kHz to 1 MHz (Joseph 2016). The relationship

N. Panwar (✉) · R. Sharma
Indian Institute of Technology, Roorkee, Uttarakhand, India
e-mail: npanwar@es.iitr.ac.in

K. H. Singh and R. M. Joshi (eds.), *Petro-physics and Rock Physics of Carbonate Reservoirs*, https://doi.org/10.1007/978-981-13-1211-3_9

between the magnitude of complex conductivity $|\sigma^*|$ and phase (Φ) with real (σ') and imaginary (σ'') component of the conductivity is given as (Revil et al. 2011).

$$\sigma^* = |\sigma| \exp(i\Phi) = \sigma' + i\sigma'', \tag{1}$$

$$|\sigma| = \sqrt{\sigma'^2 + \sigma''^2} \tag{2}$$

$$\tan\theta = \frac{\sigma''}{\sigma'} \tag{3}$$

The in-phase component (real part) refers to pure electro-migration processes. The Quadrature component (imaginary part) refers to the accumulation of reversible charges. Revil and Florsch (2010) have shown that the conductivity of water-wet porous rocks devoid of any conductive minerals are affected by the pore-geometry, the presence of type of pore fluids and the chemical interaction of porewater and the matrix minerals. The polarization of rocks is primarily due to the electrochemical reactions at the boundaries and layers separating the pore water from the grains which forms an electrical double layer known as EDL. An EDL consists of two different layers: the Stern layer and diffuse layer. The stern layer consists of counter-ions compared to mineral grain, while the diffuse layer consists of co-ions and counter-ions.

The complex conductivity of a porous material with disseminated semiconductors such as pyrite and magnetite is given by a cole–cole model expressed as (Revil et al. 2015)

$$\sigma* = \sigma\left(1 - \frac{M}{1 + (i\omega\tau)^c}\right). \tag{4}$$

Here, c denotes the cole–cole exponent that describes the width of relaxation time distribution, ω is the excitation frequency in (rad/sec) and i is the pure imaginary number. The parameter M is the chargeability written as

$$M = \frac{(\sigma_{\text{inf}} - \sigma_0)}{\sigma_{\text{inf}}} \tag{5}$$

Here, σ_{inf} and σ_0 denotes the high and low conductivities, respectively. The content of metallic or clay minerals defines the chargeability and is indicated by the strength of the polarization. The main relaxation time is given as

$$\tau = \frac{a^2}{D} \tag{6}$$

where D is the diffusion coefficient and a, is the grain radius of the metallic particles.

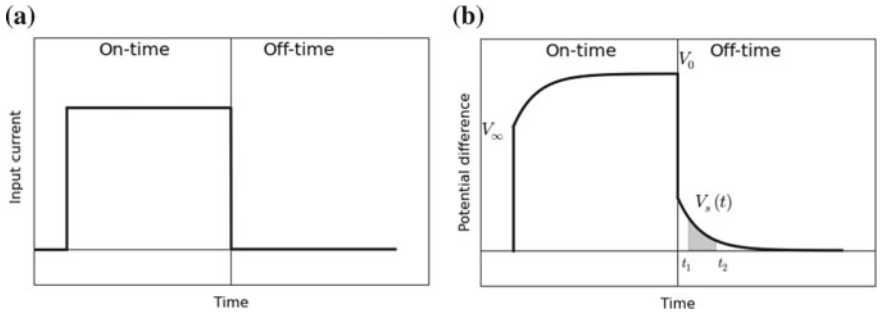

Fig. 1 Time domain induced polarization (https://em.geosci.xyz/content/geophysical_surveys/ip/index.html)

2 Time Domain IP

Induced polarization measurements can be done in both the time and frequency domains. Each method has its own advantages. In time domain induced polarization (TDIP), the primary current is applied to the material for some time and then the current is switched off (Fig. 1). Due to the current storage capacity of the material, the current does not reach its original state immediately. Hence there is some delay before the charges are redistributed within the material, and this decay of secondary current is recorded over time which provides insights to the electrical properties of the material (Mao et al. 2016).

The chargeability of the material is studied in the time domain induced polarization (TDIP). According to Revil et al. (2015) and Mao et al. (2016), the chargeability of metallic materials like pyrite and magnetite could be significant. The chargeability is directly proportional to the volumetric content of the metallic materials and is defined as

$$M = \left(\frac{9}{2}\right) * \varphi_{\mathrm{m}}. \tag{7}$$

Here, M is the chargeability and φ_{m} is the volume content of metallic materials.

For non-metallic materials, it is best to determine normalized chargeability because normalized chargeability is directly related to the cation exchange capacity (CEC). The CEC is the major component related to clay mineralogy.

3 Frequency Domain IP

The Induced polarization study in Frequency Domain is also known as spectral-induced polarization. Harmonic current is applied to the material and the resulting voltage difference is measured. Due to the capacitance of the material, a phase dif-

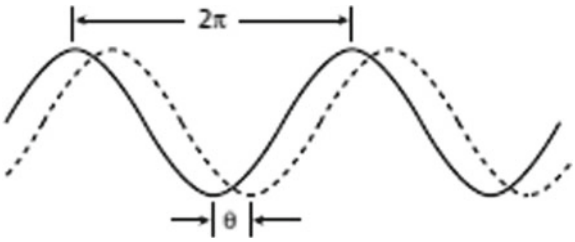

Fig. 2 Spectral-induced polarization showing phase and amplitude with the passage of current and the measured voltage

ference occurs between the applied current and the voltage (Joseph 2016) (Fig. 2). Thus, the study of phase and amplitude provides information of the material.

Here, phase is considered as the major parameters while studying metallic materials. The phase is directly related to the weight content of the metallic particles (φ_w) (Revil et al. 2015; Mao et al. 2016).

$$\varphi = \left(\frac{9}{4}\right) * \frac{\rho}{\rho_{\mathrm{m}}} * \varphi_w \tag{8}$$

Here, ρ denotes the mass density of the background porous material without the metallic grains, and ρ_{m} denotes the mass density of the metallic particles.

4 Influence of Mineralogy on IP

As discussed above, both the time domain and frequency domain IP can be beneficial in the determination of the mineralogy. Relaxation time is also measured which is directly related to the grain radius.

It is considered that the IP effect is dominant below 100 Hz but with higher frequencies, Maxwell Wagner polarization or the dielectric effect is more prominent (Revil et al. 2014). Thus, the presence of metallic particles in the material introduces the dielectric effect. The phase spectra for three samples each for Skarn rocks, Skarn ores and carbonate rocks indicates the prominent dielectric effect at high frequencies (Fig. 3).

Figure 3a, c show the frequency response of Skarn and Carbonate rocks and is nearly constant up to 100 Hz, which indicates that the frequency is more influenced by the dielectric effect than the Induced Polarization. However, the frequency response in Fig. 3b shows a more pronounced variation even below 100 Hz. The results suggest that Skarn ores contain a high abundance of metallic minerals below 100 Hz and are the strongest candidates for Induced Polarization studies among all rocks and ores studied here.

As discussed above, the chargeability is directly proportional to the metallic content in the material. It is clear from Fig. 4a, b, c that in the case of Skarn rocks, metallic minerals like magnetite (Mt) and Pyrite (Py) are present which shows high charge-

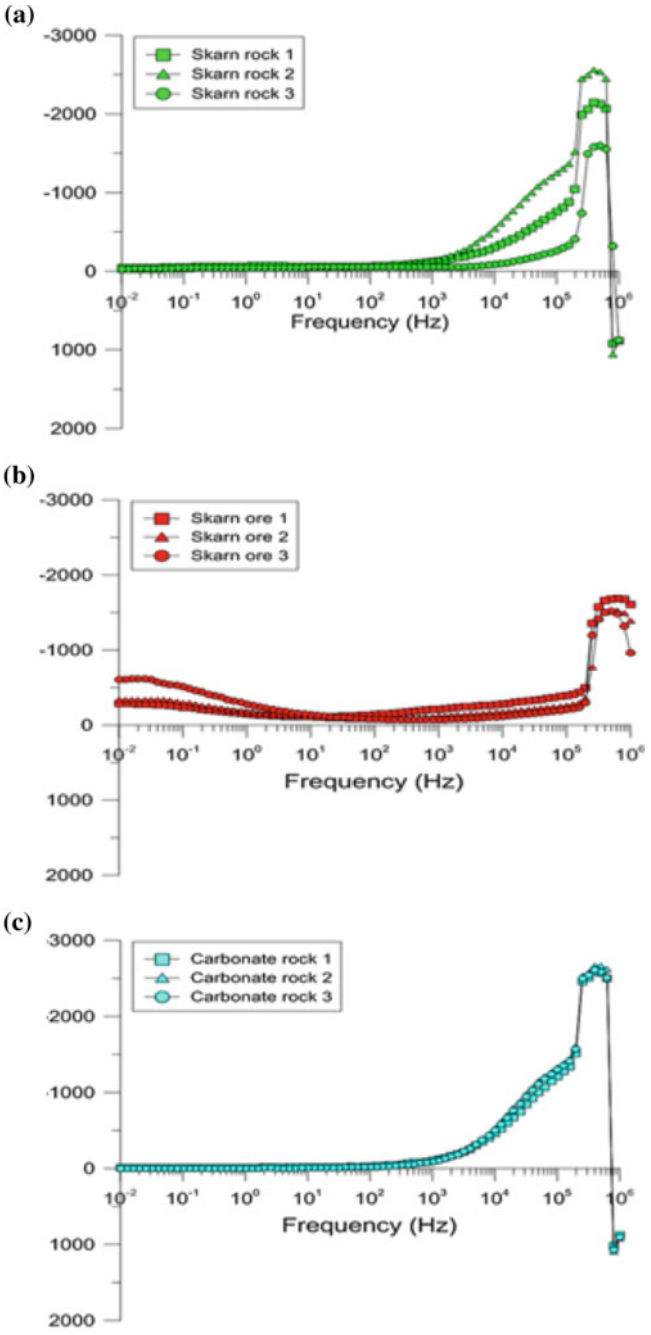

Fig. 3 Phase spectra of **a** Skarn rocks, **b** Skarn ores, **c** Carbonate rocks (reproduced with permission from Shin et al. 2016)

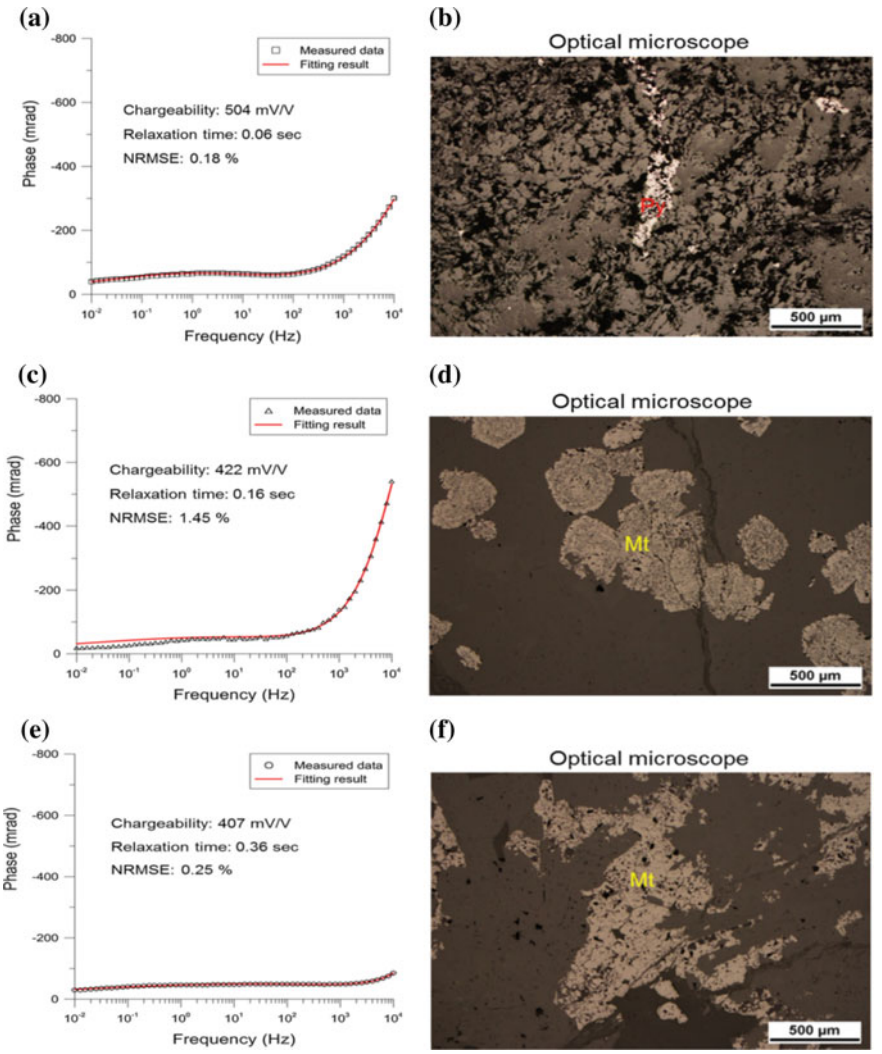

Fig. 4 Chargeability and relaxation time for Skarn rock 1 in (**a**), Skarn rock 2 in (**c**) and Skarn rock 3 in (**e**) while images obtained from Optical microscope are shown for Skarn rock 1 in (**b**), Skarn rock 2 in (**d**) and Skarn rock 3 in (**f**) (reproduced with permission from Shin et al. 2016)

Table 1 Minerals identified from the XRD analyses for Skarn rocks 1, 2 and 3

Mineral content (wt%)	Skarn rock 1	Skarn rock 2	Skarn rock 3
Grossular	35.5	52.7	15.6
Hastingsite	36.7	39.2	68.4
Augite	12.0	–	–
Chlorite	3.6	–	2.1
Calcite	3.4	5.7	3.8
Quartz	1.1	2.2	7.6
Montmorillonite	2.7	–	–
Magnetite	5.0	0.2	2.5
Total	100.0	100.0	100.0

ability. This is also confirmed from the XRD results shown in Table 1. In the case of all three Skarn ores (Fig. 5a, c, e), the magnetite content is significantly increased (Table 2) and hence the chargeability value increases proportionally compared to those measured in Skarn rocks.

The XRD results (Table 2), shows that pyrite is also present in Skarn ore 2 which also enhances the chargeability of Skarn ore 2. According to Pelton et al. (1978) pyrite has the highest chargeability followed by magnetite. The non-metallic materials like carbonate rocks do not add to the chargeability. This is demonstrated in phase spectra of carbonate rocks shown in Fig. 6a, c, e, and that the chargeability values are small in Carbonates compared to Skarn rocks and ores.

Relaxation time is directly proportional to the square of the grain radius. Thus, it does not depend on the presence or absence of metallic minerals. The optical microscope images shown in Figs. 4b, d, f, 5b, d, f and 6b, d, f indicates the grain sizes of minerals present in the thin sections. In the case of Skarn ore, the grain sizes are large compared to the Skarn and Carbonate rocks. Therefore, the relaxation time should be large in Skarn ore (Figs. 4b, d, f, 5b, d, f, 6b, d, f). Also, in the case of Carbonate rocks, the relaxation time of Carbonate rock 3 is significantly higher compared to carbonate samples 1 and 2. It can be verified from the optical microscope image (Fig. 6f) that carbonate rock 3 has large grain sizes in comparison to carbonate rocks 1 and 3. The minerals identified from the X-ray diffraction experiments for carbonate rocks are enlisted in Table 3.

According to Revil et al. (2014), IP effect is influenced by the pore size in non-mineralized rocks while the pore size, in turn, is affected by the grain size. The large sizes of grains in carbonate rock 3 may be due to the recrystallization of calcite (Sharma 2015). Hence, it can be concluded that in the case of non-mineralized rocks, relaxation time could be a parameter which can be an indicator of hydrothermal alteration, since recrystallization may occur due to hydrothermal alteration.

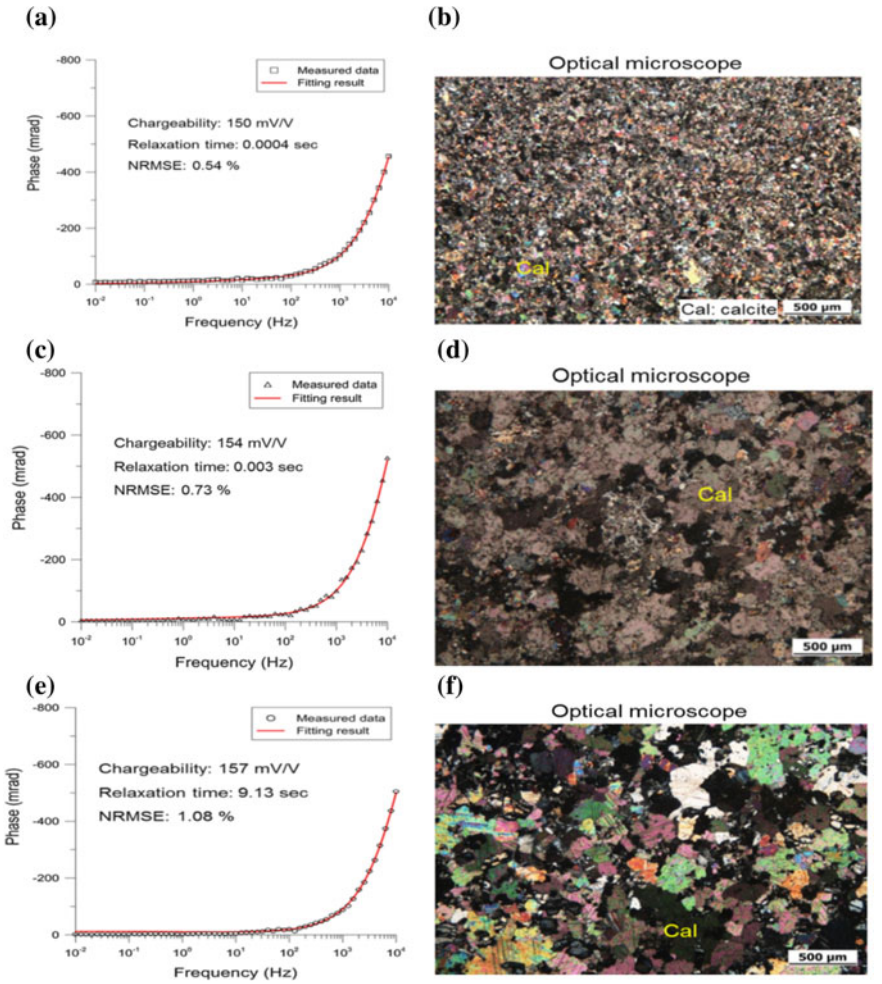

Fig. 5 Chargeability and relaxation time for Skarn ore 1 in (**a**), Skarn ore 2 in (**c**) and Skarn ore 3 in (**e**) while images obtained from Optical microscope are shown for Skarn ore 1 in (**b**), Skarn ore 2 in (**d**) and Skarn ore 3 in (**f**) (reproduced with permission from Shin et al. 2016)

Table 2 Minerals identified from the XRD analyses for Skarn ores 1, 2 and 3

Mineral content (wt%)	Skarn ore 1	Skarn ore 2	Skarn ore 3
Biotite	10.3	8.9	13.5
Calcite	2.9	16.0	9.7
Quartz	1.0	2.4	–
Fluorite	–	0.6	–

(continued)

Table 2 (continued)

Mineral content (wt%)	Skarn ore 1	Skarn ore 2	Skarn ore 3
Magnetite	85.8	71.0	76.8
Pyrite	–	1.2	–
Total	100.0	100.1	100.0

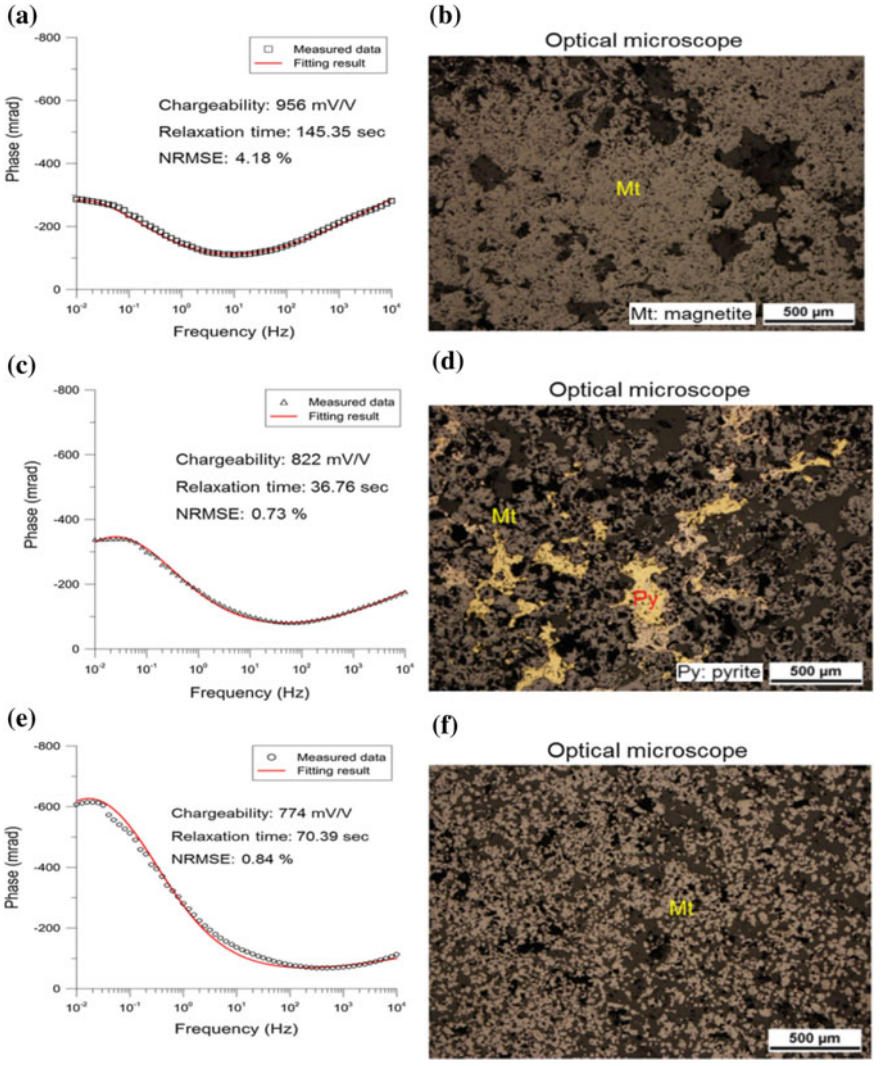

Fig. 6 Chargeability and Relaxation time for Carbonate rock 1 in (**a**), Carbonate rock 2 in (**c**) and Carbonate rock 3 in (**e**) while images obtained from Optical microscope are shown for Carbonate rock 1 in (**b**), Carbonate rock 2 in (**d**) and Carbonate rock 3 in (**f**) (reproduced with permission from Shin et al., 2016)

Table 3 Minerals identified from the XRD analyses for Carbonate rocks 1, 2 and 3

Mineral content (wt%)	Carbonate rock 1	Carbonate rock 2	Carbonate rock 3
Calcite	30.4	80.7	76.7
Forsterite	8.4	12.9	–
Biotite	14.1	5.5	–
Chlorite	8.1	–	–
Diopside	37.2	–	–
Fluorite	1.8	–	–
Lizardite	–	0.8	4.5
Brucite	–	–	18.7
Total	100.0	99.9	99.9

5 Conclusion

A review is provided of induced polarization in time domain and in frequency domain through one of the application of IP in determination of mineralogy, which is important before any other petrophysical analysis. Through the examples of different rocks, it is clear that IP can be a better geophysical method in characterization of the rocks. A little work is done in characterization of the carbonate rocks using IP. So the biggest challenge is to explore these complex reservoirs, which can be done using spectral-induced polarization.

Acknowledgements We acknowledge Dr. Andre Revil, Director of Research, ISTERRE, CNRS, UMR CNRS 5275, Université de Savoie Mont-Blanc, for the personal communications and discussion for this work.
We acknowledge the permission accorded by S. W. Shin, Samgyu Park and D. B. Shin, for using illustrations from their work originally published by Springer Environmental Earth Sciences.
We acknowledge the support and encouragement from our colleagues in the Petrophysics and Rock Physics (PP&RP) research group at IIT Roorkee.

References

Joseph S (2016) The application of spectral induced polarization to the determination of hydraulic conductivity. Ph.D. Thesis, Victoria University of Wellington. https://researcharchive.vuw.ac.nz/xmlui/bitstream/handle/10063/4988/thesis.pdf?sequence=1

Mao D, Hinton J, Revil A (2016) Induced polarization response of porous media with metallic particles—Part 4: detection of metallic and nonmetallic targets in time-domain-induced polarization tomography. Geophysics 81:D359–D375

Pelton W, Ward S, Hall P, Sill W, Nelson P (1978) Mineral discrimination and removal of inductive coupling with multifrequency IP. Geophysics 43:588–609

Revil A, Florsch N (2010) Determination of permeability from spectral induced polarization in granular media. Geophys J Int 181(3):1480–1498

Revil A, Schmutz M, Batzle ML (2011) Influence of oil wettability upon spectral induced polarization of oil-bearing sands. Geophysics A31–A36

Revil A, Florsch N, Camerlynck C (2014) Spectral induced polarization porosimetry. Geophys J Int 198(2):1016–1033

Revil A, Abdel Aal GZ, Atekwana EA, Mao D, Florsch N (2015) Induced polarization response of porous media with metallic particles—Part 2: comparison with a broad database of experimental data. Geophysics 80(5):D539–D552

Sharma R (2015) Impact of heterogeneity and saturation on elastic and viscoelastic properties in carbonates. Ph.D. Thesis, Colorado School of Mines, Golden, USA

Shin S, Park S, Shin D (2016) Spectral induced polarization characterization of rocks from the Handuk iron mine, South Korea. Environ Earth Sci 75:827

Part III
Petrophysical and Rock Physical Models

Chapter 10
Partitioning of Porosity for Carbonate Reservoirs Using Differential Effective Medium Models

Kumar Hemant Singh, Anil Kumar, Sanjay Pandit and Ashok Soni

Abstract Carbonate reservoirs are extremely heterogeneous owing to its variation in primary and secondary porosity types that affect the elastic properties of the reservoir. The Differential Effective Medium modelling approach is applied to determine the elastic properties of rocks and porosity partitioning of carbonate reservoir located in the western offshore region, India. The modelling requires the input from sonic derived logs and experimental data from the core samples. The Scanning Electron Microscope images of cores from two different depths are analyzed by watershed algorithm and binary digitization method to quantify the type of pores into cracks, interparticle and stiff defined by their aspect-ratios. The sonic velocities were inverted using Sequential Least-Squares Programming (SLSQP) optimization technique for the entire depth range of the well log from X110.20 m to X611.90 m. The partitioning of porosity derived by the DEM technique provides the relative percentage of the porosity types with depth and varies between 2 and 28% for the carbonate reservoir. In the reservoir section, most of porosity is contributed from stiff and interparticle types while the cracks contribute less than 20% of the total porosity.

Keywords Differential effective medium · SEM · Porosity partition · Carbonate reservoir

1 Introduction

Carbonates precipitate in shallow, warm oceans to form sediments of variable sizes, textures and chemical compositions. The post-depositional processes and complex diagenesis in various environments leads to alteration of the texture and mineralogy of the original rock matrix. This causes carbonate rocks to display large variations in

K. H. Singh (✉) · A. Kumar · S. Pandit
Indian Institute of Technology Bombay, Mumbai 400076, India
e-mail: kumar.h.singh@iitb.ac.in

A. Soni
GEOPIC, ONGC, KDMIPE Campus, Kaulagarh Road, Dehradun 248195, India

K. H. Singh and R. M. Joshi (eds.), *Petro-physics and Rock Physics of Carbonate Reservoirs*, https://doi.org/10.1007/978-981-13-1211-3_10

the porosity types such as intercrystal, interparticle, intraparticle, moldic, fenestral, vuggy, fracture and microcracks which causes heterogeneity in the reservoir (Lucia 1999).

The aim of reservoir characterization is to estimate the economic recoverable reserves and for that the permeability of the reservoir system must be known. In carbonate reservoirs, the permeability is strongly related to the types and connectedness of the complex pore system. Thus, predicting the pore types and their distribution in depth from core, log and seismic data becomes extremely important. This, however, is regarded as a daunting task as a rock physics model derived from the data may not be valid in another reservoir in the same well due to large inherent heterogeneities of carbonate reservoirs (Zhao et al. 2013).

The study of rock physics establishes the relationship between the elastic properties of rock and geophysical observables (Sun et al. 2006; Lian et al. 2012). Xu-Payne (2009) studied the elastic property (shear wave) and the types of porosity in a carbonate reservoir. In general, carbonate rocks exhibit good cementation and grain contact and is therefore not very useful in determining the elastic properties (Han 2004). Therefore, the scatter that is observed in porosity-velocity relationship for a given mineralogy and fluid type of carbonate rock is due primarily to types of pores present in the reservoir (Eberli et al. 2003; Misaghi et al. 2010). Thus, it is important to quantify the types of pores geometries which may vary from spherical to highly elliptical in a typical carbonate reservoir. The ellipticity of pores, i.e. the ratio of short to long axis defines the aspect ratio (α) of the pore. The spherical pores are resistant to the stress due to their round shape and make rock stronger which make P-wave travel faster compared to the rocks which have relatively higher number of elliptical pores (Ghosh et al. 2017). As elliptical pores are prone to be affected by stress, their shape and volume can be altered and therefore their large numbers in a rock make them weaker.

The present work evaluates core and log data from a carbonate reservoir located in the western offshore region of India. The evaluation is done using the following steps. First, the aspect ratios of the pores are estimated from Scanning Electron Microscope (SEM) images of the core. This step is important for porosity segregation and or partitioning. The watershed algorithm is applied to segregate complex pores and throats into simple pore types. Second, the image is digitally processed to fit ellipses to all such simple pore types–microcracks, interparticle and stiff. Third, the processed images are fed into a DEM-based rock physics model to estimate sonic velocities and is compared to that measured in the well. The derived logs provided for the well is used for the purpose. A Sequential Least-Squares Quadratic Programming (SLSQP) optimization routine is used to perform inversion and thus minimize the error between the observed and the predicted variables. The routine is fast and calculates asymptotically the global optimum providing the porosity partitioning with depth. The results are discussed with respect to the average porosities with depth in the reservoir, their geological history and implications to reservoir properties.

2 Background

Among the rock physics models, the Effective Medium Theories have been consistently used along with the Gassmann's equation to calculate the relationships between porosity and elastic wave properties. The models take into account the various shape geometry (aspect ratio) to model complexities in carbonate reservoir. Due to the heterogeneity of carbonates, the porosity partitioning continues to be an important area of research in the petroleum industry. The rock physics model developed by Xu-Payne (Xu and Payne 2009) has now become the standard to address the inherent complexity. The pioneering work by Kuster and Toksöz (1974) computes the dry-frame moduli following wave-scattering theory and demonstrated that the rock modulus ratio in dry conditions relates to the pore aspect ratio. The limitations associated due to inefficient handling of iterative algorithms of KT theory was simplified by Xu-White model (1995) by assuming a constant dry rock Poisson's ratio. However, the presumption of a constant dry rock and Poisson's ratio is not valid as they also show lot of variability in carbonate rocks (Keys and Xu 2002) which incidentally also happens to be the limitation of both Xu-White and Xu-Payne models.

2.1 Differential Effective Medium Theory

The DEM theory is applied to determine effective elastic properties of porous rocks that are either dry or saturated by fluid (Zimmerman 1985; Berryman et al. 2002). The expressions for the effective bulk moduli of a rock with N inclusions using the long-wavelength first-ordering scattering theory is given using Eq. 1 and Eq. 2 (Berryman 1992).

$$(1-\emptyset)\frac{\mathrm{d}}{\mathrm{d}\emptyset}\left[K^*(\emptyset)\right] = \left(K_2 - K^*\right)P^{*2}(\emptyset) \tag{1}$$

$$(1-\emptyset)\frac{\mathrm{d}}{\mathrm{d}\emptyset}\left[G^*(\emptyset)\right] = \left(G_2 - G^*\right)Q^{*2}(\emptyset) \tag{2}$$

where $K^*(0) = K_1$ and $G^*(0) = G_1$ are the bulk and shear moduli of the host rock material respectively; K_2 and G_2 are the bulk and shear moduli of the inclusions, respectively, with $K_2 \cong 0$ and $G_2 = 0$ for a dry rock. The terms P^{*2} and Q^{*2} are called the geometric factors that depend on the aspect ratios of the inclusions of phase 1, i.e. fluid inclusions. They describe the effect of the ith inclusion in an effective medium. For a proper derivation of P^{*2} and Q^{*2} the authors refer to the work of (Neto et al. 2014). The DEM theory assumes that a composite material can be formed by adding infinitesimal changes in an already existing composite (Norris 1985; Berryman et al. 2002; Mavko et al. 1998). This model also assumes isolated pores which have been embedded in a host rock material which is continuous at all porosities. Simulation involves addition of small amounts of pores, $d\emptyset$ to the matrix

phase until the total porosity ϕ is attained (Berryman 1992). Despite the limitations and the assumptions of the various rock physics models discussed above it is very common to use parameter calibration to study the methodologies for predicting the properties under concern. Idealized ellipsoidal pore inclusion shapes were statistically estimated from the digital image analysis of the SEM images.

2.2 *Sequential Least-Squares Quadratic Programming Optimization*

Sequential Least-Squares Quadratic Programming (SLSQP) (Kraft 1988), in each step is composed of calculating a descend direction and a step size. In addition to that its ability to process the equality and inequality constraints makes it a good choice for constrained optimization. For our purposes, we only have inequality constraints where we want to find x which is a 6 element vector.

$$\min_{x \in R^n} f(x)$$
$$\text{such that } g_j(x) = 0,\ j = 1, \ldots, m_e, \quad g_j(x) \geq 0,\ j = m_e + 1, \ldots, m,\ x_l \leq x \leq x_u \tag{3}$$

where m is the number of equality and inequality constraints and m_e is the number of equality constraints. This forms a constrained optimization problem which can further be reformulated using the Lagrangian method. The descend direction is obtained by reformulating the minimization problem in terms of a standard quadratic program. This standard quadratic program can be equivalently expressed as a linear least-squares problem that can be expressed as,

$$\min_{p \in R^n} \left|\left| D_k^{1/2} L_k^T p + D_k^{-1/2} L_k^{-1} \nabla f(x_k) \right|\right|, \tag{4}$$

$$\text{Such that } \nabla g_j(x_k) d + g_j(x_k) = 0,\ j = 1, \ldots, m_e \tag{5}$$

$$\nabla g_j(x_k) d + g_j(x_k) \geq 0,\ j = m_e + 1, \ldots, m \tag{6}$$

With $B = LDL^T$. In order to avoid calculation of the Hessian, the matrix B is approximated with first derivatives. To summarize, the SLSQP minimizes a quadratic approximation to the Lagrange function with a linear approximation of the constraints at each iteration, by solving an equivalent linear least-squares problem.

3 Methodology

A Python program was developed to implement the Xu-Payne model (Xu and Payne 2009). Prior to the implementation of the model, SEM images were processed to estimate the aspect ratios of different pore types which were used as inputs to the DEM model. The detailed approach to invert for aspect-ratios and their relative fractions has been outlined below:

Step 1: The Voigt–Reuss–Hill (Hill 1952) average technique was used to prepare the solid rock matrix. The minerals were detected using the X-Ray Diffraction experiment (XRD). The relative frequency or count from the XRD result was used for mixing different minerals. Effective elastic moduli were obtained using the DEM approach. A fourth-order Runge–Kutta integration scheme along with a step size of 0.001 was used for numerical integration. The SEM analysis shows the pore shapes broadly elliptical to spherical in shape with the lowest aspect ratio of ~0.01 and the highest to be ~0.99.
Step 2: The different pore types are added in different proportions during the inversion process. Initially, a dry rock frame is created that served as the starting rock frame to which different porosity fractions were added iteratively. These intermediate frames are called effective media. Consequently, effective bulk and shear moduli are calculated numerically by solving the DEM equations.
Step 3: Wood's suspension model (Wood 1955) has been used to calculate the effective bulk and shear moduli of various types of pore fluids. Prior to mixing of pore fluids, the process developed by (Batzle and Wang 1992) was used to calculate the elastic properties of individual pore fluids. Bulk and shear modulus of the saturated media was calculated using Gassmann's equation (Gassmann 1951; Biot 1956). Volumetric mixing law helped in calculating the density of saturated media.
Step 4: The Shear-wave (V_S) was calculated using the bulk and shear moduli of the saturated rock. Inversion proceeded by minimizing the cost function between the predicted V_S and those measured by the Sonic log. Upon minimizing the cost function, the relative fractions of different pore types were predicted for each depth along the entire column of the reservoir.

4 Problem Formulation for Optimization

4.1 Input Data

The input to the inversion algorithm is V_P from the sonic log and the SEM images. The resolution of the SEM images is 10 μm. The depth range chosen from the well log was X110.20 m to X611.90 m. The log used was sonic derived V_P log which acted as the true or measured compressional wave velocities. Initial rock matrix was derived using an estimate from the XRD data.

4.2 Procedure

1. It was found from the XRD analysis that the dominating minerals were Ankerite, Calcite, Gypsum, and Dolomite. Their relative proportions were also estimated from the XRD data. Table 1 shows the values used for Bulk modulus, Shear modulus, density and relative fractions for these minerals.

Voigt–Reuss–Hill averaging was used to prepare the dry rock host which are used as inputs to the DEM model.

2. A fourth-order integration is performed to solve the DEM equations. The aspect-ratios were estimated by fitting ellipses on individual simple pores to contribute to P^{*2} and Q^{*2} in Eqs. 1 and 2. At each depth, an inversion is performed for the aspect-ratios and their relative volume fractions.
3. In order to partition the porosity into different types, the procedure used is listed below:

   a. Initially, at each depth point, it was considered that only interparticle primary porosity existed. With this assumption, the DEM equations were solved to get the V_P reference.
   b. This V_P reference, if found to be less than equal to V_P measured than crack type porosity was included in addition to the interparticle porosity.
   c. Conversely, if V_P reference is found to be greater than V_P measured than stiff type porosity was included in addition to the interparticle porosity.
   d. From these assumptions, at each depth point, only two types of porosities co-existed at a time along the depth.

4. A simple local optimizer based on SLSQP technique is used for the inversion purpose. This requires a prior initialization. Because the concept of DEM is a thought experiment (Mavko et al. 1998), the choice of a local optimizer is justified. This means that as the integration of new minute porosities is included the path taken to reach the final porosity is not unique. Moreover, with a proper choice of step-size SLSQP can be made to find the global optima.

The objective function to be minimized is:

$$\text{cost} = \frac{1}{n}\sum_{i}^{n}\sqrt{\left(V^{i}_{\text{Model}} - V^{i}_{\text{True}}\right)^{2}}, \tag{7}$$

Table 1 Elastic parameter used for the minerals detected from XRD analysis

Mineral	Bulk modulus (K)	Shear modulus (G)	Density (g/cm^3)	Relative fraction
Ankerite	73	32	3.05	0.56
Calcite	77	32	2.71	0.38
Gypsum	04	1.5	2.36	0.04
Dolomite	95	45	2.71	0.00

where n is the total number of points, V^i_{Model} is the modelled or predicted compressional velocity at the ith depth point and V^i_{True} is the compressional velocity derived from the Sonic log at the corresponding ith depth point.

Initialization of the two variables forms the first step (Fig. 1). The aspect ratios, α's are initialized by keeping their values constant as described in Table 2. The volume fractions, v's are also initialized with the upper and lower bounds of 1 and 0 respectively. The DEM requires these 4 inputs (corresponding to two types of pores at each depth point) in order to embed infinitesimal fluids into the host 'dry' rock. In particular, the α's go as inputs to the geometric factors P^{*2} and Q^{*2}.

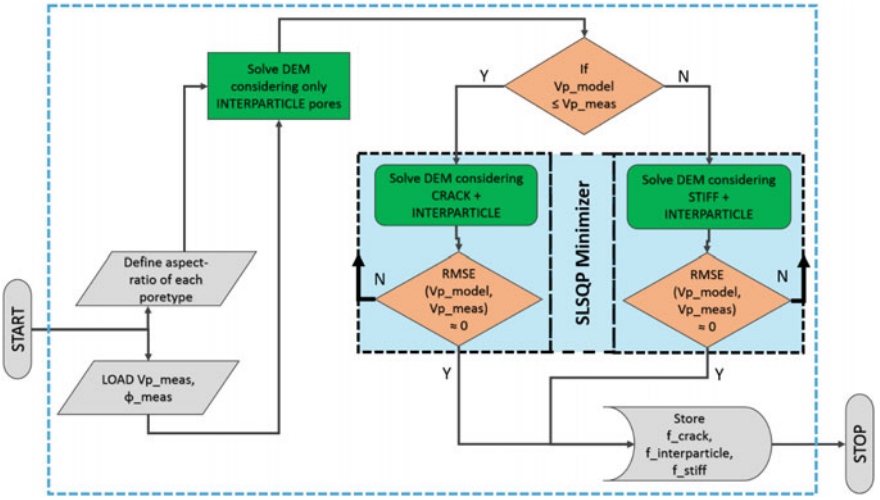

Fig. 1 Flowchart showing the inversion being performed at each of the 1640 depth points

Table 2 Aspect ratios used to define various pore types seen in core sample

	Avg. values of aspect-ratios for different pore types		
Pore-types	Crack	Interparticle	Stiff
Range estimated from histogram	(0 to 0.03]	(0.03 to 0.5]	(0.5 to 1]
Used values	0.02	0.3	0.8

5 Results

5.1 *Analysis of SEM Images and Segmentation Using Watershed Transform*

The SEM images were analyzed to accommodate major and minor types of pores. The raw images and their respective segmentation are shown in Fig. 2. The resolution of all SEM images is 10 μm. The procedure adopted makes use of the Watershed algorithm to segment composite pores into pores and throats (Sarkar et al. 2018).

The procedure adopted to evaluate the aspect-ratios is illustrated in Fig. 3. The raw SEM images are first converted to binary images using the thresholding technique. The grayscale range is from 0 to 255. The threshold of 40 is used to binarize the images such that all the values below 40 are assigned to pores and the values higher than that are assigned to matrix. All the images in Fig. 2a, c used the same parameter value for the threshold. This binarization step segregates the foreground (pore space) from the background (matrix space). After binarization, the Watershed algorithm is applied to separate composite pores into simple pores. The Watershed algorithm finds the local minimum of each composite pore by first calculating the gradient of the binary image resulting into the formation of several centres within the composite

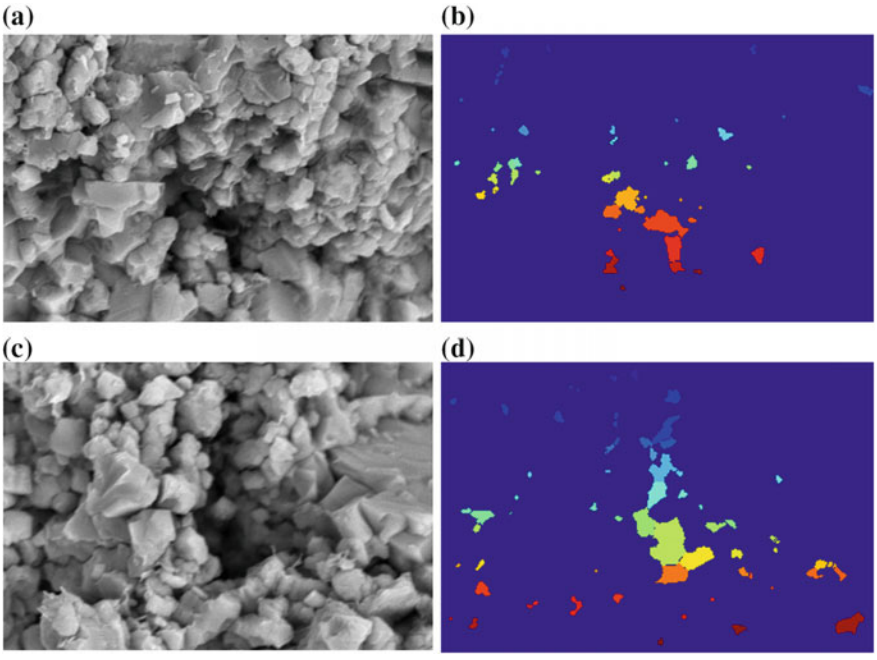

Fig. 2 SEM images at 10 μm resolution for carbonate samples from western offshore, India (**a** and **c**); images (**b** and **d**) show the respective segmentation of images **a** and **c** into pores and throats

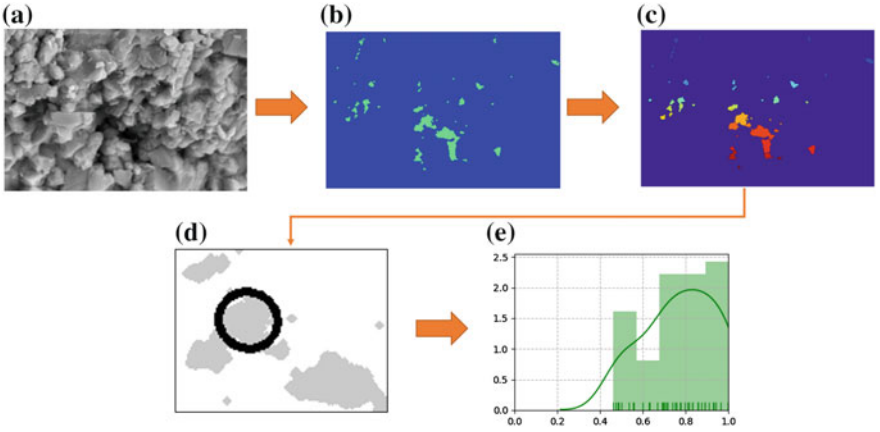

Fig. 3 Generalized workflow for Digital Image Analysis; From LEFT to RIGHT: Raw greyscale image (**a**), Binarization and Morphological Closing (**b**), Watershed Transform and Segmentation (**c**), Fitting Ellipses to segmented pores (**d**) and Histograms showing Aspect-ratio estimation (**e**)

pores. These centres act as the starting point for flooding. The pores are flooded until they meet the waters of the adjacent pores if any or encounter the background. This technique effectively separates composite pores into individual simple pores. These simple pores characterize different types of pore systems of the sample under test.

Upon analyzing different SEM images, it is found that the pores are broadly spherical to elliptical in shape. Upon plotting the histograms of the types of pores seen in the SEM images, three ranges were decided for three types of pore systems (Table 2). Figure 4 shows the histogram representing various proportion of different aspect-ratios found in the SEM images. The different ellipses derived from fitting various α's into different parts of composite pores are shown in Fig. 5. The respective aspect ratios have also been mentioned depending on the ellipse that fits the respective pores.

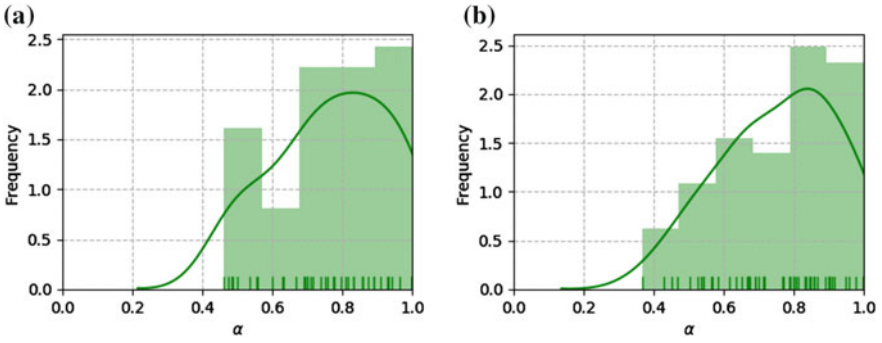

Fig. 4 Histograms showing aspect-ratios calculated from SEM images in Fig. 2a, c, respectively shown in (**a**) and (**b**)

Fig. 5 Ellipses fitted on Watershed segmented pores for calculating aspect ratios; α's denote the respective aspect ratios of the pores segmented by the Watershed transform

5.2 *Comparison of* V_S *Predicted and* V_S *Observed*

Availability of shear-wave velocity from logs is not often. But for the current study, S-velocity was available from the logs helping to verify the developed DEM model. Moreover, the convergence was numerically verified from error values achieved during the minimization process. Unlike sandstones the complex nature of pore types can complicate the V_P/V_S ratio, therefore the same rock physics model which was obtained by inverting for the pore types using V_P is used to obtain bulk and shear moduli at the saturated condition at each depth which in turn are used to predict the shear-wave velocity. Figure 7e shows the V_S prediction based on the pore-type inversion result. Both the, predicted and observed S-wave velocity match well throughout the depth range. This indicates that the model has captured the pore-type distributions along the depth.

5.3 *Inversion of Aspect-Ratio and Their Relative Fractions*

Sequential Least-Squares Quadratic Programming method was used to minimize for the respective volume fractions of various pore-types. The x, which is a four-element vector representing the two co-existent pore-types, is optimized. The Lagrangian method is used to incorporate the equality constraints for both the two variables such that the volume fractions should sum to 1. Each minimization step required almost 19 iterations. Each iteration included calculation of first-order gradients and number of function evaluations ranging from 100 to 200. The errors achieved during all the 3293 depth points were excellent with a minimum and maximum error not exceeding values 2.55×10^{-10} and 1.50×10^{-2}, respectively. Figure 6 shows typical stages achieved during minimization process of function and gradient evaluations.

Inversion was performed along the entire depth range of the well log from X110.20 m to X611.90 m (Fig. 7). A trend can be observed in the Fig. 7a, that whenever the difference between the V_P_ref and V_P_measured is high the addition of crack/stiff pores is high and vice versa.

```
Done :  1 ; Remaining :  3292
Optimization terminated successfully.    (Exit mode 0)
            Current function value: 1.5549212584176075e-08
            Iterations: 9
            Function evaluations: 76
            Gradient evaluations: 9
Done :  2 ; Remaining :  3291
Iteration limit exceeded    (Exit mode 9)
            Current function value: 1.1905891383889866e-08
            Iterations: 21
            Function evaluations: 211
            Gradient evaluations: 21
Done :  3 ; Remaining :  3290
Iteration limit exceeded    (Exit mode 9)
            Current function value: 4.3995918019845703e-11
            Iterations: 21
            Function evaluations: 132
            Gradient evaluations: 21
Done :  4 ; Remaining :  3289
Iteration limit exceeded    (Exit mode 9)
            Current function value: 6.06292926974561e-08
            Iterations: 21
            Function evaluations: 181
            Gradient evaluations: 21
```

Fig. 6 Typical minimization steps during optimization; Exit mode 9 shows that the stopping criterion for the optimizer was met before 21 gradient evaluations. This was purposefully done because the error reduction was acceptable and of the order of 10^{-5} beyond this criteria

5.4 Qualitative Comparison of Inverted Pore-Types with the Pore-Types in SEM Images

As can be seen in Fig. 8, the majority type of pore-type present is interparticle shadowed in green. Similarly, in Fig. 9, it is observed that apart from the interparticle porosity the other dominant porosity present is stiff again demarcated with green patches. The inversion results at the two depths viz. X273.40 m and X304.80 m shown in Figs. 8 and 9 match with the type of pores present in the SEM images of the two depths. This can be visually verified from Figs. 8 and 9.

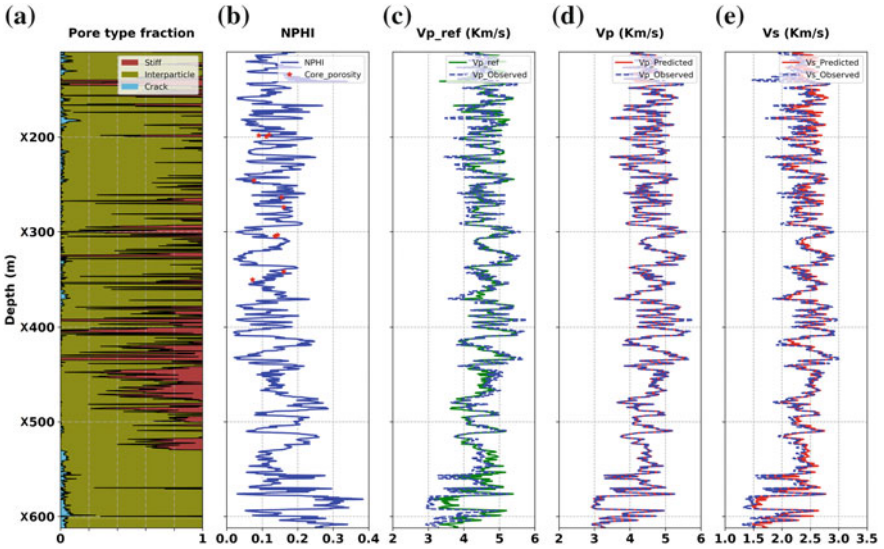

Fig. 7 **a** Relative volume fractions, **b** Neutron porosity overlaid with core porosities (red *), **c** V_P_ref and V_P_measured (**d**). V_P_Predicted from inversion and V_P_measured (**e**). The predicted (modelled) shear-wave velocities derived from inversion compared against the observed (measured) velocities taken from the sonic logs

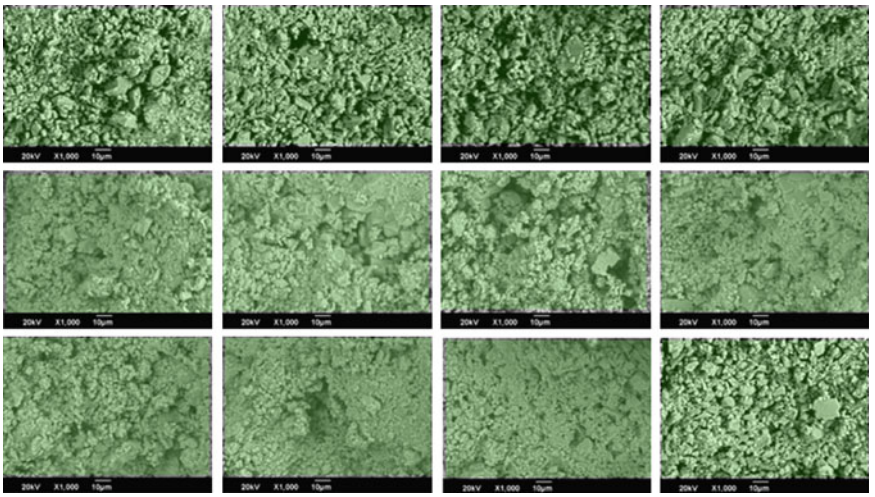

Fig. 8 Qualitative analysis of pore-types present in sample #1 (X273.40 m). Majority pore-type is interparticle porosity

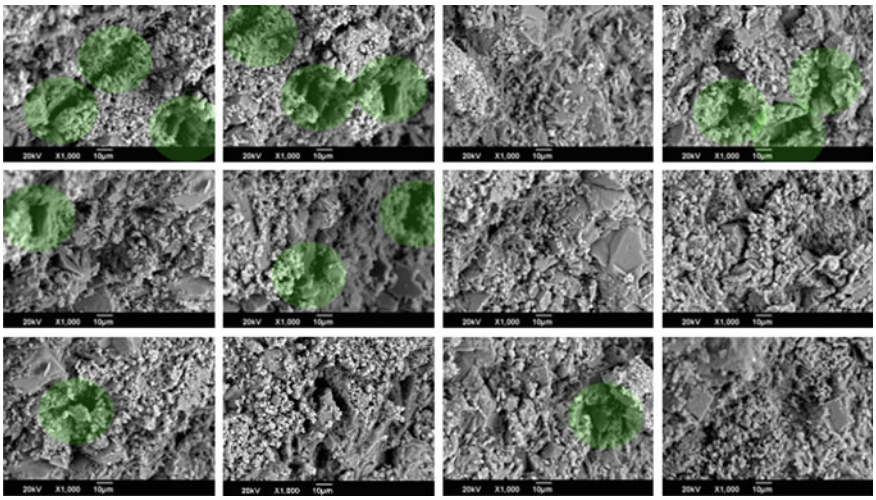

Fig. 9 Qualitative analysis of pore-types present in sample #2 (X304.80 m). Majority pore-type is stiff porosity

6 Geological Implications of Pore-Type Distribution

The spatial distribution of porosity types is controlled by the geological processes and reveals the geological history of the deposition and post-depositional changes that occurred in the reservoir. The reservoir belongs to the Ratnagiri formation which shows Limestone of Lower to Middle Miocene as the primary formation. The limestone is accompanied with occasional shale layers in the upper region of the reservoir. The section produces water with traces of oil and gas and the porosity range is 2-28%. The dominant contribution to the porosity comes from the stiff type and the cracks present in the reservoir sections are small. Stiff porosity due to dissolution shows dominance at parts along the depth. The limestone shows strong presence of interparticle porosity throughout the depth of the reservoir but the regions located at X300 m, X325 m, X354 m, X393 m, X404 m and X434 m till X500 m show increased values of stiff type pores. At these depths it seems after compaction and cementation, the pore spaces of the reservoir are reorganized by dissolution hence both interparticle and stiff porosity dominates while the cracks are sparingly prominent along the entire reservoir depth. This is also verified from the visual inspection of the inversion.

7 Conclusions

The DEM rock physical modelling was performed on core and log data obtained from carbonate reservoirs located in the western offshore region, India. SEM images

from two core samples were used to estimate aspect ratios and they relate to pore structures ranging from elliptical to spherical sizes. These were used as inputs and the DEM equations were solved at each depth locations and inverted for relative fractions of different pore types. Iterative SLSQP optimization method was used to minimize between predicted and measured V_P. An initial estimate of the mineral composition was done using XRD data and volumes calculated from mineral volume log. The reservoir belongs to the Ratnagiri formation dominantly Limestone bearing. The porosity estimated from the analysis shows cracks, stiff and interparticle types and the range vary from 2 to 28%.

The present work is limited in the sense that ellipses that fit individual simple pores in SEM images are although automated but often over- and under-estimates the aspect-ratio. Thus the pore-type distribution in the core sample representation is not entirely accurate and taking into account the irregular boundaries of the pore geometry is beyond the scope of the present work. In the future study, it is envisaged that smart Deep Neural Network based algorithms may be able to represent the aspect ratios more accurately and can be developed with more training data sets from the core samples.

References

Batzle M, Wang Z (1992) Seismic properties of pore fluids. Geophysics 57(11):1396–1408. https://doi.org/10.1190/1.1443207

Berryman JG (1992) Single-scattering approximations for coefficients in Biot's equations of poroelasticity. J Acoust Soc Am 91:551–571. https://doi.org/10.1121/1.402518

Berryman JG, Pride SR, Wang HF (2002) A differential scheme for elastic properties of rocks with dry or saturated cracks. Geophys J Int 151:597–611

Biot MA (1956) Theory of propagation of elastic waves in a fluid saturated porous solid. I. Low frequency range. J Acoust Soc Am 28:168–178. https://doi.org/10.1121/1.1908239

Eberli GP, Baechle GT, Anselmetti FS, Incze ML (2003) Factors controlling elastic properties in carbonate sediments and rocks. Lead Edge 22:654–660. https://doi.org/10.1190/1.1599691

Gassmann F (1951) Über die Elastizität poröser Medien: Veirteljahrsschrift der Naturforschenden Gesellschaft in Zürich. Zürich 96:1–23

Ghosh A, Nagar A, Vasudevan K, Lal H (2017) A robust algorithm to predict porosity partition for carbonate reservoirs. In: SEG Technical program expanded abstracts, Houston, https://doi.org/10.1190/segam2017-17784137.1

Han DH (2004) Velocity in carbonate rocks: Annual report, rock physics and fluid consortium

Hill R (1952) The elastic behaviour of a crystalline aggregate. Proc Phys Soc Sect A 65:349. https://doi.org/10.1088/0370-1298/65/5/307

Keys RG, Xu S (2002) An approximation for the Xu-White velocity model. Geophysics 67:1406–1414. https://doi.org/10.1190/1.1512786

Kraft D (1988) A software package for sequential quadratic programming. Forschungsbericht-Deutsche Forschungs- und Versuchsanstalt fur Luft- und Raumfahrt, DFVLR, Köln

Kuster GT, Toksöz MN (1974) Velocity and attenuation of seismic waves in two-phase media: part 1—theoretical formulations. Geophysics 39:587–606. https://doi.org/10.1190/1.1440450

Lian J, Xiao-Tao W, Dong-Hong Z, Zhen-Hua H, Xi-Lei H (2012) The constructing of pore structure factor in carbonate rocks and the inversion of reservoir parameters. Appl Geophys 9:223–232. https://doi.org/10.1007/s11770-012-0333-5

Lucia FJ (1999) Carbonate reservoir characterization: an integrated approach. Springer-Verlag, Berlin Heidelberg. http://dx.doi.org/10.1007/978-3-66203985-4

Mavko G, Mukerji T, Dvorkin J (1998) The rock physics handbook: tools for seismic analysis of porous media. Cambridge University Press, New York

Misaghi A, Negahban S, Landrø M, Javaherian A (2010) A comparison of rock physics models for fluid substitution in carbonate rocks. Expl Geophys 41:146–154

Neto IAL, Misságia RM, Ceia MA, Archilha NL, Oliveira LC (2014) Carbonate pore system evaluation using the velocity–porosity–pressure relationship, digital image analysis, and differential effective medium theory. J Appl Geophys 110:23–33

Norris AN (1985) A differential scheme for the effective moduli of composites. Mech Mater 4(1):1–16. https://doi.org/10.1016/0167-6636(85)90002-X

Sarkar P, Kumar A, Singh KH, Ghosh R, Singh TN (2018) Pore system, microstructure and porosity characterization of Gondwana shale of Eastern India using laboratory experiment and watershed image segmentation algorithm. Marine and Petrol Geol 94:246–260. https://doi.org/10.1016/j.marpetgeo.2018.04.006

Sun YF, Berteussen K, Vega S, Eberli GP, Baechle GT, Weger RJ (2006) Effects of pore structure on 4D seismic signals in carbonate reservoirs. In: 76th Annual international meeting, SEG, expanded abstracts, pp 3260–3264

Wood AW (1955) A textbook of sound. McMillan Co., New York, USA

Xu S, White RE (1995) A new velocity model for clay-sand mixtures1. Geophys Prospect 43:91–118. https://doi.org/10.1111/j.1365-2478.1995.tb00126.x

Xu S, Payne MA (2009) Modeling elastic properties in carbonate rocks. Lead Edge 28:66–74. https://doi.org/10.1190/1.3064148

Zhao L, Nasser M, Han D-H (2013) Quantitative geophysical pore-type characterisation and its geological implication in carbonate reservoirs. Geophys Prospect 61(4):827–841. https://doi.org/10.1111/1365-2478.12043

Zimmerman RW (1985) The effect of microcracks on the elastic moduli of brittle materials. J Mater Sci Lett 4:1457–1460. https://doi.org/10.1007/BF00721363

Chapter 11
Effective Medium Modeling of CO_2-Sequestered Carbonate Reservoir

Ranjana Ghosh and Mrinal K. Sen

Abstract An appropriate rock physics model to monitor seismic properties of carbonate reservoir sequestered with CO_2 imposes a grand challenge as carbonate rocks have complex microstructure and chemically active fluid-rock system. Existing rock physics theories based on Gassmann's theory are not suitable for modeling a dynamic system (system in which rock matrix changes with time due to rock-fluid interaction). On the other side, self-consistent approximation (SCA), differential effective medium (DEM), etc. theories based on Eshelby's inclusion model do not incorporate pressure, which is very important for gas saturated reservoirs. The DEM theory modified for pressure (PDEM), which can explain rocks' heterogeneous microstructure and squirt flow, has been applied successfully to match the laboratory-measured (ultrasonic) elastic properties of CO_2-rich water-saturated carbonate rocks. The PDEM theory correlates well with the laboratory experiment that shows reduction in P- and S-wave velocities of saturated rocks as a result of permeability and porosity enhancement due to dissolution of carbonates by acidic saturating fluid. This theory can be up-scaled from laboratory to field measurements demonstrating the predicted elastic properties in the seismic frequency range decrease significantly. The joint effect of free CO_2 gas saturation and chemical dissolution on velocities of rock show that both attenuation and dispersion decrease from complete water to gas saturation. This theory can be applied to identify variations in elastic properties of CO_2-saturated carbonate reservoir and monitor the movement of CO_2 gas. These important factors guarantee that CO_2 storage will not destroy subsurface geology and sequestration is safe for the environment.

Keywords Effective medium · CO_2-sequestration · Rock physics · Elastic properties

R. Ghosh (✉)
CSIR-National Geophysical Research Institute, Hyderabad, India
e-mail: ranjana159@gmail.com

M. K. Sen
University of Texas at Austin, Austin, USA

K. H. Singh and R. M. Joshi (eds.), *Petro-physics and Rock Physics of Carbonate Reservoirs*, https://doi.org/10.1007/978-981-13-1211-3_11

1 Introduction

Carbon-dioxide (CO_2) is the major supplier to global warming among all the greenhouse gases (Cox et al. 2000). CO_2 injection into subsurface is a promising technique to reduce the net issue of greenhouse gases into the atmosphere (Chen and Zhang 2010) and thus help to decrease global warming. Also, extraction of oil and gas could be improved by injecting CO_2 into an oil and gas reservoir—a method termed as enhanced oil recovery (EOR). Therefore, CO_2 sequestration aids both by reducing environmental pollution and increasing oil recovery. Generally, bulk emitters of CO_2 like power plants are located in the zone of hydrocarbon reservoirs, un-mineable coal seams, and deep saline aquifer, which have option for CO_2 sequestration. However, an exhaustive study on reservoir characteristics is important for effective subsurface CO_2 storage.

Carbonates constitute almost 60% of the total hydrocarbon reservoirs in the world. Even though they have been explored extensively, their reservoir characterizations pose great challenge due to complex heterogeneous microstructure and fluid-rock interaction (Hoefiner and Fogler 1988; Vialle and Vanorio 2011). Injection of CO_2 in carbonate rocks formulates a physico-chemical reactive fluid-rock system, which modifies the pore-structure of the rock. This phenomenon alters the microstructure of the rock and its elastic properties with time. Knowing the seismic responses of rocks undergoing such mechanisms is crucial both for prediction and monitoring purposes (Lumley 2010). But limited data are available to interpret seismic response of gas injected rock quantitatively. First extensive study in laboratory on the effect of chemical dissolution to elastic properties of carbonate rocks due to CO_2 injection is reported by Vialle and Vanorio (2011). Well known existing rock physics theories failed to predict such changes in elastic properties with time. Hence, the pressure-dependent differential effective medium (PDEM) theory is developed to overcome the limitations of the existing models.

Two types of fluid interactions during wave propagation are created by wave-induced pressure gradient caused by different sizes, shapes, and orientations of pores of a rock, namely, (1) Global Flow, created by large pressure gradients at seismic wavelength scale along the wave propagation direction and (2) Squirt Flow, created by small pressure gradients at the pore scale and propagate not necessary along the wave propagation directions. Effective medium theories available in literatures are categorized into two types: inclusion-based theories and phenomenological theories (Jakobsen and Chapman 2009). First type of theories (Mavko and Nur 1975; O'Connell and Budiansky 1977; Hudson et al. 1996; Jakobsen et al. 2003a, b; Jakobsen 2004; Chapman et al. 2002; Chapman 2003; Jakobsen and Chapman 2009) consider Eshelby's (1957) inclusion model assuming rocks are having ideal microstructure. Second type of theories (Biot 1956, 1962; Dvorkin and Nur 1993; Mavko and Jizba 1991; Mukerji and Mavko 1994; Dvorkin et al. 1995), use empirical model parameters, which are not dependent on the true microstructure of the rock. Global flow is better explained by the phenomenological theories, pioneered by Biot in 1956, whereas, the squirt flow is explained better by inclusion-based theories.

The recent inclusion-based squirt flow model includes energy interaction method (Chapman et al. 2002; Chapman 2003), which assumes isotropic background medium composed of a single mineral and spherical pores filled with water. But, squirt flow in shale can't be explained by this theory as shale itself is intrinsically anisotropic and comprises of several minerals. Self-consistent approximation (SCA) theory combined with the differential effective medium (DEM) theory (Hornby et al. 1994) has been applied successfully to model clay-rich reservoirs (Jakobsen et al. 2000; Chand et al. 2006; Ghosh et al. 2010a, b). But those theories do not contain the pressure term and hence cannot explain squirt flow that is obvious in rocks having heterogeneous microstructure. Therefore, an effective medium-modeling algorithm has been developed by modifying the differential effective medium (DEM) modeling to incorporate the effect of pressure to explain the squirt flow mechanism. The pressure-dependent DEM (PDEM) theory is used here to predict the elastic properties of CO_2-saturated carbonate rocks, which demonstrates the squirt flow effect at pore scale. The effect of squirt flow due to the presence of meso-scale fractures in the same carbonate rock are also presented here. The proposed theory is suitable for the crucial statistics for monitoring CO_2 migration and oil production by tracking variations in elastic responses caused by mechanical and chemical effects of a CO_2-saturated carbonate field and the amount of CO_2 migration.

2 Theory

The development of the PDEM theory (Ghosh and Sen 2012; Ghosh et al. 2015) is based on Eshelby's inclusion model (Eshelby 1957) that calculated the response of a single ellipsoidal inclusion establishing the fact that the strain due to a homogeneous applied stress at infinity inside an inclusion within an infinite, homogeneous matrix is also homogeneous.

The DEM hypothesizes a matrix known as host material and other components as inclusions. For a two-phase composite medium, infinitesimal increase in volume fraction of the inclusion (phase 2) corresponds to infinitesimal replacement of the host material (phase 1). The process is repeated till the desired volume of each component has been reached. At every step of addition, the effective medium is updated as the host medium (Nishizawa 1982; Berryman 1992; Hornby et al. 1994). Similar process can be followed to increase the number of components.

The present static DEM (without pressure term) theory has been used fruitfully to describe clastic rocks (Hornby et al. 1994; Jakobsen et al. 2000; Ghosh and Sain 2008; Ghosh et al. 2010a, b), which is described below

$$\frac{\mathrm{d}C}{\mathrm{d}v_i} = \frac{1}{1 - v_i}(C_i - C)K_i C \tag{1}$$

where dc is the change in effective stiffness C due to an increment dv_i in volume concentration v_i of the ith component, C_i is stiffness of the ith inclusion. K_i is a

fourth rank tensor that relates the applied stress σ to the average inclusion strain e_i as (Hudson et al. 1996),

$$e_i = K_i \sigma, \tag{2}$$

For fluid-filled pores or cracks, the inclusion stress (σ_i) can be replaced with the pore fluid pressure tensor $p_i\delta$, δ being the Dirac delta function. The relation between inclusion strain (e_i) and inclusion stress (σ_i) is given below (Zatsepin and Crampin 1997; Chapman et al. 2002),

$$e_i = (I - PC)^{-1} C^{-1} (\sigma - C P p_i \delta) \tag{3}$$

where I and P are rank four identity matrix of and a fourth rank tensor (Mura 1982, page 119).

The PDEM theory is formed by replacing A2 and A3 in A1 that takes the formula as (Ghosh and Sen 2012)

$$\frac{\mathrm{d}C}{\mathrm{d}v_i} = \frac{1}{1 - v_i} (C_i - C)(I - PC)^{-1} C^{-1} (\sigma - C P p_i) \sigma^{-1} C \tag{4}$$

Here, dual-porosity model is assumed, specifically spherical and ellipsoidal pores. Pore pressure is different in different type of pores, which causes squirt flow in the medium. The pore pressure for a spherical pore (p_p) is denoted by (Chapman 2003),

$$p_\mathrm{p} = D_\mathrm{p} \sigma_{ii} \tag{5}$$

where

$$D_\mathrm{p} = \gamma_1 / \gamma \tag{6}$$

$$\begin{aligned} \gamma &= (3/8) * (\pi / ((1 - \upsilon) * (1 + k_\mathrm{c}))) * (1 + k_\mathrm{p}) \\ \gamma_1 &= \gamma * ((1 - \upsilon)/(1 + \upsilon)) * (1/(1 + k_\mathrm{p})) \\ k_\mathrm{p} &= ((4/3) * \mu)/k_\mathrm{f} \\ k_\mathrm{c} &= (\pi * \mu * r)/(2 * (1 - \upsilon) * k_\mathrm{f}) \end{aligned} \tag{7}$$

Pore pressure for an ellipsoidal pore (p_c) is denoted by (Chapman 2003)

$$p_\mathrm{c} = G_1 \sigma_i + G_2 \sigma_{ii} \tag{8}$$

where

$$G_1 = \frac{i\omega\tau_\mathrm{m}}{(1 + k_\mathrm{c})(1 + i\omega\tau_\mathrm{m})}, \tag{9}$$

$$G_2 = \frac{1 + i\omega\gamma\tau_{\mathrm{m}}}{1 + i\omega\tau_{\mathrm{m}}} D_{\mathrm{c}} - \frac{i\omega\tau_{\mathrm{m}}\gamma'}{1 + i\omega\tau_{\mathrm{m}}} \tag{10}$$

$$D_{\mathrm{c}} = ((1 - \iota) * \gamma_1) + (\iota * ((1 + i\omega\tau_{\mathrm{m}}\gamma_1)/(1 + i\omega\tau_{\mathrm{m}}))) \tag{11}$$

$$\iota = (\phi_{\mathrm{c}}/r)/((\phi_{\mathrm{c}}/r) + \phi_{\mathrm{p}}) \tag{12}$$

where σ_i, σ_{ii} are normal stress to a crack plane and total normal stresses, respectively, τ_{m} is the squirt flow time for heterogeneous medium at pore-scale, ω is the circular frequency, ϕ_{c} is crack porosity p_{v}, c_{v} are pore and crack volumes respectively, k_{f} is bulk modulus of fluid, κ is permeability of fluid, η is viscosity of fluid, ζ is size of grain, υ and μ are Poisson's ratio and shear modulus of the matrix respectively, r is the aspect ratio of non-spherical (ellipsoidal) pore.

A homogeneous medium, comprised of a single set of voids, do not induce local pressure gradient and hence squirt flow because pore-pressure p_i is equal for all voids. Whereas, heterogeneous medium, comprised of thin cracks, spherical pores, large fractures, etc. induce local pressure gradient and squirt flow because pore-pressure p_i is not equal for various types of voids. The rock then exhibits a visco-elastic property, i.e., at higher frequencies both rigidity and bulk moduli will be higher if pressure (gradient) is not released than at lower frequency if pressure (gradient) is released.

3 Results and Discussion

The applications of the PDEM theory are elaborated here for I. the impact of dissolution due to chemical reaction on elastic properties at laboratory (ultrasonic) scale, II. seismic (field) scale, III. impact of pressure on elastic properties and IV impact of both dissolution and presence of free gas (CO_2) on seismic velocities.

Case I: Impact of dissolution due to chemical reaction on elastic properties: ultrasonic (laboratory) scale

Vialle and Vanorio (2011) performed laboratory experimentations to monitor how CO_2-rich water, if injected on carbonate rocks affects its microstructure and mineralogical compositions. They have described fully how elastic properties of pure calcite ($CaCO_3$) alters due to chemical dissolution causing primarily enhancement of permeability and porosity and compression of the sample undergoing confining pressure.

Sample classification consists of porosity (Helium) and permeability (Klinkenberg-corrected nitrogen) measured pre and post CO_2 injection, within error ± 1 and $\pm 2\%$, respectively. The experimental setup contains a core holder, a hydrostatic pressure container and a fluid injection device. The sample approximately 1-in. of length is covered with rubber tube and mounted into the pressure container at fixed 1.1 MPa

overburden (confining) pressure. The variation in length as a function of pressure is measured, which allows to measure the change in porosity due to change in volume of the sample under mechanical compaction.

Velocities were measured in laboratory on dry sample and after that monitored with CO_2 injection. The error of measured ultrasonic velocities was determined as $\pm 1\%$. The experiment was conducted under the constant confining pressure 1.1 MPa and the pore-fluid pressure 1 MPa. In both dry and completely saturated conditions, V_P and V_S both decrease continuously with injected CO_2 volumes (Fig. 1). After injection of approximately 700 pore-volume (~2600 mL), it is observed that dry V_P and V_S reduced by ~24.7% (871 m/s) and ~21.2% (443 m/s) respectively; porosity increased from 26.5 to 31.5% and permeability increased from 75.3 to 448.9 mD due to a joint effect of dissolution and compression (Vialle and Vanorio 2011).

Here, the outcomes from the laboratory test has been modeled by assessing P- and S-wave velocities of CO_2-sequestered carbonate rock applying the PDEM theory

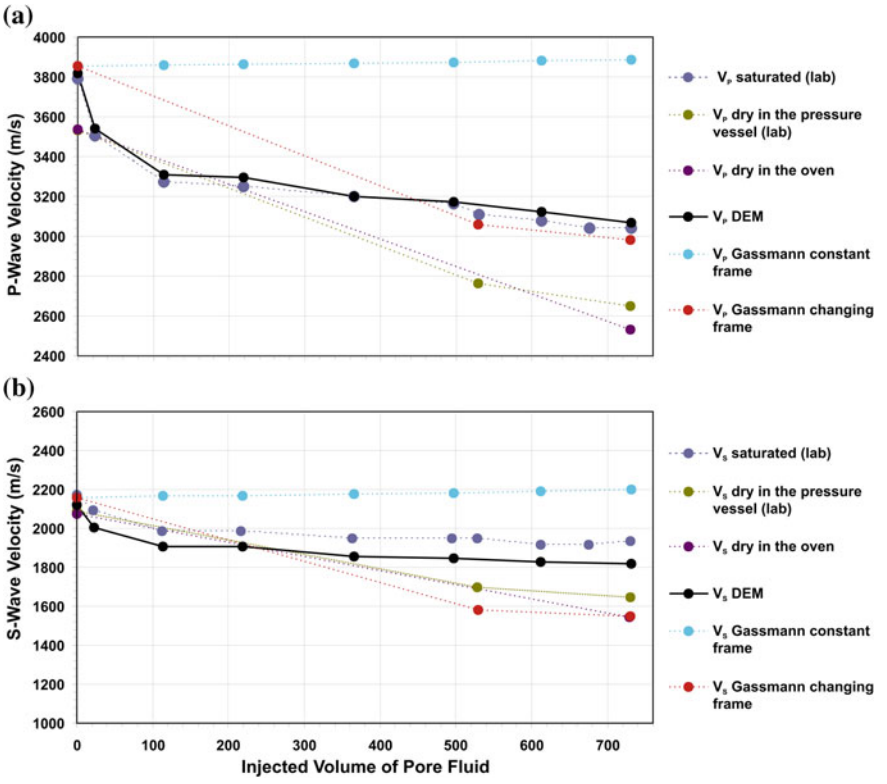

Fig. 1 Measured P-wave (V_P) and S-wave (V_S) velocities of CO_2-saturated pure Calcite (carbonate rock) at ultrasonic frequency (1 MHz) considering matrix of the rock alters because of dissolution, precipitation, and compaction. Calculated V_P and V_S for the same rock with similar setup applying the PDEM theory and Gassman's theory are also shown

(Eq. 4) incorporating similar alterations in permeability and porosity, and precipitation under the identical pore and confining pressures. Here, large pores are assumed as spherical with the aspect ratio 1. The spherical pores are presumed to be linked by the ellipsoidal pores oriented randomly. In this case, unknown parameters are the fraction of ellipsoidal and spherical pores, aspect ratio of ellipsoidal pores, which are estimated by matching the calculated velocities using the PDEM at frequency 1 MHz with the measured velocities of Calcite rock saturated with water. The time τ_m for squirt flow can be determined (Chapman 2003) from the grain size (ζ), crack volume (c_v), number of linked cavities with pores and cracks (c_1), permeability (κ), and viscosity (η). But the parameters c_v and c_1 cannot be determined easily. Thus, τ_m has been taken as a fitting parameter. The unknown parameters spherical pores and non-spherical (ellipsoidal) pores, aspect ratio of non-spherical pores and characteristic time τ_0 are determined as respectively 24.5, 2, 0.03, and 2×10^{-7} s for the Calcite rock saturated with water. τ_m has been expressed as a function of permeability (κ) as shown below

$$\tau_m = \tau_0/\kappa(v) \tag{13a}$$

$$\kappa(v) = \kappa_0 * (d\kappa/dv) * v \tag{13b}$$

$$d\kappa/dv = (\kappa_f - \kappa_0)/(v_f - v_0) \tag{13c}$$

where $\tau_0 = 2 \times 10^{-7}$ s, $\kappa_0 = 75.3$ mD, $\kappa_f = 448.9$ mD, v =injected pore volume,$v_0 = 0$, $v_f = 700$.

Shear modulus of any linearly viscous fluid is expressed as $i\omega\eta$ instead of zero (Walsh 1969), where, i symbolizes the imaginary component, ω is the circular frequency and viscosity η is 1 cP for water (Chapman et al. 2002). The elastic properties of the components of the carbonate rock are shown in Table 1.

Enhancement of permeability and porosity and precipitation are accustomed following a way that the calculated velocities agree with the velocities measured in laboratory at each step of CO_2 injection. In this modeling, porosity and permeability enhancement are simulated by increase of the spherical and ellipsoidal pores by 1–5% and 7–22%, respectively, whereas the precipitation is simulated by substitut-

Table 1 Elastic moduli and densities of different constituents of carbonate rocks used for modeling (Lumley 2010; Vanorio et al. 2008, 2010). Fluids properties are taken for 1.1 MPa pressure

Components	Bulk-modulus (GPa)	Shear modulus (GPa)	Density (kg/m^3)
Calcite	71	32	2170
Pure water	2.2	–	980
CO_2-rich water	2.28	–	1000
Pure CO_2	0.05	–	100

ing CO_2-rich fluid from the non-spherical pores with host mineral Calcite. Figure 1 compares the results from the modeling with the laboratory measurements.

Fluid substitution model of Gassmann's (Gassman 1951) has also been used to calculate saturated P- and S-wave velocities for comparison. Velocities have been determined (Fig. 1) from Gassmann's theory for both measured pre-injection dry elastic moduli (constant frame) and measured post-injection dry elastic moduli (changing frame). Visibly, saturated velocities determined taking constant frame are considerably higher than the measured laboratory velocities. Whereas, taking changing frame saturated, P-velocity decrease with CO_2 injection but S-wave velocity is much less than the laboratory-measured values.

Case II: Impact of dissolution due to chemical reaction on velocities: seismic (field) scale

Figure 2 displays the calculated velocities using the PDEM modeling at 60 Hz, which falls in the seismic frequency range, keeping other parameters unchanged. The separation between calculated velocities at 60 Hz and 1 MHz reduces as permeability increases because the characteristic squirt flow time decreases. Evaluating in time lapse seismic monitoring purpose, the probable decline in V_P and V_S due to chemical dissolution are respectively 550 m/s (~15%) and 263 m/s (~13%), whereas, in laboratory, the values are respectively ~21 and ~15%. The decrease of density due to this chemo-mechanical effect on Calcite rock is ~4%, and decrease in P- and S-wave acoustic impedances within seismic frequency range are respectively ~18 and ~16%.

Case III: Impact of pressure on elastic properties

In the previous sections, the velocities are predicted at ultrasonic and seismic frequency keeping both overburden and pore fluid pressures unchanged. However, confining and pore pressure in geological reservoir are much higher than the values used during laboratory experiments. Here, variations of predicted velocities are shown with overburden and pore fluid pressure for both anisotropic and isotropic rocks.

Isotropic rock

The isotropic rock resembles here with water-saturated Calcite rock having spherical macro-pores and randomly distributed micro-cracks. Figures 3 and 4 display the calculated V_P and V_S, which increase as overburden pressure increases and decrease as fluid pressure decrease. In this case, dispersion is not observed in seismic frequency range.

Anisotropic rock

Anisotropic rock resembles with long, thin, parallel aligned fractures in the isotropic rock. The aspect ratio and length of the fractures are assumed as respectively 0.001 and 0.1 m. The squirt flow time is taken same as the isotropic medium. Velocities calculated for this anisotropic (vertically transversely isotropic) medium are presented in Fig. 5. In case of P-wave propagates normal to the fractures, velocities disperse significantly within seismic frequency range. If P-wave propagates parallel to the

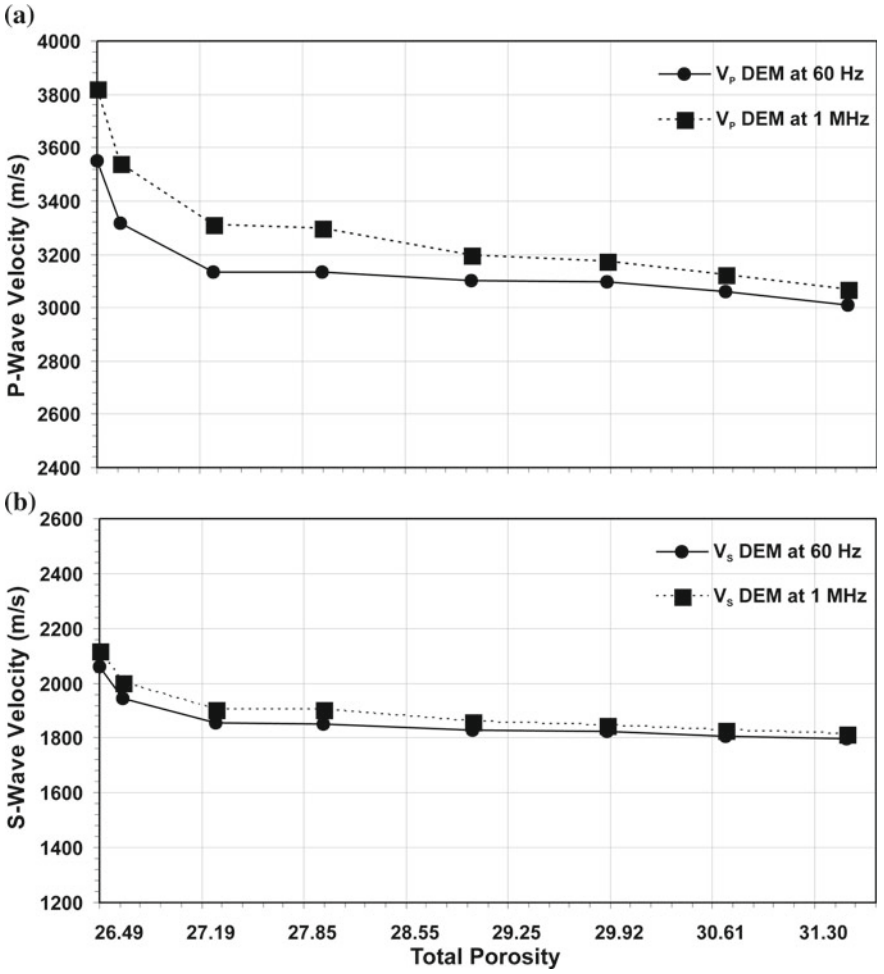

Fig. 2 Calculated V_P and V_S of the same rock at 60 Hz frequency (seismic range) and at ultrasonic frequency for similar experimental setup applying PDEM theory

fractures, no dispersion is observed. Figure 6 displays calculated dispersive S-wave velocity propagating at 45° angle.

Case IV: Impact of both dissolution due to chemical interaction and free gas (CO_2) on elastic properties

Thermal equilibrium of CO_2-rich water alters due to upward migration of CO_2 gas causing the modification in the proportion of dissolved and free gases (Lumley 2010; Vanorio et al. 2008). As a consequence, seismic properties of CO_2 are suppressed by ambiguities aroused due to changes in microstructure as a result of chemical reaction. Figure 7 expresses the calculated velocities at 60 Hz for the joint effect of free CO_2

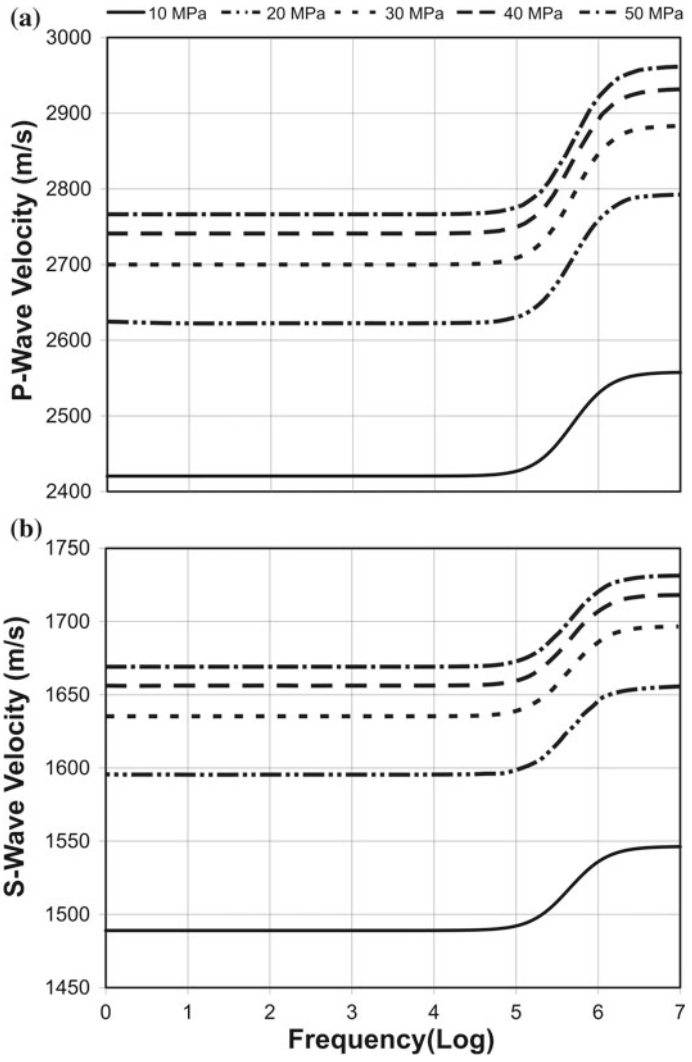

Fig. 3 Calculated V_P and V_S for isotropic rock at different overburden pressure and fixed fluid (pore) pressure (10 MPa)

gas distribution in uniform and patchy form in pores and chemical reaction. The microstructure assumed here is similar to Case I.

The results show that the calculated S-wave velocity change with CO_2 concentration like P-wave velocity. This is because pore-pressure gradient is induced at the pore scale by a seismic wave while passing through the medium, which impacts both bulk and shear moduli.

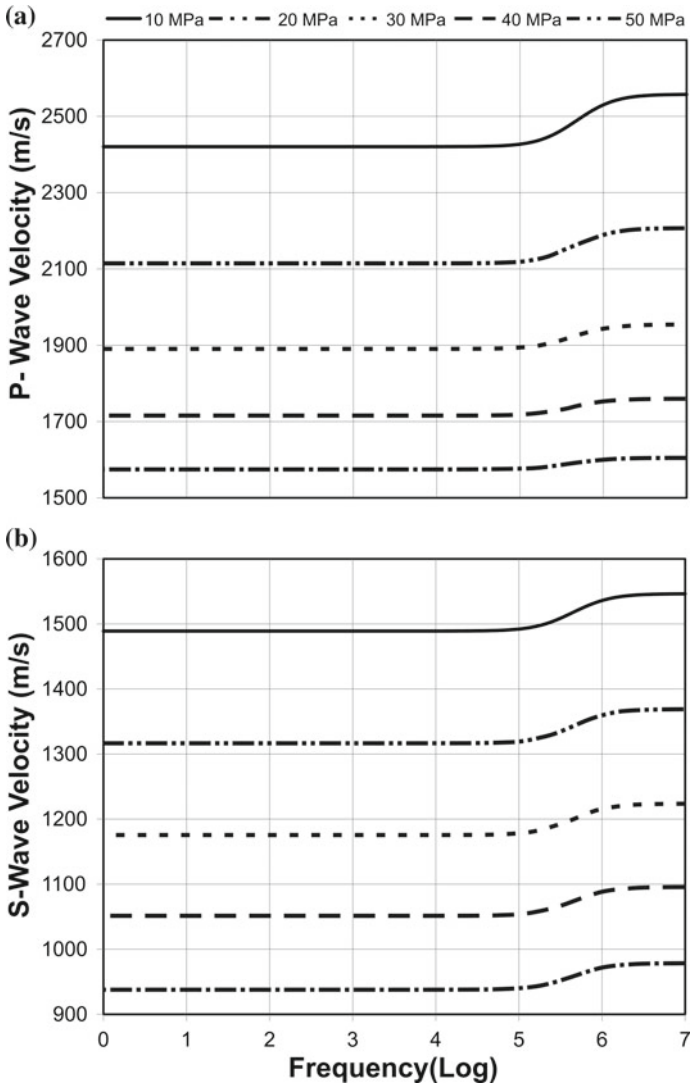

Fig. 4 Calculated V_P and V_S for isotropic rock at different fluid (pore) pressure and fixed confining pressure (10 MPa)

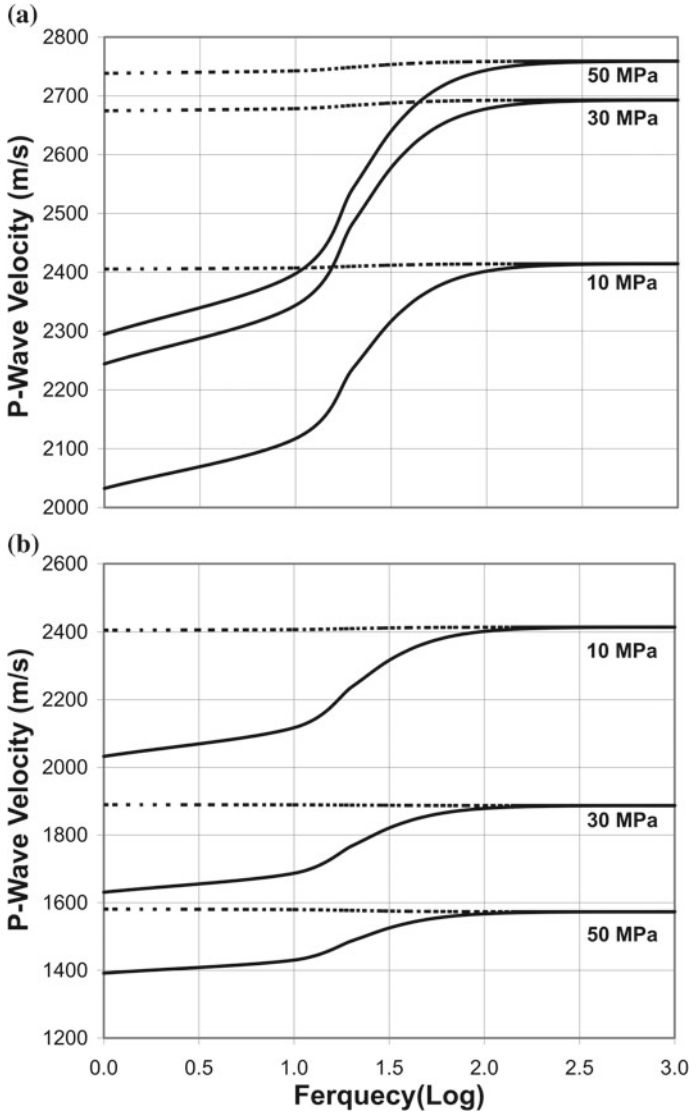

Fig. 5 Calculated V_P propagating parallelly (dashed) and normal (continuous) to the meso-fracture at different overburden pressure and fixed (10 MPa) fluid pressure (**a**); calculated V_P at different fluid pressure and fixed (10 MPa) overburden pressure (**b**)

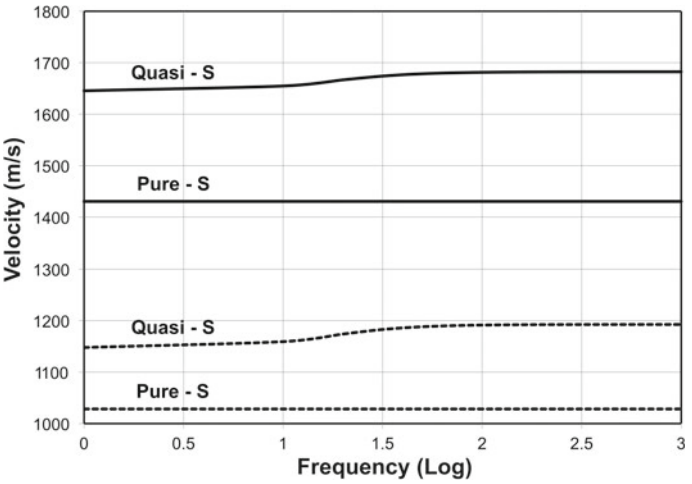

Fig. 6 Calculated pure and quasi shear velocities at 10 MPa fluid pressure and 30 MPa overburden pressure (continuous, upper panel); at 30 MPa fluid pressure and 10 MPa overburden pressure (dashed, lower panel)

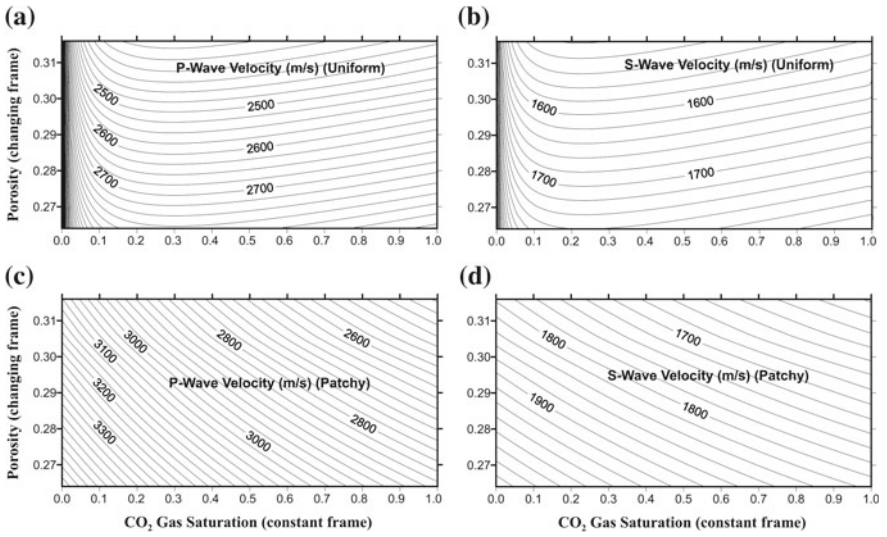

Fig. 7 Calculated V_P and V_S for the same rock at similar experimental setup applying PDEM theory at 60 Hz frequency (seismic range) because of the joint effect of changing matrix due to dissolution, and uniform (**a**–**b**) and patchy (**c**–**d**) distribution of free CO_2 gas

Dispersion and attenuation

The results show dispersion decreases because pressure gradient diminishes with CO_2 saturation. Velocity and attenuation are correlated, which decrease with fully water saturation to fully gas saturation (Figs. 8, 9 and 10).

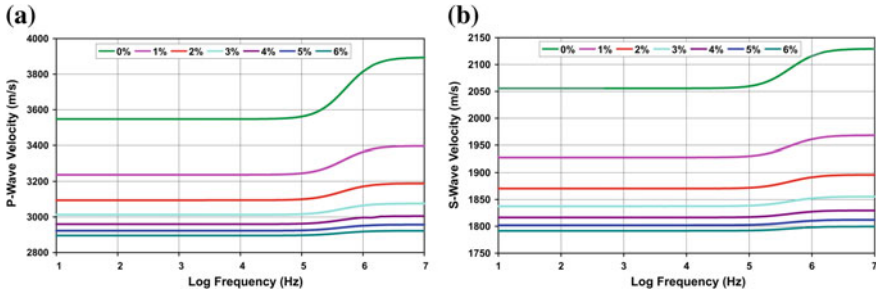

Fig. 8 Dispersion of V_P and V_S at various CO_2 concentrations distributed uniformly in pores

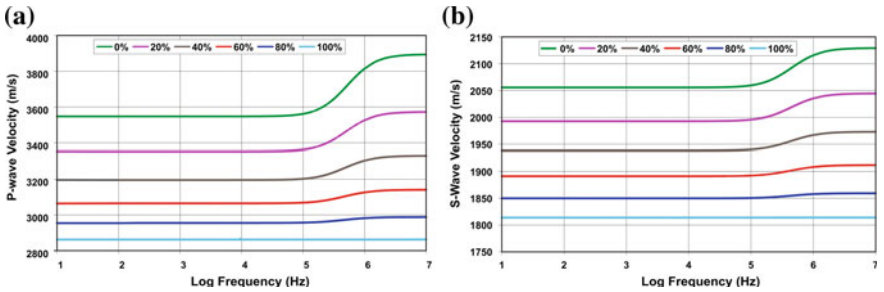

Fig. 9 Dispersion of V_P and V_S at various CO_2 concentrations distributed as patches in pores

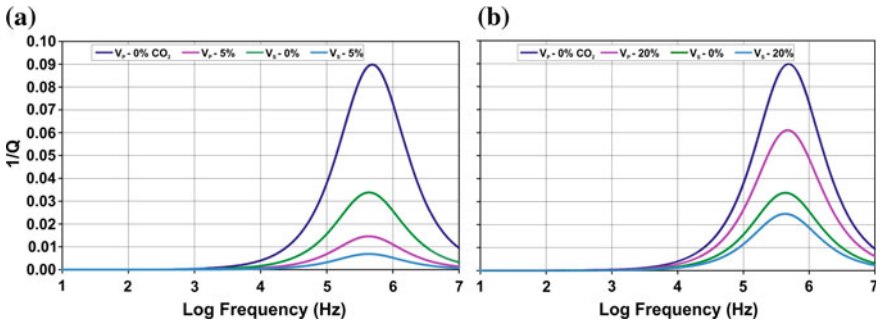

Fig. 10 Attenuation of V_P and V_S at various CO_2 concentration for uniform and patchy type distribution

4 Conclusions

The PDEM theory is applied here to model CO_2-sequestered carbonate reservoir. The theory can account for heterogeneous microstructure consisting of micro-cracks to meso-fractures. The theory is useful to incorporate alteration of microstructure as a consequence of chemo-mechanical effect induced by CO_2 injection in carbonate reservoir and can be used for quantitative interpretation of time lapse 4D seismic data acquired from such reservoirs—a challenging task till date. This frequency-dependent theory can be up-scaled (laboratory to field or ultrasonic to seismic frequency) to detect changes in the velocities of the rock and can be applied to understand the effect of visible changes in 4D seismic data for monitoring the impact of sequestration on our geological environment.

The theory predicts no velocity dispersion in seismic frequency range in case of heterogeneity at pore-scale. But velocity dispersion observed considerably in seismic frequency range in presence of meso-scale fractures.

Acknowledgements The author is thankful to the Director, National Geophysical Research Institute, Hyderabad for his kind permission to publish this work.

References

Berryman JG (1992) Single-scattering approximations for coefficients in Biot's equations of poroelasticity. J Acoust Soc Am 91:551–571

Biot MA (1956) Theory of propagation of elastic waves in a fluid-saturated porous solid—I: low-frequency range. J Acoust Soc Am 28:168–178

Biot MA (1962) Mechanics of deformation and acoustic propagation in porous media. J Appl Phys 33:1482–1498

Chand S, Minshull TA, Priest JA, Best AI, Clayton CRI, Waite WF (2006) An effective medium inversion algorithm for gas hydrate quantification and its application to laboratory and borehole measurements of gas hydrate-bearing sediments. Geophys J Int 166:543–552

Chapman M (2003) Frequency-dependent anisotropy due to meso-scale fractures in the presence of equant porosity. Geophys Prospect 51:369–379

Chapman M, Zatsepin SV, Crampin S (2002) Derivation of a microstructural poroelastic model. Geophys J Int 151:427–451

Chen C, Zhang D (2010) Pore-scale simulation of density-driven convection in fractured porous media during geological CO_2 sequestration. Water Resour Res 46:W11527

Cox PM, Betts RA, Jones CD, Spall SA, Totterdell IJ (2000) Acceleration of global warming due to carbon-cycle feedbacks in a coupled climate model. Nature 408:184–187

Dvorkin J, Nur A (1993) Dynamic poroelasticity: a unified model with the squirt and the Biot mechanisms. Geophysics 58:524–533

Dvorkin JG, Mavko G, Nur A (1995) Squirt flow in fully saturated rocks. Geophysics 60:97–107

Eshelby JD (1957) The determination of the elastic field of an ellipsoidal inclusion, and related problems. Proc R Soc Lond A241:376–396

Gassmann F (1951) Über die Elastizität poröser Medien. Vierteljahrsschrift der Naturforschenden Gesellschaft in Zürich 96:1–23

Ghosh R, Sain K (2008) Effective medium modelling to assess gas hydrate and free-gas evident from the velocity structure in the Makran accretionary prism, offshore Pakistan. Mar Geophys Res 29:267–277

Ghosh R, Sain K, Ojha M (2010a) Effective medium modelling of gas hydrate-filled fractures using the sonic log in the Krishna-Godavari basin, offshore eastern India. J Geophys Res 115:B06101

Ghosh R, Sain K, Ojha M (2010b) Estimating the amount of gas-hydrate using effective medium theory: a case study in the Blake Ridge. Mar Geophys Res 31:29–37

Ghosh R, Sen MK (2012) Predicting subsurface CO_2 movement: from laboratory to field scale. Geophysics 77:1–11

Ghosh R, Sen MK, Vedanti N (2015) Quantitative interpretation of CO 2 plume from Sleipner (North Sea), using post-stack inversion and rock physics modelling. Int J Greenhouse Gas Control 32:147–158

Hoefiner ML, Fogler HS (1988) Pore evolution and channel formation during flow and reaction in porous media. AIChE J 34:45–54

Hornby BE, Schwartz LM, Hudson JA (1994) Anisotropic effective-medium modelling of elastic properties of shales. Geophysics 59:1570–1583

Hudson JA, Liu E, Crampin S (1996) The mechanical properties of materials with interconnected cracks and pores. Geophys J Int 124:105–112

Jakobsen M, Hudson JA, Minshull TA, Singh SC (2000) Elastic properties of hydrate-bearing sediments using effective medium theory. J Geophys Res 105:561–577

Jakobsen M (2004) The interacting inclusion model of wave-induced fluid flow. Geophys J Int 158:1168–1176

Jakobsen M, Chapman M (2009) Unified theory of global flow and squirt flow in cracked porous media. Geophysics 74:WA65–WA76

Jakobsen M, Hudson JA, Johansen TA (2003a) T-matrix approach to shale acoustics. Geophys J Int 154:533–558

Jakobsen M, Johansen TA, McCann C (2003b) The acoustic signature of fluid flow in complex porous media. J Appl Geophys 54:219–246

Lumley D (2010) 4D Seismic monitoring of CO_2 sequestration. Lead Edge 29:150–155

Mavko G, Nur A (1975) Melt squirt in the asthenosphere. J Geophys Res 80:1444–1448

Mavko G, Jizba D (1991) Estimating grain-scale fluid effects on velocity dispersion in rocks. Geophysics 56:1940–1949

Mukerji T, Mavko G (1994) Pore fluid effects on seismic velocity in anisotropic rocks. Geophysics 59:233–244

Mura T (1982) Micromechanics of defects in solids. Kluwer Academic Publishers, Dordrecht

Nishizawa O (1982) Seismic velocity anisotropy in a medium containing oriented cracks: transversely isotropic case. J Phys Earth 30:331–347

O'Connell RJ, Budiansky B (1977) Viscoelastic properties of fluid saturated cracked solids. J Geophys Res 82:5719–5735

Vanorio T, Scotallero C, Mavko G (2008) The effect of chemical and physical processes on the acoustic properties of carbonate rocks. Lead Edge 27:1040–1048

Vanorio T, Mavko G, Vialle S, Spratt K (2010) The rock physics basis for 4D seismic monitoring of CO_2 fate: are we there yet? Lead Edge 29:156–162

Vialle S, Vanorio T (2011) Laboratory measurements of elastic properties of carbonate rocks during injection of reactive CO_2-saturated water. Geophys Res Lett 38:L01302

Walsh JB (1969) New analysis of attenuation in partially melted rock. J Geophys Res 74:4333–4337

Zatsepin SV, Crampin S (1997) Modelling the compliance of crustal rock, I. Response of shear-wave splitting to differential stress. Geophys J Int 129:477–494

Chapter 12
Computation Methods in Petrophysics for Addressing Redundancy and Reservoir Property Prediction

Abhijeet S. Bhardwaj and Ravi Sharma

Abstract The insight provided by well logs for the reservoir properties has been established beyond doubt. Often only standard logs are obtained to run routine calculations of porosity and saturation. Information about reservoir mineralogy and therefore effective geomechanical properties are generally missing because the well logs required (e.g., Shear, PEF, Litho scanner) for successful estimation of these properties are not acquired on routine basis. Additionally, when available, these logs are limited in their coverage of subsurface sections. Therefore, core plugs from the well or empirical correlations from analog settings are used to run the reservoir property analysis. However, such estimates and their geological significance is rarely verified and accounted for. In this work, we propose a method to predict the missing/discontinuous shear log statistically and testify it by binding the predictions to lithology. We also tackled the issue of core sample redundancy which is quite a challenge in selection of core sample for running rock property analysis. The predicted shear log values combined with other suitable logs are used to find lithofacies distribution in the reservoir section which constitutes our physical model. A sensitivity check is also made by using different combinations of logs for determining the statistical and physical models.

Keywords Petrophysics · ANN · Regression analysis · Rock properties

1 Introduction

The better understanding of the reservoir helps in optimizing its lifetime performance. It is of vital importance to predict the rock properties to estimate the future flow behavior of complex geological settings. Rock properties are traditionally estimated from the cuttings obtained during drilling as well as from the cores drilled out. However, the samples collected from cuttings are lost sometimes and are generally not large enough to give precise prediction of porosity, permeability and other log properties (Serra and Abbott 1982). Cores, on the other hand, give excellent measure

A. S. Bhardwaj (✉) · R. Sharma
Department of Earth Sciences, Indian Institute of Technology Roorkee, Roorkee, India
e-mail: abhijeet.bhardwajiitr@gmail.com

K. H. Singh and R. M. Joshi (eds.), *Petro-physics and Rock Physics of Carbonate Reservoirs*, https://doi.org/10.1007/978-981-13-1211-3_12

of the rock properties. However, coring is a very expensive process and due to safety measures extensive coring cannot be done, thus resulting in discontinues cores. Well log data is continuing and thus can be used to estimate the properties of the formations crossed by the well with greater accuracy and consistency. However certain well logs are not measured during wireline logging due to the high cost involved and often leave us wondering for a particular log type for a detailed analysis. Shear wave log (DTS) is one such type of log, the importance of which is significant in calculating the porosity along with various geomechanical parameters. Due to its immense importance, various empirical relations have already been developed (Castagna et al. 1985). However, these relations tackle site-specific challenges and are rarely bounding to lithology. The prediction of lithology within a well is a complicated task as there are limited workflows in literature on how to obtain information about lithology using suitable combinations of logs.

Thus, geo-statistical methods can be used to solve these problems by taking into consideration an acceptable range of accuracy and no requirement of new measurements (Akhundi et al 2014). The connection between reservoir properties and well log data is made through "statistical based" and "physics-based" approaches. The physics-based approaches, also known as physical model, attempt to map the changes in log responses due to changes in rock properties. Here the key lies in the uniqueness and sensitivity of the solution. Statistical approach ties the rock properties to prediction values obtained by examining the data only. It would be reasonable to argue that a combination of strengths of both these methods would provide us the most accurate result (Sandham and Leggett 2003). Thus, we present a research that tackles the problem of predicting DTS log using predictive analysis techniques (the statistical model) and bind our predictions independently to lithology (the physical model) using various geomechanical parameters such as Poisson's Ratio, Bulk Modulus and Shear Modulus by avoiding double-dipping to a maximum extent. The geomechanical parameters are obtained from the volumes of individual minerals by applying standard literature methods of determining effective moduli. The volumes of different minerals are computed by solving a convex optimization problem on a system of linear equation. A sensitivity check for the combination of logs used in DTS log prediction is also made by using the predicted log to determine the electrofacie based on the hierarchical clustering method (Serra and Abbott 1982). The electrofacie obtained are then compared to the lithofacie obtained by clustering the volumes of individual minerals.

2 Theory and/or Method

The study area is a carbonate reservoir consisting of various wells, of which four wells had DTS log and were used to build the statistical model. The data from three wells is used to train the supervised learning algorithms while the data from fourth well is used as validation set. The trained algorithm is used to predict DTS log in the prediction well which consist of Photoelectric (PEF) log in addition to the routine

logs like gamma-ray (GR), density (RHOB), neutron porosity (NPHI) and resistivity log (RT) which are used to build the physical model. While dealing with multivariate data sets like well logs it is of great importance to realize the dependencies of variables on each other. Thus, the correlation coefficient plays a vital role as it quantifies the relation between any two logs (Lim and Kang 1997). The correlation test (Fig. 1) carried out showed that the dependency of DTS log lies primarily on compressional sonic wave log (DTP) and after that on RHOB log and then upon NPHI log. The correlation coefficient between GR log and DTS log is quiet low that could well be due to the low-resolution of GR log (Fig. 2). The RT log also has very low correlation coefficient suggesting non-linear dependency on DTS log (Akhundi et al. 2014).

DTP, RHOB, NPHI and GR logs are considered for further analysis. The dependency of DTS on other logs can be demonstrated as in Eq. (1).

$$\mathrm{DTS} = f(\mathrm{DTP}, \mathrm{RHOB}, \mathrm{NPHI}, \mathrm{GR}) \tag{1}$$

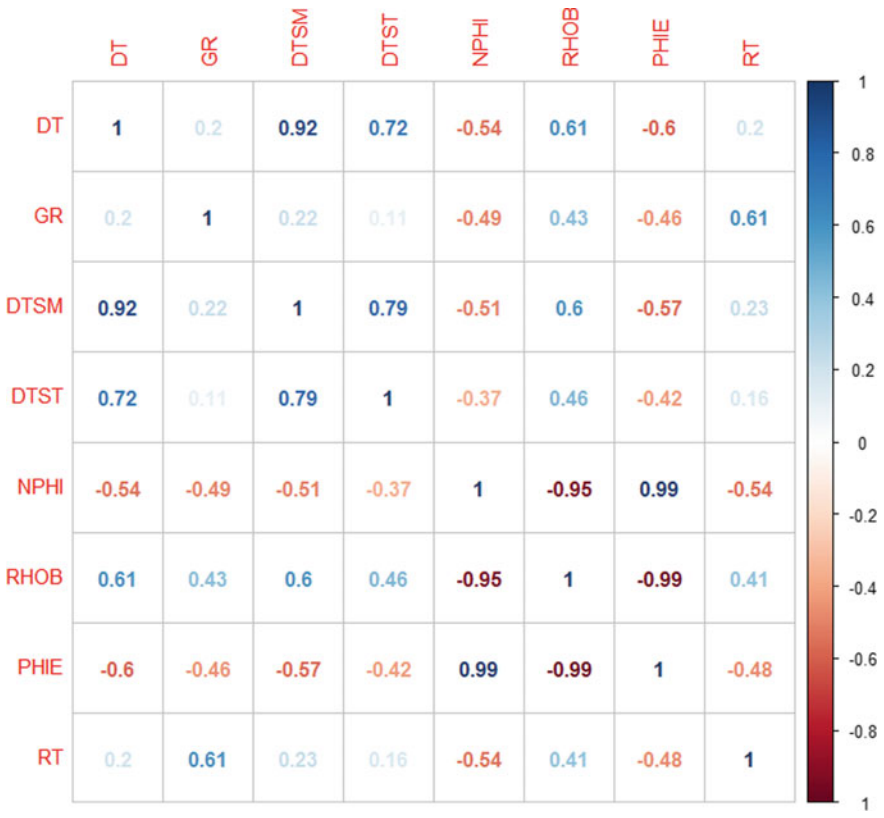

Fig. 1 The correlation coefficients between different logs

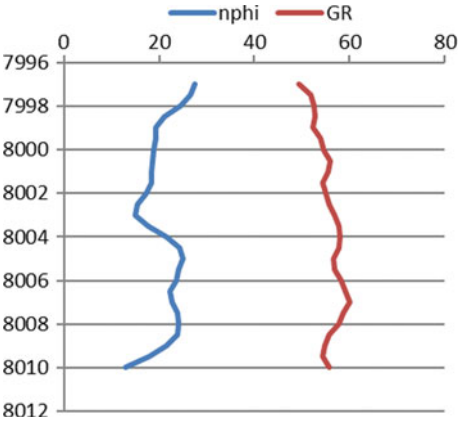

Fig. 2 GR versus NPHI plot suggesting a low-resolution GR log (Depth given in feets)

Regression Analysis is carried out having DTS as the dependent variable and DTP, RHOB, NPHI, and GR as explanatory variables to justify the worthiness of all the explanatory variables that are to be used to make different sets of three variables. The significant *F* score (Table 1) obtained is very low, suggesting that all the four logs can be used to build the statistical model (Draper and Smith 2014). It is also observed that the *R*-square and Adjusted *R*-square both increases with the number of explanatory variables (Fig. 3) and as the Significance *F* score is negligible we could use all four logs to build the statistical model.

From the given suite of logs, if we use four independent well logs (DTP, RHOB, NPHI, and GR) to build the statistical model we are left with just one independent PEF log to build the physical model. This clearly makes for an underdetermined problem. Since the objective is to make a physical model comprising of 4 components of the sedimentary reservoir systems (common minerals and fluids: quartz, clay, calcite, and water), we clearly need more logs. We, therefore, use different sets of three logs

Table 1 Regression analysis

ANOVA					
	df	SS	MS	*F*	Significance *F*
Regression	4	21124.84891	5281.212	90.02739	2.62959E−55
Residual	423	24814.14496	58.66228		
Total	427	45938.99387			
	Coefficients	Standard error	*t* stat	*P*-value	
Intercept	−6.048803482	19.99770383	−0.30247	0.762439	
DTP	1.086675998	0.061356481	17.71086	6.53E−53	
RHOB	30.19542757	7.061514071	4.276056	2.35E−05	
NPHI	0.476077673	0.111899736	4.254502	2.58E−05	
GR	−0.157960258	0.040784437	−3.87305	0.000124	

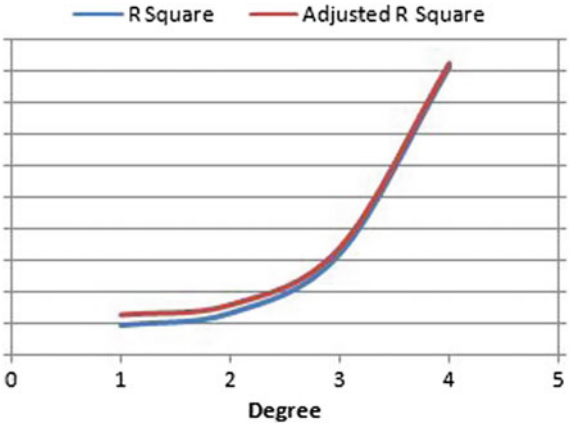

Fig. 3 *R*-square and adjusted *R*-square versus number of variables

to predict DTS and use the remaining log (along with computed V_{sh} and PEF) to build the physical model. But still the problem is underdetermined and thus one log from the statistical model set is double dipped in the physical model. The sensitivity of the logs used to build the statistical and physical model is tested along with the sensitivity of the double-dipping log. The *p*-value for DTP log is very low (Table 2) suggesting that the sets would always include DTP log while other logs are rotated either to predict DTS log or to build the physical model.

The target is to predict the continuous distribution of DTS log, which would depend functionally on other well logs. The best estimation of the functional form is given by a Supervised learning algorithm which gives the best approximate of dependent variable (DTS) on independent variables (other well logs). We used Gradient Boosting Regressor and Artificial Neural Network as supervised learning algorithms to train the data set. Gradient Boosting (Fig. 4) (Zemel and Toniann 2001) is an ensemble technique (Dietterich 2000) where we add weak models to the ensemble orderly to create a strong model.

Table 2 Sets of well log data

Combination number	Statistical model			Physical model			
Set 1	DTP	RHOB	GR*	GR*	PEF	NPHI	V_{sh}
Set 2	DTP*	RHOB	NPHI	GR	PEF	DTP*	V_{sh}
Set 3	DTP	RHOB	NPHI*	GR	PEF	NPHI*	V_{sh}
Set 4	DTP	RHOB*	NPHI	GR	PEF	RHOB*	V_{sh}
Set 5	DTP*	NPHI	GR	DTP*	PEF	RHOB	V_{sh}
Set 6	DTP	NPHI	GR*	GR*	PEF	RHOB	V_{sh}
Set 7	DTP	NPHI*	GR	NPHI*	PEF	RHOB	V_{sh}

The (*) marked logs are the logs which are double-dipped for both statistical and physical model prediction

```
reg = GradientBoostingRegressor(n_estimators=100,
                          ...learning_rate=1.0, max_depth=1)

reg.fit(x_train, y_dts)
predicted_dts_TA=reg.predict(v_train)
```

Fig. 4 Applying gradient boosting regressor

```
## MODEL DTP RHOB NPHI

clf = MLPRegressor(hidden_layer_sizes=(300,300), alpha= 0.001 ,solver="sgd"
                   ,learning_rate_init=0.00006, learning_rate='invscaling')

neural_model = clf.fit(train_TA[[c for c in train_TA.columns if c != "DTS" and c != "RHOB"]],
                       train_TA["DTS"])

validation_data_predictions = neural_model.predict(
    test_TA_ann[[c for c in train_TA.columns if c != "DTS" and c != "RHOB"]])

validation_predictions_pd = pd.DataFrame(data=validation_data_predictions,
                                         index=test_TA_ann.index.values,
                                         columns=["DTS"])

error=np.mean(np.abs((test_TA_ann["DTS"] - validation_predictions_pd["DTS"]) /test_TA_ann["DTS"])) * 100
```

Fig. 5 Implementing ANN algorithm

Artificial Neural Network (Fig. 5) takes their very basic form from the human brain. The mathematical equation describing the implementation of Artificial Neural Network is

$$y(x) = f(w_{m+1} \sum_{j=0}^{m} w_j x_j) \tag{2}$$

where the first coefficient is the bias term, w_j are the weights that are multiplied to the input layer neuron denoted by x_j having j features, f is the activation function which is generally sigmoid function or a hyperbolic tangent function and $y(x)$ is the output layer for the input neurons (Cranganu et al. 2015). In this work, the neural net consists of two layers having 300 neurons each. Relu function is used as the activation function while Steepest Gradient is used for iterating the weights along with a regularization coefficient to penalize overfitting of variable.

The outputs of both the algorithms are compared thus suggesting a better algorithm for the statistical model. The output is quantified by calculating Mean Absolute Percentage error for the (MAPE) calculated on a subset of training data. The trained algorithms are used to predict DTS log in a prediction well, which is used to compute Poisson's ratio by using:

$$1/2\left(\frac{\mathrm{DTS}^2}{\mathrm{DTP}} - 2\right)/\left(\frac{\mathrm{DTS}^2}{\mathrm{DTP}} - 1\right) \tag{3}$$

The development of the physical model is based on the motivation to evaluate the volumes of minerals for a four-component system. The minerals included are illite, calcite, quartz, and water suggesting clay, carbonate and siliciclastic lithology along with porosity. The physical model revolves around the idea that neglecting environmental errors, the log response at each depth point is a combination of the log response of each mineral at that depth point. Thus, a system of linear equation is formed as shown:

$$V_{\mathrm{Qz}} + V_{\mathrm{Cal}} + V_{\mathrm{Clay}} + \phi = 1 \tag{4}$$

$$\gamma_{\mathrm{Qz}} V_{\mathrm{Qz}} + \gamma_{\mathrm{Cal}} V_{\mathrm{Cal}} + \gamma_{\mathrm{Clay}} V_{\mathrm{Clay}} + \gamma_{\mathrm{w}} \phi = V_{\mathrm{sh}} \tag{5}$$

$$\rho_{\mathrm{Qz}} V_{\mathrm{Qz}} + \rho_{\mathrm{Cal}} V_{\mathrm{Cal}} + \rho_{\mathrm{Clay}} V_{\mathrm{Clay}} + \rho_{\mathrm{w}} \phi = \mathrm{RHOB} \tag{6}$$

$$\psi_{\mathrm{Qz}} V_{\mathrm{Qz}} + \psi_{\mathrm{Cal}} V_{\mathrm{Cal}} + \psi_{\mathrm{Clay}} V_{\mathrm{Clay}} + \psi_{\mathrm{w}} \phi = \mathrm{NPHI} \tag{7}$$

$$\zeta_{\mathrm{Qz}} V_{\mathrm{Qz}} + \zeta_{\mathrm{Cal}} V_{\mathrm{Cal}} + \zeta_{\mathrm{Clay}} V_{\mathrm{Clay}} + \zeta_{\mathrm{w}} \phi = \mathrm{PEF} \tag{8}$$

Here V_{mineral} is the volume of the corresponding mineral, $\gamma_{\mathrm{mineral}}$ describes the shale response log for the corresponding mineral, similarly ρ_{mineral}, ψ_{mineral}, ζ_{mineral}, gives us the RHOB response, NPHI response, and PEF response, for various minerals respectively. Thus, a system of linear equation is established from these six equations Eqs. (5)–(8) constrained to Eq. (4) to predict the volumes of the minerals in the four-component system. As volumes of four minerals are to be predicted we select four combinations of equations along with the constrain equation to form a set. As already stated, while selecting the four equations corresponding to four log responses, for the physical model the repetition of the logs used in statistical model is avoided to a good extent to reduce the double-dipping in the error being propagated by the log. Thus, the different sets of well log data used in statistical and physical model prediction (Table 2) are.

Using the combinations shown for the physical model a system of linear equations is created of the form $AX = B$, where A is the matrix of log responses for minerals (Table 3), X is the vector of unknown volumes at a given depth point and B is vector of true response at that depth point.

The system of linear equation along with the constraints forms a Lagrangian equation of the form

$$AX - B - \lambda G(x) = 0 \tag{9}$$

where $G(x)$ includes all the constraints.
Equation for optimization is:

Table 3 Mineral response to various logs

	Calcite	Quartz	Clay	Water
Pef	5.08	1.81	2.6	0.36
GR	11	1	160	9.6
NPHI	0	−0.05	0.4	0.9529
V_{sh}	0.015	0.01	0.7	0
DTP	49	56	85.34	189
RHOB	2.71	2.65	2.52	1.049

$$\text{minimize norm}||AX - B||\text{Subject to} \sum_{\text{minerals}} V = 1 \text{ and } 0 < V_{\text{minerals}} \tag{10}$$

The Lagrangian is solved using convex optimization tool (Boyd and Vandenberghe 2010) which implies interior-point polynomial method for convex programming (Nemirovski 1996).

The volumes obtained were used to calculate Poisson's ratio by estimating bulk and shear moduli using two methods of effective medium theory: (1) Hill average of Voigt upper bound and Reuss Lower bound (Eq. 14). (2) Gassmann's Relation for isotropic, saturated rock (Eq. 15). For both the methods the moduli for rock minerals were calculated by scaling the mineral volumes to sum up to 1.

Voigt upper bound for bulk and shear modulus of minerals is given by:

$$\begin{aligned} \acute{\mathrm{K}}_{\text{voigt, mineral}} &= V_{\text{calcite}} K_{\text{calcite}} + V_{\text{quartz}} K_{\text{quartz}} + V_{\text{clay}} K_{\text{clay}} \\ \bar{\mathrm{G}}_{\text{voigt, mineral}} &= V_{\text{calcite}} G_{\text{calcite}} + V_{\text{quartz}} G_{\text{quartz}} + V_{\text{clay}} G_{\text{clay}} \end{aligned} \tag{11}$$

The Reuss lower bound for bulk and shear modulus of minerals is given by:

$$\begin{aligned} \acute{\mathrm{K}}_{\text{reuss, mineral}}{}^{-1} &= V_{\text{calcite}} K_{\text{calcite}}{}^{-1} + V_{\text{quartz}} K_{\text{quartz}}{}^{-1} + V_{\text{clay}} K_{\text{clay}}{}^{-1} \\ \bar{\mathrm{G}}_{\text{reuss, mineral}}{}^{-1} &= V_{\text{calcite}} G_{\text{calcite}}{}^{-1} + V_{\text{quartz}} G_{\text{quartz}}{}^{-1} + V_{\text{clay}} G_{\text{clay}}{}^{-1} \end{aligned} \tag{12}$$

The average of Voigt upper bound (assuming very hard mineral packing) and Reuss lower bound (assuming soft mineral packing) is taken to estimate the moduli of mineral material making up the rock ($\acute{\mathrm{K}}_{\text{mineral}}, \bar{\mathrm{G}}_{\text{mineral}}$) which also gives us the upper bound of the saturated rock framework.

$$\begin{aligned} \acute{\mathrm{K}}_{\text{mineral}} &= (\acute{\mathrm{K}}_{\text{voigt, mineral}} + \acute{\mathrm{K}}_{\text{reuss, mineral}})/2 \\ \bar{\mathrm{G}}_{\text{mineral}} &= (\bar{\mathrm{G}}_{\text{voigt, mineral}} + \bar{\mathrm{G}}_{\text{reuss, mineral}})/2 \end{aligned} \tag{13}$$

The lower bound of moduli for saturated rock is given by the Reuss average of the fluids in the rock. As water is the only fluid assumed to make a 4 component system,

the Reuss bound/lower bound for saturated Rock is the moduli of water ($\acute{K}_{water}$, $\bar{G}_{water}$).

The bulk and shear modulus for the rock by Hill average of Voigt and Reuss Bounds are than given by:

$$\begin{aligned} \acute{K}_{rock\ vrh} &= (\acute{K}_{mineral} + \acute{K}_{water})/2 \\ \bar{G}_{rock,\ vrh} &= (\bar{G}_{mineral} + \bar{G}_{water})/2 \end{aligned} \tag{14}$$

To calculate the rock moduli using Gassmann's relation for the saturated rock an oversimplified assumption was made, where we estimated the dry rock moduli by subtracting the pore space from the rock framework and multiplying it with the moduli of mineral material making up the rock.

$$\acute{K}_{dry} = (1 - \phi)\acute{K}_{mineral}$$

$$\bar{G}_{dry} = (1 - \phi)\bar{G}_{mineral,}$$

where ϕ is the porosity which in this case is the estimated volume of water in a four-component system. The bulk and shear modulus for the rock by Gassmann's relation are than given by:

$$\acute{K}_{rock\ Gassmann}/(\acute{K}_{mineral} - \acute{K}_{rock,\ Gassmann}) = \acute{K}_{rdry}/(\acute{K}_{mineral} - \acute{K}_{dry}) + \acute{K}_{water}/\phi(\acute{K}_{mineral} - \acute{K}_{water})$$

$$\bar{G}_{rock\ Gassmann}/(\bar{G}_{mineral} - \bar{G}_{rock,\ Gassmann}) = \bar{G}_{rdry}/(\bar{G}_{mineral} - \bar{G}_{dry}) + \bar{G}_{water}/\phi(\bar{G}_{mineral} - \bar{G}_{water}) \tag{15}$$

Poisson's Ratio is then calculated using moduli determined by both the methods and is given by PR_{vrh} and $PR_{Gassmann}$:

$$(3\acute{K} - 2G)/2(3\acute{K} + 2G) \tag{16}$$

The statistical and physical method were then compared by using the average percentage error between Poisson's ratios calculated by predicted DTS (PR_{ANN}, PR_{GBR}) and effective medium theory methods (PR_{vrh} and $PR_{Gassmann}$) for different combinations of logs (Table 2).

However, to check the accuracy of the physical model and its sensitivity over the well log data sets (Table 2) lithofacies are generated from mineral volumes (physical model) which are compared to electrofaice (Serra and Abbott 1982) generated using the logs which are in high correlation to the calculated porosity (PHIE) log. While generating electrofaices, the predicted DTS log was also included for all the combination sets to provide another test for the accuracy of statistical and physical model. To generate lithofacies we cluster the volumes obtained by solving the Lagrangian. As the volumes lie between 0 and 1 we directly use Agglomerative Hierarchical Clustering (Fig. 6) Algorithm (AGNES) introduced by (Kaufman and Rousseeuw

```
install.packages("cluster")
library(cluster)
clust_2=agnes(train_1)
plot(clust_2,  main="plotit", which.plot = 2)
bannerplot(clust_2)
D_2=cutree(clust_2,k=3)
```

Fig. 6 Hierarchical clustering

2005) to generate lithofacies. The three lithofacies obtained are represented numerically by '1', '2', and '3' as also suggested by the geological background of the area. The concept of electrofacies was introduced by (Serra and Abbott 1982), where electrofacies are defined as "a set of log responses describing the rock." (Lim and Kang 1997) described a method for multivariate statistical analysis of well log data to form electrofacies. Using the basics of the method electrofacies are generated using AGNES.

Prior to clustering the logs, a correlation test with PHIE is carried out suggesting the logs to be used in clustering (Fig. 7 gives an example for logs used in set 1).

It can be observed that NPHI and RHOB have the maximum correlation with PHIE logs and hence they are used without standardizing in our clustering algorithm to give them higher weights than other logs (Kaufman and Rousseeuw 2005). The predicted DTS and RT log also have considerable correlation coefficients but as their absolute values are higher (in tens or hundreds) as compared to the absolute values of RHOB and NPHI (in units or tens) they are standardized before being included in clustering. The need to standardize can also be understand by observing the fact that the difference in values of final dissimilarity observed when logs are standardized and when they are unstandardized is quite large as depicted in Fig. 8.

3 Results and Conclusions

MAPE calculated for both the algorithms predicting DTS log shows that ANN works better in predicting DTS log as compared to Gradient Boosting Regressor algorithm. As already mentioned, the accuracy of the statistical model with respect to the physical model is tested by computing the average percentage difference in the Poisson's Ratio calculated using the Physical model and the Statistical Model (Table 4). Also, the sensitivity of the models with the log data set (along with the accuracy of the physical model) is reported using the number of mismatch obtained in the data points, where we have classified each data point by clustering the Well logs thus generating electrofacies and by clustering the mineral volumes thus generating lithofacies out of 28 data points (Table 4).

Based on the Summary of results shown in Table 4, it can be inferred that the statistical model developed using Artificial Neural Network technique are more converging than that developed using Gradient Boosting Regressor Technique in estimating the

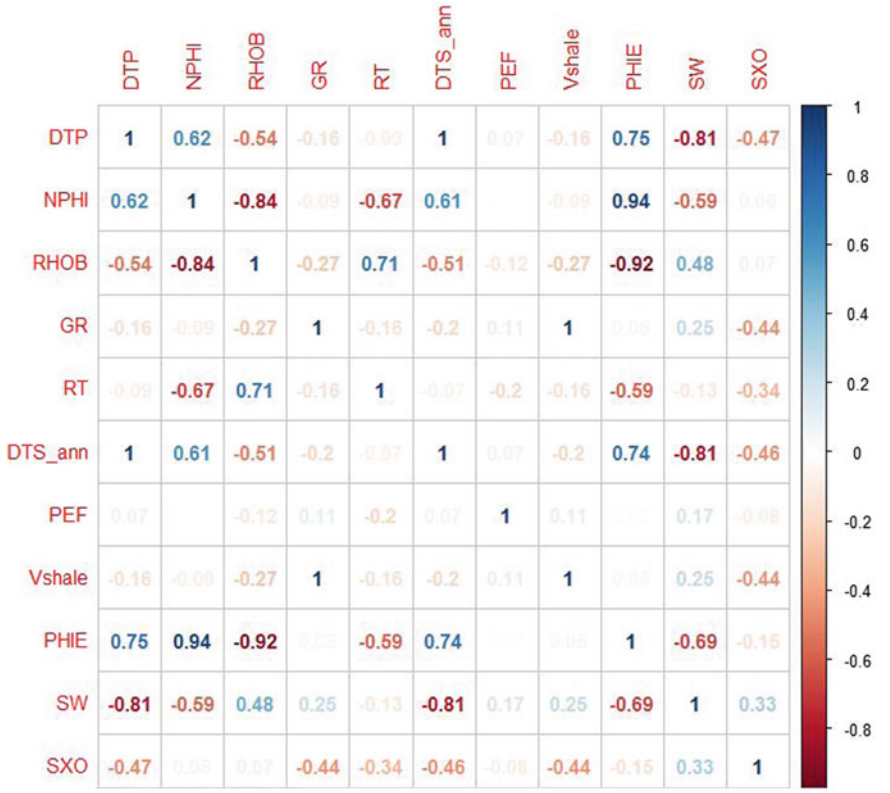

Fig. 7 Correlation coefficients of various logs with PHIE log

Poisson's ratio. Two rock physics models, VRH and Gassmann are used to calculate the Poisson's ratio. However, MAPE of GBR is slightly better than ANN and tends to capture the high-frequency component (Fig. 9). Thus, it is evident that both algorithms ANN and GBR have similar performances if we combine all measures of performance.

It can be seen that the Poisson's Ratio predicted using Voigt Reuss Hill average method is penalizing as it increases the error in comparing Poisson's Ratio for most sets. However, the Poisson's Ratio predicted using Gassmann's relation have a moderate effect on the error. Set 1, 5 and 7 seem to have an outstanding match of Poisson's Ratio. But set 5 and 7 fail the sensitivity test as there is high number of mismatch in the lithofacies predicted by using physical model and electrofacies predicted using the output of statistical model. Set 2, 4 and 6 also have a high number of mismatch of the data points also the average error in Poisson's Ratio prediction is relatively high for them and thus they do not form the optimum combination. We see that Set 3 have a very good sensitivity check as it only has 2 data points mismatching, however, the difference in agreement with the physical model is very high for Set 3. Thus,

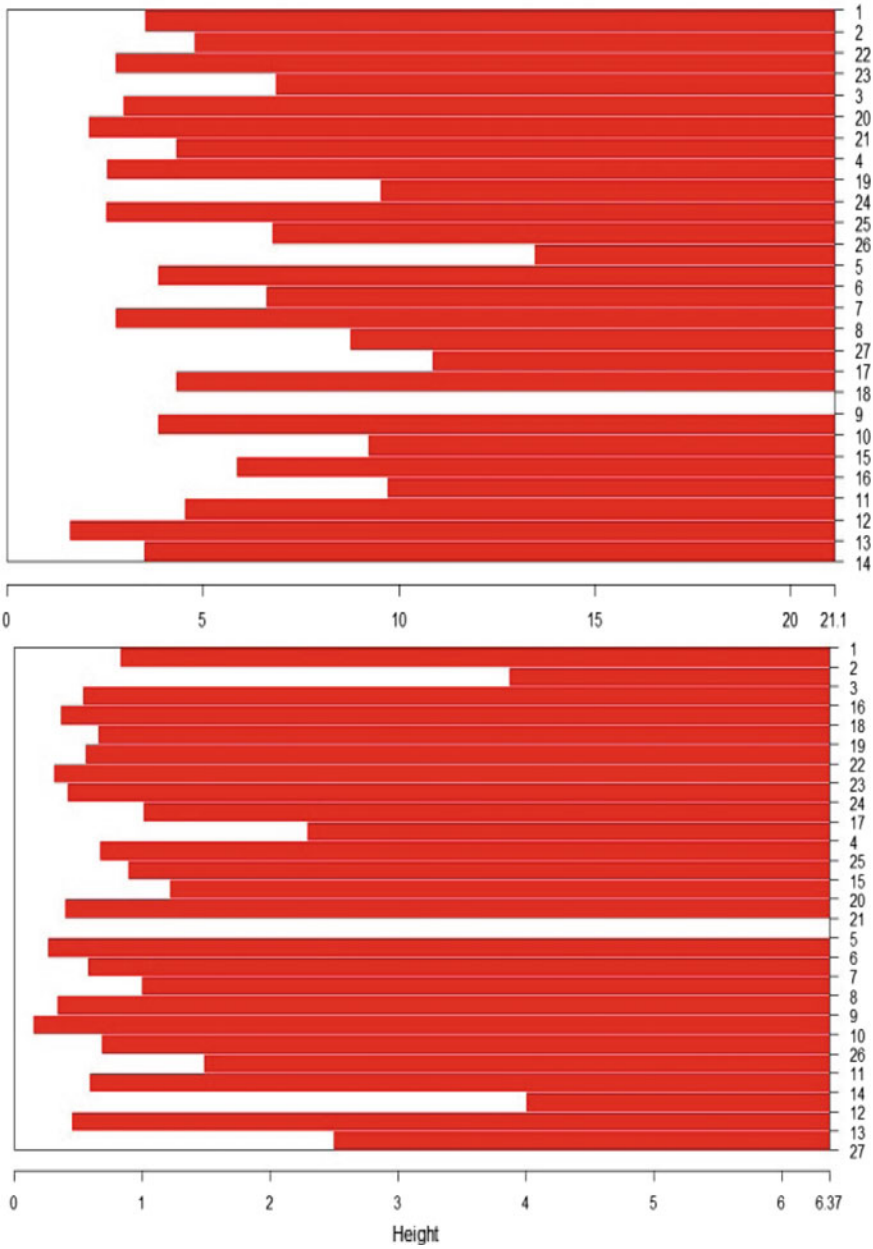

Fig. 8 Banner plot for set 1 (as example) showing the dissimilarity of clustering unstandardized logs is 21.1 and for standardized logs is 6.35

Table 4 Summary of different sets of well log data

Set No.	MAPE ANN	MAPE GBR	Diff ANN vrh	Diff ANN Gassmann	Diff GBR vrh	Diff GBR Gassmann	Miss match in number of data points	Average mineralogy
Set 1	3.23%	3.28%	2.70%	2.20%	4.80%	6.86%	2	60.74% calcite; 30.02% clay; 9.24% water
Set 2	3.38%	3.22%	11.03%	7.85%	22.38%	20.17%	17	53.75% calcite; 30.08% clay; 16.17% water
Set 3	3.38%	3.22%	10.85%	7.40%	22.85%	19.84%	2	60.74% calcite; 30.02% clay; 9.24% water
Set 4	3.38%	3.22%	10.62%	6.89%	22.06%	19.43%	22	70.08% calcite; 29.92% clay
Set 5	3.18%	3.09%	0.75%	1.61%	4.42%	4.78%	13	76.02% calcite; 23.98% water
Set 6	3.18%	3.09%	3.20%	7.52%	5.59%	9.19%	23	70.08% calcite; 29.92% clay
Set 7	3.18%	3.09%	0.75%	1.66%	4.42%	4.77%	13	78.16% calcite; 21.84% water

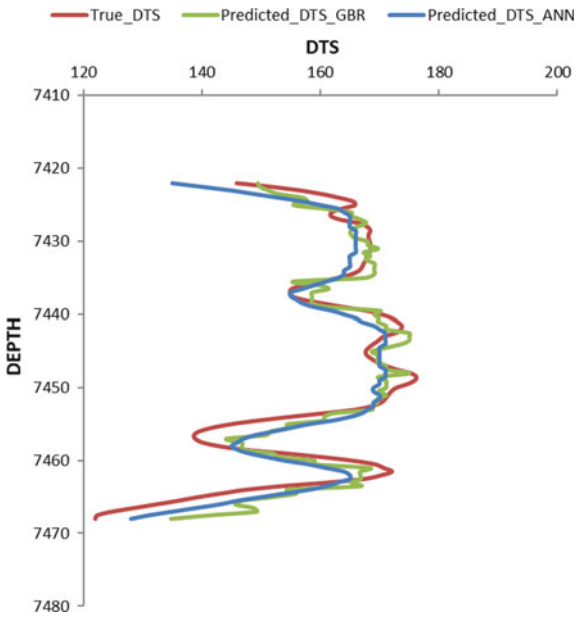

Fig. 9 Validation results for DTS predicted by ANN and GBR for set 1 (Depth given in feets)

taking the strengths of both physical and statistical models and summarizing the observations we can conclude that Set 1 forms the best combination for the physical and statistical model as it has a very low difference in Poisson's Ratio prediction and satisfies the sensitivity test significantly. After Set 1, all the Sets fail either the sensitivity check or the Poisson's Ratio comparison test.

Figure 10 shows the Poisson's Ratio predicted using Statistical Models (ANN and GBR) and using Physical models (rock physics methods like VRH and Gassmann) for Set 1. It can be seen that the physical methods have low variance in Poisson's Ratio while the statistical prediction does involve a decent amount of variance. The prediction using ANN is more closely related to the predictions using Physical methods (VRH and Gassmann) than GBR. This could be related to the higher frequency components introduced by GBR algorithm than ANN.

Figure 11 shows the comparison of lithofacies and electrofacies predicted for Set 1. Also, NPHI log is plotted against the predicted Lithology to give the verification of the physical model. As per the NPHI log plot, it could be said that the lighter versions of blue color (used to represent different lithology) consists higher amount of Clay component in them as the NPHI value is large for the lighter shades of blue. Core sample in any well is a luxury for the petro-physicist however, the emphasis should be to avoid redundancy in core sample selection using the strengths of electrofacies and lithofacies outputs, which help us, estimate the lithology. Thus using this approach, we can arrive at estimating the required coring sections to avoid collecting cores from similar geological settings.

After looking at the facies comparison between Fig. 11a, b, it can be concluded that our physical and statistical models are almost converging, except for a mismatch

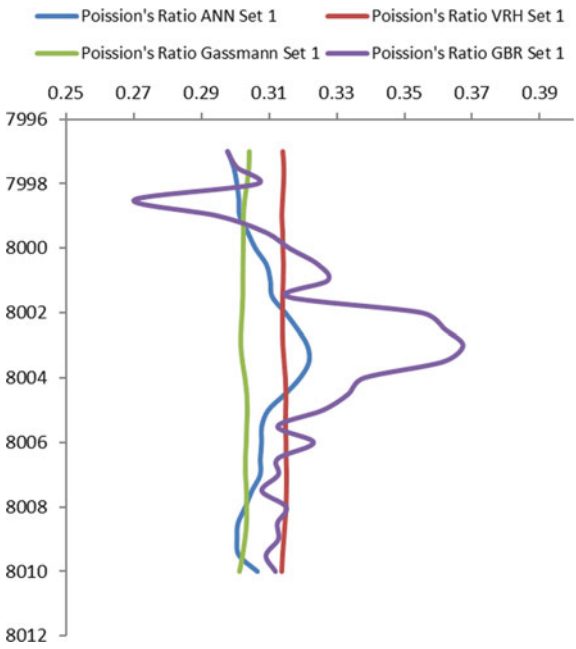

Fig. 10 Predicted versus actual DTS for set 1 for ANN

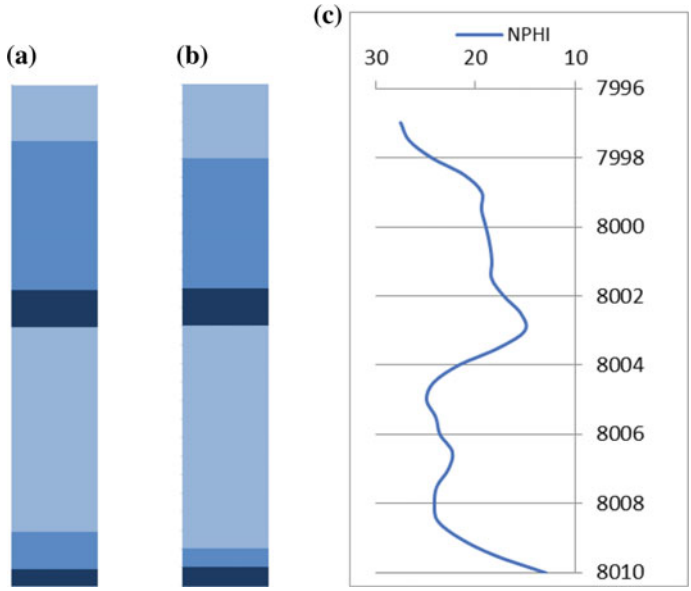

Fig. 11 **a** Lithofacies from physical model. **b** Electrofacies from Set_1 and **c** Electrofacies from Set_3 (Depth given in feets)

at few points for Set 1. However, for Poisson's Ratio estimates developed from physical models (based on rock physics methods VRH/Gassmann) the sensitivity of the estimated values of PR, appears to be missing the facie variation in the middle of the section. At the time we believe that there are possibilities such that of a different fluid combination or volumes of the softer constituents are probably under-predicted by our physical model. This point would be further looked at by merging this work with the available core data. Apart from the central region the PR match looks consistent with acceptable error limits.

Acknowledgements We acknowledge the support and encouragement from the Department Head and other colleagues from the Reservoir Characterization Group at IIT Roorkee and Yatin Katyal.

References

Akhundi H, Ghafoori M, Lashkaripour G (2014) Prediction of shear wave velocity using artificial neural network technique, multiple regression and petrophysical data: a case study in Asmari Reservoir (SWIran). Open J Geol 2014(July):303–313

Boyd S, Vandenberghe L (2010) Convex optimization, vol 25. Cambridge University Press, Cambridge

Castagna JP, Batzle ML, Eastwood RL (1985) Relationships between compressional-wave and shear-wave velocities in clastic silicate rocks. Geophysics 50(4):571–581

Cranganu C, Luchian H, Breaban ME (2015) Artificial intelligence approaches in petroleum geosciences. Springer International Publishing, Switzerland

Dietterich TG (2000) Ensemble methods in machine learning. International workshop on multiple classifier systems. Springer, Berlin

Draper NR, Smith H (2014) Applied regression analysis. Wiley, New York

Kaufman L, Rousseeuw PJ (2005) Finding groups in data: an introduction to cluster analysis. Wiley-Interscience 33(1):368

Lim JS, Kang JM (1997) Multivariate statistical analysis for automatic electrofacies determination from well log measurements. Soc Pet Eng 38028

Nemirovski A (1996) Interior point polynomial time methods in convex programming. Georgia Institute of Technology School of Industrial and Systems Engineering. https://www2.isye.gatech.edu/~nemirovs/Lect_IPM.pdf Accessed on 21 Mar 2019

Sandham WA, Leggett M (2003) Geophysical application of artificial neural networks and fuzzy logic. Ser: Mod Approaches Geophys 21

Serra O, Abbott HT (1982) The contribution of logging data to sedimentology and stratigraphy. Soc Petrol Eng J 22(1):117–131

Zemel RS, Toniann P (2001) A gradient-based boosting algorithm for regression problems. Advances in neural information processing systems, 13 (NIPS 2000) https://papers.nips.cc/paper/1797-a-gradient-based-boosting-algorithm-for-regression-problems Accessed on 21 Mar 2019

Chapter 13
Scaling Issues in Estimation of Pore Space Using Digital Rock Physics

Shruti Malik and Ravi Sharma

Abstract Core samples have always been a luxury for measuring reservoir properties. However, in most cases, the cores become non-usable after a single experiment. The methods such as Digital Rock Physics (DRP) based on image processing offer an alternative to model these reservoir properties with better control on subjective biases of the experimentation and are non-destructive in nature. DRP involves imaging the formation and simulating the field performance to account for various non-homogeneities in the reservoir formation. Over some time, now, it has become a popular method, but in case of complex reservoirs such as carbonates and unconventional resources, it is still at the feasibility stage only. The reasons are plenty ranging from availability of calibration libraries and transition space error and its quantification. In this paper, we used DRP to obtain porosity in carbonate samples at various scales and compared the results obtained using established laboratory methods which at the moment serves as ground truth for reservoir characterization challenges. We found that DRP results mostly align with the results obtained using methods like QEMSCAN. The analysis mostly points to the resolution limit input to the respective techniques.

Keywords Digital rock physics · Porosity · Segmentation · Optimization

1 Introduction

Carbonate reservoirs account for most of the world's oil and gas reserves and thus are likely to dominate the hydrocarbon production through the next century (Akbar et al. 1995). The extremity of carbonate reservoirs is such that these can be extremely large while having pores which are microscopic in nature. This makes the characterization of these heterogeneous reservoirs very complex and important (Akbar et al. 2000; Sharma 2015).

In DRP, 3D pore volume is a favourite output involving FIBSEM for deconstruction and COMSOL for meshing and simulation (Brown 2011). As a result of

S. Malik (✉) · R. Sharma
Department of Earth Sciences, Indian Institute of Technology Roorkee, Roorkee, India
e-mail: smalik@es.iitr.ac.in

K. H. Singh and R. M. Joshi (eds.), *Petro-physics and Rock Physics of Carbonate Reservoirs*, https://doi.org/10.1007/978-981-13-1211-3_13

flow simulation, absolute permeability is another attribute that can be successfully obtained from this exercise. But, obtaining a 3D scanned volume of the sample is a costly method. So, 2D scanned images can be used to obtain a 3D volume of the sample by conditional reconstruction process (Karimpouli and Tahmasebi 2016) or empirical relations (Karimpouli et al. 2018). This reconstructed 3D volume is then used to determine the permeability of the sample. Dvorkin and Nur (2009) attempted the DRP processes on a heterogeneous Berea Sandstone sample and investigated the variation of properties on various scales by subdividing the digital volume into eight small cubes. A similar work with overlapping volume in carbonates was attempted by Saenger et al. (2016). Grader et al. (2010) compared the material property in carbonates in different facie types, such as granular and vuggy. DRP techniques have also been extended for elastic property estimation (Zhang et al. 2011). A Fontainebleau Sandstone sample was used, wherein the rock compressibility was replaced by the elastic parameter of the pore-filling material as suggested by Ciz and Shapiro (2007). DRP workflow on drill cuttings was discussed in detail by Dvorkin et al. (2003). The work considered three shale cuttings photographed using thin sections and scanning electron microscope (SEM) to resolve the pore space. Kalam (2012) compared the special core analysis (SCAL) tests with the DRP measurements for the case of complex carbonates obtained from Middle East reservoirs.

As evident from the literature review, DRP has been successfully attempted in various forms for physical property estimation, but specific work addressing the optimization of algorithm to address scaling issue is still missing. The objective of this work was to highlight the issues of scales and resolution across homogenous to heterogeneous carbonate facies. We used micro-CT images of the two carbonate samples that had same mineralogy but were distinctly different in fabric morphology. The porosities were determined and compared with the respective values from conventional methods, and the limitations were deliberated upon.

2 Method

In order to characterize a reservoir and thereby determine the petrophysical parameters, various conventional methods are used. Conventionally, there are two ways of measurement, i.e. laboratory method based on Archimedes principle and steady-state CMS-300 method (core measurement system) based on Boyle's law. In both these methods, the porosity of the whole core sample, which was of the size 2–4 in., was determined. But with the advent of technology, we have been able to look at the rock at a much higher scale of resolution which helps us to better understand the pore network. This is specially required in the cases where rock structure is heterogeneous, such as carbonates.

Digital Rock Physics is a non-invasive and non-destructive method, wherein the core sample is at first scanned and then a binary image of the rock (separating pore space from the mineral matrix) is constructed through a process called segmentation. Different procedures are applied on the segmented image/volume to visualize

its internal structure (Andrae et al. 2013) and simulate the physical properties thereof. However, the approach of "image and compute" relies largely on the chosen magnification of image acquisition. Image processing is then performed to correct the image for noise if any by applying filters, and then, segmentation is done for segregating different volumes of energy intensity and identifying them as possible mineral and pore volumes. Segmentation can be performed using different algorithms depending upon the problem to be solved. Some of them are:

1. Thresholding method: In this step, a histogram is generated, which shows the pixel distribution in the image and a threshold value for segmenting the pores and grains is decided such that the pixel value more than threshold value is given value 1 (i.e. white indicating grains) and pixel value less than threshold value is given value 0 (i.e. black indicating pore space) (Kalam 2012). The thresholding can be global; i.e., a single value is used for the entire image or variable; i.e., the threshold value varies over the image.
2. Morphological method: In this, the image is segmented on the basis of the shape of the white patches on black background. This also includes the watershed segmentation which is performed to extract the boundaries in an image (Gonzalez and Woods 2008).

The segmentation process plays a very important role in determining the petrophysical properties accurately, as the results obtained from this are used as an input to the simulation step. In the end, physical processes are simulated computationally to calculate the effective porosity, permeability, elastic properties, etc. (Andrae et al. 2013).

In this paper, in the first step, we have worked on the SEM images of different resolutions, such as 1 mm, 1, 5, 20, 100 and 500 μm. Also, we have used the sliced images obtained from micro-CT scan of the same carbonate sample. Then, we have used MATLAB code to perform segmentation based on thresholding method on these carbonate data and then determined the porosity of each SEM image, the bulk porosity of the sliced images, i.e. combining all the slices to give a single porosity and also the porosity from the sections combining 50 slices each.

In the second step, the porosities obtained in the previous step were then compared with the conventional methods. In doing so, we determined the factors or issues that could be responsible for or reason behind the difference in the porosity values, if any.

The entire procedure was applied to two carbonate samples ($S1$ and $S2$) with same mineralogy, i.e. comprising of around 98% volume of calcite with distinct morphology and thus porosity measured from laboratory. The $S1$ has a lower porosity, while $S2$ has a higher porosity.

Workflow Adopted

1. Load the image file and define the number of slices to be segmented.
2. Convert the image to an 8-bit greyscale format (suited for SEM images).

3. Perform segmentation by manually setting a threshold, decided from the histogram of the image (the threshold set should be able to detect all the pores present in the images).
4. Create an iterative loop such that all the image slices are processed.
5. Using another iterative loop, calculate the total porosity from the equation given by:

$$\text{Porosity} = (\text{Area of pores}) * 100/(\text{total area of the image}) \quad (1)$$

3 Result

We had the porosity values of the entire core obtained from the conventional methods.

1. Laboratory measurements gave the porosity value of 18% for $S1$ and 23% for $S2$.
2. CMS measurement gave the porosity value of 17% for $S1$ and 23.5% for $S2$.
3. QEMSCAN measurement gave the porosity value of 6.27% for $S1$ and 22.8% for $S2$.

The segmentation process performed on these SEM images (shown in Figs. 1, 2, 3, 4, 5 and 6) and sliced micro-CT scanned images [shown in Fig. 7 (i) and (ii)] of the two carbonate samples ($S1$ and $S2$), respectively, using the MATLAB algorithm resulted in the porosity values, shown in Table 1.

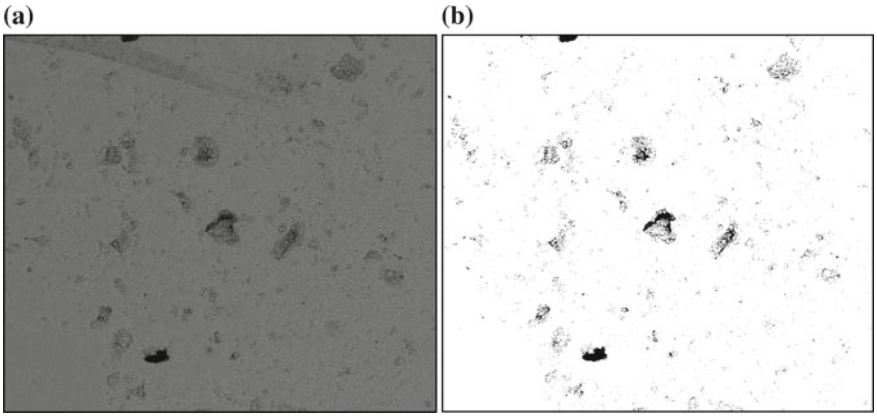

Fig. 1 SEM images for $S1$ carbonate sample, **a** at 1-mm resolutions, **b** segmented image, where black represents pore spaces and white portion represents solid matrix

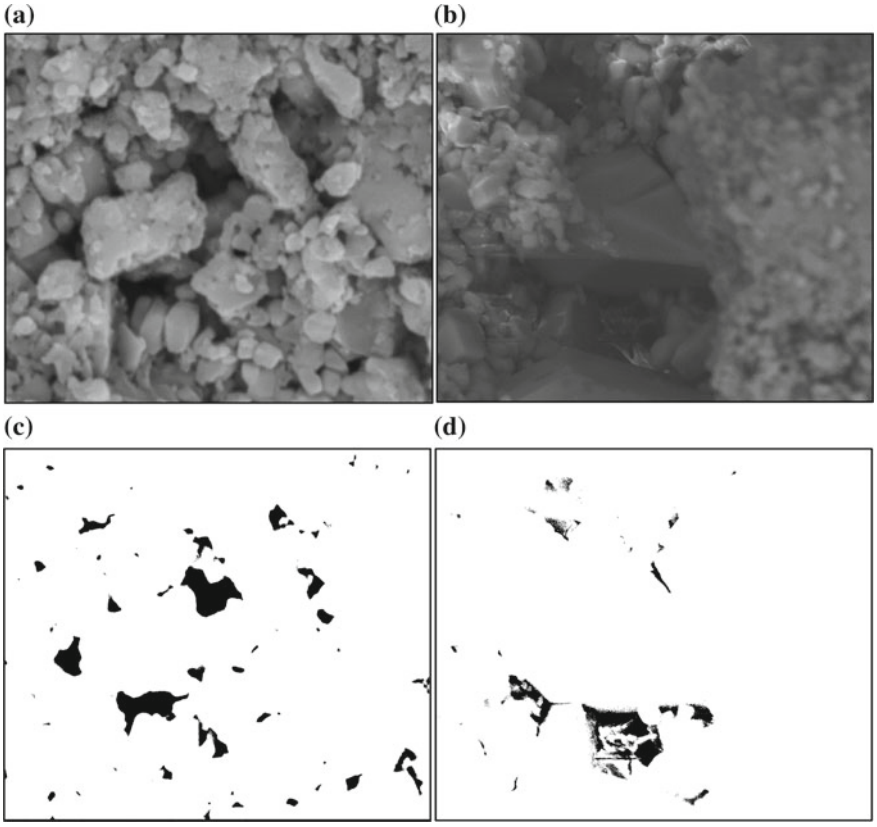

Fig. 2 SEM images of different resolutions: **a** 5 μm, **b** 20 μm, with segmented images **c** and **d** for *S*1 carbonate sample

4 Discussion

In this paper, for *S*1, it was found that the bulk porosity obtained from the sliced micro-CT images resulted in the porosity of 6.30%, the porosity obtained from sections containing 50 micro-CT slices each resulted in an average porosity of 6.1%, whereas individual SEM images of different resolutions resulted in an average porosity of 7.8%. So, the calculated porosity lies in the range 6–8%.

This calculated porosity is comparable to the QEMSCAN porosity because the micro-CT images are of the order of 25 μm, whereas QEMSCAN is of the order of 2–10 μm. So, QEMSCAN scans the images at a very high resolution and thus helps in quantifying the porosity which is smaller than the resolution of the traditional methods, i.e. the microporosity. Since the scales of these two measurements are almost similar, they resulted in comparable porosities.

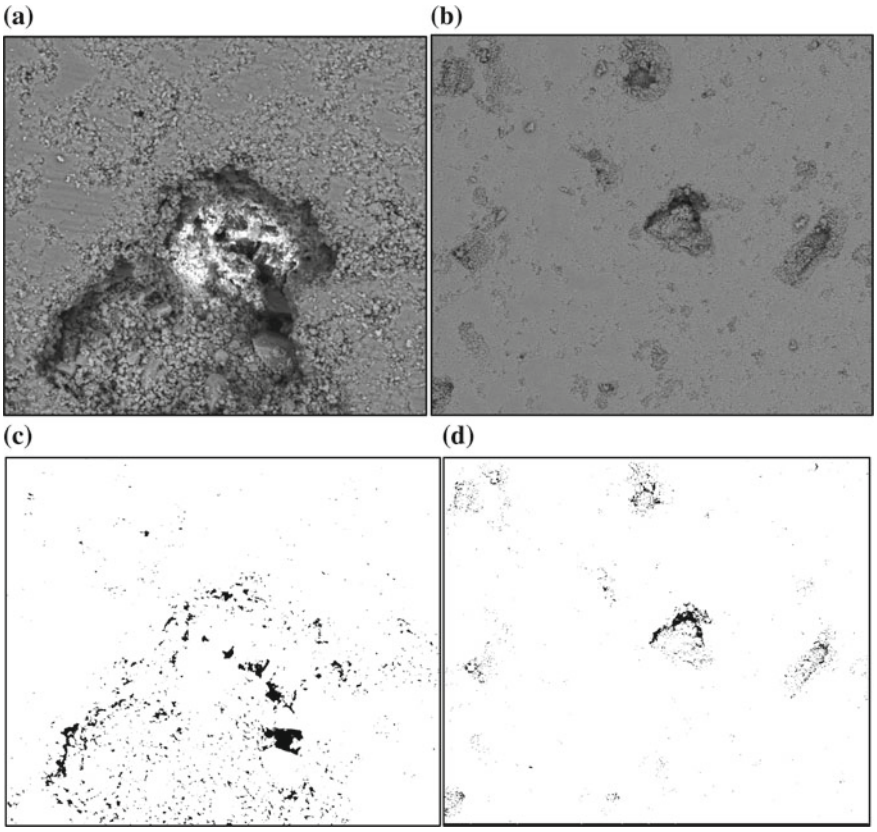

Fig. 3 SEM images of different resolutions for *S*1 carbonate sample, **a** 100 μm, **b** 500 μm, with segmented images **c** and **d**, respectively

For *S*2, though the laboratory, CMS and QEMSCAN measurements resulted in a higher porosity, they are almost comparable to the DRP results, i.e. around 20–22% porous.

It is found that in the cases where porosity is either high or too low, the results are almost comparable. This is because in case porosity is high, it becomes easier to identify the darker region and classify it as pore space, while in case of low porosity, it becomes easier to identify the white region and classify it as grains. On the contrary, in case of intermediate porosity, the image has both pores and grains in good proportion, thus making it difficult to identify any one class distinctly.

Apart from the two basic classes, i.e. pores and grains present in an image, there is another class, termed as pore mineral transition (PMT) zone. It comprises the region present in between what we call as confidently in pore space (ϕ) and confidently in grains. So, the total porosity is given by ϕ + PMT value.

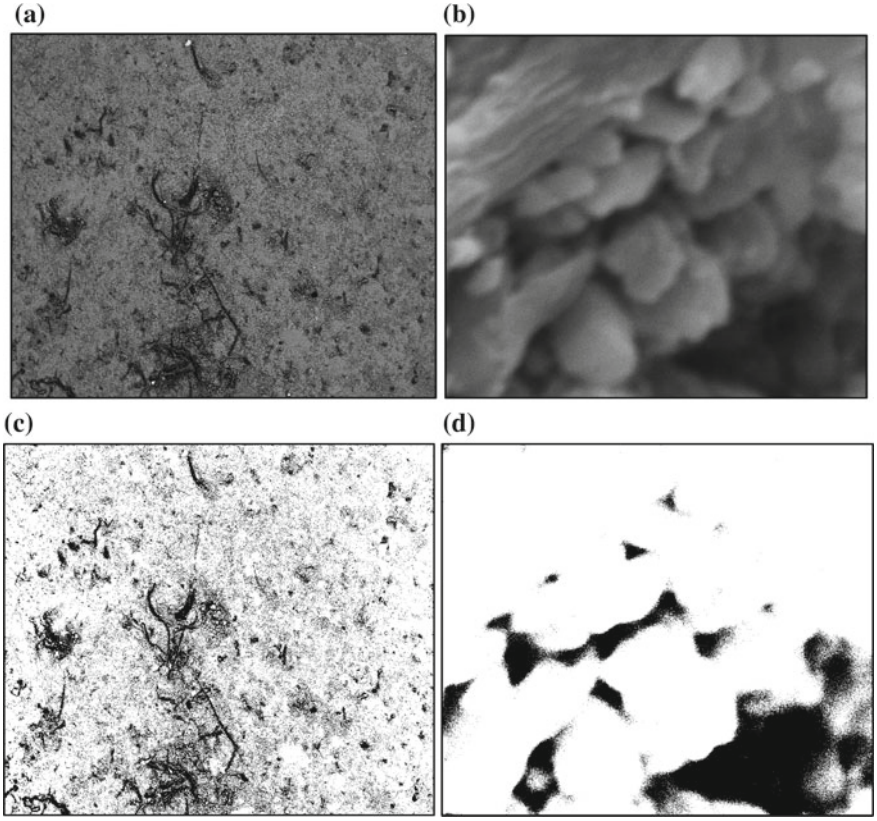

Fig. 4 SEM images at **a** 1-mm and **b** 5-μm resolutions with segmented images **c** and **d**, respectively, for *S*2 carbonate sample, where black represents pore spaces and white portion represents solid matrix

The CMS and laboratory measurements always result in a higher porosity than QEMSCAN, indicating that some porosity is being considered in the PMT values (Jobe 2013).

The laboratory and CMS measurements resulted in porosity higher than the calculated porosity, specifically for *S*1. This could be due to many reasons as follows:

The laboratory measurements consider the entire core and are carried out at a lower resolution and thus have larger field of view, whereas in DRP the measurements are done at higher resolution, and it looks at the core at micro- or nanoscale. So, in DRP, a lot of space is not sampled which the laboratory measurements are able to do. Another reason could be the pore mineral transition zone not being identified clearly.

In order to overcome this problem, there is a need to optimize a scale at which the simulated results can be compared to the field scale values. One way to optimize

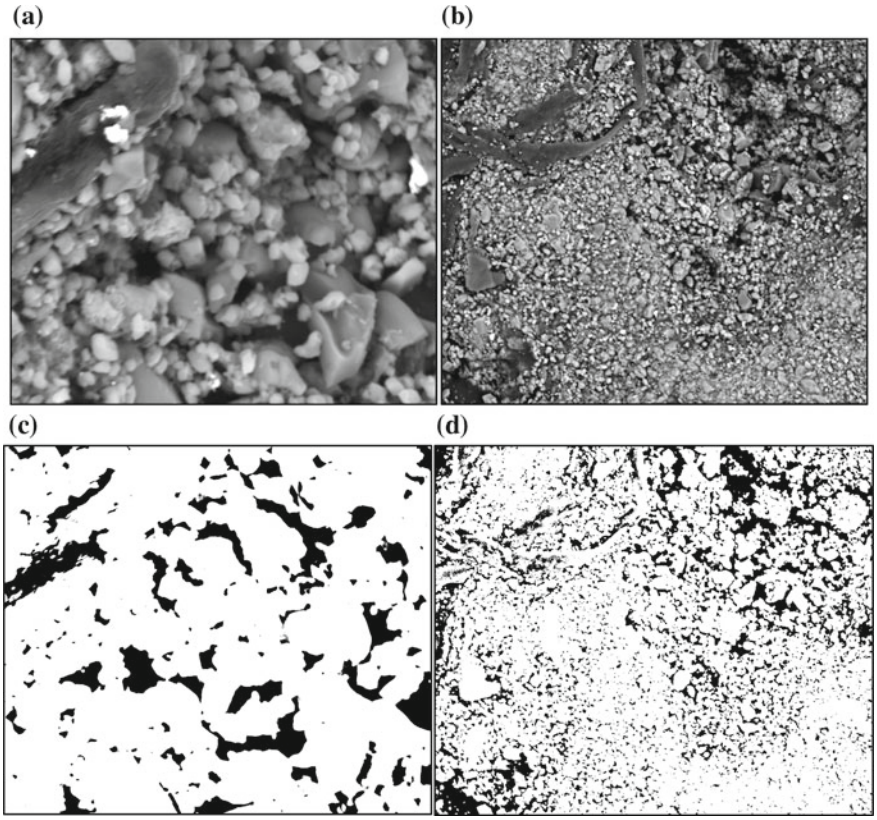

Fig. 5 SEM images at **a** 20-μm and **b** 100-μm resolutions with segmented images **c** and **d**, respectively, for *S*2 carbonate sample

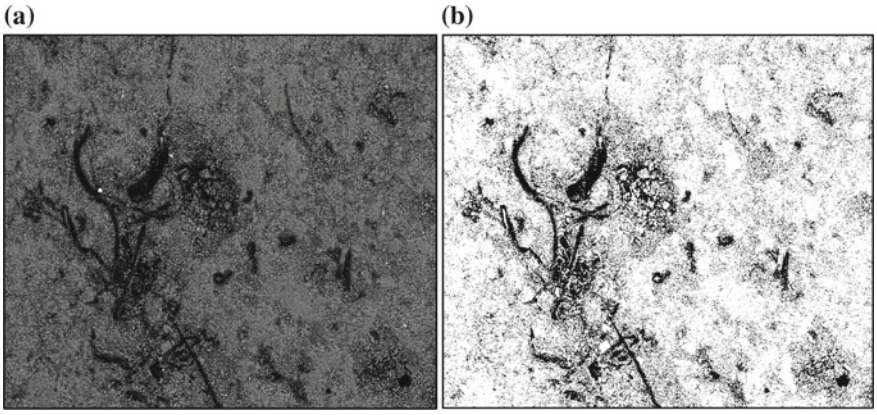

Fig. 6 SEM images **a** at 500-μm resolutions **b** segmented images for *S*2 carbonate sample

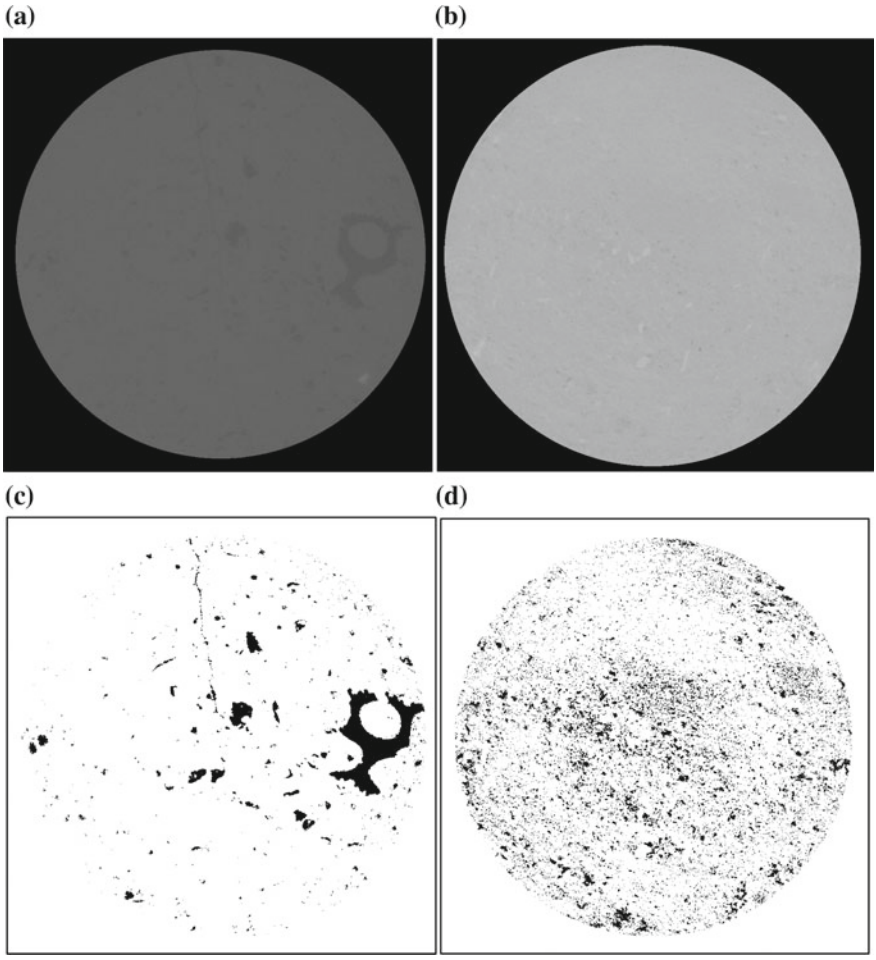

Fig. 7 Slice of scanned micro-CT image **a** and **b** along with its segmented view for: **c** *S*1 and **d** *S*2 carbonate samples

is by capturing enough 2D images of the sample and at different angles, in order to have the information of the sample on unseen sides also.

Radon transform can also be performed. It is an integral transform that is used for analysing the image using its projections. So, a 3D sample is transformed into multiple 2D views at different angles. This helps in analysing how a pore in 3D looks like in its 2D projection. Its inverse can be used to reconstruct the 3D image of the sample from the 2D projections obtained from CT scans of the sample (Sobani et al. 2015). So, in order to identify the pore mineral transition zone which could be one of the reasons responsible for the difference, the Radon transform of the sample can be done.

Table 1 Porosity values obtained for both SEM images with different resolutions and micro-CT images for the two carbonate samples (*S*1 and *S*2)

S. no.	Image type	Resolution	Calculated porosity (%)	
			*S*1	*S*2
1	SEM	1 mm	6.97	21.00
		5 μm	9.80	19.00
		20 μm	7.87	17.00
		100 μm	8.30	20.20
		500 μm	6.43	20.60
2	Micro-CT (Bulk)		6.30	20.10
3	Micro-CT slices			
	1–50		6.2	19.00
	51–100		7.5	18.50
	101–150		5.5	19.80
	151–200		5.7	21.50
	201–250		5.6	21.60
	251–300		5.4	20.50
	301–350		5.5	
	351–400		7.5	

5 Conclusion

This paper signifies the efficacy of digital image processing in determining imperative reservoir property, viz. porosity through various methods of segmentation. In this paper, we have addressed the scaling issues that one encounters when comparing the results obtained from Digital Rock Physics method with the conventional methods. Thus, to overcome the issues, we need to perform optimization of the algorithm which could be done by capturing enough images and at different angles. Also, Radon transform could be one of the potential methods in identifying the transition zone between pores and grains which would be very helpful in determining the accurate porosity values.

Thus, with the existing DRP resources and further customization of the programs, an algorithm can be used for pushing the DRP as a standard tool in reservoir exploitation programs.

Acknowledgements We acknowledge Dr. Kuldeep Chaudhary, Assistant Professor, Department of Geology, Kent State University, Ohio, USA, for his personal communications and discussion in shaping up this work.
We also acknowledge Dr. Mayur Pal, Team Lead EOR, Reservoir and Geosciences, North Oil Company, Doha, Qatar, for his help with data and constant encouragement in pursuing this work.
We acknowledge the support and encouragement from our colleagues in the Petrophysics and Rock Physics (PP&RP) research group at IIT Roorkee.

References

Akbar M, Petricola M, Watfa M, Badri M, Charara M, Boyd A (1995) Classic interpretation problems: evaluating carbonates. Oilfield Rev 7:38–57

Akbar M, Vissapragada B, Alghamdi AH, Allen D, Herron M, Carnegie A, Dutta D, Olesen JR, Chourasiya RD, Logan D, Stief D, Netherwood R, Russel SD, Saxena K (2000) A snapshot of carbonate reservoir evaluation. Oilfield Rev, Winter 2000/2001, 20–41

Andrae H, Combaret N, Dvorkin J, Glatt E, Han J, Kabel M, Keehm Y, Krzikalla F, Lee M, Madonna C, Marsh M, Mukerji T, Saenger EH, Sain R, Saxena N, Ricker S, Wiegmann A, Zhan X (2013) Digital rock physics benchmarks—part I: imaging and segmentation. Comput Geosci 50:25–32

Brown E (2011) Analysis and simulation of rock properties. Poromechanics investigation at pore-scale using digital rock, pp 58–59

Ciz R, Shapiro SA (2007) Generalization of Gassmann equations for porous media saturated with a solid material. Geophysics 72:A75–A79

Dvorkin J, Nur A (2009) Scale of experiment and rock physics trend. Lead Edge 28(1):110–115

Dvorkin J, Walls J, Tutuncu A, Prasad M, Nur A, Mese A (2003) Rock property determination using digital rock physics. SEG technical program expanded abstracts, 1660–1663 https://doi.org/10.1190/1.1817624

Gonzalez RC, Woods RE (2008) Digital image processing, 3rd edn. Pearson Education Inc., New Jearsey

Grader A, Nur A, Baldwin C, Diaz E, Li G (2010) Multi-scale imaging process for computations of porosity and permeability on carbonate rocks. Search and discovery article#40581. http://www.searchanddiscovery.com/pdfz/documents/2010/40581grader/ndx_grader.pdf.html. Accessed 21 Mar 2019

Jobe TD (2013) Sedimentology, chemostratigraphy and quantitative pore architecture in microporous carbonates: examples from a giant oil field offshore Abu Dhabi, UAE. Colorado School of Mines, ProQuest Dissertations Publishing, Ann Arbor

Kalam MZ (2012) Digital rock physics for fast and accurate special core analysis in carbonates. In: Gomes JS (ed) New technologies in the oil and gas industry, 201–226

Karimpouli S, Tahmasebi P (2016) Conditional reconstruction: an alternative strategy in digital rock physics. Geophysics 81:D465–D467

Karimpouli S, Khoshlesan S, Saenger EH, Koochi HH (2018) Application of alternative digital rock physics methods in a real case study: a challenge between clean and cemented samples. Geophys Prospect 66(4):767–783

Saenger EH, Vialle S, Lebedev M, Uribe D, Osorno M, Duda M, Steeb H (2016) Digital carbonate rock physics. solid. Earth 7:1185–1197

Sobani SS, Mahmood NH, Zakaria NA, Ariffin I (2015) 3D model reconstruction from multi-views of 2D images using radon transform. Jurnal Teknologi (Sci Eng) 74(6):21–26

Sharma R (2015) Impact of heterogeneity and saturation on elastic and viscoelastic properties in carbonates. Ph.D. thesis, Colorado School of Mines

Zhang S, Saxena N, Barthelemy P, Marsh M, Mavko G, Mukerji T (2011) Poromechanics investigation at pore-scale using digital rock physics laboratory. https://www.comsol.com/paper/download/83977/zhang_paper.pdf. Accessed 21 Mar 2019

Part IV
Seismic Reservoir Characterization, Latest Trends and Solutions

Chapter 14
Advanced Seismic Reservoir Characterization of Carbonate Reservoirs: A Case Study

K. Vasudevan

Abstract Successful exploration for and effective exploitation of hydrocarbons from carbonate reservoirs necessitate accurate prediction of porosity pods and fluid distribution within an intricate maze of porosity permeability corridors. Conventional qualitative interpretation of G&G data to bring out gross depositional models and facies distribution maps do not provide adequate control in effective appraisal and exploitation of these discrete reservoirs. Often, such simplistic reservoir models lead to wrong well placement and inefficient appraisal and development plans. Quantitative interpretation of the seismic and well data, integrating a myriad of G&G data for reservoir characterization, is required to mitigate the risk and exploit the carbonate reservoirs in a cost-effective manner. A robust workflow for seismic-based reservoir characterization to elucidate the complexities in carbonate reservoirs involves high-frequency cycles mapping integrating well and seismic data with sediment logical data and image logs. This framework is subsequently calibrated with seismic attributes and *P*-impedance data to develop permeability, density and diagenetic models to bring out the cyclicity of porosity creation and destruction during deposition of multiple phases of carbonates corresponding to sea level oscillations. This improvised reservoir characterization workflow was adopted to evaluate the Eocene carbonate reservoirs of Bassein Formation in a field in Mumbai offshore basin, which will be discussed in detail. The study has explicitly established that Vadose zone diagenesis along the exposed geomorphic highs led to porosity generation. While the porosity in Upper Bassein has been largely preserved, it has been completely obliterated in Middle Bassein and is patchy in Lower Bassein. After integrating heterogeneity from nano- to seismic scale, a static model was developed which led to identification of upside potential beyond the established reservoir limits and infill development locations within the field area.

Keywords Seismic reservoir characterization · Bassein formation · Seismic attributes · Diagenesis

K. Vasudevan (✉)
GEOPIC, ONGC, KDMIPE Campus, Kaulagarh Road, Dehradun, India
e-mail: vasudevan_k@ongc.co.in

K. H. Singh and R. M. Joshi (eds.), *Petro-physics and Rock Physics of Carbonate Reservoirs*, https://doi.org/10.1007/978-981-13-1211-3_14

1 Introduction

Carbonate reservoirs, owing to their depositional and diagenetic diversity, are the most complex and challenging candidates to quantitatively characterize the spatiotemporal distribution. Successful exploration for and effective exploitation of hydrocarbons from carbonate reservoirs necessitate accurate prediction of porosity pods and the fluid distribution within an intricate maze of porosity permeability corridors. Conventional qualitative interpretation of G&G data to bring out gross depositional models and facies distribution maps do not provide adequate control in effective appraisal and exploitation of these discrete reservoirs. Often, such simplistic reservoir models lead to wrong well placement and inefficient appraisal and development plans. Quantitative interpretation of the seismic and well data, integrating a myriad of G&G data for reservoir characterization, is required to mitigate the risk and exploit the carbonate reservoirs in a cost-effective manner.

In this paper, the author has presented an advanced reservoir characterization workflow for carbonate reservoirs through a case study of an oilfield, WO-16, in Western Offshore Basin, India. The field is located south-east of the giant Mumbai high oilfield and is bearing hydrocarbon in two distinct layers within the Middle-to-Late Eocene carbonate reservoirs. The exploitation of these reservoirs posed several challenges in terms of identifying the spatial extent of sweet zones as well as predicting their thickness and flow characteristics. In order to optimize the number of development wells, it was essential to assess these aspects quantitatively since they contributed to well deliverability. An advanced reservoir characterization approach was adopted integrating all the available geoscientific data including 3D seismic, 20 exploratory wells, core, FMI logs, bio-stratigraphic and petrographic data.

A high-resolution sequence stratigraphic framework was developed by mapping high-frequency cycles in logs and integrating them with core data, and these high-frequency cycles were tied with seismic to map the sequences. This high-frequency sequence model was used as an input for quantitative reservoir characterization.

Quantitative reservoir characterization is the 3D digital representation of the geology through replicating the structural disposition of the reservoir, reservoir architecture/facies distribution and petrophysical properties. It involves the analysis of geological, petrophysical and seismic data through processes like integration, reduction and quantification, thereby leading to the understanding of inter-well heterogeneity. It results in an improved geologic understanding and provides a means for integrating G&G and engineering data. This model is prepared primarily to capture the spatiotemporal facies variation as well as fluid distribution and volumetric estimation.

It involves eight main steps: (1) stratigraphic modelling, (2) structural modelling, (3) property modelling, (4) porosity modelling, (5) permeability modelling, (6) density modelling, (7) saturation modelling and (8) volumetric estimation.

The standardized workflow for quantitative reservoir characterization is placed in Fig. 1.

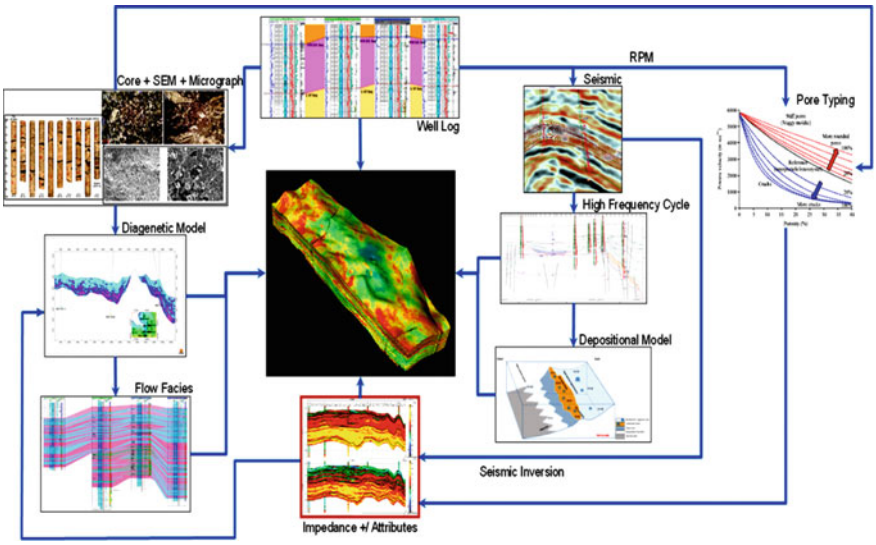

Fig. 1 Standardized workflow for carbonate reservoir characterization

2 Structural Modelling

Structural modelling involves defining the structural disposition of reservoir units. It consists of horizons/surfaces bounding the reservoir intervals, faults and inter-relationship between surfaces and faults. The aim of fault modelling is to build a consistent fault model, in which the generated fault surfaces are consistent with horizons and wells and fault lines representing the footwall and hanging wall cut-offs between the horizons and the fault surfaces. The structural model forms an input for the grid model. Structural modelling involves processes such as defining model boundary (area of interest, modelled area around 280 km^2), fault modelling and horizon modelling.

Twenty-two faults and four seismically mapped horizons, i.e. top of Early Oligocene, top of Late Eocene, top of early Eocene and top of Basement—already interpreted in CRAM-PSDM scaled back to time volume—have been used to prepare the structural framework of the area. Grid boundary polygon was selected considering the area of Middle-to-Late Eocene Bassein Formation and the extent of bounding faults. In this study, pillar-based fault modelling was carried out. Based on the analysis of pressure-production data and of initial testing data of exploratory wells, the modelled area has been divided into 16 segments (Fig. 2).

The grid is the cellular framework in which all other geological/property modelling is carried out. For the creation of grid, the final horizon and the fault model is the input. In order to perform modelling, the volume represented by the stratigraphic framework is divided into small cells. The cells constitute the 3D grid where each cell is assigned attributes during property modelling. Structural model is the input

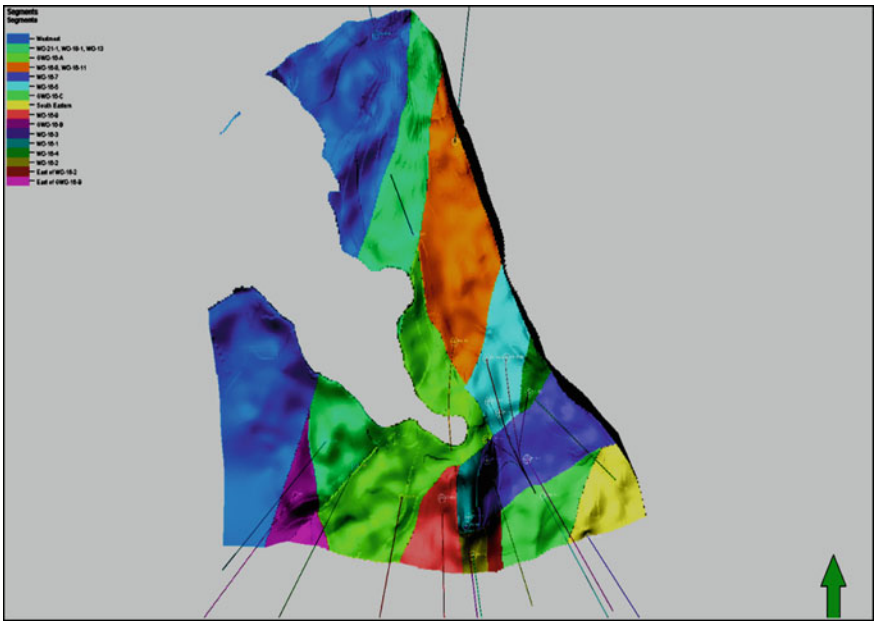

Fig. 2 16 modelled segments in WO-16 field

for grid construction. Regularized grid is preferred and the cell angles are kept as orthogonal as possible, because it is ideal for flow simulations.

3 Stratigraphic Modelling

Stratigraphic modelling defines a scheme using well data which forms the basis for well-to-well correlations. Typically, the data used in this phase of model building is the well log sets along with the core data. Tying the well data with the seismic data is necessary to establish the stratigraphic framework. Well-to-well correlation is done to describe the stratigraphic horizons representing the main boundaries of the geological sequences within the formations. This step is of immense importance for the overall correctness of the model as the reservoir's internal geometry is influenced by the presence of the fluid flow. Since geologic processes lead to the layering of geological bodies in 3D space and it is the stratigraphic framework of the model which constrains the data in 3D, it is therefore the most vital element for the derivation of an accurate reservoir model in 3D. Thus, the derived 3D reservoir model is dependent on the accuracy of the stratigraphic framework used to construct the same. Concepts of sequence stratigraphy were used to establish the stratigraphic framework of the area. Middle-to-Late Eocene Bassein Formation is divided into three units: Upper Bassein, Middle Bassein and Lower Bassein formations (Figs. 3 and 4). Upper Bassein, in

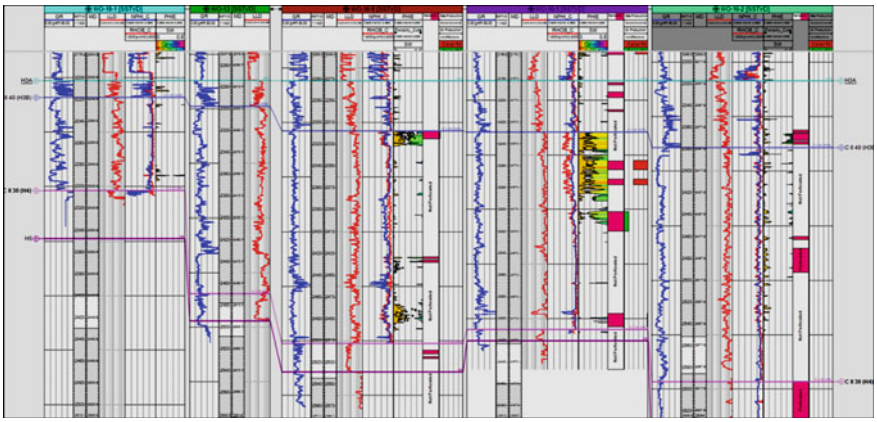

Fig. 3 Well sections showing third-order sequence stratigraphic surfaces

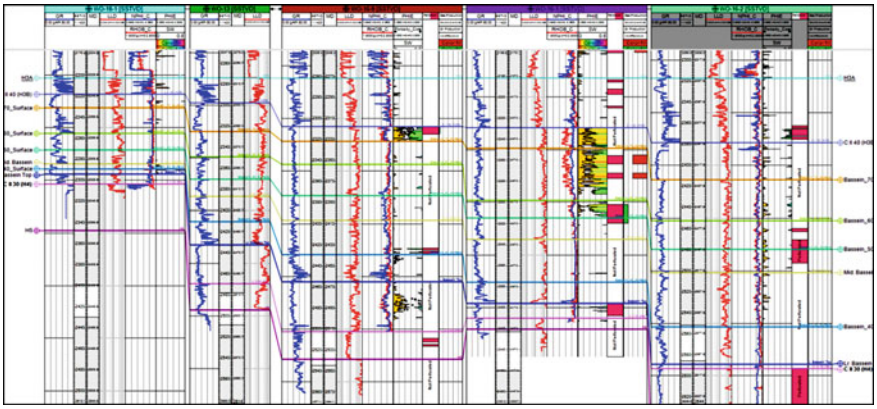

Fig. 4 Well sections showing higher-order sequence stratigraphic surfaces

turn, is divided into four sections, viz. H3B to Bassein-70, Bassein-70 to Bassein-60, Bassein-60 to Bassein-50 and Bassein-50 to Mid Bassein; Mid Bassein is divided into two parts—Mid Bassein to Bassein-40 and Bassein-40 to Lower Bassein. The Lower Bassein is kept as a single entity.

Horizon modelling was done using six seismically mapped surfaces along with higher-order surfaces like Bassein-70, Bassein-60, Bassein-50, Mid Bassein and Lower Bassein, within Bassein Formation using isochores. In the model, 9 stratigraphic zones have been defined which, in turn, have been divided into 98 proportional geological layers, keeping 50 cm as minimum thickness within the individual stratigraphic zone. This layering scheme was applied uniformly on all the zones.

4 Property Modelling

Geometrical Modelling

Geometrical modelling creates number of properties under suitable template. Under this category, bulk volume was created first to check if there was any negative cell in the model. The absence of negative cells infers that stratigraphic positioning of each cell was correct and consistent.

Petrophysical Modelling

For the population of petrophysical properties, porosity, permeability, density and saturation have been populated throughout the reservoir/model, based on the input data and knowledge of their trends and distributions, and the same was performed stochastically.

Porosity Modelling

Porosity model was conditioned to seismic data using collocated co-krigging, since *P*-impedance shows linear and inverse relationship with effective porosity (PHIE) in clean limestone (Fig. 5).

Gaussian Random Function Simulation (GRFS) using collocated co-krigging was performed taking *P*-impedance as the secondary variable. For the propagation of effective porosity, initially the probability density function (PDF) observed in the well logs (Fig. 6) was given priority. Effective porosity volume generated through this process yielded somewhat pessimistic scenario. Average effective porosity maps generated for the upper Bassein reservoir section, which is prolific producer throughout the field, show abundance of tight patch, and it became difficult to explain the production behaviour of a few development wells. The reason was the scattered presence of wells compared to the overall area of the field and PDF of effective porosity of logs at well level is more representative of vertical distribution of effective porosity in the well. In the next stage, the propagation of effective porosity in the model is biased with the PDF of *P*-impedance (Fig. 6) since *P*-impedance represents inter-well space more aptly than the scattered wells.

Permeability Modelling

A porous media is considered as a bundle of tortuous capillary tubes. The expression for k, rock permeability can be estimated by combining Darcy's Law and Poiseuille's law for flow in tubes.

$$k = \phi_e {r_0}^2 / 8\,\tau^2 \tag{1}$$

where r_0 is the pore throat radius, τ is tortuosity, and ϕ_e is effective porosity. For straight capillaries, $\tau = 1$ and the equation for permeability becomes

$$k = \phi_e {r_0}^2 / 8 \tag{2}$$

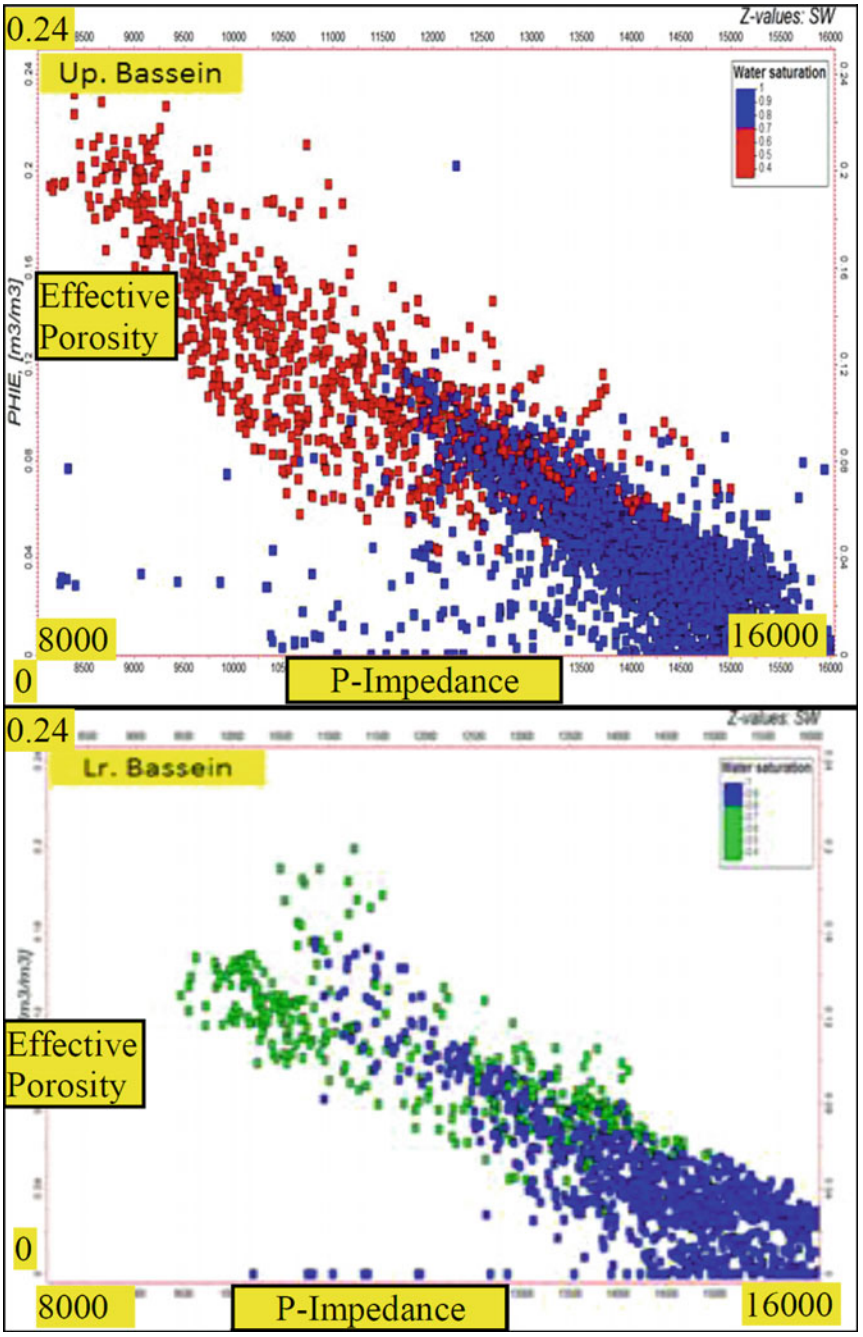

Fig. 5 Effective porosity versus *P*-impedance relationship

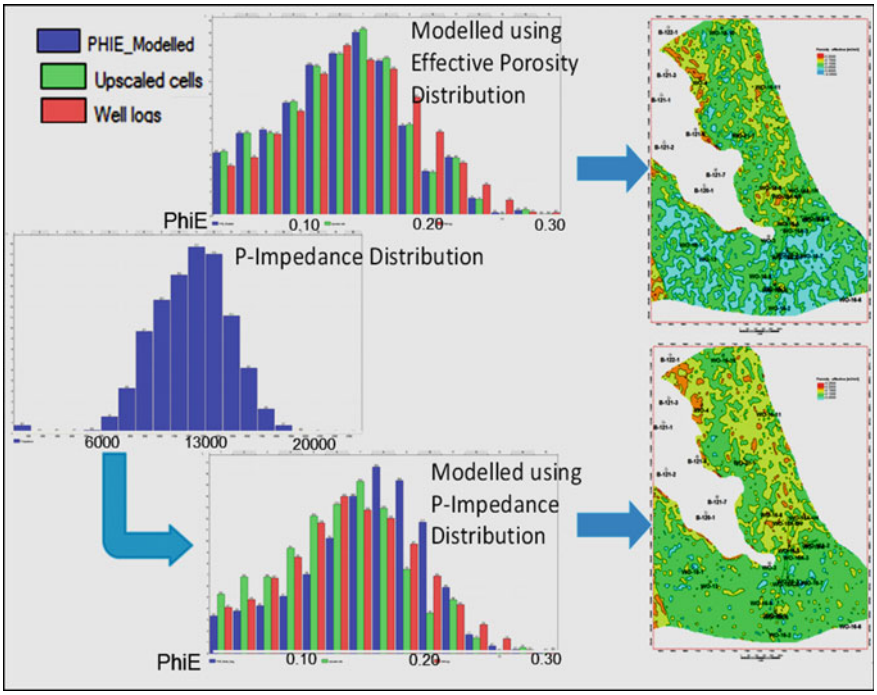

Fig. 6 Porosity model building

The above equation is a very simple but an important relationship because it shows that a major factor influencing permeability is the pore throat radius. Pore throat radius is a geological-cum-petrophysical character and can be related to depositional and diagenetic events that the rock has undergone. For realistic cases of a porous medium where pore geometry is not straight, Kozeny (1927) and later Carman (1937) introduced the concept of tortuosity, mean pore radius $r_{0\mathrm{mn}}$, surface area per unit grain volume $\mathrm{Sg_v}$ and shape factor F_s. They presented a more generalized equation now named globally as Kozeny–Carman equation:

$$k = [\phi_\mathrm{e}{}^3/(1-\phi_\mathrm{e})^2]/F_\mathrm{s}\,\tau^2\,\mathrm{Sg_v}{}^2 \tag{3}$$

where is F_s shape factor, τ is tortuosity, and $\mathrm{Sg_v}$ is surface area per unit grain volume. Mean pore radius $r_{0\mathrm{mn}}$ is defined as the ratio of cross-sectional area and wetted perimeter of the pore throat under consideration and is inversely related to surface area per unit grain volume. In the above equation, permeability (k) has the unit of $\mu\mathrm{m}^2$ and in $\mu\mathrm{m}^{-1}$. The term $F_\mathrm{s}\tau^2$ is termed as Kozeny constant, and it varies from formation to formation. The variation of Kozeny constant is the main limitation for universal application of this model. Entire term is a function of depositional condition, diagenetic alteration and mineralogical changes due to various geological reasons and varies with pore throat attributes. Hence, this term represents the geological

aspects of individual HUs. Determination and discrimination of group is the central theme of HU classification and can be described in field units (i.e. permeability in md) by altering last equation as

$$(k/\phi_e)^{1/2} = [\phi_e/(1-\phi_e)]/(\tau\ \mathrm{Sg_v}\sqrt{F_s}) \tag{4}$$

and introducing a parameter Reservoir Quality Index (RQI) defined as

$$\mathrm{RQI} = 0.0314(k/\phi_e)^{1/2} \tag{5}$$

where 0.0314 is the conversion factor from μm^2 to md. From above equation, flow zone indicator (FZI) and normalized porosity ϕ_z are defined as

$$\mathrm{FZI} = 1/(\tau\ \mathrm{Sg_v}\sqrt{F_s}) \tag{6}$$

and

$$\phi_z = \phi_e/(1-\phi_e) \tag{7}$$

Substituting all equations in the last equation, we get

$$\mathrm{RQI} = 0.0314\phi_z\ \mathrm{FZI} \tag{8}$$

Taking logarithm on both sides, we get

$$\ln \mathrm{RQI} = \ln \phi_z + \ln \mathrm{FZI} \tag{9}$$

Therefore, a plot of RQI versus FZI on a log–log space will yield straight line of unit slope and its intercept on RQI axis will be the FZI for the respective flow units. Permeability of the sample point is then recalculated for the pertinent HU using median FZI values and corresponding sample porosity.

The calculation of RQI and FZI values leads to the identification of HU which is based on the FZI values. Theoretically, there should be one single line and one single FZI value for each HU. However, if there exists a cloud instead of a line, then this will indicate existence of multiple HU groups. In such a case, the overall FZI distribution function is calculated by overlaying of the individual distribution function around their median FZI. This needs decomposition of overall FZI distribution into its constituting elements which is solved using histogram-based cluster analysis. At each pay level, RQI values were calculated for each plug data available. Following this, FZI values for each plug data were calculated. A plot of RQI versus FZI on a log–log scale has been generated (Fig. 7). The plot showed the presence of a cloud instead of a single line. In order to identify the optimum number of clusters (HU) from the cloud, a histogram of FZI values for each pay level has been generated.

The permeability estimation from the uncored intervals/wells forms the next important aspect of the part of an effective reservoir characterization activity. To

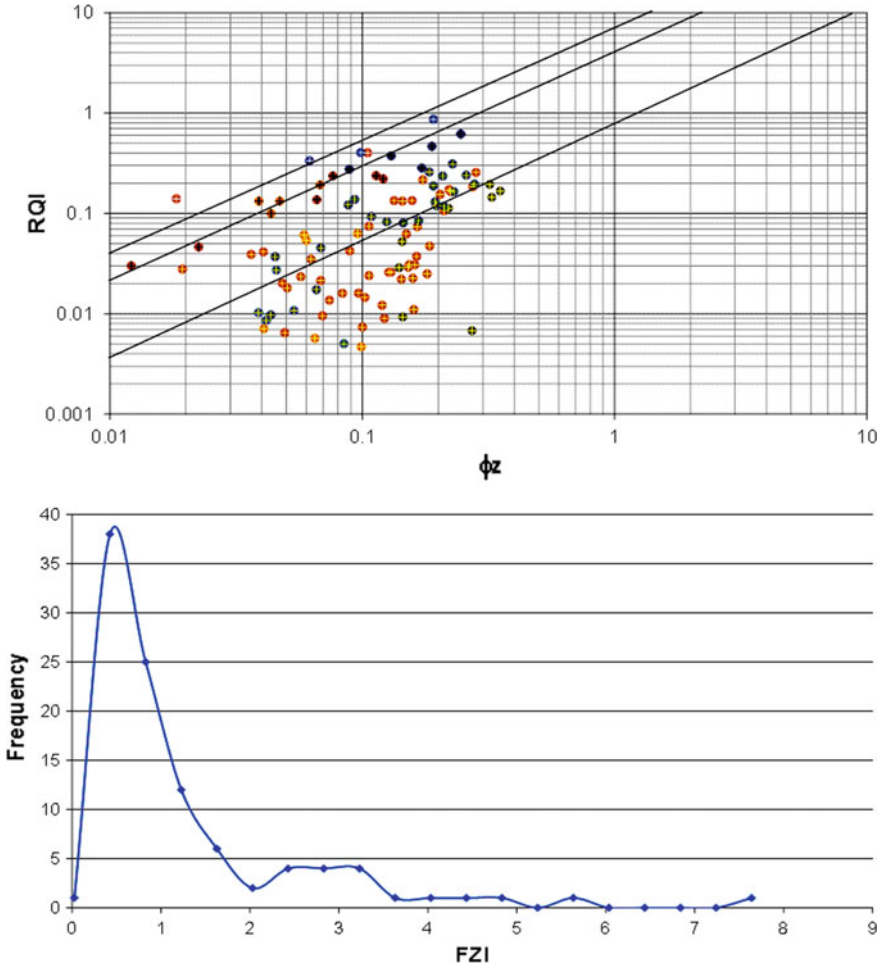

Fig. 7 Identification of flow zones

complete the analysis, HU units are predicted in the uncored sections/wells from the log data. Permeability profiles are then generated from the selected log data which are used as variables in a transform equation. Here, using a multi-attribute nonlinear regression analysis and a normal multi-attribute linear regression analysis and using a novel approach of alternating conditional expectancy (ACE) (Breiman and Friedman 1985), the results from the two have been computed and compared. Spearman's rho statistical technique is used on a set of environmentally corrected log tool responses related to DT, LLD, GR, RHOB, NPHI and were rank-correlated to FZI. Finally, for each pay level, the core-to-log permeability transform is employed through ACE algorithm for proliferating permeability in uncored section/wells.

For the population of permeability in the mode, the permeability data was conditioned to effective porosity model using collocated co-krigging. Gaussian Random Function Simulation (GRFS) using collocated co-krigging was performed taking effective porosity volume as the secondary variable. Model slices of logarithm of permeability for each zone are placed at Fig. 8. The slice corresponding to the Upper Bassein window shows higher permeability in the northern part of the field, whereas the slice corresponding to Lower Bassein indicates the permeability is patchy and sporadic throughout the field.

Density Modelling

Density modelling was carried out during the static model building to understand the spatio-temporal distribution of dolomitization and to infer the effect of diagenesis throughout the field. For the propagation of density in the static model, a process flow similar to effective porosity modelling has been performed. Density also has a linear relationship with *P*-Impedance. This would allow us to propagate density using collocated co-krigging taking *P*-impedance as the secondary variable. To understand the effect of dolomitization, a series of density simulations were carried out by changing the percentage volume of calcite–dolomite in the system with predefined porosity, water and gas saturation (Fig. 9).

It was found that in case of porosity of 5% effect of dolomites up to 40% volumetric proportion would lead to density of 2.68 gm/cc if the pores are completely filled with water. The same situation was repeated by taking gas-filled pores, and density was found to be 2.62 gm/cc. This process was repeated for porosity values 10, 15 and 20%, and the corresponding density values were noted. This exercise leads to restrict the

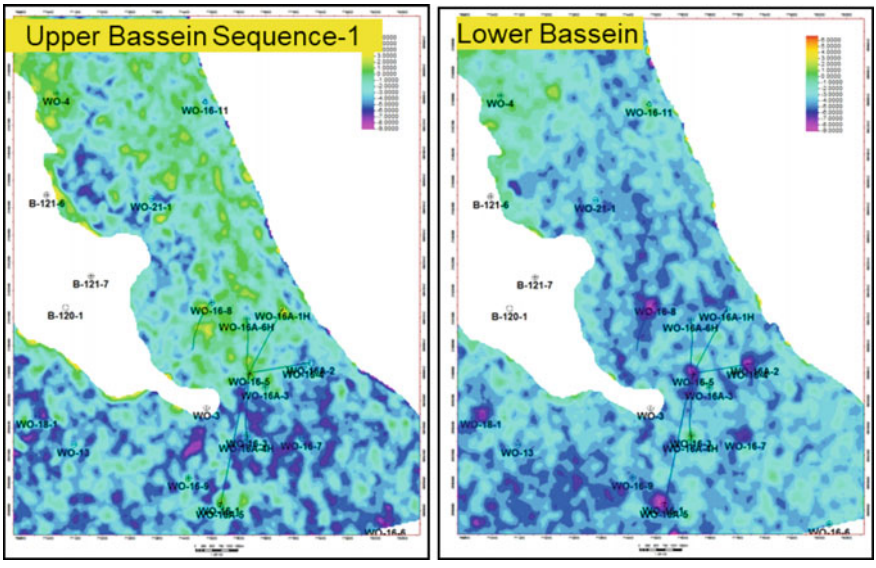

Fig. 8 Permeability model slices

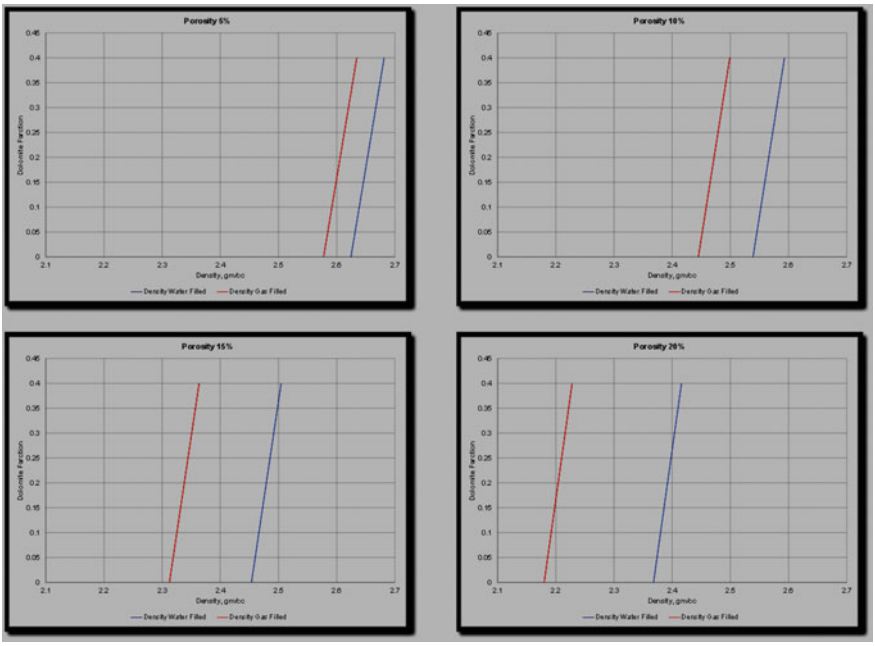

Fig. 9 Density simulation with varying calcite and dolomite percentage

upper density limit of calcite effect up to 2.68 gm/cc and lower limit being 2.4 gm/cc, considering 15% being the close to average porosity and that will be filled with gas. Applying this cut-off, calcite–dolomite model had been prepared. 3D perspective view of the calcite–dolomite distribution modelled through the density simulation approach at each level is shown in Fig. 10. It is evident that effect of dolomitization has increased Middle Bassein downward.

Incorporating this observation, a conceptual diagenetic model was prepared (Fig. 11) to capture the porosity evolution of Bassein Formation in WO-16 field. Vadose zone diagenesis along the exposed geomorphic highs led to porosity generation, while porosity destruction is attributed to diagenesis in phreatic zone along the low axis. During Palaeocene–early Eocene Panna clastics were deposited over basement making the country rock for the carbonate deposition. Rising sea level, scarcity of clastic input, and greenhouse climatic condition favoured the carbonate deposition and Lower Bassein Carbonate Formation was deposited over Panna Formation. Towards the Basement high, Lower Bassein Carbonate Formation lies nonconformably over Basement, ultimately forming wedge-out structure. After Lower Bassein Carbonate deposition, sea level dropped exposing part of the carbonate over the basement highs. These carbonates were exposed to weathering and underwent diagenesis in vadose and meteoric realm leading to karstification at the structural highs. Due to lowering of sea level, restricted marine environment would prevail in sags between two adjacent highs. In the restricted marine environment due to

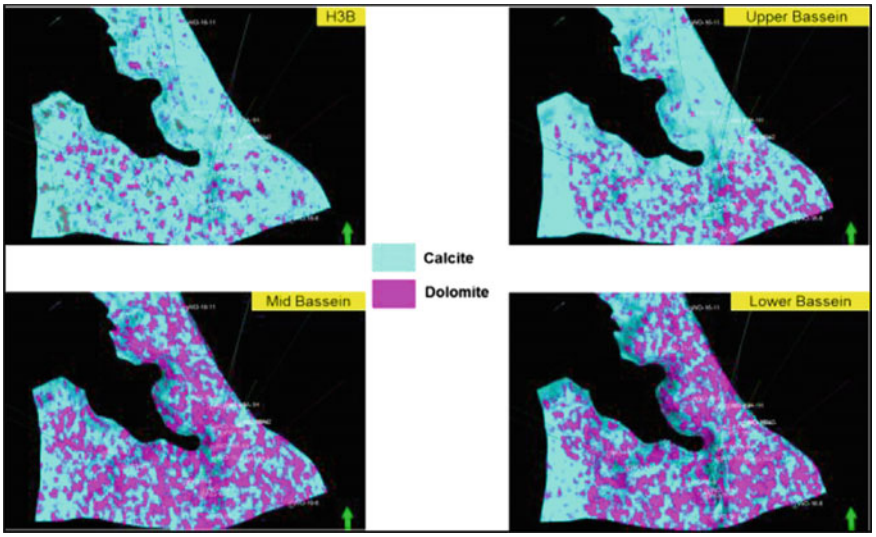

Fig. 10 Density slices showing modelled calcite and dolomite percentage

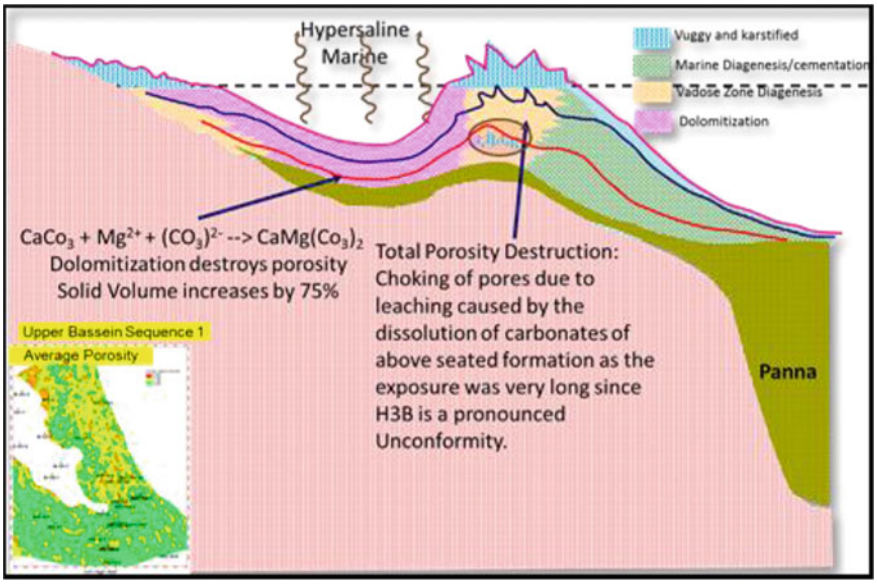

Fig. 11 Diagenetic model

evaporation, hyper-saline environment leads to dolomitization and destruction of porosity. Following this Middle and Lower Bassein Carbonate Formation deposited due to cyclic rise of sea level and lowering of sea level leads to karstification at the structurally higher places. Middle Bassein karstification due to lower exposure time partially filled up the already karstified pores of Lower Bassein Formation due to leaching. Pronounced unconformity at the Bassein top leads to very long exposure at the Upper Bassein time resulted in extensive karstification in Upper Bassein, whereas the percolating calcium-enriched water precipitated it below the vadose zone which completely filled up the pores of Middle Bassein karstified portion leading to destruction of porosity.

Integrated analysis of porosity, permeability, density and diagenetic models leads to identification of three exploratory prospects and infill development locations for the further exploitation of Bassein hydrocarbon.

5 Conclusions

- Successful exploration for and effective exploitation of hydrocarbons from carbonate reservoirs necessitate accurate prediction of porosity pods and the fluid distribution within these intricate maze of porosity permeability corridors.
- Conventional qualitative interpretation of G&G data to bring out gross depositional models and facies distribution maps do not provide adequate control in effective appraisal and exploitation of these discrete reservoirs. Quantitative interpretation of the seismic and well data, integrating a myriad of G&G data for reservoir characterization, is required to mitigate the risk and exploit the carbonate reservoirs in a cost-effective manner.
- Advanced reservoir characterization workflow adopted in this study involved preparation of a high-frequency sequence stratigraphy framework followed by structural model and property modelling including porosity, permeability and diagenetic models culminating in saturation model and volumetric estimation.
- Porosity modelling was carried out using the post-stack *P*-impedance volume that gave a very good inverse linear fit, as the secondary input which yielded a stable porosity volume.
- Permeability model was prepared by first analysing the core data for calculating Reservoir Quality Index (RQI), Flow Zone Index (FZI) and identifying hydraulic units (HU).
- Prediction of permeability in uncored intervals/wells employing the alternating conditional expectancy (ACE) (Breiman and Friedman 1985) algorithm. For each pay level, the core-to-log permeability transform is employed through ACE algorithm for proliferating permeability in uncored section/wells.
- For the population of permeability in the model, Gaussian Random Function Simulation (GRFS) using collocated co-krigging was performed taking effective porosity volume as the secondary variable.

- Density modelling was carried out using *P*-impedance as secondary trend, and the resulting density volume was rendered into calcite–dolomite percentage model.
- A conceptual diagenetic model was prepared to capture the porosity evolution of Bassein Formation. Vadose zone diagenesis along the exposed geomorphic highs led to porosity generation, while porosity destruction is attributed to diagenesis in phreatic zone along the low axis.
- Integrated analysis of porosity, permeability, density and diagenetic models leads to identification of exploratory prospect and infill development locations for the further exploitation of Bassein hydrocarbon.

The advanced workflow elucidated in this study can be adopted for reservoir characterization of complex multi-cyclic carbonate reservoirs to build quantitative property models.

References

Breiman L, Friedman JH (1985) Estimating optimal transformations for multiple regression and correlation. J Am Stat Assoc 80(391):580–598

Carman PC (1937) Fluid flow through granular beds. Trans Inst Chem Eng Lond 15:150–166

Chapter 15
Interpreting Carbonates Generated AVO Anomaly in Clastic Regime: A Case Study in Deepwaters of Indian Basin

N. K. Khatri and P. K. Chaudhury

Abstract Since compression-wave velocity V_p and shear-wave velocity V_s are affected differently by variation in rock properties and pore fluids, seismic amplitude variation with offset (AVO) and multicomponent seismic emerges as a key tool for exploration and reservoir evaluation. Compression-wave and shear-wave velocities of water-saturated sandstones and shales often closely obey a linear relationship, mudrock equation. Reflections from the interface of such layers exhibit the well-defined background trend of decrease in AVO. Layers with V_p and V_s not honoring the mudrock equation are elastically anomalous. Hydrocarbon-saturated sands and the carbonate rocks are two of the several cases which do not honor the mudrock equation, and therefore, their V_p/V_s (Poisson ratio) is different for the same V_p than had they been honoring the mudrockline relation. Such layers when interfaced with layers honoring the mudrock equation generate the seismic responses anomalous to the background AVO response. Low-impedance and low-Poisson ration hydrocarbon-saturated sands in clastic regime reflect negative amplitudes increasing with offsets (termed as class III AVO anomaly). First offshore well in deepwater in Mahanadi Basin was drilled to probe the amplitude anomaly showing increase in amplitudes with offsets. Well encountered limestone encased in incompacted shale generating increasing amplitude with offset . AVO response was computed from well logs to help explaining the observed AVO anomaly of increase in amplitudes with offset from limestone. Anomaly could not be explained from approximated Aki and Richards (Quantitative seismic: theories and methods. W. H. Freeman and Company & Co. New York 1980) relations of Zoeppritz equation alone. Angle of incidence approaching critical 40° at about offset of 2000 m at shale-limestonetop interface depth caused the amplitude to increase with offset. Case study is presented to show how such expressions can, prior to drilling, be inferred as generated by other than hydrocarbon sands.

Keywords Seismic gathers · Seismic AVO modeling · Carbonates characterization · Reflection coefficient · Impedance · Poisson ratio

N. K. Khatri (✉) · P. K. Chaudhury
Independent Consultant and Faculty, EX-DGM, ONGC, Ahmedabad, India
e-mail: nkkhatri@hotmail.com

K. H. Singh and R. M. Joshi (eds.), *Petro-physics and Rock Physics of Carbonate Reservoirs*, https://doi.org/10.1007/978-981-13-1211-3_15

1 Introduction

The Mahanadi Basin is located in the north-eastern part of eastern continental margin of Indian Plate between Bengal Basin towards NE and Krishna Godavari Basin to the SW (Fig. 1). Data indicate that basin fill consists of sediments of Early Cretaceous to recent. Total sedimentary thickness in the study blocks is expected to be more than 6 km. A basaltic lava flow (Rajmahal trap) is present between Early and Late Cretaceous sediments. Middle Eocene carbonate is also a well-established litho marker in shelfal part of the basin.

Organic shales of Cretaceous to Oligocene age serve as the source rocks in the basin. Cretaceous and Paleocene shale in depth range of 3–4.5 km is reported to be matured for oil generation and below this range for the gas generation.

Vertical cross sections along dip and strike profiles from seismic volume are shown (Fig. 2). Reflection marked in magenta color in Mio-Pliocene interval, had been the prospective target for characterization of hydrocarbon for exploration, and are mapped. Corresponding CMP gathers showed increase in amplitude with offset (Fig. 3). Considering regime to be clastic, increasing AVO had been inferred as class III type (reflected amplitudes which increase with offsets are from the interfaces of encased low-impedance, low-Poisson ratio layers which commonly is caused by hydrocarbon saturations in porous sands in clastic regime). Encouraged by this understanding, first offshore well in deepwaters of Mahanadi Basin was drilled. However, drilling results showed that increase in amplitude with offset was generated by limestone layers encased in uncompacted shale. This necessitated post-drill analysis to explain the increase in amplitude with offsets generated by limestone, and how such expressions can, prior to drilling, be inferred as generated by other

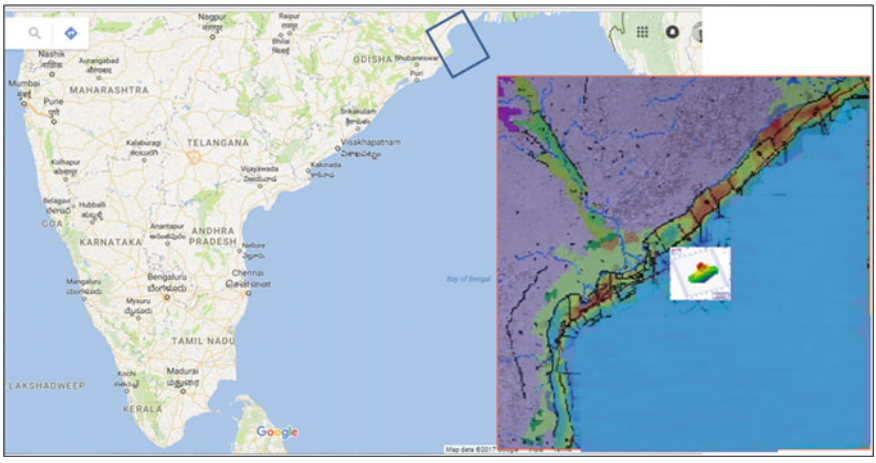

Fig. 1 Location Map of the study area in Mahanadi Basin, located in the north-eastern region of Indian continental margin

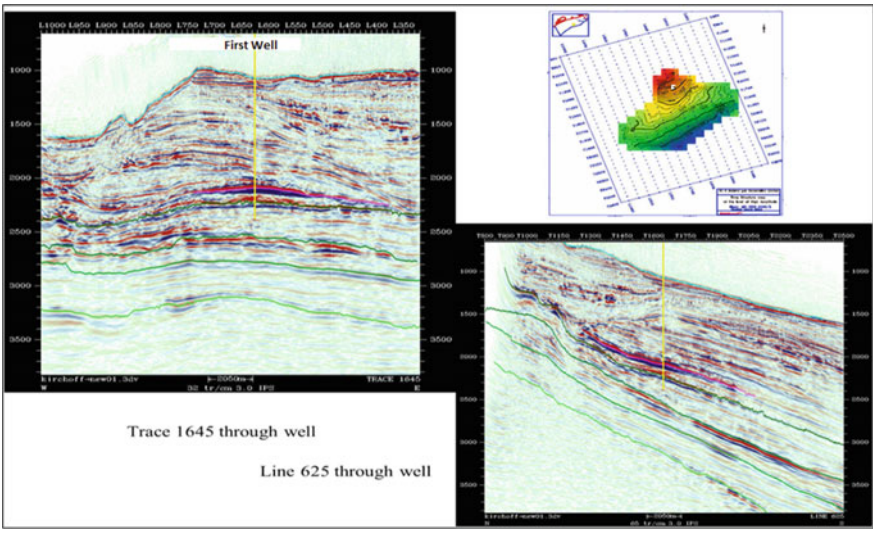

Fig. 2 Map of the targeted amplitudes marked by the magenta color on dip and strikelines

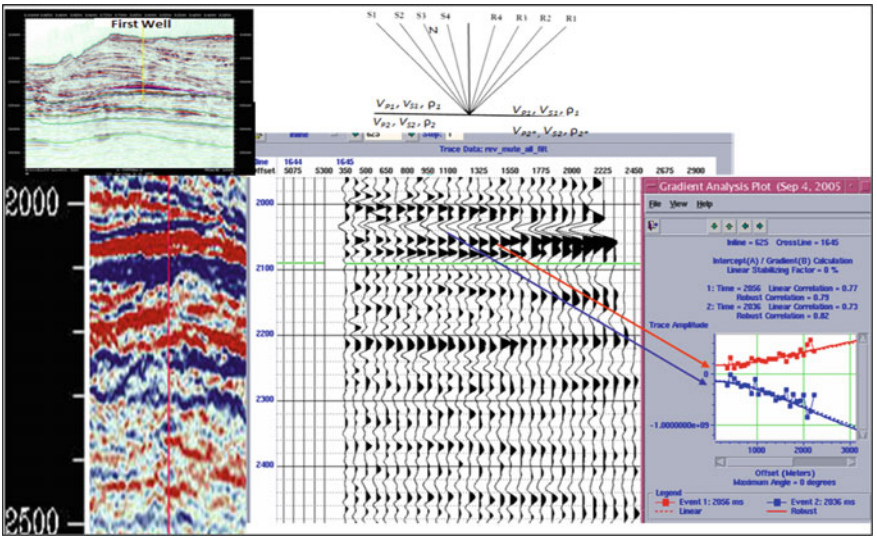

Fig. 3 Increase in amplitude with offset has been observed corresponding to the reflections marked on seismic section by magenta color

than hydrocarbon sands. The understanding inferred from the study and is presented below.

- Rock physics studies show that V_p and V_s are affected differently by limestone and the hydrocarbons sands; Poisson ration, V_p/V_s, of limestone is higher as compared to given by background mud rock equation trends, whereas that is lesser for the hydrocarbon sands.
- Aki and Richards approximation of Zoeppritz equation here fails to explain the observed AVO anomaly from limestone encased in uncompacted shale. Exact computation of Zoeppritz equation explains the observed AVO responses, with the lead to infer AVO anomaly not only generated by other than hydrocarbon, but also to analyze its source.

2 Rock Physics Part

Since compression-wave velocity V_p and shear-wave velocity V_s are affected differently by variation in rock properties and pore fluids, seismic amplitude variation with offset (AVO) and multicomponent seismic emerges as a key tool for exploration and reservoir evaluation. V_p and V_s of both the brine-saturated sands and shale honor closely a common linear relationship (Eq. 1) as shown by the laboratory measurements and form the background trend in clastic sedimentary deposits. It is also called mudrockline, as is suited the best to shaley samples (Fig. 4)

$$V_p = 1.16\ V_s + 1360\ \text{(m/s)} \quad \text{or} \quad V_s = 0.8621\ V_p - 1128\ \text{(m/s)} \tag{1}$$

Reflected amplitudes decrease with offset generated from the interfacing layers obeying the V_p and V_s linear relation of the mudrock equation irrespective of their velocities and forms the background seismic AVO response. V_p and V_s of the layer not honoring the mudrockline equation define the anomalous intervals and the layer interface generate seismic responses anomalous to the background AVO response,

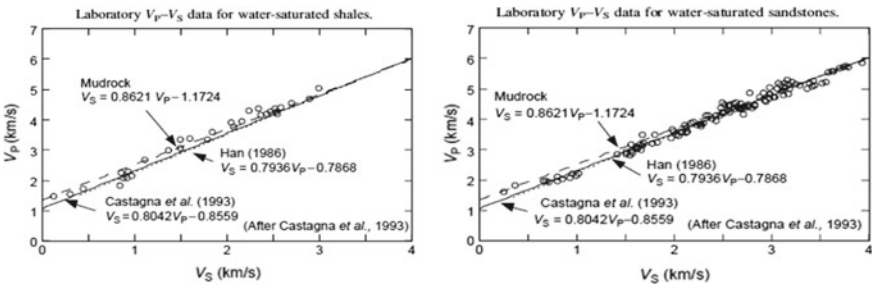

Fig. 4 Illustration of the $V_p - V_s$ relationship for sandstone (right) and shales (left) from laboratory measurements (reproduced with permission from Castagna and Swan 1997)

which is interpreted on $A - B$ cross-plot (Castagna et al. 1998) and Smith and Gidlow's (1992) fluid factor.

Hydrocarbon-saturated sands and carbonate rocks are two of the several cases which in a different ways do not honor the mudrockline equation (Fig. 5) and therefore are interpretable from seismic AVO response. The points corresponding to limestone are below the mudrockline (V_p plotted on x-axis) contrary to the gas sands where points are placed above the line (Fig. 5a, b).

Following Rock physics understanding describes how V_p and V_s are affected differently by hydrocarbon-saturated sands and carbonate rocks:

V_p and V_s of the isotropic and homogeneous rocks are related with their bulk modulus K and rigidity modulus μ by the following relations.

$$V_s = (\mu/\rho)^{1/2} \tag{2}$$

$$V_p = ((K + 4/3 * \mu)/\rho)^{1/2} \tag{3}$$

where ρ is the bulk density of the rock.

K and μ of rock composite are governed by individual elastic moduli of the constituents and their volume fractions besides geometric details of how the various constituents are arranged. Bulk moduli of sandstone matrix $k = 36.5$ and water $k =$ ~2.5 and their volume fractions contribute to K of the water-saturated sandstone rock

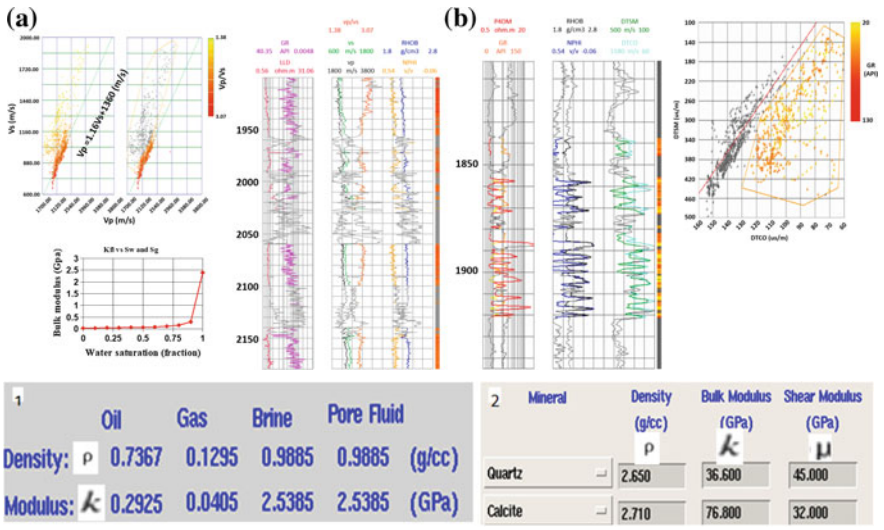

Fig. 5 Plots show the break in linear mudrock relationship between V_p and V_s for the gas sand and limestone cases. Points are below the background trend corresponding to limestone indicating higher Poisson ratio contrary to the gas sand points which are above the background trend indicating lower Poisson ratio (Examples from KG basin and Mahanadi basin respectively). Typical values of elastic parameters of fluids (Table 1), and elastic constants of quart sandstone and calcite rocks (Table 2)

composite. Rigidity moduli of sandstone matrix $\mu = 45$ and water $\mu = 0$ and their volume fractions contribute to μ of the rock composite. Volume fraction of water is equal to the porosity of the composite. Since μ of non-viscous liquids is zero, μ of the rock composite is governed by volume fraction of matrix and therefore is not affected by the fluid replacement.

Single-phase mixture of liquids is isostress composite, and therefore, its effective modulus K_f is given by the volume weighted harmonic average of moduli of the constituents as given by Wood's formula (Eq. 4).

$$1/K_f = S_w/K_w + S_o/K_o + S_g/K_g \tag{4}$$

where S_w, S_o, and S_g are volume fractions of water, oil, and gas constituents, respectively, forming the single-phase mixture of fluid, and K_w, K_o, and K_g are their bulk moduli. Typical values of K_w, K_o, and K_g are shown in Table 1 which vary with pressure, gas gravity, temperature, gas–oil ratio, and salinity. K_g is many folds smaller than K_o, and K_o is many fold smaller than K_w. It is clear from Eq. 4 that K_f is biased towards modulus of the constituent of mixture having the lowest value (Fig. 5c).

If water is partly or fully replaced by hydrocarbon in the rock, the K_f of mixture of fluids in the pore space becomes many folds smaller than that bulk modulus of water, K_w, bringing down the contribution from fluid constituent to K of rock composite substantially, resulting K to be substantially lesser. Lower K of hydrocarbon substituted rock composite brings the V_p down (Eq. 3). μ of the rock composite is not affected by the fluid replacement. Change in density alone affects V_s marginally (Eq. 3). As the outcome of water replacement by hydrocarbon in the rock, V_p comes down and V_s practically not affected. This results water sand points on the $V_p - V_s$ mudrock cross-plot shift towards left (V_p on x-axis) i.e., hydrocarbon sands having lesser V_p/V_s than the corresponding points obeying the mudrockline. Example from KG offshore shows the hydrocarbon points on the $V_p - V_s$ cross-plot shifted towards left (V_p on x-axis) with reference to mudrockline (Fig. 5a).

Values of μ of limestone and sandstone matrix (grain) are 32 and 45 GPA, respectively (Table 2). μ of rock composite consisting of limestone and non-viscous fluid is solely contributed by volume fraction of limestone matrix of 32 GPA. Similarly, μ of sandstone rock composite is solely contributed by volume fraction of sandstone matrix of 45 GPA. Therefore, μ is always lower for the limestone rock composite than sandstone rock composite for the same porosity considering the contributions caused by geometric details of arrangement of the various constituents are at par. Therefore, V_s of carbonate rock composite of same porosity is commonly lower than that of sand stone rock composite (Eq. 2).

Values of K of limestone and sandstone matrix are 77 and 36.5 GPA, respectively (Table 2); therefore, K is always higher for the limestone composite than that of sandstone for the same porosity and same fluid mixture considering the contributions caused by geometric details of arrangement of the various constituents are at par.

$K + 4\mu/3$ in numerator in Eq. (3) computes V_p. K of limestone rock composite of same porosity and fluids is higher than that of quartz sandstone, whereas μ in limestone composite is lower than that of sandstone rock composite. However,

$k + 4\mu/3$ for limestone composite is higher than that of sand stone of the same porosity and fluids which broadly explains the limestone composite having higher velocity than that of sandstone.

As the outcome of higher V_p and lower V_s of limestone rock composite results the points on the $V_p - V_s$ cross-plot shift towards right and below (V_p on x-axis) with reference to mudrockline, i.e., limestone composite having higher V_p/V_s than the corresponding water sand points obeying the mudrockline.

Example from Mahanadi Basin of first offshore well shows the points from limestone composite on the $V_p - V_s$ cross-plot are placed below (V_p on x-axis) the mudrockline (Fig. 5b).

3 Aki and Richards Approximation and Exact Zoeppritz Equation

Reflected amplitudes offset generated from the interface of layers obeying the mudrockline decrease with offsets irrespective of their velocities and forms the background seismic AVO response. In case V_p and V_s of the any of the interfacing layers is not related by mudrockline equation, the seismic responses anomalous to the background AVO response is generated.

Encased low-impedance layers which reflect amplitudes with increase in offsets from the interfaces are of low Poisson ratio (termed as class III AVO anomaly) and are commonly hydrocarbon-saturated porous sands in clastic regime. Limestone layers encased in clastic regime are generally of higher impedance and higher Poisson ratio and therefore also generate the AVO anomalous to the background trend.

$R_p(\theta)$ in Zoeppritz equation has complicated dependence on elastic parameters of two media across the interface and angle of incidence. To relate coefficients and elastic parameters at a given incidence angle, approximated expressions as derived by Aki and Richards are instructive (Eq. 5). It assumes two half spaces have properties, i.e., the ratios $\Delta V_p/(V_p)$, $\Delta V_s/(V_s)$, and $\Delta\rho/(\rho)$ much lesser than unit and all incidence angles are less than any critical angle and less than 90°. This mathematical expression greatly simplifies the behavior of reflection coefficients (RCs) with angles and provides more insight into which changes in elastic parameters affect reflection coefficients.

$$R_p(\theta) = A + B\sin^2\theta + C\sin^2\theta\tan^2\theta \tag{5}$$

where

$$A = R_p = 0.5 * (\Delta V_p/V_p + \Delta\rho/\rho) \tag{5a}$$

$$B = 0.5 * (\Delta V_p/V_p) - 4 * \left(V_s/V_p\right)^2 * \Delta V_s/V_s - 2 * \left(V_s/V_p\right)^2 * \Delta\rho/\rho \tag{5b}$$

$$C = 0.5 * (\Delta V_p / V_p) \tag{5c}$$

where ΔV_p is the change in compressional velocity across the interface ($V_{p2} - V_{p1}$), V_p is the average compression velocity across the interface ($V_{p2} + V_{p1}$)/2, $\Delta\rho$ is the change in density across the interface ($\rho_1 - \rho_2$), ρ is the average density across the interface ($\Delta\rho_1 + \rho_2$)/2, ΔV_s is the change in shear velocity across the interface ($V_{s2} - V_{s1}$), and V_s is the average shear velocity across the interface ($V_{s2} + V_{s1}$)/2, with V_{p1}; V_{s1}; ρ_1 and V_{p2}; V_{s2}; ρ_2 being the medium properties in the first (overlying) and second (underlying) media, respectively.

Linearized reflection coefficients (dashed line) are computed from Eq. (5) and computed from Zoeppritz equation (solid line) for two models (Fig. 6); one model yields critical angles, and other yields no critical angle. The linear approximation tracks exact solution computed from Zoeppritz equation quite well before it breaks down prior to critical angle (Fig. 6a). Zoeppritz equation computes amplitude increase close to approaching critical angle contrary to Aki–Richards approximation. For model without critical angle, the linear approximation still breaks down although at larger angles.

$$R_p(\theta) = A + B \sin^2 \theta \tag{6}$$

Equation (6) is two-term approximation as $\sin^2\theta \tan^2\theta$ in the third term in Eq. (6) is significantly small up to 35° of angle. It shows that $R(\theta)$ and $\sin^2\theta$ are linearly related through A as the intercept and B as gradient. $R(\theta) = R_p = A$ at $\theta = 0$; A is reflection coefficient (RC) at normal incidence.

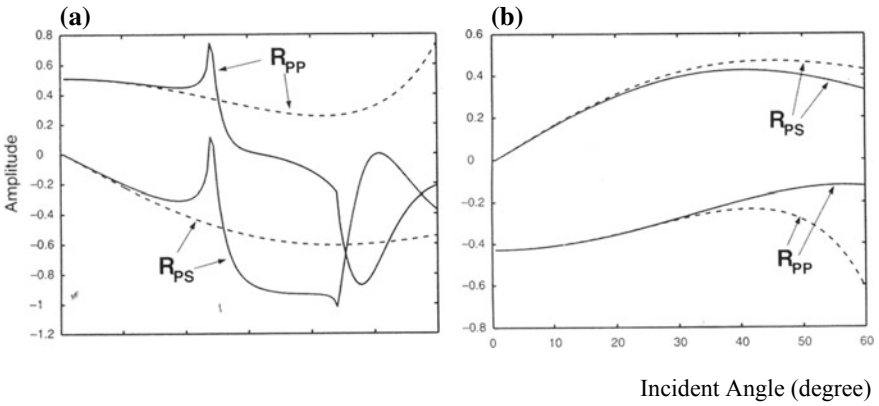

Fig. 6 Comparison of exact solution of Zoeppritz equation (solid curve) and linearized solution (dashed curve) for two half space layers models, viz. $V_{p2}/V_{p1} = 2.5$, $\rho_2/\rho_1 = 1.22$, and $\sigma_1 = \sigma_2 = 0.25$ yields critical angles, and that of $V_{p2}/V_{p1} = 0.5$, $\rho_2/\rho_1 = 0.8$, and $\sigma_1 = \sigma_2 = 0.25$ does not yield any critical angle. Linear approximation tracks exact solution computed from Zoeppritz quite well before it breaks down prior to critical angle

By equating $V_p/V_s = 2$, Eq. (6) is simplified for more insight as

$$B = R_p - 2R_s \tag{7}$$

where $R_s = 0.5 * (\Delta V_s/V_s + \Delta\rho/\rho)$; the shear wave reflectivity at normal incidence.

Equation (7) shows how AVO gradient B is related with R_p and R_s. Since V_p and V_s are affected differently by variation in rock properties and pore fluids, the R_p and R_s are also affected differently, indicating rock properties and pore fluids interpretability on seismic AVO, i.e., intercept A and gradients B and multicomponent seismic.

By equating $V_p/V_s = 2$, Eq. (6) is also simplified for more insight as

$$R_p(\theta) = R_p \cos^2\theta + 2(R_p - R_s)\sin^2\theta \tag{8}$$

where $2(R_p - R_s) = \Delta(V_p/V_s)/(V_p/V_s)$ is the Poisson reflectivity (PR) at the interface.

Following, insight from Eq. (8) has been utilized to explain the AVO anomaly generated from limestone.

1. First term in Eq. (8), irrespective of R_p being positive or negative, contributes to decreases in reflection amplitude magnitude $R_p(\theta)$ with increasing angle of incidence; i.e., gradient is negative in case of positive R_p and positive in case of R_p negative.
2. Second term shows that negative Poisson reflectivity (high-to-low Poisson ratio interface) contributes increasingly negative amplitude with increase in angle, i.e., towards the negative gradient to $R_p(\theta)$.
3. Positive Poisson reflectivity (low-to-high Poisson ratio interface) contributes to increasingly positive amplitude with increase in angle, i.e., contributes to the positive gradient to $R_p(\theta)$

Relationship between R_p and Poisson reflectivity is shown for the layers obeying mudrockline (Fig. 7a). Mudrock equation obeying layers of higher V_p have lesser V_p/V_s, and of lower V_p values the higher V_p/V_s. The high- and low-impedance models are discussed as two possible scenarios. The negative gradient given by first term is added by negative gradient given by the second term, therefore resulting in decrease in positive amplitude from top interface of the model and similarly decrease in negative amplitude generated from base interface of the high-impedance model (Eq. 8). The positive gradient given by first term is added by positive gradient given by the second term, therefore resulting in decrease in negative amplitude generated from top interface of the model. Similarly, decrease in positive amplitude generated from base interface of the low-impedance model.

Substitution of water by hydrocarbon lowers the positive reflection amplitude magnitude or increases the negative reflection amplitude and lowers the Poisson ratio. Signs and magnitudes of R_p and Poisson reflectivity govern the increase or decrease in amplitude with angle as dictated by Eq. (8), yielding four possible scenarios known as four classes of AVO anomalies (Fig. 7b).

Shale–limestone generates positive reflection amplitude as limestone has higher impedance than the shale, which is generally the case. Therefore, first term in Eq. (8)

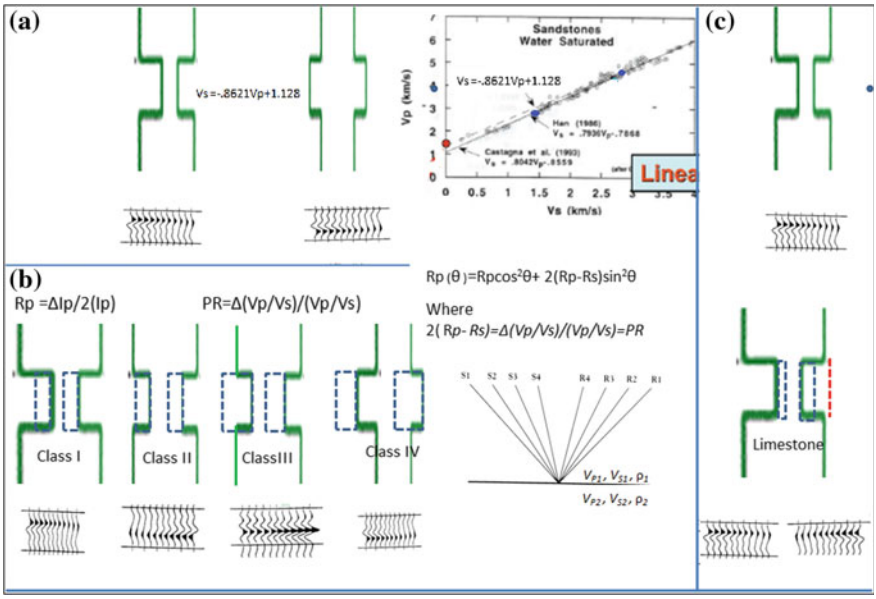

Fig. 7 Three layered Models and their intercept and gradient expressions on CMP gathers; **a** Shale-sand-shale models, V_p and V_s of layers are obeying mudrockline, **b** four possible scenarios after hydrocarbon substitution of water in sands in models obeying the mudrockline, and **c** Shale-limestone-shale model, limestone may have V_p/V_s lesser, equal or more than encasing uncompacted shale

contributes to positive R_p and negative gradient (decrease in positive amplitude with angle increase) and second term depending upon the sign and magnitude of Poisson reflectivity may slow down the decrease caused by the first term or overcome the decrease to the extent of increases in the amplitudes with incident angle (Fig. 7c) as compared to the background trends given by the layers obeying the mudrockline.

Poisson ratio computed from the well log data (Table 3 of Fig. 8) for the limestone layers is higher, but it is still lesser than that of the uncompacted shale encasing it.

Table3

	Vp	Vs	Density	Vp/Vs
Shale	140/2177	360/846	2.05	2.57
limestone	90/3386	220/1385	2.35	2.45
shale	140/2177	360/846	2.05	

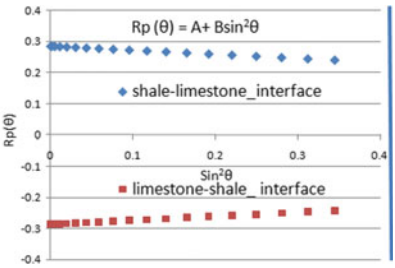

Fig. 8 $R_p(\theta)$ computed from two-term Aki–Richards equation for the elastic parameters from the well log data (Table 3) is plotted against $\sin^2\theta$ upto incidence angle 35°

This results negative Poisson reflectivity from shale–limestone interface, thereby contributing toward decrease in amplitude though lesser than had this been layers honoring mudrockline. The synthetic gathers generated from these parameters upto 35° using two terms Aki–Richards equation show decrease in amplitudes with angle (Fig. 8) in alignment with parameters in table. Explaining the increase in amplitude from shale–limestone–shale interfaces still remains an issue.

Offset domain represents the acquisition geometry in which each trace corresponds to fixed offset in the CMP gathers, but angle of incidence at interfaces varies (Fig. 9a), whereas the angle domain represents theoretical acquisition geometry in which each trace corresponds to a constant incidence angle, but offset varies (Fig. 9b). Synthetic seismic offset gathers at well location are generated from log curves using Zoeppritz equation. Gathers are hanged with appropriate replacement velocity to match with field seismic gathers and overlain by iso-incident angle curves in the step of 10° starting from 5° to show how incident angle at interfaces is related with offsets (Fig. 9c).

Incidence angle of 35° at limestone top (the brick color) and 50° at the base at ~2000 m offset indicates angle 35° to be close to critical (Fig. 9c), i.e., breaking down the validity of Aki–Richards approximation at these offsets. This necessitates the exact solution of Zoeppritz equation to explain the observation. Angle 40° is computed as the critical angle from the sonic well log (Table 3 of Fig. 8) which corresponds to 2000 m offset at shale-limestone top generating increasing amplitudes. Exact solution of Zoeppritz equation for this set of logs is rapid amplitude increase with offset as angles approaching critical angle (Fig. 9). Synthetic seismic gathers generated from log curves using Zoeppritz equation matched with muted post-critical offset field seismic CMP gathers at well location (Fig. 10) which reveals that increase

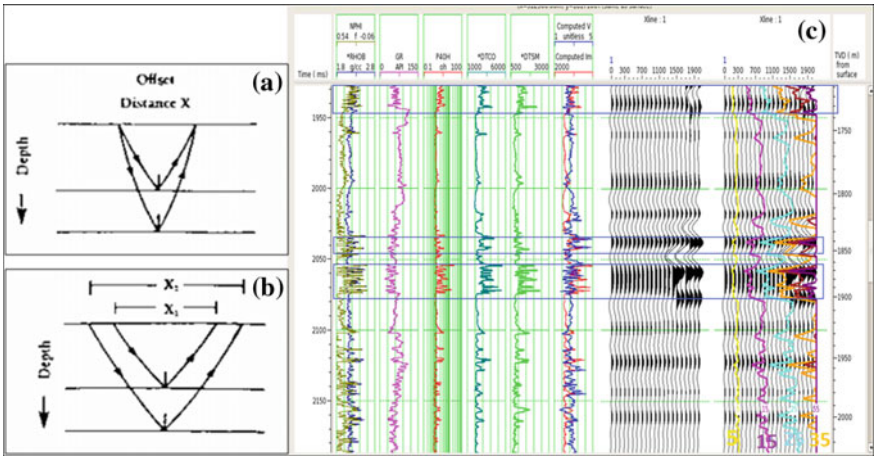

Fig. 9 Synthetic offset seismic gathers at well location overlain by iso-incident angle curves in the step of 10° starting from 5°

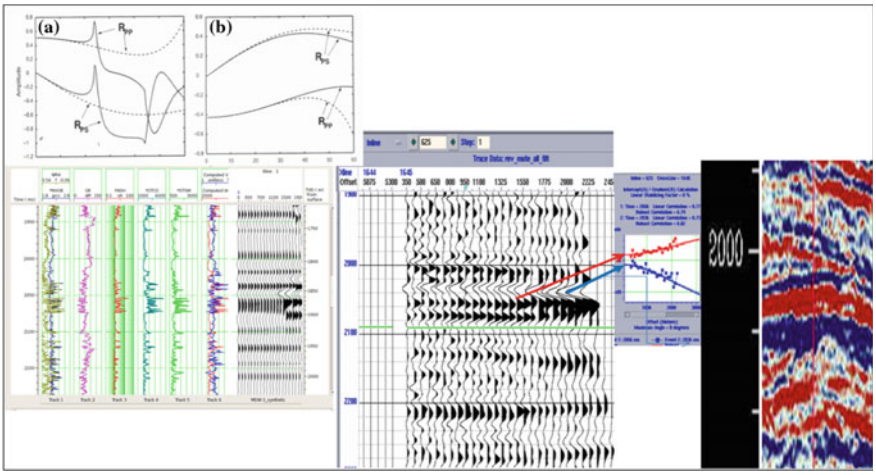

Fig. 10 Synthetic gathers generated using Zoeppritz equation match with field PSTM gathers, showing shale–limestone interface generated increase in amplitude with offsets correspoding to incidence angle nearing to critical

in amplitudes with offset approaching 2000 m is caused by shale–limestone interface as incidence angle nearing critical.

Understanding that such AVO expressions can, prior to drilling, be inferred generated by other than hydrocarbon sands. Top and bottom of the layers can be identified based on the reflections from the seabed which is low-to-high impedance interface. Positive amplitudes at top increase with offset of layer (shale–limestone interface) as angle approaches to critical, whereas from base of layer (limestone–shale interface) there has been a decrease in amplitudes with offsets. This is contrary to the class III type of AVO anomaly where both the negative amplitudes from the top and positive reflection from the base interfaces of layer increase with offset. Therefore, study of sign of reflections and their gradients from top and base of the layer must distinguish if anomaly is caused by other than hydrocarbon sands.

4 Conclusion

Limestone in clastic regime is anomalous on $V_p - V_s$ relation, therefore it generates seismic AVO anomaly when interfaced with shale. Aki and Richards approximation of Zoeppritz equation does not explain the observed increase in amplitude with offset from shale–limestone interface.

Critical angle ~40° is commuted to correspond to the offset ~2000 m at shale–limestone top interface depth. There is no critical angle from limestone base-shale interface sonic logs. Incident angle approaching critical angle breaks down the validity of Aki–Richards approximation, necessitating exact solution of Zoeppritz

equation to explain the increase in amplitude from shale–limestone interface with offsets.

Refletion from the top of layer increases rapidly with offset (shale–limestone interface) as angle approaches to critical, whereas from base of layer (limestone–shale interface) the decrease in amplitudes with offsets has been modeled. This is contrary to the class III type of AVO anomaly where negative reflected amplitude from the top and positive bottom interfaces of layer increase with offset. Therefore, study of sign and gradient of reflected amplitudes from top and base of the layer distinguish increse in amplitudes caused by other than hydrocarbon sands.

Acknowledgements The authors are thankful to ONGC for permitting to publish the work as the technical paper. Authors are thankful to SPG, India for permitting the article to be published in Springer. Original article is published in Geohorizons issued in December 2015. The work carried out in 2005 at GEOPIC, Dehradun, is presented as the case study. Article is rewritten to align with the theme of the workshop held at IITB, Mumbai. The views expressed in the paper are those of the authors only. The authors express their gratitude to Ex-Director (Expl.), D. K. Pande, ONGC, for assigning the project. The authors are thankful to V. Rangachari Ex-ED-Basin Manager, KG-PG, Chennai, for support and encouragement while supervising the project at GEOPIC, ONGC, Dehradun.

References

Aki K, Richards PG (1980) Quantitative seismic: theories and methods. W. H. Freeman and Company & Co., New York

Castagna JP, Swan HW (1997) Principle of AVO crossplotting. Lead Edge 16(4):337–342

Castagna JP, Swan HW, Foster DJ (1998) Framework for AVO gradient and Intercept interpretation. Geophysics 63:948–956

Smith GC, Gidlow PM (1987) Weighted stacking for rock property estimation and detection of gas. Geophys Prospect 35(9):993–1014

Verm R, Hilterman F (1995) Lithology color-coded seismic sections: the calibration of AVO crossplotting to rock properties. Lead Edge 14(8):847–853

Chapter 16
Application of Hilbert–Huang Transform in Effective Reservoir Characterization

Vaibhav Jayaswal and Gaurav S. Gairola

Abstract One of the paramount goals in petroleum exploration is the identification of the reservoir. The foremost objective of reservoir characterization is for prediction of reservoir precisely. Nowadays, geophysical characterization is used to characterize a reservoir; mainly, seismic data is being used for understanding the reservoir's properties and internal structure. The reservoir can cause anomalies in the frequency of seismic signals. Over the past few decades, various transforms such as Fourier transform (FT) and wavelet transform (WT) have been used to extract the concealed attributes in the data. In the case of the Fourier transform (FT), it is the global transform that cannot reflect local specialty. This transform is the best applicable for stationary and linear data, but most of the geophysical data are non-stationary, nonlinear, and aperiodic in nature. Therefore, FT is good for spectral analysis but not fit for elucidating the temporal characteristics of the data. Wavelet transform (WT) overcomes the problem faced by Fourier transform as it is one of the efficient techniques for both spectral and temporal analysis of the data. The main problem with WT is that it does not work well with nonlinear data and suitable mother wavelet is needed to be assumed. This study focuses on highlighting the anomalies using the Hilbert–Huang Transform, which comprises two techniques, i.e., empirical mode decomposition (EMD) technique and Hilbert spectral analysis (HSA). EMD will decompose a signal into mono-components of frequency termed as intrinsic mode functions (IMFs). In this study, the EMD technique followed by HSA is applied to the data set which highlights the anomalies in the data set and makes facile to characterize a reservoir. It is difficult to characterize a reservoir because of varying properties such as porosity and permeability within small sections of the reservoir. This method shows its effectiveness in characterizing a reservoir.

Keywords Reservoir characterization · Empirical mode decomposition · Intrinsic mode functions · Hilbert spectral analysis

V. Jayaswal · G. S. Gairola (✉)
Department of Petroleum Engineering and Earth Sciences, University of Petroleum and Energy Studies, Dehradun, India
e-mail: gsgairola@ddn.upes.ac.in

K. H. Singh and R. M. Joshi (eds.), *Petro-physics and Rock Physics of Carbonate Reservoirs*, https://doi.org/10.1007/978-981-13-1211-3_16

1 Introduction

A remarkable proportion of the world's oil reserves are found in carbonate reservoirs. To efficiently characterize a reservoir is the basic need in petroleum exploration. Various challenges have been faced in characterizing a reservoir due to the changes in the properties of a reservoir after deposition. After formation of rocks, it undergoes various physical and chemical changes which will change the fundamental characteristics of the rock. Four types of porosity are present in siliciclastic reservoir: intergranular, dissolution, microporosity, and fracture. Three types of porosity are present in a carbonate reservoir: fracture porosity which is due to the stresses; vugs which are separate pores resulting from dissolution and connected porosity which exist between grains. Various transforms are used for signal processing such as Fourier transform (FT) and wavelet transform (WT) which comprises two different transforms, i.e., continuous wavelet transform (CWT) and discrete wavelet transform (DWT). Among all the transforms, HHT is proved to be the best for nonlinear and non-stationary signals.

Hilbert–Huang Transform is a fully adaptive technique which further comprises two processes, i.e., empirical mode decomposition (EMD) technique and Hilbert spectral analysis (HSA) (Huang and Wu 2008; Huang et al. 1998). EMD will decompose a signal into mono-components of frequency termed as intrinsic mode functions (IMFs). Since seismic signals are nonlinear, non-stationary and aperiodic in nature, HHT is one of the best techniques for determining spatiotemporal features for such type of signals (Battista et al. 2007). IMF is a function which will fulfill the following requirements:

- Difference between the number of extrema and the number of zero-crossings must be equal to zero or at most one.
- At any point, the mean value of the upper envelope and the lower envelope is zero (Huang et al. 1998).

First IMF is of the highest frequency and last will be of the lowest frequency. The method of converting the signal into IMFs is called *sifting*. EMD is widely used in various domains such as well logging (Gairola and Chandrasekhar 2017), seismics (Xue et al. 2013), sequence stratigraphy (Zhao and Li 2015), atmospheric sciences (McDonald et al. 2007), Magnetotellurics (Cai et al. 2009; Cai 2013; Neukirch and Garcia 2014), and medical science (Li et al. 2011). HSA is applied to the data in order to determine instantaneous amplitude and instantaneous frequency of IMFs which can be used to determine the anomaly in the data.

HHT algorithm is applied on seismic data of the F3 block situated in the Dutch sector of the North Sea provided by OpendTect (dGB Earth Science). Inline range varies from 100 to 750, crossline range varies from 300 to 1250 and time varies from 0 to 1848 ms. The area in the seismic section which is taken into this study is located in 425 inline section at 1600 ms.

2 Methodology

Initially, EMD is applied on inline section 425 and time slice 1600 ms. EMD algorithm is mentioned below:

1. A seismic section is taken out from seismic data. HHT algorithm is applied separately on all the traces present in that particular seismic section.
2. Each trace has certain local maxima and local minima.
3. All the local minima and local maxima in a trace $s(t)$ is joined by using interpolation. This will result in two envelopes, i.e., the upper envelope which comprises all the local maxima and lower envelope which comprises all the local minima.
4. Mean of both the envelopes (m_{11}) are taken which is subtracted from the original signal $s(t)$. The new signal is called as proto IMF ($h_1 = s(t) - m_1$).
5. This first sifting process is repeated k times, i.e., $h_{1k} = h_{1(k-1)} - m_{1k}$.
6. For the second sifting process, h_1 is considered as data and m_{11} is the mean envelope of the upper and lower envelope of new data, i.e., h_1.

$$h_{11} = h_1 - m_{11} \tag{1}$$

7. The number of times the sifting process is repeated depends on the stopping criterion which is taken as the normalized square difference between two sifting processes. Eventually, the process will result in IMF1.
8. Now, IMF1 is subtracted from the original signal $s(t)$ which gives $x_1(t)$. The whole process is repeated on $x_1(t)$. This will result in IMF2.
9. The process will stop when $x_n(t)$ will give a monotonic trend r_n. Therefore, we have $(n - 1)$ IMF and a monotonic trend for each trace in a seismic section.

$$s(t) = \text{IMF}_{(n-1)} + r_n \tag{2}$$

10. IMF1 of all the traces are extracted to form IMF1 for the seismic section. Similarly, all the IMFs of the seismic data are evaluated.
11. In this study, inline section 425 and time slice 1600 ms is decomposed into five different frequencies which consist of the highest frequency component (IMF1) to the lowest frequency component (IMF5).

Hilbert spectral analysis (HSA) is then applied to all the five IMFs. HSA is used to determine the instantaneous frequency, instantaneous amplitude, and instantaneous phase. Analytic representation of the signal is given by Hilbert transform which means it will convert the signal into real and complex parts.

$$A(s) = a(s) + ib(s) \tag{3}$$

Instantaneous amplitude = absolute value of Hilbert transform, i.e., $[a(s)^2 + b(s)^2]^{1/2}$ (Huang and Wu 2008).

$$\text{Instantaneous phase} = \tan^{-1}[b(s)/a(s)] \tag{4}$$

$$\text{Instantaneous frequency} = \mathrm{d}(\theta(s))/\mathrm{d}s. \tag{5}$$

3 Result

See Figs. 1, 2, 3, 4, 5, 6, 7, 8, 9 and 10.

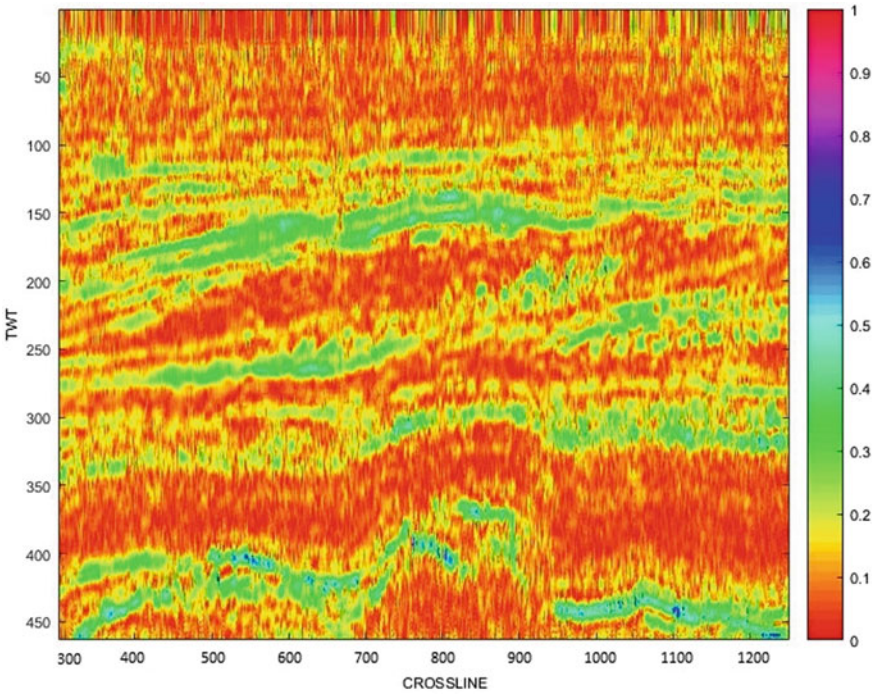

Fig. 1 Illustration of first monofrequency slice, i.e., first IMF of inline section 425 of 3D Seismic data of F3 block, North Sea

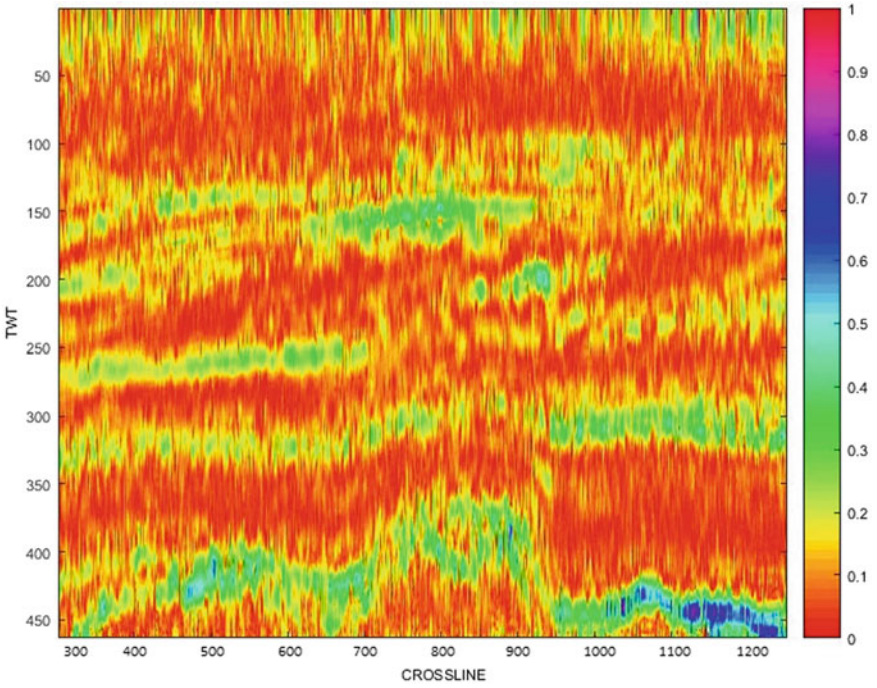

Fig. 2 Illustration of second monofrequency slice, i.e., second IMF of inline section 425 of 3D Seismic data of F3 block, North Sea

4 Conclusions

IMF1 is the highest frequency component, and it mostly consists of noise. In inline section 425, various features are highlighted with green color as green is having the highest amplitude (approximately 0.3) which is more than the orange color feature which is approximately 0.1. As we move on to IMF2 which is having frequency lower than that of IMF1, it also contains noise and not properly highlights the features present in the seismic section. Moving on to IMF3 which is having a frequency which is lower than IMF1 and IMF2 and feature gets highlighted in this IMF. Geological feature is predominantly visible in low-frequency data and a layer is clearly highlighted at 1600 ms. That layer might be a gas reservoir as gas has the property to appear in low-frequency data.

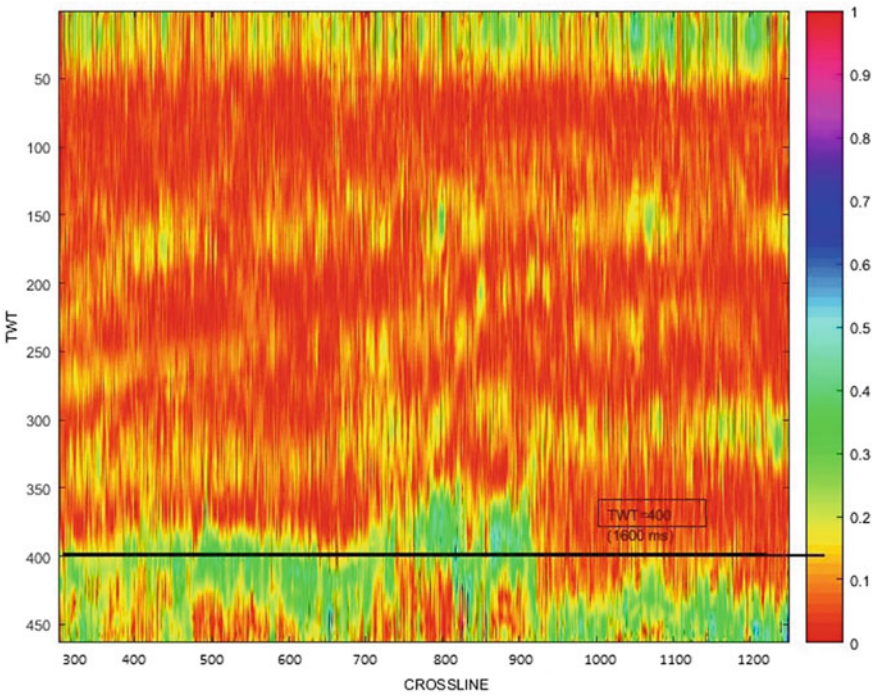

Fig. 3 Illustration of third monofrequency slice, i.e., third IMF of inline section 425 of 3D Seismic data of F3 block, North Sea

Similarly in time slice 1600 ms, IMF1 and IMF2 are mostly consisted of noise and did not provide accurate information about the features present in the seismic section. In IMF3 of time slice 1600 ms, at inline 425 and crossline range 500–600 a feature is appeared in green color, i.e., with the highest amplitude among all the features. This feature gets appeared in lower frequency components such as IMF4 and IMF5, but other features disappear. Therefore, we can say that gas is present at that location. Moreover, validation with well data is not possible in this study due to the limited availability of data.

On the basis of results obtained in this study, we can conclude that HHT can be used to characterize a reservoir efficiently.

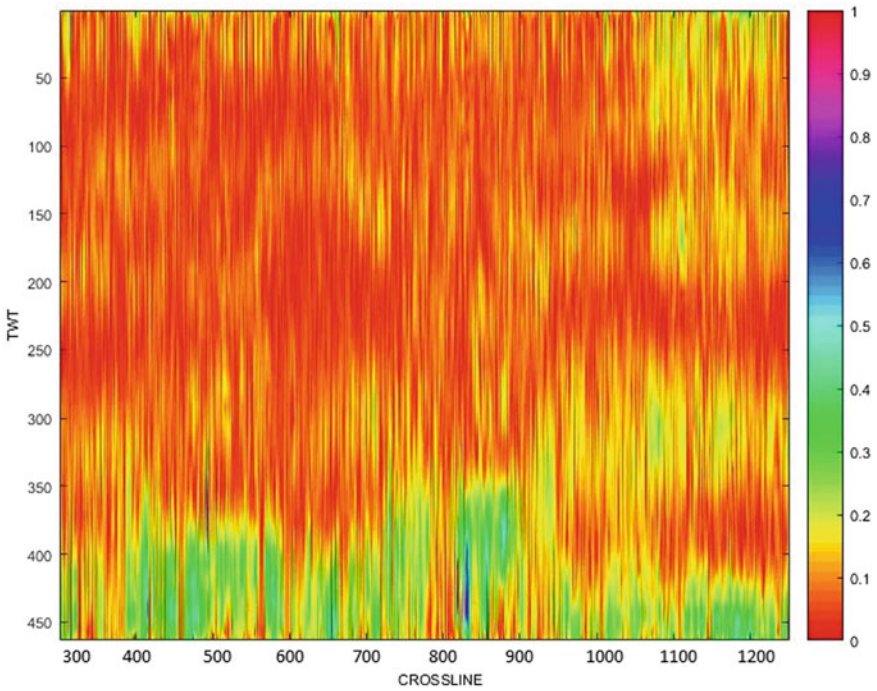

Fig. 4 Illustration of fourth monofrequency slice, i.e., fourth IMF of inline section 425 of 3D Seismic data of F3 block, North Sea

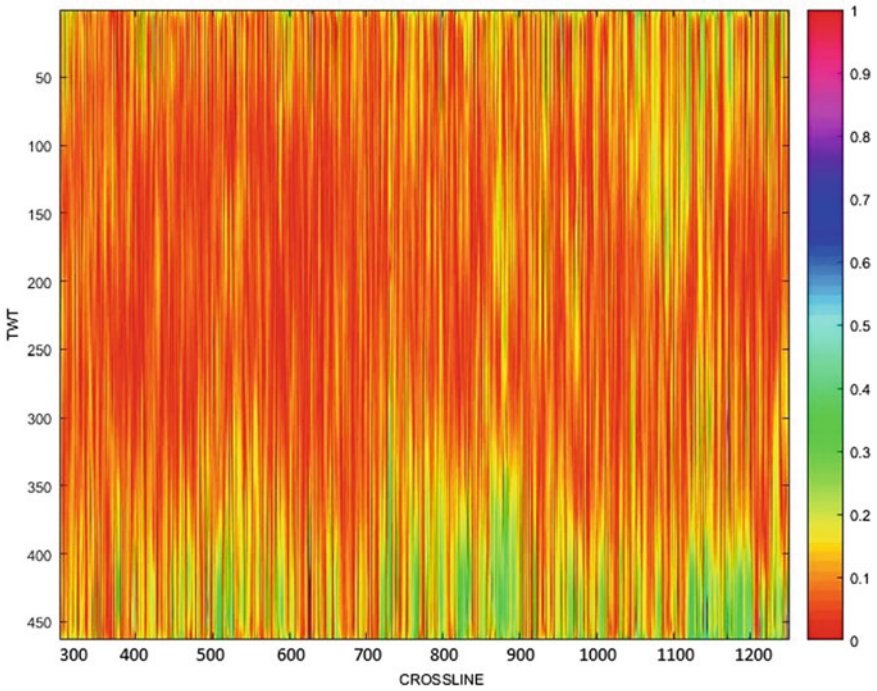

Fig. 5 Illustration of fifth monofrequency slice, i.e., fifth IMF of inline section 425 of 3D Seismic data of F3 block, North Sea

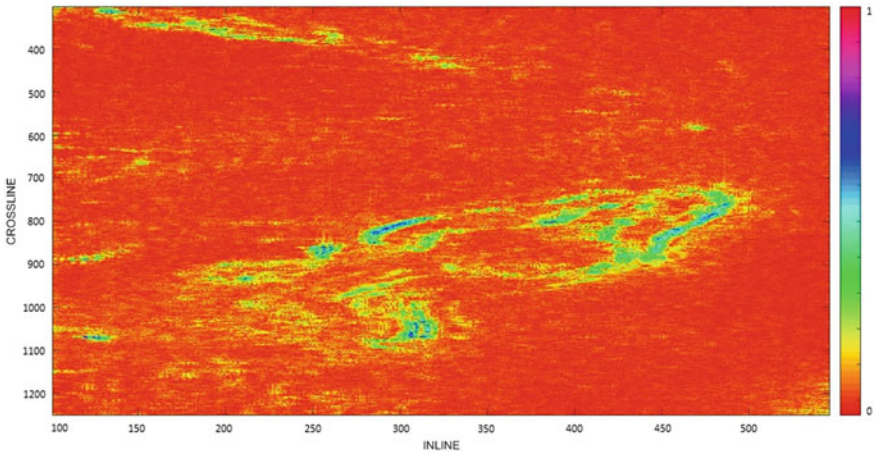

Fig. 6 Illustration of first monofrequency slice, i.e., first IMF of time slice of 1600 ms of 3D seismic data of F3 block, North Sea

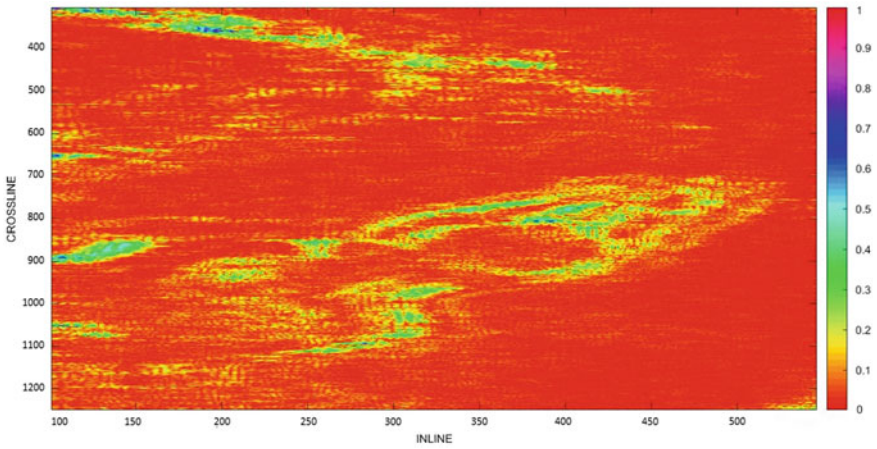

Fig. 7 Illustration of second monofrequency slice, i.e., second IMF of time slice of 1600 ms of 3D seismic data of F3 block, North Sea

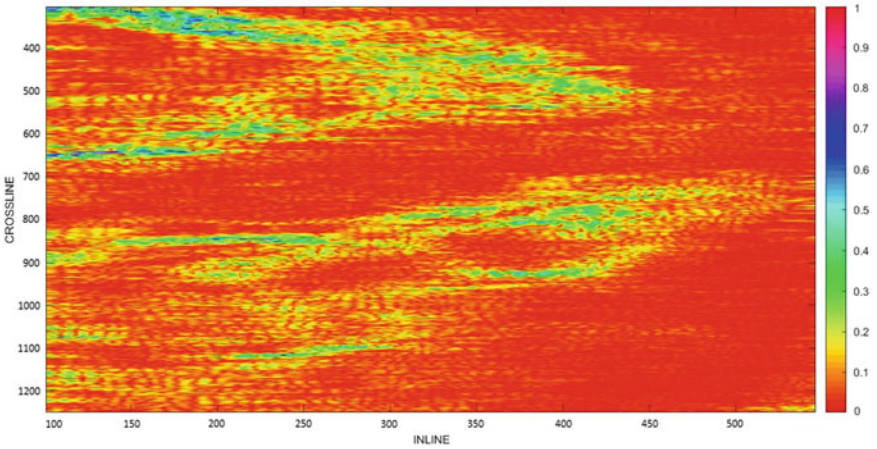

Fig. 8 Illustration of third monofrequency slice, i.e., third IMF of time slice of 1600 ms of 3D seismic data of F3 block, North Sea

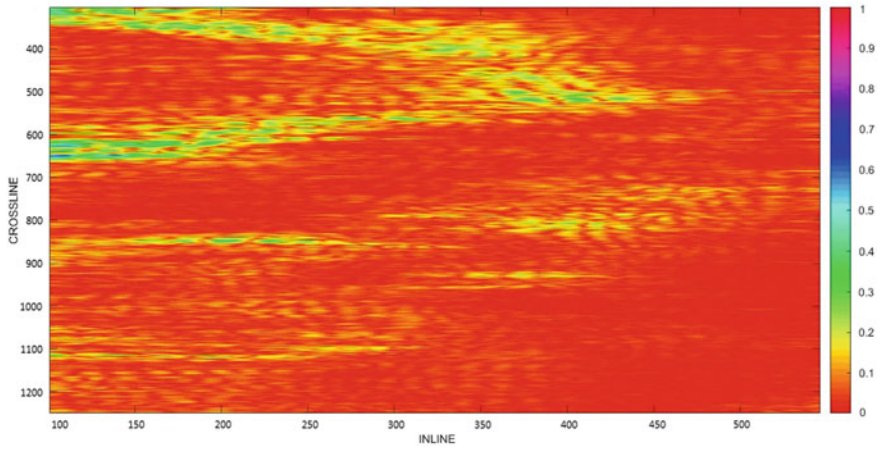

Fig. 9 Illustration of fourth monofrequency slice, i.e., fourth IMF of time slice of 1600 ms of 3D seismic data of F3 block, North Sea

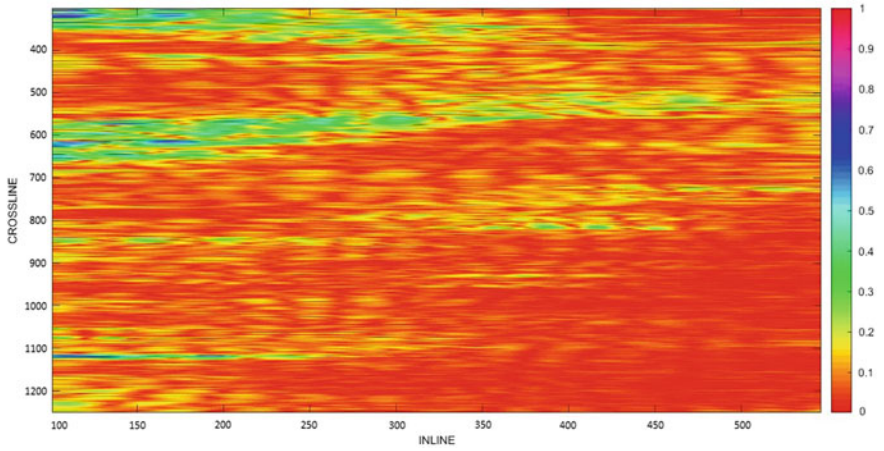

Fig. 10 Illustration of fifth monofrequency slice, i.e., fifth IMF of time slice of 1600 ms of 3D seismic data of F3 block, North Sea

References

Battista BM, Knapp CC, McGee T, Goebel V (2007) Application of the empirical mode decomposition and Hilbert-Huang transform to seismic reflection data. Geophysics 72(2):H29–H37

Cai JH (2013) Magnetotelluric response function estimation based on Hilbert-Huang transform. Pure Appl Geophys 170:1899–1911

Cai JH, Tang JT, Hua XR, Gong YR (2009) An analysis method for magnetotelluric data based on the Hilbert-Huang Transform. Explor Geophys 40:197–205

Gairola GS, Chandrasekhar E (2017) Heterogeneity analysis of geophysical well-log data using Hilbert-Huang transform. Phys A 478:131–142

Huang NE, Wu Z (2008) A review on Hilbert-Huang transform: method and its application to geophysical studies. Rev Geophys 46:RG2006

Huang NE, Shen Z, Long SR, Wu MC, Shih HH, Zheng Q, Yen NC, Tung CC, Liu HH (1998) The empirical mode decomposition and the Hilbert spectrum for nonlinear and nonstationary time series analysis. Proc R Soc Lond Ser A Math Phys Eng Sci 454:903–993

Li H, Kwong S, Yang L, Huang D, Xiao D (2011) Hilbert-Huang transform for analysis of heart rate variability in cardiac health. IEEE/ACM Trans Comput Biol Bioinform 8:1557–1567

McDonald AJ, Baumgaertner AJG, Frasher GJ, George SE, Marsh S (2007) Empirical mode decomposition of atmospheric wave field. Ann Geophys 25:375–384

Neukirch M, Garcia X (2014) Nonstationary magnetotelluric data processing with instantaneous parameter. J Geophys Res: Solid Earth 119:1634–1654. https://doi.org/10.1002/2013JB010494

Xue Y, Cao J, Tian R (2013) A comparative study on hydrocarbon detection using three EMD-based time frequency analysis methods. J Appl Geophys 89:108–111

Zhao N, Li R (2015) EMD method applied to identification of logging sequence strata. Acta Geophys 63(5):1256–1275. https://doi.org/10.1515/acgeo-2015-0052

Chapter 17
Reservoir Characterization of Carbonate Facies Towards Hydrocarbon Exploration in Jaisalmer Sub-basin, India

Raman Chahal and Saurabh Datta Gupta

Abstract The current study has been conducted in Jaisalmer sub-basin which is a part of Rajasthan Basin. This sub-basin has been contained with clastic and carbonate both reservoir facies. The carbonate facies are mostly fractured limestone in the Jaisalmer formation which is just below of Baisakhi-Bedisar clastic sequence. Measurements at all scales from pores to sedimentary basin are analysed and interpreted to generate the micro and macro-geological models. It integrates all the available information to understand the reservoir rock and fluid information to delineate the prospects zone. It helps to simulate the behaviour of fluid and determines the distribution of properties, viz. lithology, porosity and thickness. Seismic reservoir description is a model which incorporates the hydrocarbon storage and production. Few numbers of wells have been drilled in this region, which are dry wells. The current study has been conducted based upon full-stack and partial-stack seismic data only with the help of nearby drilled well and analogue data. AVO analysis, EEI analysis and attribute study over this volume within certain time have shown some encouraging results of the study towards characterizing the carbonate reservoir facies for hydrocarbon exploration. One pseudo-well was positioned as blind well for testing the evaluated result with prospecting location position. The final result has proved that the location was placed at a sweet spot. The more prominent response from AVO analysis may be developed from the better high-resolution data set. In view of volumetric and available data set with this kind of challenging geological reservoir condition, the study has given a satisfactory outcome.

Keywords Reservoir characterization · Jaisalmer formation · AVO analysis · EEI analysis

R. Chahal (✉) · S. Datta Gupta
Indian Institute of Technology (Indian School of Mines) Dhanbad, Dhanbad, India
e-mail: ramanchahal75@gmail.com

K. H. Singh and R. M. Joshi (eds.), *Petro-physics and Rock Physics of Carbonate Reservoirs*, https://doi.org/10.1007/978-981-13-1211-3_17

1 Introduction

Jaisalmer sub-basin is the part of Rajasthan Basin with a geographical extent of 42,000 km^2. It is a pericratonic shelf basin situated on the north-western slope of the Indian Peninsular Shield (Pandey et al. 2009). It is lying in the eastern shelf part of Indus Basin and to the west of Aravalli. While traversing from north to south, we come across four sub-basins, namely Kishangarh sub-basin, Jaisalmer–Mari high, Shahgarh and Miajlar sub-basin. An alternate sequence of clastic and carbonate rocks is present in the sedimentary column of thickness 10,000 m (Singh 2006). Bikaner–Nagaur basin is separated from Jaisalmer sub-basin by Pokhran–Nachna high in the northwest, and Banner basin is separated from Jaisalmer sub-basin by Banner–Birmama–Nagarpaikar high in the south. From Jaisalmer to Mari, there is an NW-SE trending regional step-faulted high zone traversing the central path of the basin (Awasthi 2002). Marine Jurassic succession of Jaisalmer basin from older to younger are Bedesir, Baisakhi and Jaisalmer. Extension of Yellow Limestone is mainly restricted to Jaisalmer formation. In the western side of Jaisalmer basin, a prominent NNW-SSE trending fault acts as the separator between the limestone of the Jaisalmer formation and the younger shale bed of the Baisakhi formation (Srivastava and Ranawat 2015). In the formations of Jaisalmer basin namely Lower Goru and Pariwar, petroleum has been explored (www.dghindia.org).

Carbonate is the major reservoir of the oil and gas fields throughout the world. It is generally formed in shallow Warm Ocean either by the direct precipitation or by the calcium carbonate extraction out of seawater to form skeletal materials. Carbonate sediments may be confined together by the covered organisms or remain as the loose sediments transported by the ocean water (SPE 2015). Carbonate sediments are poorly sorted having a wide range of size and shapes leading to the variable primary intergranular porosity. Dunham classification for the carbonate divides it into two categories, namely organic bound and loose sediments. Pore sizes in carbonates vary considerably from micron scale to cave system, and pore spaces are classified into inter-particle and vuggy porosity. Inter-particle includes inter-grain and inter-crystal created by the porosity between the particles, and the vuggy porosity is created by the pore spaces within the grains (Shepherd 2009).

Carbonate facies are the output of the processes that are active in the depositional setting. The depositional processes like water depth, wind, current and temperature all effect the carbonate deposited (SEPM 2013). Depositional environment of the carbonate sediments ranges from tidal flats to the deepwater basin. Most of them originated in the shallow water shelf and are transported towards land or basin.

Reservoir quality modifies and often decreases after the diagenesis process. Modern carbonate sediments have enough porosity and permeability in comparison with the antique carbonate sediments (SPE 2015). As carbonate has the tendency of mixed wettability, there is greater uncertainty and difficulty in the calculation of the petrophysical parameters in case of carbonate than in case of sandstone (Shepherd 2009). The study area is situated in the highly tectonically affected zone with fault and arch.

The study area has been placed in between Shahgarh and Kishangarh sub-basins near Shahgarh area (Fig. 1).

Highly varying petrophysical properties like porosity, permeability and flow mechanism pose a great problem for characterizing the carbonate reservoir. An elaborate study of the permeability, pore size, fluid saturation, fracture system and reservoir rock type needs to be done. Fracture passage of the carbonate reservoir lies in the range of tens of metres to hundreds of kilometres (Slb information).

In this study, reservoir characterization of carbonate facies has been done by taking into account of three basic steps, namely reservoir architecture, geological model and geophysical model study of the area (Beucher and Renard 2005). Reservoir architecture includes the geometry of the reservoir and gives the information about the size and structure of the subsurface geological sedimentary rock type. The geological model includes the integrated study of geology, seismic reservoir characterization and petrophysical model development including analogue data. Geological model development can be done from the correlation between rock physics and petrophysical properties guided by the various quantitative interpretation and attribute analysis, whereas the attribute analysis for qualitative and quantitative interpretation and for capturing the distribution of reservoir lithofacies comes under geophysical study as one of the major milestones. Cross-plots of the rock physics properties with petrophysical properties were emphasized for the reservoir characterization at a finer

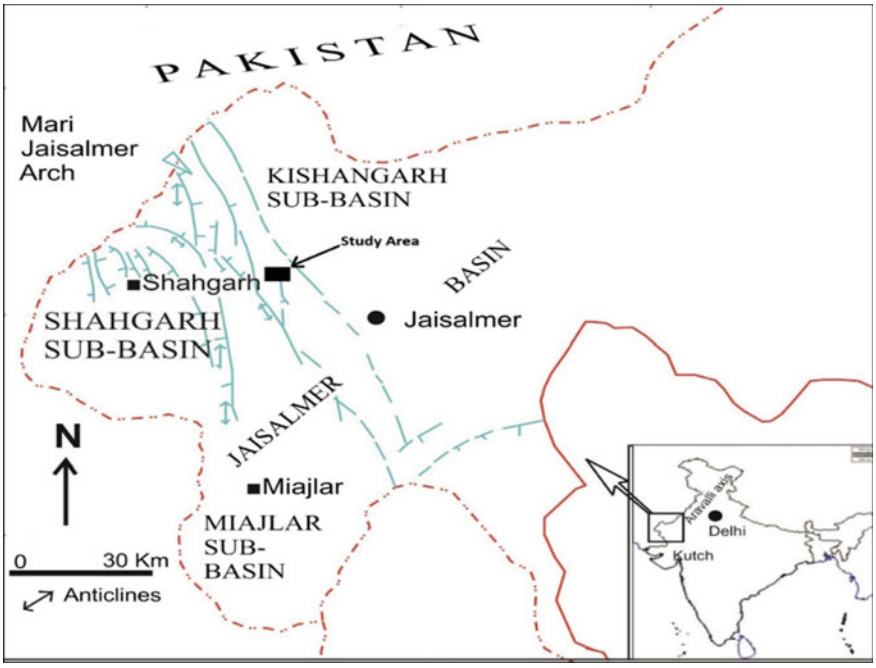

Fig. 1 Tectonic map of the Jaisalmer basin (modified after Pandey et al. 2009)

level. AVO (amplitude versus offset) analysis was performed to get a good response from high-resolution data as the reservoir fluid is gas. The study has been performed based on full-stack and partial-stack seismic data analysis, and one pseudo-well was planned for a tentative location to capture the gas bearing sand in the study area. The pseudo-well was planned based upon structural and stratigraphical analysis of the area. AVO analysis has been performed based upon partial-stack data mostly near and far angle stack data was used for this purpose. Intercept and gradient was output product after analysis of the AVO; another elastic property of the area has been analysed as extended elastic impedance (EEI). The surface attribute was analysed based on volume-based AVO and EEI operator evaluation, and extension of reservoir gas bearing limestone has been evaluated. The surface attribute was generated in the certain time window from Jaisalmer formation, i.e. 30 ms below of Jaisalmer formation.

2 Methodology

The 3D seismic coverage of the study area sector comprises of 160-km^2 full-fold seismic zero offset and partial-stack data. In general, the quality of the 3D seismic data is fair for full-stack seismic data, whereas the partial-stack seismic data quality is moderate with the presence of acquisition footprints (Fig. 2). Seismic reflectors correspond to different sequence boundaries.

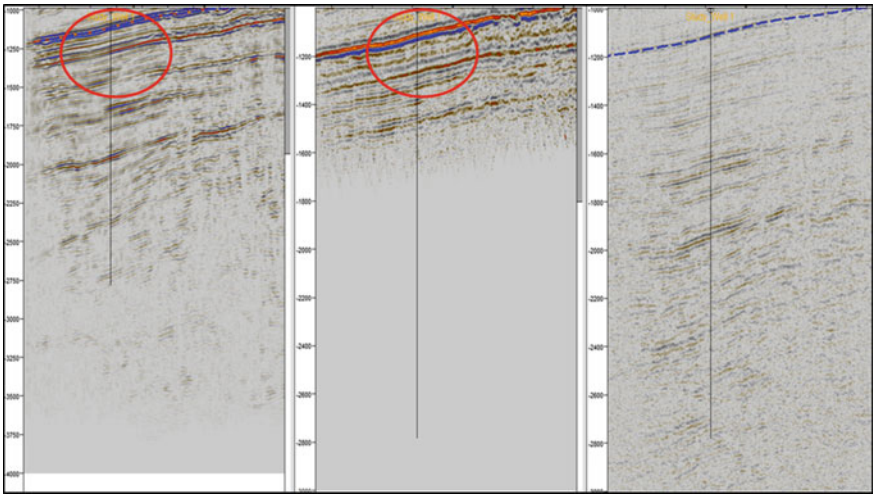

Fig. 2 Seismic section of zero, far and near offset, respectively

2.1 Well-to-Seismic Tie

Relevant log curves (compression sonic and density log) of drilled well are used to generate well-to-seismic tie. The product of sonic and density values from the respective plots generates the acoustic impedance (AI) curve. An increase in AI, therefore, corresponds to a corresponding increase in either the density or/and velocity of the respective lithology at the well location (Fig. 3). The AI curve was used to extract the reflection coefficient (Rc) which was then convolved with a selected zero phase wavelet derived from seismic data to calculate synthetic seismogram. The accuracy of synthetic seismogram will depend on the quality of well log and seismic data, the rigour of processing methodology and the efficiency in extracting a representative wavelet from seismic data (http://www.slb.com/services/software/geo/petrel/seismic/seismic_multitrace_attributes.aspx).

The derived synthetic seismograms are then used to study the discrepancies with the seismic data measured at the few selected well locations. The wavelet was estimated based upon a deterministic approach through frequency domain. The synthetic seismogram was reasonably matched with seismic data. However, the minor limitation was encountered during the creation of the synthetic as the sonic log was not available for the full length. However, horizons under the scope of work, i.e. Baisakhi-Bedisar, Jaisalmer and Lathi, are captured properly. Deeper intervals are generally less reliable on seismic section due to attenuation of signals with depth.

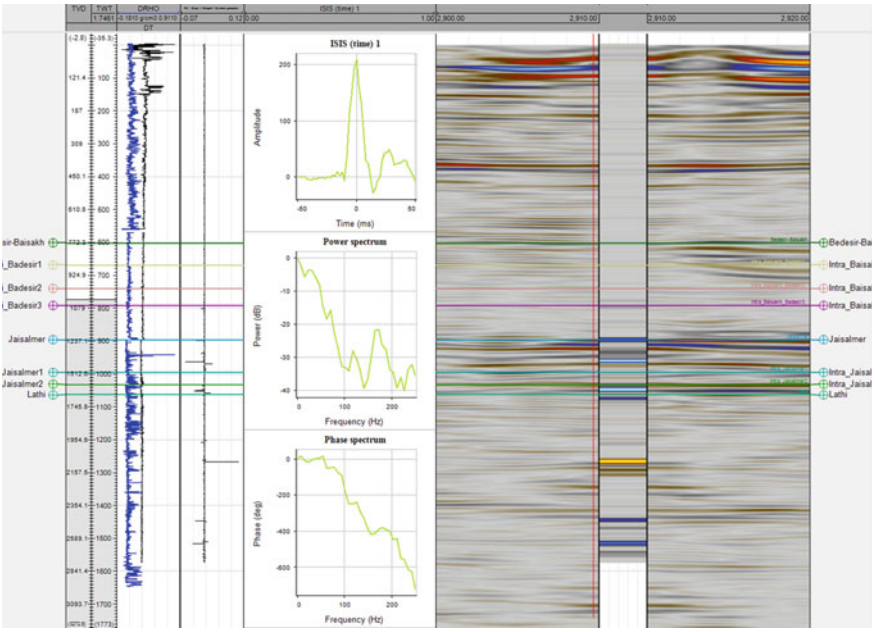

Fig. 3 Well-to-seismic tie for dry drilled well for initialization surface interpretation

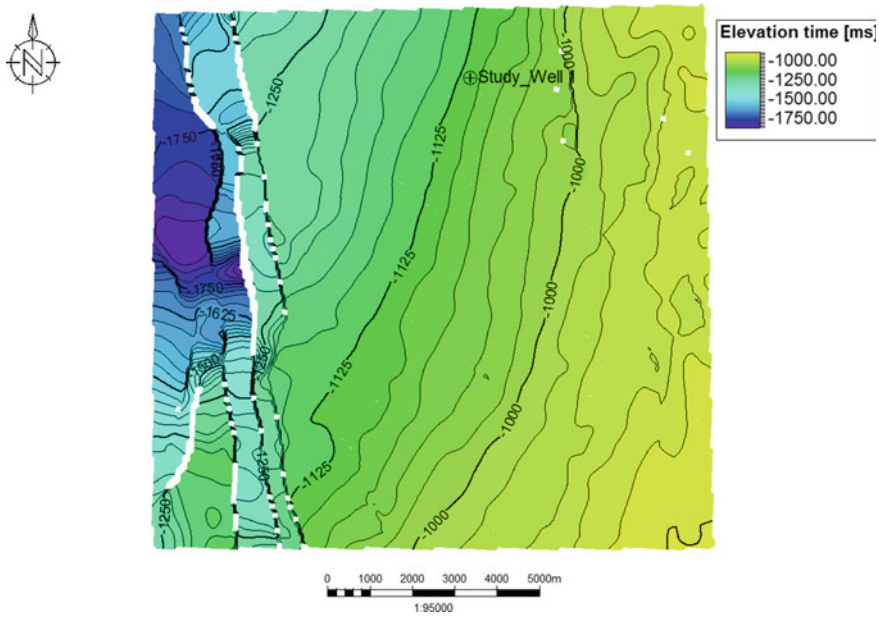

Fig. 4 Two-way structural contour map of Jaisalmer formation of the study area

Correlation is improved by the ability to observe the features of seismic data near synthetic seismogram (Willingham et al. 2013).

2.2 Time Structure Maps

The time structure map has been prepared based on well-to-seismic tie match of dry drilled well data which is away from the study area sector. Three major markers have been chosen to cover the Jaisalmer limestone lithology which is the study zone of the stratigraphic succession. The three major interpreted surfaces area Baisakhi-Bedisar, Jaisalmer and Lathi formation. The Jaisalmer formation mostly consists of Jaisalmer limestone and claystone. Figure 4 shows two-way travel time structural contour map with study well which has been placed as pseudo-well based on seismic data interpretation for Jaisalmer formation.

2.3 Velocity Modelling

A comprehensive methodology was followed in developing a best-fit velocity model by integrating all available seismic and well velocity data taken from sonic logs. The presence of velocity volume and reasonably adequate well data produce a satisfactory depth model.

2.4 Fault Interpretation

Existing reports and analogue studies show that there were at least two major tectonic events occurred in this part of the basin in Palaeocene which controlled faulting system in the area. The dense fault block has been generated with a trend of NNW-SSE which is known as Jaisalmer–Mari fault zone (Mitra et al. 1993). Initially, these fault zone is extensional in the age of early Tertiary, but latter period it has been converted to transgressional in the age of Plio-Pleistocene and reactivation evidence has been observed in the area of Jaisalmer–Mari fault zone (Mitra et al. 1993). Faults have been interpreted from mapping variance attribute as a useful edge enhancement method. This approach facilitated a clearer image of fault, thus improving confidence in their correlation.

2.5 Amplitude Versus Offset (AVO) Analysis

The current study has been focused mainly on Jaisalmer formation which is mostly limestone and claystone. As per the petroleum system analysis, the formation has the potential for production of natural gas which is also analysed by the analogue well data (Luthi 2001). Drilled well in the study area is not encouraging, and eventually, all wells have been converted as dry well. The current study has been performed over seismic data including partial stack. Since drilled well result is not encouraging, one pseudo-well has been placed tentatively based on structural and stratigraphical interpretation result. Few post-stack seismic attribute analysis also performed before positioning the pseudo-well. The objective was to characterize the reservoir based on AVO analysis and to demark the areal extension of gas bearing limestone reservoir. The AVO analysis has been performed in the Ikon Science RokDoC application. Intercept and gradient volume has been generated during the AVO operation.

The amplitude distribution for both the volumes (Figs. 5 and 6) has shown subtle amplitude development towards high impedance side from low impedance with respect to full- and partial-stack seismic volume (Fig. 2) which is turned to be an encouraging outcome for deciding sweet spot further possible location for drilling.

The relation between the reflection/transmission coefficients with incident angle was investigated by Zoeppritz equation. With the simplified form of this equation, AVO inversion can be computed to estimate elastic parameter using amplitude variation with incident angle. Simplified form as the first order of Zoeppritz equation was given by the Aki and Richards (1980) for the P-P (incident and reflected P-wave).

$$R_{\mathrm{pp}}(\theta) \approx \frac{1}{2}\left[1 - 4\left(\frac{\beta}{\alpha}\right)^2 \sin^2\theta\right]\frac{\Delta\rho}{\rho} + \frac{1}{2}\left(1 + \tan^2\theta\right)\frac{\Delta\alpha}{\alpha} - 4\left(\frac{\beta}{\alpha}\right)^2 \sin^2\theta\left(\frac{\Delta\beta}{\beta}\right) \tag{1}$$

α is the average of two P-wave velocities on both sides of the reflector

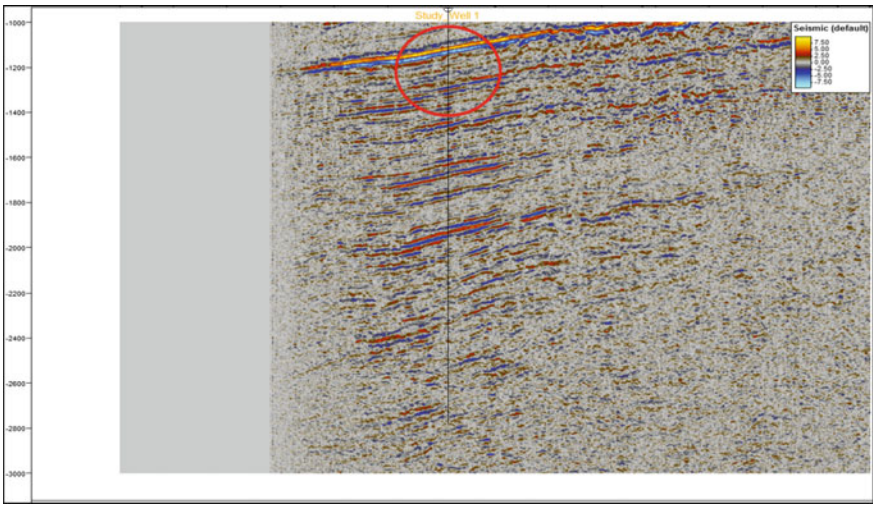

Fig. 5 Intercept volume generated from AVO analysis from near and far angle stack data

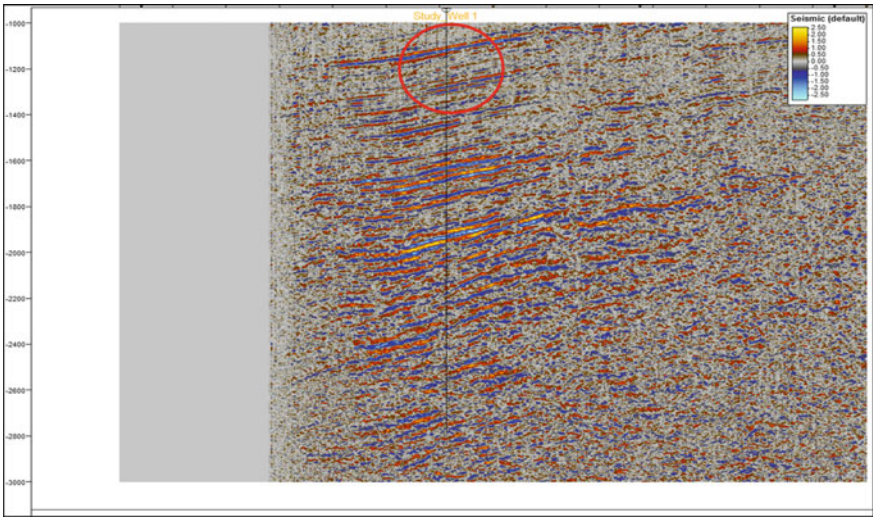

Fig. 6 Gradient volume generated from AVO analysis from near and far angle stack data

β is the average of two S-wave velocities on both sides of the reflector
ρ is the average of two density on both sides of the reflector
θ is the average of the incident and transmitted P-wave angle

$$\Delta\alpha = \alpha_2 - \alpha_1, \quad \Delta\beta = \beta_2 - \beta_1, \quad \Delta\rho = \rho_2 - \rho_1$$

An alternate simplification by Shuey (1985) where β is written in terms of σ

$$R_{PP}(\theta) \approx R_{PO} + \left[A_O R_O + \frac{\Delta\sigma}{(1-\sigma)^2} \right] \sin^2\theta + \frac{\Delta a}{2a}\left(\tan^2\theta - \sin^2\theta\right) \tag{2}$$

R_{PO} is the reflection coefficient at normal incidence
$R_{PP}(\theta)$ is the reflection coefficient at an intermediate angle
A_O is the amplitude at normal incidence

$$A_O = B_O - 2(1 + B_O)\left(\frac{1-2\sigma}{1-\sigma}\right), B_O = \frac{\frac{\Delta\alpha}{\alpha}}{\left(\frac{\Delta\alpha}{\alpha} + \frac{\Delta\rho}{\rho}\right)} \tag{3}$$

$$\Delta\sigma = \sigma_2 - \sigma_1, \quad \sigma = (\sigma_1 + \sigma_2)/2$$

Equation (3) can be simplified to

$$R_{PP}(\theta) = R_{PO} + G\sin^2(\theta) \tag{4}$$

R_{PO} is the intercept, and G is the AVO gradient (Almutlaq and Margrave 2010).

The estimation of intercept and gradient has been made based on conditioned near and far angle stack data as in the mid angle stack data there is no such kind of variation with respect to near and far angle stack data. The near angle stack data is restricted in 15°, whereas for far it is 45°. It has been observed that far angle stack seismic data has better seismic resolution than near angle stack although few features have developed in near angle stack data.

2.6 AVO Attribute

Attribute analysis is one of the important and powerful tools for capturing the fluid (natural gas) presence and extension of reservoir limestone in the study area. Primarily two AVO attributes have adopted for capturing the fluid presence in the study area. First, AVO analysis (Schlumberger 2019) and second, the AVO fluid strength which is given by

$$\text{AVO strength} = [X * (A1) + Y * (A2)] \tag{5}$$

where $A1$ is the intercept and $A2$ is the gradient. Here, $X = Y = 1$.

Equation 5 has been adopted for AVO analysis for intercept and gradient. The X and Y have been quantified as a scalar entity, whereas A1 and A2 are the intercept volume and gradient volume. Figure 7 shows the AVO analysis volume.

The surface attribute has been analysed based on volume-based operator for AVO analysis product. The volume shown in Fig. 7 was used for surface attribute analysis. The controlled surface has been chosen Jaisalmer formation. A certain time window of 30 ms was selected based on seismic and nearby well log signature of the study area. The 30 ms investigation window has been proportionally classified into 15 layers with 2 ms interval. All layers have been analysed with AVO analysis volume operator, and 28 ms window has shown some encouraging result where the amplitude has been distributed with geological significance manner. The window has been fallen under Jaisalmer formation.

To get those sweet spot "extract value" surface attribute has been implemented towards capturing reservoir limestone extension. Figure 8 is showing the areal extension of limestone reservoir facies.

The second attribute adopted for AVO analysis is fluid strength. The attribute is one of the major attributes for detecting the presence of hydrocarbon. The AVO resolution and fluid deviation are captured during analysis of this attribute. The attribute basically controlled by background trend which is deflected by fluid angle from zero to certain value of angle and increment of fluid angle has made some anomaly from normal trend (Fig. 9).

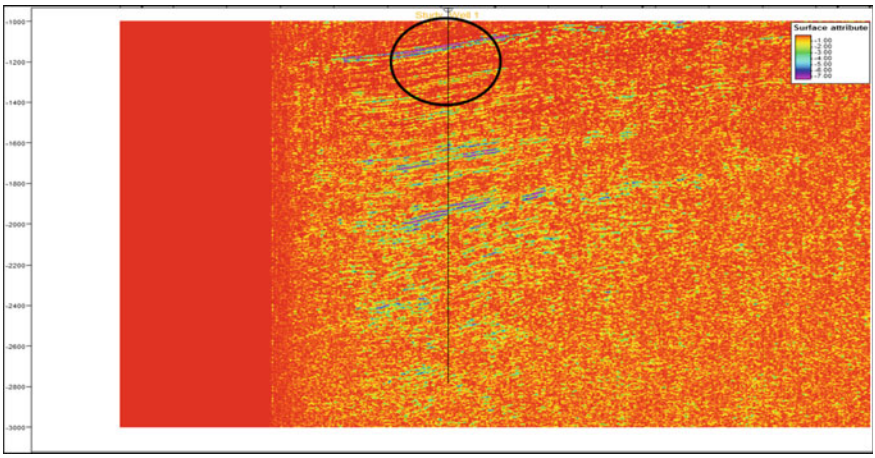

Fig. 7 AVO analysis product after generation of intercept and gradient from partial stack

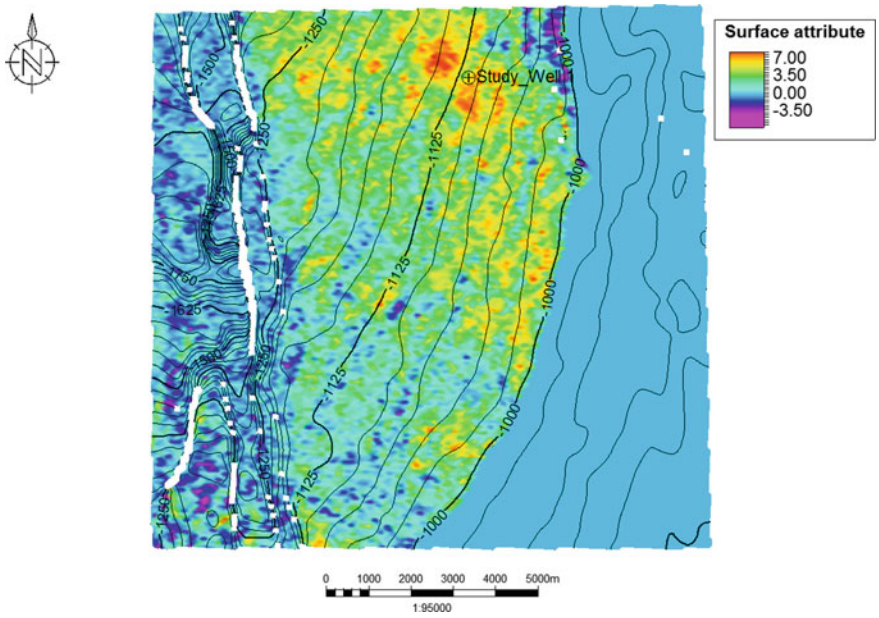

Fig. 8 Extract value attribute on AVO analysis product operator (as shown in Fig. 7)

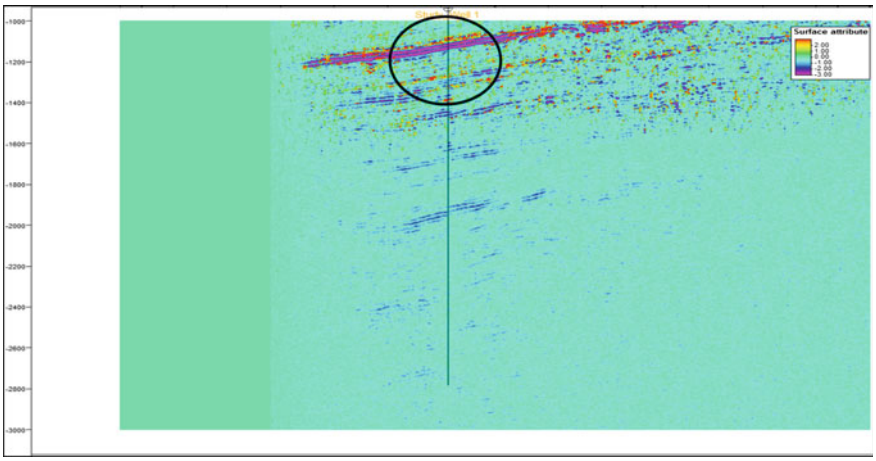

Fig. 9 Fluid strength attribute has been developed based upon fluid angle, AVO fluid strength

2.7 Extended Elastic Impedance (EEI) Attribute

EEI is one kind of strong volume-based attribute analysis which has been evaluated based upon rotation angle χ, intercept and gradient. The reservoir limestone is sensitive to subtle change of amplitude with facies, and it is sensitive with fluid angle like fluid strength attribute. So EEI has also captured reservoir limestone. Equation 6 (www.wiki.seg.org) (Whitcombe et al. 2002) has been used for calculation of EEI.

$$R(\chi) = A\cos(\chi) + B\sin(\chi) \tag{6}$$

In the above equation, A and B are showing the intercept and gradient.

The EEI has been calculated in two rotation angles 21° and 36° based upon synthetic correlation and resolving capability of Jaisalmer reservoir limestone. The 36° rotation angle evaluation of EEI has produced more detectable image for reservoir (Fig. 10).

The surface attribute has been generated based on EEI operator with same search window analogy, i.e. 30 ms with 2 ms proportionate layer classification. The reservoir limestone has been captured nicely at 28 ms with proper correlation. Figure 11 shows the limestone reservoir facies captured in EEI operator. The EEI has been generated from intercept and gradient. Better data quality from near stack data may produce high-resolution image.

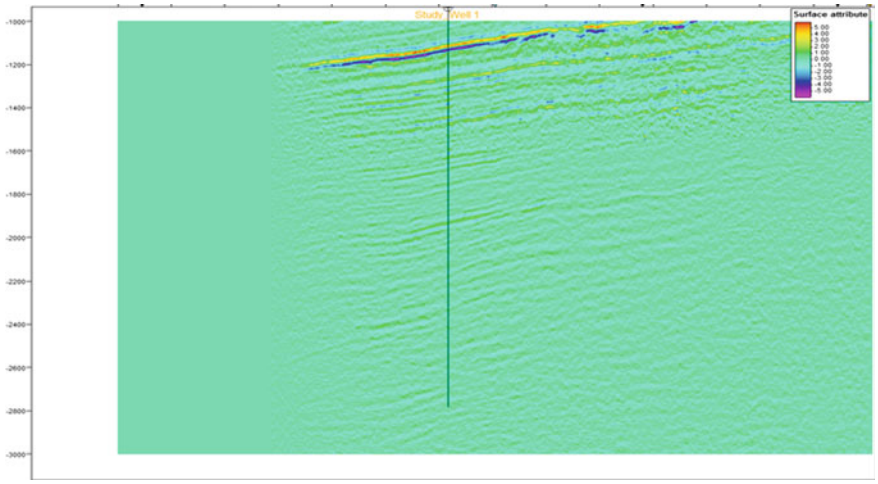

Fig. 10 EEI volume has been generated based upon 36° rotation angle

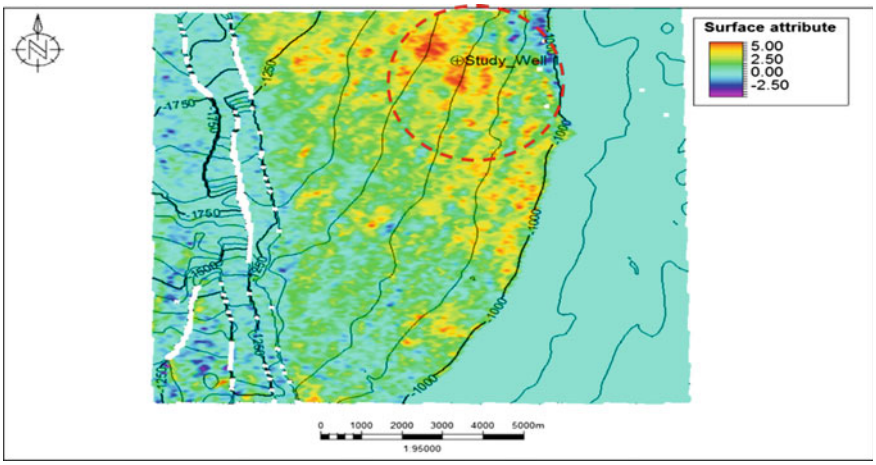

Fig. 11 Extract value attribute on EEI operator

3 Results and Discussions

The full study has been conducted based on seismic data analysis with support of nearby dry drilled well and analogue data. Primarily, the seismic interpretation has been carried out based on full-stack seismic data and later on partial-stack seismic data. Both structural and stratigraphical study was conducted based on above-mentioned data and post-stack seismic attribute analysis. The study was capable to find out one tentative location in the study area which is considered as pseudo-well for the current study. Petroleum system has shown the presence of natural gas in the study area. But current seismic data quality, earlier drilled well results and presence of local reservoir lithofacies are not enough supportive for further encouraging result.

In the second instance finer level study with partial-stack seismic data with subtle changes of amplitude has been captured through AVO analysis and EEI analysis. The surface-based attribute analysis from Jaisalmer with fine layering has captured the tentative presence of gas bearing limestone of Jaisalmer formation. Near and far angle stack data was used for AVO analysis where during EEI volume estimation, intercept and gradient along with 21° and 36° chi angle were used. Apart from intercept and gradient, AVO fluid angle and AVO fluid strength were also evaluated for surface attribute analysis.

The study has shown that increase in impedance, i.e. the high amplitude, has been reduced with offset. The scenario has made chances of Class 1 AVO response in the study under Jaisalmer reservoir limestone (Fig. 12). The classes have been estimated based on Aki–Richards two-term and Zoeppritz compressional wave evaluation. The classes was evaluated based on P-wave and S-wave velocity and density values. P-wave velocity has been estimated from seismic velocity estimation model, and from P-wave value, S-wave velocity was estimated.

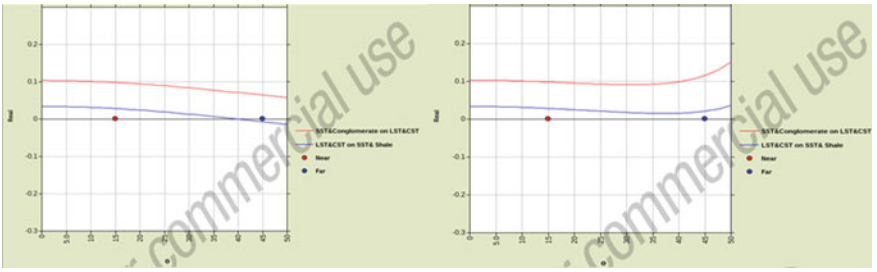

Fig. 12 AVO classes evaluated from V_p, V_s and density value of pseudo-well position

Figure 12 shows the AVO classes which have been estimated between Baisakhi-Bedisar formation and Lathi formation. Sandstone and conglomerate lithology is primarily dominating in Baisakhi formation, Jaisalmer formation has been dominated by limestone and claystone rock type, whereas sandstone and shale are in dominating position in Lathi formation. Red colour line is showing Baisakhi-Bedisar as upper lithology and Jaisalmer as lower lithology, whereas blue colour line is showing Jaisalmer as upper lithology and Lathi as lower lithology.

Monte Carlo iteration (Kroese et al. 2014; Macary et al. 1999) has run over V_p, V_s and density value-based intercept and gradient output with 1000 number of iteration through weighted stack for capturing gradient positioning of data point towards evaluating of AVO classes (Fig. 13).

The estimated weighted stack relation may be defined as,

$$W_s = 0.0527 * I - 0.084 - G \tag{7}$$

W_s is weighted stack value, and I and G are intercept and gradient.

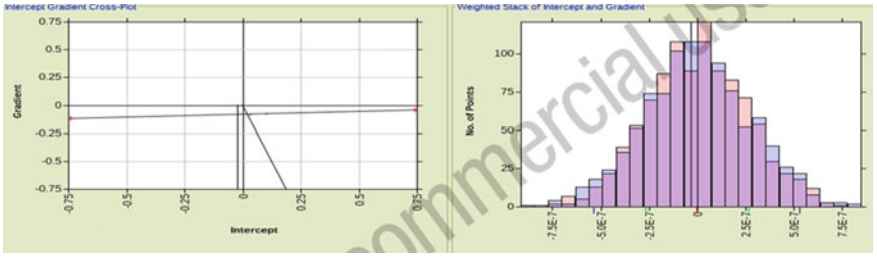

Fig. 13 Monte Carlo (Wikipedia information) simulation with 1000 iteration for weighted stack estimation towards AVO class findings

4 Conclusions

The study has been conducted in such kind of area where success ratio is very less towards hydrocarbon exploration from Jaisalmer formation. The current study has been performed using only seismic data (full and partial). One pseudo-well was proposed as blind well to test the final output result for location proposal area. This has been proved that location was positioned in right place. AVO and EEI operator-based attribute analysis and window extracted value surface attribute analysis have shown the nice distribution of Jaisalmer limestone reservoir facies distribution. The carbonate reservoir facies is carrying Class 1 AVO response. Good-quality high-resolution seismic data with special well log data such as FMI and NMR/CMR will take this quantitative analysis in advance stage, and through detailed advance study, chances will be high of Jaisalmer formation from hydrocarbon production point of view.

Acknowledgements The authors extend their thanks to the Gujarat State Petroleum Corporation (GSPC, Gandhinagar, Gujarat) for making available all log and seismic data for research purposes. Schlumberger Petrel, Ikon Science RokDoc and IHS Kingdom are kindly acknowledged for providing the academic licences to the Department of Applied Geophysics, IIT (ISM) Dhanbad, for carrying out the research and development work. Prof. Rima Chatterjee, IIT (ISM) Dhanbad, is gratefully acknowledged for her invaluable suggestions during the entire tenure of this work.

References

Aki KT, Richards PG (1980) Quantitative seismology: theory and methods. In: Freeman WH (ed) and Co, vol 1

Almutlaq MH, Margrave GF (2010) Tutorial: AVO inversion. CREWES research report, vol 22. https://www.crewes.org/ForOurSponsors/ResearchReports/2010/CRR201002.pdf. Accessed 20 Mar 2019

Awasthi AM (2002) Geophysical exploration in Jaisalmer Basin—a case history. http://www.spgindia.org/geohorizon/jan2002/am_awasthi.PDF. Accessed 20 Mar 2019

Beucher H, Renard D (2005) Reservoir characterisation. Centre de Géostatistique, Ecole des Mines de Paris, France. https://www.geovariances.com/wp-content/uploads/2016/08/beucher-2005.pdf. Accessed 20 Mar 2019

Kroese DP, Brereton T, Taimre T, Botev ZI (2014) Why the Monte Carlo method is so important today. WIREs Comput Stat 6(6):386–392. https://doi.org/10.1002/wics.1314

Luthi SM (2001) Geological well logs. Springer, Berlin, pp 317–318

Macary SM, Hassan A, Ragaee E (1999) Better understanding of reservoir statistics is the key for reliable Monte Carlo simulation. Society of Engineers, SPE-53264-MS. https://doi.org/10.2118/53264-MS

Mitra P, Mukherjee MK, Mathur BK, Bhandari SK, Qureshi SM, Bahukhandi GC (1993) Exploration and hydrocarbon prospect in Jaisalmer, Rajasthan. In: Biswas SK, Pandey J, Dave A, Maithani A, Garg P, Thomas NJ (eds) Proceedings of the second seminar on petroliferous basins of India, vol 2. West Coast Basins, Indian Petroleum Publishers, pp 235–284

Pandey DK, Fürsich FT, Sha J (2009) Inter-basinal marker intervals—a case study from the basins of Kachchh and Jaisalmer, western India. Sci China Ser D Earth Sci 52(12):1924–1931

Schlumberger (2019) Carbonate reservoirs. http://www.slb.com/services/technical_challenges/carbonates.aspx. Accessed 20 Mar 2019

SEPM (2013) Depositional setting and geometry of carbonate facies. http://www.sepmstrata.org/page.aspx?pageid=90. Accessed 20 Mar 2019

Shepherd M (2009) Carbonate reservoirs. In: Shepherd M (ed) Oil field production geology: AAPG Memoir 91, pp 301–309. http://wiki.aapg.org/Carbonate_reservoir. Accessed 20 Mar 2019

Shuey RT (1985) A simplification of the Zoeppritz equations. Geophys 50:609–614

Singh NP (2006) Mesozoic lithostratigraphy of the Jaisalmer Basin, Rajasthan. J Palaeontol Soc India 51(2):1–25

SPE (2015) Carbonate reservoir geology. http://petrowiki.org/Carbonate_reservoir_geology. Accessed 20 Mar 2019

Srivastava N, Ranawat TS (2015) An overview of Yellow Limestone deposits of the Jaisalmer Basin, Rajasthan, India. Volumina Jurassica XIII(1):107–112

Whitcombe DN, Connolly PA, Reagan RL, Redshaw TC (2002) Extended for and prediction. Geophysics 67:63–67. https://doi.org/10.1190/1.1451337

Willingham CR, Rietman JD, Heck RG, Lettis WR (2013) Correlation procedures between well logs and seismic reflection data. U.S. Department of the Interior, U.S. Geological Survey Bulletin 1995-CC, p 105

Part V
Clastic Reservoir Characterization

Chapter 18
Petrophysical Characterization of Sandstone Reservoir from Well Log Data: A Case Study from South Tapti Formation, India

N. P. Singh, S. P. Maurya and Kumar Hemant Singh

Abstract The present study is aimed at evaluating the reservoir potentials of South Tapti Basin of India with limitation to the available data. A number of petrophysical parameters, i.e., effective porosity (Φ), water saturation (S_w), formation water resistivity (R_w), hydrocarbon saturation (S_o), and true resistivity (R_t), are evaluated using the well log data, and the reservoir characterization is performed. The analysis shows a hydrocarbon-bearing zone in between 1866 and 1874 m, which contains gamma ray (GR) value of 34.4 API, resistivity of 117.3 Ω m, and average porosity of 35.7%. To know the fluid type in the reservoir zone, neutron porosity and density porosity are plotted together and a crossover has been noticed at 1866–1874 m depth which indicates that the reservoir is filled with gas. The analysis of petrophysical parameters and cross-plots shows that the reservoir is filled with sandstone with some clay content separated by shale markers, which act as seal rock for the reservoir.

Keywords Petrophysical characterization · South Tapti Basin · Sandstone reservoir · Cross-plots · Hydrocarbon saturation

1 Introduction

Well logs have been successfully used in exploration and development wells and are routinely used to quantify depth and thickness of productive zones (Adeoti et al. 2009; Maurya and Singh 2015). Schlumberger brothers in Alsace, France, first introduced geophysical well logging technique in 1927. Logging is carried out by physical measurements (sonde) made by instruments lowered into the hole (geophysical logs) and supported by laboratory experiments on core samples (Ofwona 2014). Immediately after the well is drilled, the formations are exposed to well-bore and this is

N. P. Singh · S. P. Maurya (✉)
Department of Geophysics, Institute of Science, Banaras Hindu University, Varanasi 221005, India
e-mail: spm.iitb@gmail.com

K. H. Singh
Department of Earth Sciences, Indian Institute of Technology, Bombay, Maharashtra 400076, India

K. H. Singh and R. M. Joshi (eds.), *Petro-physics and Rock Physics of Carbonate Reservoirs*, https://doi.org/10.1007/978-981-13-1211-3_18

the best time to determine the properties of rocks in the vicinity of borehole using open-hole logging tools. In wells with complex trajectories, logging tools are used as part of drilling tool assembly. This approach is termed as logging while drilling (LWD) (Economides and Nolte 1989). Important logs include temperature, pressure, gamma, neutron, caliper log, and resistivity. The main objective of petrophysical well log analysis is to transform well log measurements into reservoir properties like permeability, porosity, oil saturation, water saturation, mineralogy, etc. The proposed study aims at interpretation of well log data and quantitative evaluation of petrophysical properties such as water saturation in parts of South Tapti Basin.

The South Tapti field covers an approximately area of 570 square miles and lies approximately 100 miles north-northwest of Mumbai City, India. In this paper, well log analysis is performed on the logs obtained from wells comprising the clastic sediments of late Oligocene Daman formation in South Tapti Field (Wandrey 2004; Saha et al. 2009). The quality of reservoir in terms of parameters like shale volume, effective porosity, water and hydrocarbon saturation, and permeability are evaluated, and the results are discussed.

2 Methodology

The well log data from the South Tapti Field is made available for research and development by BG, India. An essential step in formation evaluation process is the determination of amount of shale present in the formation (Opuwari 2010; Adaeze et al. 2012). This helps to calculate the correct formation porosity and fluid content within the pay zone. Volume of shale is calculated following the integrated approach by utilizing the gamma ray log, SP log, neutron–density log, and resistivity log data (Adeoti et al. 2009). Porosity is also calculated from density log. From the qualitative observation of log plots, the crossover in neutron–density log, low intensity value of natural gamma ray log, separation in shallow and deep resistivity log values, suppression in SP log and higher value in sonic log suggested the presence of hydrocarbons between 1866 and 1874 m depth in the study area.

The analysis is performed in the depth range of 1830–1930 m as the reservoir zone is expected within this interval. Water saturation is calculated using Archie's equation. The other important petrophysical parameters, i.e., permeability, are calculated using the Timur equation in which irreducible water saturation is calculated from the bulk volume water (BVW). The bulk volume water is calculated at several depths within the reservoir zones. A constant or near constant values indicate a single rock-type bearing zone at irreducible water saturation. When a zone is at irreducible water saturation, water in the uninvaded zone (S_w) does not move as it is held on grains by capillary pressure.

3 Petrophysical Evaluation

The log data from South Tapti Formation is evaluated, and the derived petrophysical parameters along with other logs are shown in Fig. 1. The figure shows the natural gamma ray (GR), resistivity (R_t/R_{xo}), porosity (PhiD/Nphi), shale volume (VshND/VshGR), and effective porosity (PhiE) log calculated from the well log data. The analyses of log data show interesting features between depth interval 1866–1874 m. The natural gamma ray values are very low, the flushed zone and the invaded zone resistivity is very high, and there is marked crossover when the density and the neutron porosity logs are plotted together. Within the same interval, the shale volume calculated from gamma ray log and neutron log shows a low value, while the estimated effective porosity is very high. This analysis suggests that this could be a prospective hydrocarbon-bearing zone which needs further detailed analysis for its characterization.

Cross-plots are charts based on the slope and intercept of two porosity log responses (depending on matrix lithology, and pore fluid). The cross-plots of bulk density against P-impedance and lambda-rho against Poisson's ratio are generated for the depth interval 1830–1930 m (Fig. 2a). The cross-plot in Fig. 2a shows concentration of low bulk density and P-impedance values indicating prospective reservoir zone between 1866 and 1874 m. This low value indicates the presence of hydrocarbon

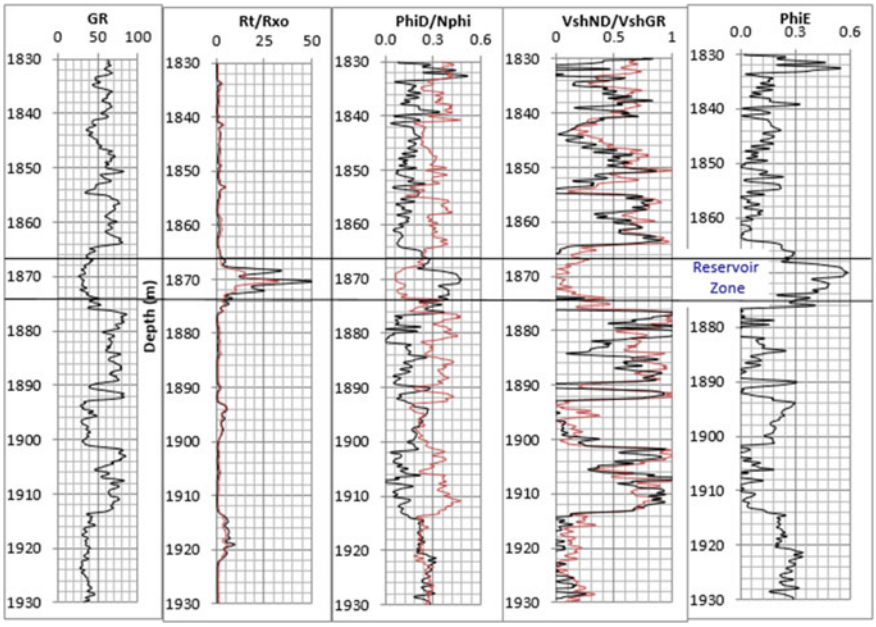

Fig. 1 Gamma ray, resistivity log, porosity log, shale volume, and effective porosity log calculated from well log data

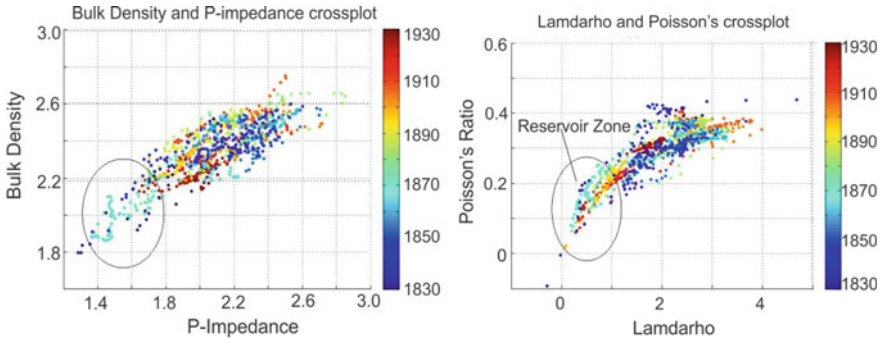

Fig. 2 Cross-plot between **a** the bulk density and the P-impedance and Poisson's ratio and **b** the Lambda-rho cross-plot. The color bar indicates depth

in this zone. The cross-plot between Lambda-rho and Poisson's ratio shows a similar concentration of low values within the zone between 1866 and 1874 m (Fig. 2b). The cross-plots in Fig. 2a, b suggest that this zone is possibly hydrocarbon bearing and reiterates the qualitative analysis of gamma ray, neutron and density porosity, and resistivity logs.

4 Lithology Identification

An interpretation of lithology is performed through a systematic approach. The gross lithology is collaborated and compared at the same depth, horizontally, to the gamma ray log. Cross-plots are prepared for classification of sandstone, limestone, and dolomite lithologies. When data points from lithology are plotted, they fall on the charts lithology lines.

When combinations of those lithologies are present, the points mostly fall between the lines. The porosity is determined by joining the data points and constructing a porosity scale between major lithologies (Rider 2000).

4.1 Neutron–Density Cross-Plot

One of the methods available for porosity log analysis involves the density–neutron cross-plot. A cross-plot method, called the shaly sand model, is widely used. However, this model is considered to be a poor model for any sandstone that contains other minerals in addition to quartz. The complex lithology model works well in quartz sands and is a preferred model for analysis (Adaeze et al. 2012).

Neutron–density cross-plot shows scattered data distributed on the entire line (dolomite, limestone, and sandstone) suggesting the presence of these three minerals

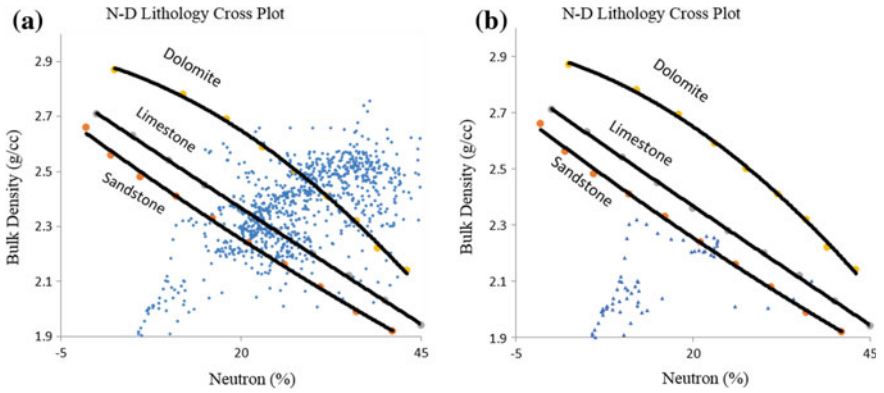

Fig. 3 Bulk-density versus neutron–density cross-plot **a** for depth 1830–1930 m, **b** for reservoir zone (1866–1974 m)

between 1830 and 1930 m (Fig. 3a). The neutron and density porosity cross-plot for reservoir zone (depth 1866–1874 m) is shown in Fig. 3b. The figure shows that almost all plots lie on or below the sandstone line shows the rock type dominated by sandstone in the reservoir zone with some level of limestone.

4.2 Sonic–Neutron Cross-Plot

The sonic–neutron cross-plot method involves the simultaneous solution of the sonic and neutron response equations for porosity. Complex lithology is best suited to this method. Since both logs respond to shale, the formulae do not work in shaly sands with same accuracy (Crain 2002).

The sonic–neutron cross-plot shows the scatter of points spreading across all three rock types (sandstone, limestone, and dolomite) but mostly lies between sandstone and limestone (Fig. 4a). The figure suggests that a mixture of sandstone, limestone, and dolomite in small quantity is present between depth intervals 1830 and 1930 m. Figure 4b shows the cross-plot in the depth range of reservoir (1866–1877 m) which shows data lying along the sandstone line or above it. This figure indicates that the reservoir zone is dominated by sandstone rock types.

4.3 Sonic–Density Cross-Plot

The sonic–density cross-plot method involves a simultaneous solution of the sonic and density response equations for porosity. The sonic–density cross-plot works

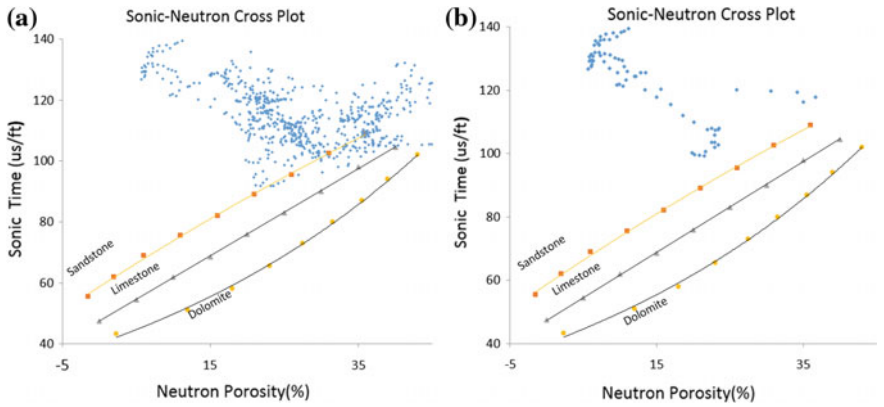

Fig. 4 Sonic time versus neutron porosity cross-plot **a** for depth 1830–1930 m, **b** for reservoir zone (1866–1877 m)

ideally in shaly sands with no gas. The resolution is poor in carbonates, and the presence of gas makes the result too high (Rider 2000).

The sonic–density cross-plot in Fig. 5a shows the scatter of plotted points inclined toward dolomite line indicating the presence of dolomite in the formation. The sonic–density cross-plot for reservoir depth also shows a similar response suggesting the dominance of dolomite in the reservoir zone (Fig. 5b). The cross-plot does not appear to be accurately predicting the lithology compared to other cross-plots (Figs. 3 and 4) because the distance between the sandstone, limestone, and dolomite line is too small to reliably predict the lithology. Thus, the cross-plot in Fig. 5 is not reliable and not considered for our analysis.

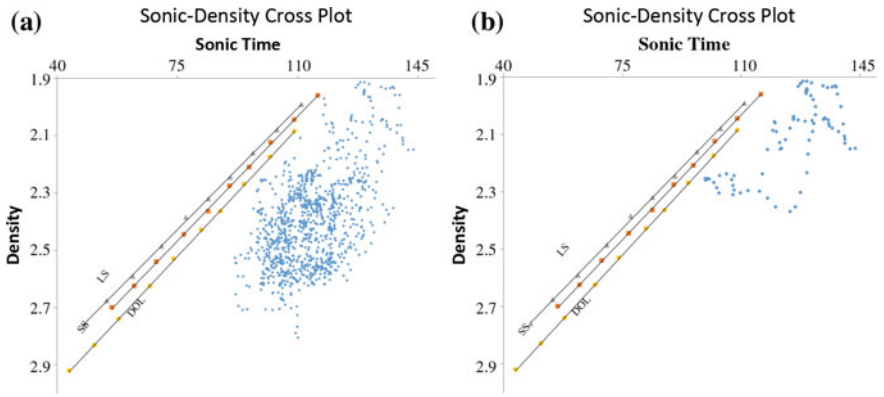

Fig. 5 Sonic time versus density porosity cross-plot **a** for depth 1830–1930 m, **b** for reservoir zone (1866–1877 m)

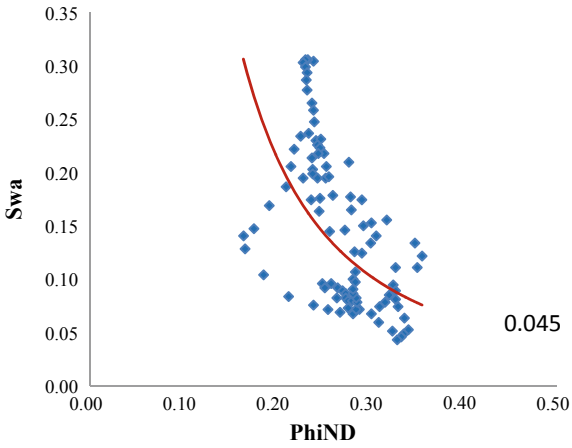

Fig. 6 Bulk-volume-water cross-plot (Swa vs. PhiND)

4.4 Bulk Volume Water

The product of a formation's water saturation (S_w) and its porosity is the bulk volume water (BVW) , BVW $= S_w * \emptyset$. If values for bulk volume water calculated at several depths in a formation are constant or very close to constant, they indicate that the zone is of a single rock type with irreducible water saturation (S_{wirr}). When a zone has irreducible water saturation, water in the uninvaded zone (S_w) does not move because it is held on grains by capillary pressure. Therefore, hydrocarbon production from a zone at irreducible water saturation should be water-free (Morris and Biggs 1967).

The Buckles plot (Asquith et al. 2004) is a graph of porosity (φ) versus S_w. Points of equal *BVW* form hyperbolic curves across this plot. If *BVW* is plotted using data from a formation at irreducible water saturation, the points fall along a single hyperbolic curve. If the data come from reservoirs with higher percentages of produced water, the points are more scattered. For the reservoir zone (1865–1875 m), the Buckles plot shows saturation value of 0.045. So, it is irreducible water. Figure 6 shows the plot of bulk volume water.

4.5 Residual Oil Saturation (ROS)

ROS is the saturation value of the oil that remains after a displacing process of crude oil system by water or gas injection. Residual oil saturation is oil saturation that cannot be produced from an oil reservoir from gas or water displacement. It is usually considered the immobile oil saturation after conventional (gas or water displacement) (Crain 2002).

ROS is given by:

$$\text{ROS} = 1 - S_{\text{xo}} \tag{1}$$

where S_{xo} is water saturation in flushed zone.

4.5.1 Movable Oil Saturation (MOS)

It is important to recognize that only a fraction of oil in place is ultimately produced in most reservoirs. This poses a challenge to attain better recovery, requiring a thorough understanding of reservoir behavior (Waldschmidt et al. 1956). This necessitates the estimation of movable oil saturation, which represents the maximum volume of oil that can be moved or produced. Hence, the movable oil saturation is defined as:

$$\text{Movable oil saturation} = \text{initial oil saturation} - \text{residual oil saturation}$$

$$\text{MOS} = S_{\text{xo}} - S_{\text{w}} \tag{2}$$

where S_{w} is water saturation and S_{xo} is saturation in flushed zone (Asquith et al. 2004).

4.6 Movable Hydrocarbon Index (MHI)

The movable hydrocarbon index is given by

$$\text{MHI} = \frac{S_{\text{w}}}{S_{\text{xo}}} \tag{3}$$

Water saturation of the flushed zone (S_{xo}) can be used as an indicator of hydrocarbon moveability. If the value of S_{xo} is much larger than S_{w}, then hydrocarbons in the flushed zone have probably been moved or flushed out of the zone nearest the borehole by the invading drilling fluids (R_{mf}). If the ratio $S_{\text{w}}/S_{\text{xo}}$ is equal to or greater than 1.0, then hydrocarbons were not moved during invasion. This is true regardless of whether or not a formation contains hydrocarbons. Whenever the ratio $S_{\text{w}}/S_{\text{xo}}$ is less than 0.7 for sandstones or less than 0.6 for carbonates, moveable hydrocarbons are indicated (Schlumberger 1991).

The computed bulk volume water, residual oil saturation, moveable oil saturation, and moveable hydrocarbon index are given in Table 1 along with the depth, porosity estimated from neutron (NPHI) and density (PHID) log and water saturation for reservoir zone only. Table 2 contains the estimated lithology from cross-plots with PEF-derived lithology, volume of shale, and porosity estimated from density log (PhiD) for a depth range of 1854–1874 m.

Table 1 Reservoir properties estimated for depth from 1866 to 1874 m (reservoir zone)

DEPTH	NPHI	PHID	SW	BVW	ROS	MOS	MHI
1866.0	0.24	0.25	0.24	0.06	−0.14	0.89	0.21
1866.5	0.23	0.28	0.18	0.05	0.06	0.77	0.19
1867.0	0.22	0.27	0.20	0.05	0.09	0.71	0.22
1867.5	0.20	0.24	0.21	0.05	0.12	0.67	0.24
1868.0	0.12	0.20	0.12	0.02	0.23	0.65	0.15
1868.5	0.09	0.35	0.05	0.02	0.62	0.33	0.14
1869.0	0.06	0.44	0.05	0.02	0.64	0.30	0.15
1869.5	0.06	0.46	0.07	0.03	0.60	0.33	0.17
1870.0	0.06	0.48	0.04	0.02	0.71	0.25	0.13
1870.5	0.07	0.46	0.03	0.02	0.81	0.15	0.17
1871.0	0.12	0.39	0.05	0.02	0.51	0.43	0.11
1871.5	0.11	0.36	0.07	0.02	0.48	0.45	0.13
1872.0	0.07	0.39	0.05	0.02	0.57	0.37	0.13
1872.5	0.08	0.39	0.07	0.03	0.57	0.35	0.17
1873.0	0.12	0.38	0.12	0.05	0.50	0.38	0.25
1873.5	0.16	0.37	0.10	0.04	0.54	0.36	0.21
1874.0	0.35	0.28	0.17	0.05	0.37	0.46	0.28

5 Determination of Cutoff and Net Pay

The final aim of any petrophysical analysis is to find net pay thickness with proper petrophysical cutoffs. Net pay determination usually involves defining threshold values (or cutoffs) of the characteristics of interest. These limiting values are designed to define those rock volumes that are not likely to contribute significantly to the hydrocarbon production. The starting point in determining cutoff is to identify reference parameter that allows us to distinguish between intervals that have reservoir potential and intervals that do not. There is no single applicable approach to the identification of cutoff (Worthington and Cosentino 2005).

There are several techniques or criteria to define cutoffs; clean rocks with low volume of shales Vsh usually have few problems and have capability to store hydrocarbons (Hamada 1996). As a rock becomes shalier, it becomes a poor reservoir rock. There is a point of Vsh beyond which there are no more significant contribution to store hydrocarbons. That point could be taken as Vsh cutoff for pay rocks. The same concept applies for total porosity ϕ_t.

Table 2 Predicted lithology on the basis of PE factor and cross-plots

DEPTH (m)	PEF	Vshale (%)	PhiD (%)	Lithology (On the basis of PEF)	Lithology (On the basis of xplot)
1850.0–1850.1	2.9	63	7	Sandy shale	Dolomite + limestone + sandstone
1850.2–1851.1	3.6	84	9	Compact shale	Dolomite + limestone + sandstone
1851.2–1852.5	2.7	58	18	Sand + shale (18% Phi)	Dolomite + limestone + sandstone
1852.6–1853.3	3.4	45	9	Compact shale	Dolomite + limestone + sandstone
1853.4–1854.6	2.4	25	19	Sand + dolomite	Dolomite + limestone + sandstone
1854.7–1855.1	1.8	44	16	Sand with water (16% Phi)	Dolomite + limestone + sandstone
1855.2–1855.3	2.4	68	10	Sandy shale	Dolomite + limestone
1855.4–1855.5	3.4	70	13	Shale	Dolomite + limestone
1855.6–1855.8	4.1	77	17	Shale + limestone(17% Phi)	Dolomite + limestone
1855.9–1856.4	3.5	87	9	Shale	Dolomite + limestone
1856.5–1857.0	3.9	83	11	Compact shale	Dolomite + limestone
1857.1–1858.7	2.6	73	12	Sandy shale	Dolomite + limestone
1858.8–1859.4	2.2	62	14	Sand + uncompact shale	Dolomite + limestone
1859.5–1859.7	2.9	73	12	Uncompact sandy shale	Dolomite + limestone
1859.8–1860.0	3.7	84	9	Compact shale	Dolomite + limestone
1860.1–1860.7	4.5	68	9	Halite + shale	Dolomite + limestone
1860.8–1860.8	3.7	73	5	Compact shale	Dolomite + limestone
1860.9–1862.1	3.1	66	8	Sandy shale	Dolomite + limestone
1862.2–1862.3	3.8	69	10	Compact shale	Dolomite + limestone
1862.4–1863.8	4.3	89	8	Shale + limestone	Dolomite + limestone
1863.9–1864.1	3.4	86	9	Shale	Dolomite + limestone

(continued)

Table 2 (continued)

DEPTH (m)	PEF	Vshale (%)	PhiD (%)	Lithology (On the basis of PEF)	Lithology (On the basis of xplot)
1864.2–1864.2	2.5	67	11	Sand + shale	Dolomite + limestone
1864.3–1865.6	2.0	15	33	Sand with water (33% Phi)	Dolomite + limestone
1865.7–1866.0	2.2	19	24	Sandstone	Dolomite + limestone
1866.1–1866.2	2.0	14	26	Sandstone	Sandstone
1866.3–1869.5	2.1	15	31	Sandstone with gas (31% Phi)	Sandstone
1869.6–1869.9	1.8	9	40	Sandstone with water (40% Phi)	Sandstone
1874.0–1874.0	2.7	42	28	Dolomite + sand	Dolomite + limestone + sandstone
1874.1–1874.6	3.3	29	27	Dolomite + sand	Dolomite + limestone + sandstone

5.1 Determination of Petrophysical Cutoff

Net pay is defined as the thickness of rock that contributes to economically viable production with today's technology, today's prices, and today's costs. Net pay is obviously a moving target since technology, prices, and costs vary almost daily.

Tight reservoirs or shaly zones that were bypassed in the past are now prospective pay zones due to new technology and continued demand for hydrocarbons. We determine net pay by applying appropriate cutoffs to reservoir properties so that unproductive or uneconomic layers are not counted. This can be done with both log and core data (if available).

Cumulative reservoir properties, after appropriate cutoffs are applied, provide information about the pore volume (PV), hydrocarbon pore volume (HPV), and flow capacity (KH) of a potential pay zone. These values are used to calculate hydrocarbon in place, recoverable reserves, and productivity of wells. The following algorithm is a highly simplified one-pass approach, which would need considerable adjustment to run on a real computer. However, it is suitable for discussion purposes (Guo 2004).

It is normal to apply cutoffs to each calculated result to eliminate poor quality or unproductive zones. Cutoffs are usually applied to shale volume, porosity, water saturation, and permeability. The layer is not counted as "pay" if it fails any one of the four cutoffs. Typical cutoffs are:

$$\mathrm{IF}(\mathrm{VSH}_{\max} \leq \mathrm{SH}_{\max}) * (\mathrm{PHI}_{\mathrm{e}} \geq \mathrm{PHI}_{\min}) * (S_{\mathrm{w}} \leq \mathrm{SW}_{\max}) = 1 \tag{5}$$

$$\mathrm{THEN\ PAYFLAG} = 1$$

$$\mathrm{ELSE\ PAYFLAG} = 0$$

$$H_{\mathrm{net}} = \mathrm{SUM}(\mathrm{PAYFLAG} * \mathrm{INCR}) \tag{6}$$

where:

H_{net} = net pay
INCR = digitizing increment
$\mathrm{PHI}_{\min}$ = porosity cutoff (fractional)
$\mathrm{PHI}_{\mathrm{e}}$ = effective porosity (fractional)
S_{w} = water saturation (fractional)
$\mathrm{SW}_{\max}$ = saturation cutoff (fractional)
VSH = volume of shale (fractional)
$\mathrm{VSH}_{\max}$ = shale volume cutoff (fractional).

Typically:

$\mathrm{VSH}_{\max}$ = 0.25–0.45
$\mathrm{PHI}_{\min}$ = 0.03–0.16
$\mathrm{SW}_{\max}$ = 0.30–0.70.

These values must be appropriate for the rock sequence. Values in unconventional reservoirs may be more extreme. In reservoir simulation work, the net reservoir is also needed. In this case, set $SW_{max} = 1.00$ (Guo 2004). The effective porosity, water saturation, reservoir, and net pay zone are shown in Fig. 7. Table 3 describes the numerical values of the net pay estimation. The pay thickness is estimated to be 10.8 m, whereas residual and non-residual thicknesses are estimated to be 12 m and 1 m, respectively.

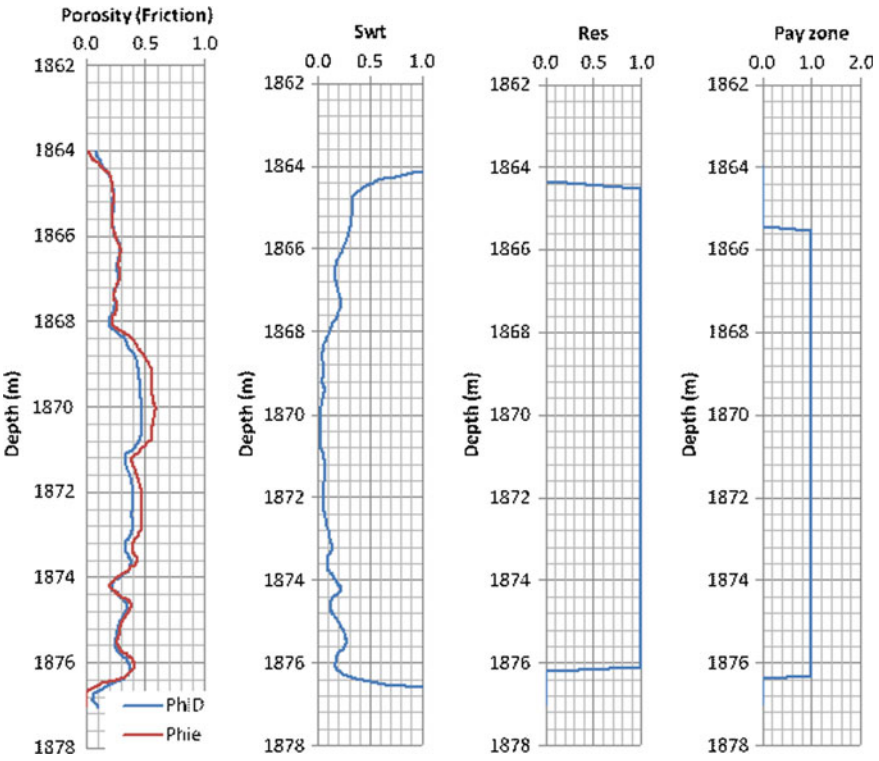

Fig. 7 Porosity, water saturation, reservoir, and net pay zone (left to right) of the area

Table 3 Net pay estimation of the South Tapti basin

Top (m)	Bottom (m)	Interval (m)	Pay (m)	Res	Non-res	Total thickness (m)
1864	1877	13	10.8	12	1	13

6 Conclusions

1. The volume of shale is calculated using gamma ray and neutron–density log which shows a trend without much variation till 1865 m before it shows a marked decrease in volume until a depth of 1876 m. The volume of shale decreases again between 1914 and 1930 m depth.
2. The depth interval between 1866 and 1874 m witnesses the neutron and the density porosity crossover indicating the presence of a gas zone. The gamma ray count is also low in this zone. The average porosity however is high (30–45)%. This suggests along with the cross-plot results that the reservoir is sandstone with high porosity between 1866 and 1874 m.
3. The water saturation is very low in the reservoir zone, and resistivity curve in deep region (R_t) is high concurring with our inference for the presence of a gas zone.
4. The lithology is predicted using different cross-plots like neutron–density, sonic–neutron, and sonic–density which also indicates the presence of sandstone reservoir at (1866–1874) m and limestone at (1841–1845) m and (1900–1915) m.
5. The flushed zone water saturation is found using resistivity of mud filtrate and resistivity of flushed zone. Residual oil saturation(ROS) , movable oil saturation (MOS), and movable hydrocarbon index (MHI) are found, and it is observed that hydrocarbons are movable as MHI < 0.7.
6. Reservoir and pay zone analysis is performed, and it is found that the reservoir is 12 m thick and pay zone is 10.8 m thick which makes it a good reservoir.

Acknowledgements I would like to thank BG, India, for providing the well log data for South Tapti Basin for research and development work.

References

Adaeze IU, Samuel OO, Cajetan JI (2012) Petrophysical evaluation of Uzek well using well log and core data, Offshore Depobelt, Niger Delta, Nigeria. Adv Appl Sci Res 3(5):2966–2991

Adeoti L, Ayolabi EA, James PL (2009) An integrated approach to volume of shale analysis: Niger Delta example, Offrire Field. World Appl Sci J 7(4):448–452

Asquith GB, Krygowski D, Gibson CR (2004) Basic well log analysis, vol 16. American Association of Petroleum Geologists, Tulsa, TX, USA

Crain ER (2002) Crain's petrophysical handbook. Spectrum 2000 Mindware Ltd., Alberta, Canada

Economides MJ, Nolte KG (1989) Reservoir stimulation, vol 2. Englewood Cliffs, Prentice Hall, NJ, USA

Guo R (2004) Supplement to determining method of cut-off value of net pay. Petroleum Exploration and Development. http://en.cnki.com.cn/Article_en/CJFDTOTAL-SKYK200405044.htm. Accessed 22 Mar 2019

Hamada GM (1996) An integrated approach to determine shale volume and hydrocarbon potential in shaly sand. In: SCA international symposium. http://www.jgmaas.com/SCA/1996/SCA1996-41.pdf. Accessed 21 Mar 2019

Maurya SP, Singh KH (2015) LP and ML sparse spike inversion for reservoir characterization—a case study from Blackfoot area, Alberta, Canada. In: 77th EAGE conference and exhibition. https://doi.org/10.3997/2214-4609.201412822

Morris RL, Biggs WP (1967) Using log-derived values of water saturation and porosity. In: Society of petrophysicists and well-log analysts, 8th annual logging symposium, Denver, CO, USA, 12–14 June

Ofwona CO (2014) Introduction to geophysical well logging and flow testing. Short Course V on Exploration for Geothermal Resources. https://orkustofnun.is/gogn/unu-gtp-sc/UNU-GTP-SC-11-35.pdf. Accessed 22 Mar 2019

Opuwari M (2010) Petrophysical evaluation of the Albian age gas bearing sandstone reservoirs of the OM field, Orange basin, South Africa. Ph.D. dissertation, University of the Western Cape. https://core.ac.uk/download/pdf/58914267.pdf. Accessed 22 Mar 2019

Rider MH (2000) The geological interpretation of well logs, 2nd edn. Whittles Publishing, Caithness, UK

Saha S, Stuart DB, Stuart G, Thurlow A, Andy T (2009) The stratigraphic and sedimentological evolution of the Mahim, Daman and Mahuva formation reservoirs of the Tapti fields: tidally-influenced deposition in an Oligo-Miocene tropical estuarine embayment on the continental shelf of Western India. In: AAPG Hedberg conference, Jakarta, Indonesia. http://www.searchanddiscovery.com/pdfz/abstracts/pdf/2010/hedberg_indonesia/abstracts/ndx_saha.pdf.html. Accessed 22 Mar 2019

Schlumberger (1991) Log interpretation principles/applications. Schlumberger Educational Services. https://www.slb.com/resources/publications/books/lipa.aspx. Accessed 21 Mar 2019

Waldschmidt WA, Fitzgerald PE, Lunsford CL (1956) Classification of porosity and fractures in reservoir rocks. Am Assoc Petrol Geol Bull 40:953–974

Wandrey C (2004) Bombay geologic province eocene to miocene composite total petroleum system, India. U.S. Geological Survey Bulletin 2208-F. https://pubs.usgs.gov/bul/2208/F/b2208-f.pdf. Accessed 17 Mar 2019

Worthington PF, Cosentino L (2005) The role of cut-offs in integrated reservoir studies. SPEREE 8(4):276–290. https://doi.org/10.2118/84387-PA

Chapter 19
Sensitivity Analysis of Petrophysical Parameters Due to Fluid Substitution in a Sandstone Reservoir

S. P. Maurya, N. P. Singh and Kumar Hemant Singh

Abstract In the present study, the CO_2 storage potential of a subsurface sandstone layer of the Blackfoot field, Alberta, Canada, is evaluated. In this study, seismic reservoir monitoring has been performed to monitor fluid flow effects in seismic amplitudes. In order to monitor CO_2 fluid viability, the Gassmann fluid substitution analysis is also performed to analyze the seismic amplitude response along with the seismic forward modeling which is used to generate seismic data from the geological model. From the seismic forward modeling, a significant variation in seismic amplitude is recognized due to fluid substitution. From the Gassmann approach, considerable changes in P-wave and S-wave velocities, densities, and impedances are observed with increasing CO_2 saturation. From the results, it is observed that the sudden drop in acoustic impedance occurs between 0 and 20% CO_2 saturation and that leads to the detectable time shift at the top of the CO_2 plume. Further, amplitude versus offset (AVO) and Lambda-mu-rho (LMR) analyses have been performed to demonstrate the detectability capacity of these parameters due to the change in fluid saturation in the porous media. In addition, time delays at the injected reflector are also measured. The changes caused by the CO_2 plume in the seismic section are also identified by subtracting the monitor model (CO_2 saturated model) from the baseline model (0% CO_2 saturated model) in time domain as well as in impedance domain. The proposed amount of CO_2 injection is considered as 10^5 tonnes for one year of injection. The study demonstrates that the CO_2 plume can be detected in a more detailed way with very high resolution by working in impedance domain rather than working in time domain.

Keywords Acoustic impedance · Model-based inversion · Gassmann's equation · Well log analysis · Fluid replacement modeling

S. P. Maurya (✉) · N. P. Singh
Department of Geophysics, Institute of Science, Banaras Hindu University, Varanasi 221005, India
e-mail: spm.iitb@gmail.com

K. H. Singh
Department of Earth Sciences, Indian Institute of Technology, Bombay, Maharashtra 400076, India

K. H. Singh and R. M. Joshi (eds.), *Petro-physics and Rock Physics of Carbonate Reservoirs*, https://doi.org/10.1007/978-981-13-1211-3_19

1 Introduction

Global warming is a major concern of the society in recent time which is increasing day by day due to an increase in the concentration of greenhouse gasses in the atmosphere, particularly carbon dioxide (CO_2) (Fanchi 2001; Chadwick et al. 2010). Many researchers from the globe are working on the principle to reduce safely the concentration of CO_2 from the atmosphere. CO_2 sequestration in geological formation is one solution to reduce the amount of CO_2 from the atmosphere (Nordbotten et al. 2005). The goal of this technique is to capture waste CO_2 from power plants and factories before releasing it in the atmosphere, transport it to the storage site, and inject into the porous formation sealed by non-porous formation.

The CO_2 sequestration to reduce its concentration from the atmosphere came into the existence in 1970 and got popular in 1980 (Ivanova et al. 2012). There are four major steps involved in CO_2 sequestration project and those are as follows: (1) CO_2 capture from large point sources, (2) compression of CO_2, (3) transport of CO_2, and (4) injection of CO_2 into the geological formation (Pevzner et al. 2011). This study is related to the fourth step especially prior to injection, modeling, and assessment.

The aim of the present study is to demonstrate that what would be the effect on time-lapse seismic response due to fluid replacement in the porous geological formation. The target is to find the most sensitive petrophysical parameters due to CO_2 plume simulation in the geological formation. For analysis, post-stack seismic data and 13 well logs are used from the Blackfoot field, Canada. Our target zone lies near to 1550 m depth that is sandstone layer. It is also noticed that the sandstone layer is sealed by non-porous shale formation. For this purpose, the Gassmann fluid substitution is performed and the variations in rock properties parameters like velocity, density and impedance, Lame parameters and AVO parameters (A and B) are calculated with increasing CO_2 saturation. The most sensitive parameters found here are Lame parameters ($\lambda\rho$ and $\mu\rho$) which show maximum change due to fluid substitution. Further, seismic forward modeling has been performed and the change in seismic pattern is examined due to fluid substitution. The P-wave velocity is found to be most sensitive parameter which shows the largest change in seismic amplitude.

2 Petrophysical Analysis Due to Fluid Substitution

One of the principle objectives of this study is to evaluate the changes in petrophysical parameters caused by the fluid substitution in geological formation. These petrophysical changes are expected to be reflected in seismic response (Gassmann 1951). The Gassmann equations are used for fluid replacement modeling, and changes in velocity, density, impedance, Lame parameters and AVO parameters are calculated with increasing CO_2 saturation (Chadwick et al. 2009). The well log data from well 08-08 is used as reference log. Velocity, density, gamma ray, etc., are plotted together, and the entire region is divided into 6 layers. Layer 5 is identified as porous formation

(sandstone) and hence is chosen to perform the fluid substitution. The above and below layers of layer 5 (sandstone) are identified as non-porous formation which acts as a sealed rock and prevents fluid leakage from porous formation. The target formation is at 1552–1576 m depth with the thickness of 24 m. Table 1 summarizes velocity and density values for each layer, and Fig. 1 shows velocity and density from well log data along with identified layers.

3 Gassmann Fluid Substitutions

Fluid substitution modeling is an important tool in time-lapse seismic modeling (Chadwick et al. 2009). In this study, Gassmann fluid substitution equation is used to evaluate CO_2 injection in geological formation. Velocities and densities are initial input used in Gassmann fluid substitution equation along with frame rock bulk modulus (K^*), matrix bulk modulus (K_0), rock shear modulus (G), and porosity (φ). If the fluid saturation will be modified, the bulk density (ρ_b) and fluid bulk modulus (K_{fl}) will be also changed (Xue et al. 2006). Gassmann established a relation among the saturated bulk modulus (K_{sat}), rock bulk modulus (K^*), porosity (φ), rock shear modulus (G), bulk density (ρ_b), and fluid bulk modulus (K_{fl}) (Gassmann 1951). The relationship is as follows:

$$K_{sat} = K^* + \frac{\left(1 - \frac{K^*}{K_0}\right)^2}{\frac{\varphi}{K_{fl}} + \frac{1-\varphi}{K_0} - \frac{K^*}{K_0^2}} \tag{1}$$

This K_{sat} is related to the P-wave and S-wave velocities using the following formula,

$$V_P = \sqrt{\frac{K_{sat} + \frac{4G}{3}}{\rho_b}} \tag{2}$$

$$V_S = \sqrt{\frac{G}{\rho_b}} \tag{3}$$

Gassmann equations are developed in MATLAB, and fluid substitution is performed. The important calculated results are P-wave velocity, the S-wave velocity, V_P/V_S change, the $\lambda\rho$ changes, and the $\mu\rho$ changes with increasing CO_2 saturation. Table 1 shows the variation of these petrophysical parameters due to fluid substitution, and Table 2 shows corresponding changes in petrophysical parameters with respect to 100% water saturation. The result shows that the P-wave velocity drops abruptly between 0 and 20% saturation and then increases slowly with increasing CO_2 saturation (Fig. 2a).

Table 1 Variation of petrophysical parameters with CO_2 saturation calculated by using Gassmann fluid substitution equation

CO_2	V_P	V_S	ρ	Z_P	Z_S	$\lambda\rho$	$\mu\rho$	A	B
0	3852	2106	2.38	9184	5020	33.93	25.20	0.114	−0.200
10	3748	2111	2.37	8894	5008	28.93	25.08	0.102	−0.218
20	3744	2116	2.36	8842	4997	28.25	24.97	0.099	−0.219
30	3748	2121	2.35	8810	4985	27.92	24.85	0.098	−0.219
40	3755	2126	2.34	8782	4973	27.67	24.73	0.097	−0.218
50	3762	2131	2.33	8757	4961	27.47	24.61	0.095	−0.217
60	3770	2136	2.32	8733	4949	27.30	24.49	0.094	−0.216
70	3778	2141	2.31	8710	4937	27.13	24.37	0.093	−0.215
80	3787	2147	2.29	8688	4924	26.97	24.25	0.092	−0.214
90	3796	2152	2.28	8665	4912	26.82	24.13	0.091	−0.213
100	3805	2157	2.27	8643	4900	26.67	24.01	0.090	−0.212

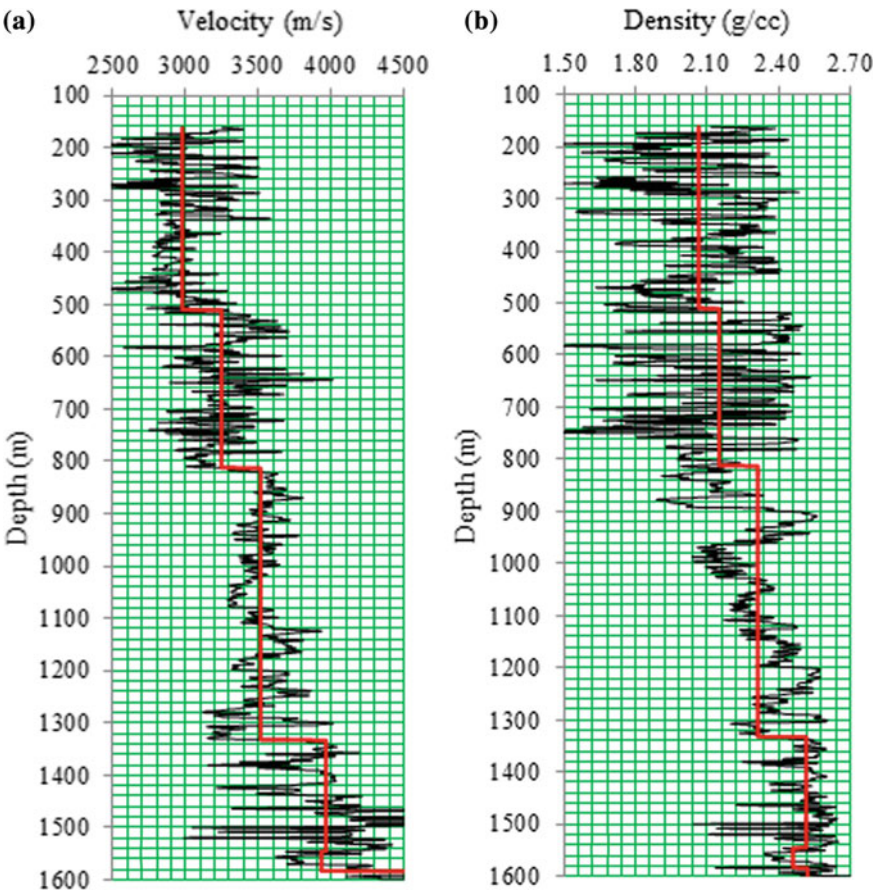

Fig. 1 Representation of layers (red line) which is defined on the basis of well log data (black line). **a** Velocity in m/s and **b** density in g/cc with varying depth in m

S-wave velocity increases with CO_2 saturation which can be seen from Fig. 2b. The density decreases inversely with increasing CO_2 saturation which is evident from Fig. 2c. The V_P/V_S decreases with the increase in CO_2 saturation due to the increase in S-wave velocities and decrease in P-wave velocities (Table 1 and Fig. 2d).

Figure 3a depicts the variation of $\lambda\rho$ with CO_2 saturation. The $\lambda\rho$ drops abruptly between 0 and 20% CO_2 saturation, and after that, it becomes approximately constant for higher value of CO_2 (Fig. 3b). The average decrease in $\lambda\rho$ is 21.4% which is much greater than V_P, V_S and ρ changes. The $\mu\rho$ decreases inversely with increasing CO_2 saturation. The average decrease in $\mu\rho$ with respect to 100% water saturation is 4.7%. The Lame parameters show more rapid change due to fluid substitution compared to the other petrophysical parameters.

Table 2 Change of petrophysical parameters due to fluid substitution (CO_2)

CO_2	V_P cha. (%)	V_S cha. (%)	ρ cha. (%)	Z_P cha. (%)	Z_S cha. (%)	$\lambda\rho$ cha. (%)	$\mu\rho$ cha. (%)	A cha. (%)	B cha. (%)
0	0.00	−0.01	0.00	0.00	0.00	0.00	0.00	0.00	0.00
10	−2.70	0.22	−0.47	−3.16	−0.24	−14.76	−0.47	−11.05	8.88
20	−2.80	0.46	−0.95	−3.72	−0.47	−16.74	−0.95	−13.13	9.43
30	−2.70	0.70	−1.42	−4.07	−0.71	−17.74	−1.42	−14.5	9.31
40	−2.53	0.94	−1.89	−4.37	−0.95	−18.45	−1.89	−15.65	8.99
50	−2.34	1.19	−2.36	−4.64	−1.19	−19.04	−2.36	−16.72	8.59
60	−2.13	1.43	−2.84	−4.90	−1.43	−19.56	−2.84	−17.75	8.13
70	−1.91	1.68	−3.31	−5.15	−1.67	−20.05	−3.31	−18.75	7.65
80	−1.68	1.93	−3.78	−5.40	−1.91	−20.51	−3.78	−19.73	7.16
90	−1.45	2.18	−4.25	−5.65	−2.15	−20.96	−4.25	−20.71	6.64
100	−1.22	2.44	−4.73	−5.89	−2.39	−21.39	−4.73	−21.68	6.12

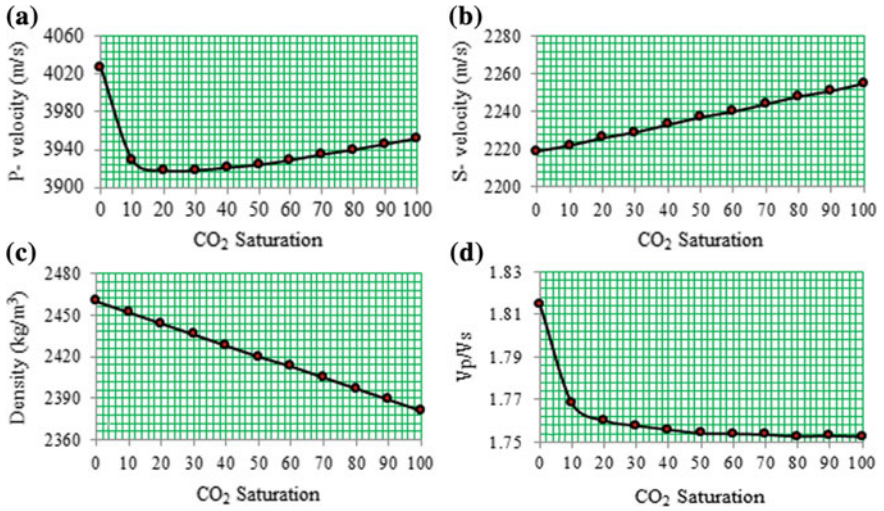

Fig. 2 Variation of **a** P-wave velocity, **b** S-wave velocity, **c** density, and **d** V_P/V_S with CO_2 saturation

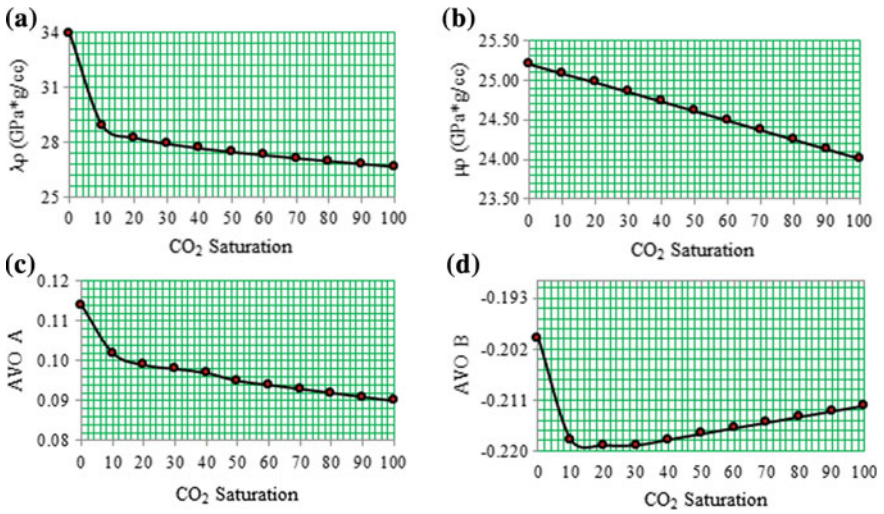

Fig. 3 Variation of **a** $\lambda\rho$, **b** $\mu\rho$, **c** AVO A (zero offset), and **d** AVO B (intercept) with CO_2 saturation

4 Amplitude Verses Offset (AVO) Analysis

Seismic amplitude versus offset (AVO) analysis is a powerful geophysical tool for direct detection of gas from the seismic records. AVO combines P-wave velocity, S-wave velocity, density, and angle of incidence to calculate the changes in seismic amplitude; therefore, it should be more sensitive for discrimination of CO_2 fluid (Bachu et al. 1994). This technique uses Shuey's (1985) approximation equation which is very simple, involves less parameters, and is easy for calculation as compared to the Zoeppritz equation (Shuey 1985; Mathieson et al. 2010).

The AVO analysis is applicable for two-layer earth models; layer 1 is considered as the layer above the injection zone, and layer 2 is considered as the injection zone. The velocities and density of layer 1 is V_{P1}= 3497 m/s, V_{S1}= 1665 m/s, and ρ_1= 2390 kg/m^3. The values of layer 2 will depend on the CO_2 saturation and are summarized in Table 1. There are two main equations which deal with the AVO analysis. The first equation relates to the reflection coefficient (R_0) with velocity and density.

$$R_0 = \frac{V_2\rho_2 - V_1\rho_1}{V_2\rho_2 + V_1\rho_1} \tag{4}$$

where V_1 and ρ_1 are the velocity and density of the first layer, respectively, whereas V_2 and ρ_2 are the velocity and density of the second layer, respectively (Ghaderi and Landrø 2009). The second equation which relates to the angle of incidence and R_{PP} is as follows:

$$R_{PP} = A + B\sin^2\theta_i + C\left(\tan^2\theta_i - \sin^2\theta_i\right) \tag{5}$$

where A is the reflection coefficient at zero offset, B is called the gradient and describes the small angle behavior, and C describes the large angle (Nordbotten et al. 2005). For small offset, Eq. 5 can be written as follows:

$$R_{PP} = A + B\sin^2\theta_i \tag{6}$$

Table 1 summarizes the results of AVO analysis and shows decrease in both the parameters A and B. The analysis shows that the AVO parameters A decreases maximum up to 22% and B decreases up to 10% with CO_2 saturation. Comparing these results with the one obtained from the Gassmann fluid substitution of V_P (change 2.8%) and V_S (change 2.5%), it is possible to see that the change in the AVO parameters A and B is considerably high due to fluid substitution. Figure 3c shows the variation of AVO parameter A, whereas Fig. 3d depicts the variation of AVO parameter B with CO_2 saturation.

5 Time-Lapse Seismic Response Evaluation

Time-lapse seismic response evaluation is traditional method for monitoring reservoir behavior due to fluid substitution. In many cases, the effect of the change in reservoir pressure and/or the fluid saturation are used to map the pattern change of the reservoir properties by obtaining seismic data repeatedly during the production phase (Moradi and Lawton 2015; Vadapalli and Vedanti 2016). Using this concept, the sensitivity analysis of petrophysical parameters has been carried out and changes in seismic pattern have been monitored. A well 08-08 is chosen for analysis. Fluids in the sandstone layer (layer 5) are systematically replaced by CO_2 in steps of 10% increase in saturation. The top of the sandstone reservoir is 1552 m, and the bottom is 1576 m; the thickness of the reservoir is 24 m. To carry out forward modeling, the velocity and density structure of the reservoir at initial saturation conditions is available from sonic and density logs. Synthetic sonic and density logs are generated for each CO_2 saturation level. To monitor the seismic response of sandstone with changes in fluid saturation, a ricker wavelet of 30 Hz frequency is convolved with the reflectivity series and zero offset synthetic seismic traces are generated (Landrø 2002). The synthetic seismic traces are also generated without CO_2 injection in the reservoir and are considered as baseline data (Fig. 4a). Synthetic seismograms generated for varying saturation of CO_2 in the reservoir represent monitored data (Fig. 4b).

The amplitude of seismic trace is increasing with increasing CO_2 saturation (Fig. 4b). Steep drop in P-wave velocity and $\lambda\rho$ is observed until CO_2 saturation reaches 20%. After that, stage variation in these quantities is subtle (Fig. 4c). Figure 4d shows the variation of seismic amplitude due to changes in S-wave velocity caused by the fluid substitution. Figure 4e shows variation in density with varying CO_2 saturation along with seismic amplitude. From Fig. 4e, it can be noticed that the density decreases as CO_2 saturation increases. Figure 4f shows $\lambda\rho$ variation with CO_2 saturation. Up to 20% CO_2 saturation, the $\lambda\rho$ shows significant difference, and after that, it looks approximately constant. Figure 4g shows variation of $\mu\rho$ with CO_2 saturation which shows a continuous decrease in values with increase in CO_2 saturation, but it decreases with very low value and hence is difficult to detect from seismic patterns.

6 2D Seismic Modeling

Seismic modeling has been performed for assessing the ability of seismic methods to detect the CO_2 plume accurately. In this regards, a 2D geological model of the site is generated to represent the structure and stratigraphy of the area. In addition, the CO_2 plume is designed and inserted as second body in the geological model to represent the post-injection scenario. A 2D seismic simulation has been performed on the geological models representing the pre-injection and post-injection scenarios.

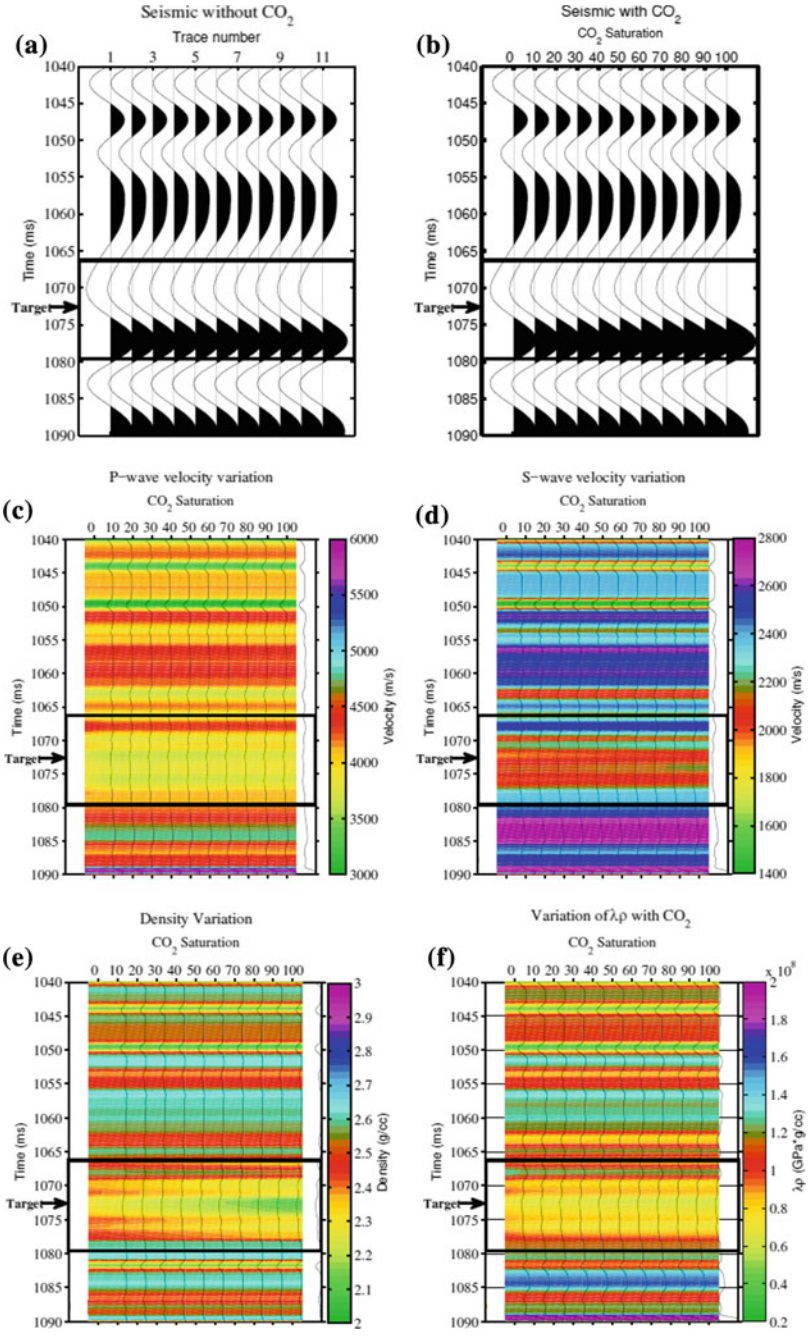

Fig. 4 **a** Baseline seismic data without CO_2 injected, **b** monitor seismic data generated with CO_2 saturation, **c** modeled P-wave velocity after CO_2 injection, **d** modeled S-wave velocity after CO_2 injection, **e** modeled density, **f** modeled $\lambda\rho$, and **g** modeled $\mu\rho$, for varying saturation of CO_2

Fig. 4 (continued)

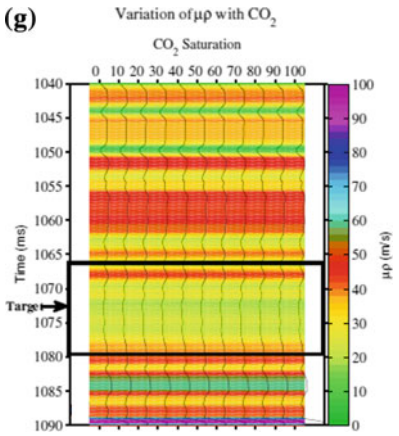

The final aim is to evaluate the time-lapse difference to demonstrate whether seismic data can be used to monitor the CO_2 plume in the sandstone target or not.

The geological model represents the subsurface structure in the zone of interest of 4 km long cross section and 2 km deep. The horizons are filled with constant V_P, V_S and ρ between the inter faces. Figure 5 shows geological model filled with P-wave velocity, and target zone is highlighted by the rectangle. Further, CO_2 plume shape and size is designed on the basis of amount that will be injected in geological formation.

The amount of CO_2 for the injection is considered 100,000 tonnes for one year. The thickness of the porous formation is 24 m, and the porosity in this zone is found

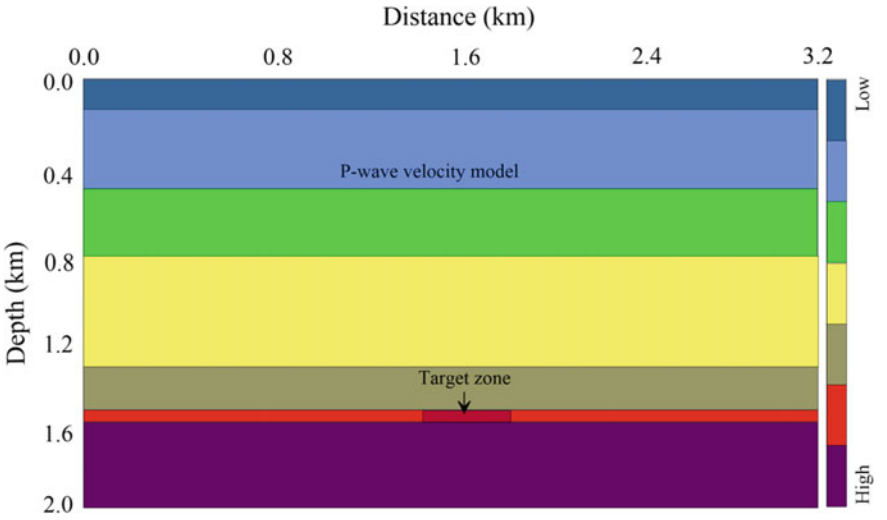

Fig. 5 Geological model inserted P-wave velocity used for modeling

to be 12%. The efficiency E is considered as the saturation of CO_2. The CO_2 plume size is calculated by considering 20% CO_2 ($E = 0.20$) saturation, and the reason behind is that at this saturation the maximum changes occur in the petrophysical parameters.

The radius of the disk is estimated approximately 297 m, and accordingly, the diameter would be 594 m. This represents the base and top of the rectangular plume in a 2D model configuration.

Thereafter, seismic NMO-corrected PP gather is generated for 2D geological model without CO_2 injected. This seismic section is termed as baseline. Further, CO_2 plume is inserted in the geological formation and the change in physical properties such as velocity, reflectivity, and time shift caused by the injection of CO_2 in a sandstone reservoir is evaluated using Gassmann and Shuey's equation. Again, a synthetic seismogram is generated and termed as monitor data. Figure 6a shows the difference between the baseline CDP (0% CO_2) and the monitor CDP (20% CO_2) seismic sections. As expected, the rest of traces outside the area of interest

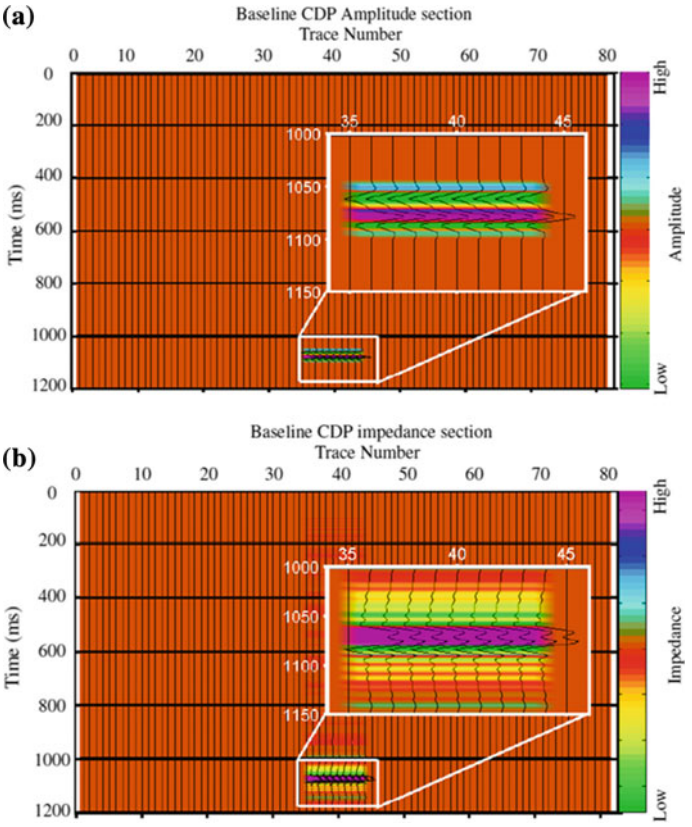

Fig. 6 **a** Difference between baseline and monitor amplitude section and **b** difference between baseline and monitor impedance section. The inserted plume zone is highlighted

are canceled, whereas the CO_2 injection zone and the reflectors underneath it are highlighted due to the amplitude differences and travel time. It is noticed that the exact shape and size of the plume cannot be predicted by the seismic amplitude.

Thereafter, model-based seismic inversion is performed on baseline as well as on monitor CDP section and inverted for acoustic impedance, with the hope that the inverted impedance section could depict the actual shape and size of the CO_2 plume and the effect of plume will be highlighted more accurately compared to the baseline seismic data. Figure 6b shows the difference between the baseline impedance section and the monitor impedance section. The larger amplitude contrast has been noticed from the impedance section as compared to the seismic amplitude section. From this study, it is concluded that the analysis in impedance domain is better as compared to time domain.

7 Conclusion

The analyses of petrophysical parameters have been performed, and the changes in these parameters due to fluid substitution have been studied by the seismic response evaluation. A series of petrophysical parameters, viz. V_P, V_S, ρ, Z_P, Z_S, $\lambda\rho$, $\mu\rho$, and the AVO parameters A(intercept) and B(gradient) changes caused by the CO_2 injection is examined by the Gassmann fluid substitution. It is noticed that the P-wave velocity decreases by 10%, whereas S-wave velocity increases by 2% and density of the subsurface decreases by 3% with CO_2 saturation. The other petrophysical parameters like Lame parameters $\lambda\rho$ drop by 27%, and $\mu\rho$ increases by 17% due to CO_2 saturation compared to the 100% water saturation. The AVO parameters (A and B) decrease with a value of 13% and 7%, respectively. The analysis shows that the Lame parameters are the most sensitive properties for detection of CO_2 saturation. Thereafter, seismic forward modeling is performed to see the changes in seismic amplitude caused by the injection of CO_2 fluid. The analysis shows that the maximum seismic amplitude change is noticed by analyzing P-wave velocity compared to other parameters discussed here. These are the fruitful outcome of this study which can be used for monitoring actual CO_2 sequestration in geological strata.

Acknowledgements The author (SP Maurya) is indebted to Science and Engineering Research Board, Department of Science and Technology, New Delhi, for the financial support in the form of National Postdoctoral Fellowship (NPDF) (grant no. PDF/2016/000888). The authors would also like to acknowledge CGGVeritas for providing data and software, without which this work could not be possible.

References

Bachu S, Gunter WD, Perkins EH (1994) Aquifer disposal of CO_2: hydrodynamic and mineral trapping. Energy Convers Manage 35(4):269–279

Chadwick RA, Noy D, Arts R, Eiken O (2009) Latest time-lapse seismic data from Sleipner yield new insights into CO_2 plume development. Energy Procedia 1(1):2103–2110

Chadwick A, Williams G, Delepine N, Clochard V, Labat K, Sturton S, Buddensiek ML, Dillen M, Nickel M, Lima AL, Arts R (2010) Quantitative analysis of time-lapse seismic monitoring data at the Sleipner CO_2 storage operation. Lead Edge 29(2):170–177

Fanchi JR (2001) Feasibility of monitoring CO_2 sequestration in a mature oil field using time-lapse seismic analysis. In: SPE/EPA/DOE exploration and production environmental conference, Society of Petroleum Engineers. https://doi.org/10.2118/66569-ms

Gassmann F (1951) Über die elastizität poröser medien. Vierteljahrss-chrift der Naturforschenden Gesellschaft in Zurich 96:1–23. http://sepwww.stanford.edu/sep/berryman/PS/gassmann.pdf. Accessed 22 Mar 2019

Ghaderi A, Landrø M (2009) Estimation of thickness and velocity changes of injected carbon dioxide layers from prestack time-lapse seismic data. Geophysics 74(2):O17–O28

Ivanova A, Kashubin A, Juhojuntti N, Kummerow J, Henninges J, Juhlin C, Lüth S, Ivandic M (2012) Monitoring and volumetric estimation of injected CO_2 using 4D seismic, petrophysical data, core measurements and well logging: a case study at Ketzin, Germany. Geophys Prospect 60(5):957–973

Landrø M (2002) Uncertainties in quantitative time-lapse seismic analysis. Geophys Prospect 50(5):527–538

Mathieson A, Midgley J, Dodds K, Wright I, Ringrose P, Saoul N (2010) CO_2 sequestration monitoring and verification technologies applied at Krechba, Algeria. Lead Edge 29(2):216–222

Moradi S, Lawton DC (2015) Time-lapse numerical modelling of the Quest carbon capture and storage (CCS) project. Poroelastic approach Geo-convention, Calgary, Canada. https://www.crewes.org/ForOurSponsors/ConferenceAbstracts/2015/CSEG/Moradi_1_CSEG_2015.pdf. Accessed 22 Mar 2019

Nordbotten JM, Celia MA, Bachu S (2005) Injection and storage of CO_2 in deep saline aquifers: analytical solution for CO_2 plume evolution during injection. Transp Porous Media 58(3):339–360

Pevzner R, Shulakova V, Kepic A, Urosevic M (2011) Repeatability analysis of land time-lapse seismic data: CO2CRC Otway pilot project case study. Geophys Prospect 59(1):66–77

Shuey RT (1985) A simplification of the Zoeppritz equations. Geophysics 50(4):609–614

Vadapalli U, Vedanti N (2016) Time-lapse seismic response evaluation based on well log data for Ankleshwar reservoir, Cambay basin, India. J Ind Geophys Union 20(5):472–481

Xue Z, Tanase D, Watanabe J (2006) Estimation of CO_2 saturation from time-lapse CO_2 well logging in an onshore aquifer Nagaoka Japan. Explor Geophys 37(1):19–29

Chapter 20
Friction-Induced Wellbore Instability Due to Drill String

Arun K. Singh, Nitish Sinha and T. N. Singh

Abstract In this chapter, we study numerically friction-induced wellbore instability due to frictional interaction between drill string and rock materials using torsional pendulum system. The classical Amontons–Coulomb (AC) friction laws are widely used for explaining the variety of sliding- and rotation-related phenomena, yet the AC laws fail to explain stiffness dependence of stick-slip motion. In recent times, the rate and state friction (RSF) model has found widespread applications for understanding the phenomena related to sliding of rock surfaces. The RSF model, which is basically modified form of the aforementioned AC laws, has not yet got any attention for studying the friction-induced wellbore instability. The RSF laws state that friction of hard surfaces such as rocks and metals at high (~MPa) normal stress depends on current slip velocity as well as nature of the sliding surfaces. The literature review reveals that rotation of drill string causes stick-slip vibration, thus potential initiation of the failure process in surrounding medium. We use linear and nonlinear stability results to discuss a critical stiffness above stick-slip behaviour of the rotating system disappears. It is also demonstrated in the numerical simulations that stick-slip motion could also be eliminated by increasing rotational velocity of the drill string.

Keywords Rate and state friction · Stick-slip vibration · Wellbore instability

1 Introduction

Drilling of wellbores is a common activity in petroleum exploration industry (Besaisow and Payne 1988; Dareing and Livesay 1968; Ghasemloonia et al. 2015; Katsui et al. 2017). However, this mechanical operation is often encountered with variety of engineering issues, for instance, appearance and propagation of cracks in

A. K. Singh (✉) · N. Sinha
Department of Mechanical Engineering, Visvasvaraya National Institute of Technology, Nagpur, India
e-mail: aksinghb@gmail.com

T. N. Singh
Department of Earth Sciences, Indian Institute of Technology Bombay, Mumbai, India

K. H. Singh and R. M. Joshi (eds.), *Petro-physics and Rock Physics of Carbonate Reservoirs*, https://doi.org/10.1007/978-981-13-1211-3_20

the surrounding materials due to friction-induced vibration of drill string (Ghasemloonia et al. 2015; Katsui et al. 2017; Liao 2011; Zoback 2007). The classical Amontons–Coulomb (AC) laws are frequently used to elucidate the frictional phenomena such as stick-slip, static and dynamic strengths (Ibrahim 1994a, b; Persson 2000; Ruina 1983). However, one of the limitations of the AC laws is that it does not take into account the effect of slip velocity and nature of the contacting surfaces or even temperature and pore pressure. In order to overcome the limitations of the classical laws, the rate and state friction (RSF) were proposed by Dieterich and Ruina (Dieterich 1978; Marone 1998; Persson 2000). This modification is based on the experimental observations that friction of hard and rough solid surfaces like rocks, metals, hard polymers, etc., depends on time of contact as well as current slip rate of the sliding surfaces (Dieterich 1978; Gu et al. 1984; Marone 1998; Persson 2000). Stick-slip (SS) instability is basically a manifestation of the interaction between elasticity and friction force (Gu et al. 1984; Persson 2000; Scholz 1990; Marone 1998). A necessary condition of stick-slip is that friction should reduce with velocity or displacement known as velocity-weakening effect (Ruina 1983). In other words, the sliding surfaces must lose its strength with slip velocity or displacement (Ruina 1983). Contact strengthening must also occur at the interface to restore its frictional strength (Dieterich 1978; Ruina 1983). In other words, friction is basically the outcome of the competition between adhesion and rupture of the sliding surfaces which give rise stable or unstable motion. In addition, friction also increases with sliding velocity known as velocity strengthening effect, thus diminishing the possibility of SS motion (Ruina 1983). Numerical simulations of the RSF laws have shown that stiffness is important in low sliding velocity for controlling the dynamics of the sliding yet that could also be eliminated by increasing the sliding velocity (Dieterich 1978; Gu et al. 1984; Marone 1998; Persson 2000; Ruina 1983; Ranjith and Rice 1999).

In the literature, there has been extensive theoretical studies on SS motion because of drill string in wellbore operation (Ghasemloonia et al. 2015; Katsui et al. 2017; Lin and Wang 1991; Plácido et al. 2002; Pasic et al. 2007; Tian et al. 2016; Xue et al. 2014). Dareing and Livesay (1968) analysed mathematically the longitudinal and drill string vibration in the presence of damping (Dareing and Livesay 1968). Lin and Wang (1991) studied the stick-slip vibration of a drill string in the light of viscous damping, rotary speed and natural frequency on stick-slip (Lin and Wang 1991). Plácido et al. (2002) have also investigated the wellbore instability owing to vibration of drill string (Plácido et al. 2002). Xue et al. (2014) have investigated the chaotic vibration of the bottom rotating drill string (Xue et al. 2014). Tian et al. (2016) have modelled and analysed longitudinal vibration of the drill string in the presence of lateral inertial effect (Tian et al. 2016). Recently, Ghasemloonia et al. (2015) have reviewed the vibration of drill string including its modelling and suppression methods (Ghasemloonia et al. 2015). Pasic has also reviewed cause and effect of wellbore instability (Pasic et al. 2007). Katsui et al. (2017) have discussed different numerical techniques for SS analysis of drill string (Katsui et al. 2017). Despite detailed numerical and theoretical investigations on the vibration of drill string, to the best of our knowledge, this problem has not been studied in the light of RSF.

Motivated by this observation, in the present numerical study, SS vibration of a typical drill string is investigated with the RSF law. It is important to note that interfacial temperature and pore pressure may be also important factors during the drilling operation, but we have not considered in the present study to avoid the complexity in the governing differential equations (Sinha et al. 2018). Nevertheless, these effects could be accommodated indirectly in the RSF model (Marone 1998).

Aiming to model the wellbore instability owing to drill string, the mathematical expressions derived for sliding motion may be replaced with $V = r\omega$ where r and ω are radius and angular rotation of the drill string, respectively. The analogous RSF model in terms of frictional stress τ, angular velocity ω, state variable θ and viscous damping C given as

$$\tau = \tau_* + A\ln\left(r\omega/R\omega_*\right) + B\ln\left(R\omega_*\theta/L\right) + C\left(r\omega/R\omega_*\right) \tag{1}$$

where τ_* and ω_* are reference frictional shear stress and reference angular velocity, respectively. Further, A and B are the frictional constants and are generally considered to be proportional to normal stress (Ranjith and Rice 1999). As mentioned, θ represents the "state" of the contacting surfaces and L is a critical slip distance over which evolution of microcontacts occurs (Marone 1998, 17; Ranjith and Rice 1999). At the same time, L is generally the order of the size of microcontacts but that also depends on size of the sliding surfaces (Marone 1998; Ruina 1983; Ranjith and Rice 1999).

Two basic empirical laws for θ have been proposed (Marone 1998; Ruina 1983; Ranjith and Rice 1999). Dieterich–Ruina ageing law is used in the present study since this particular law characterizes the true ageing of the contacting surfaces during stationary state (Marone 1998; Ruina 1983; Ranjith and Rice 1999). The ageing law, expressed in terms of radius R and angular velocity ω of the drill string, is generally given by the following expression

$$\frac{\mathrm{d}\theta}{\mathrm{d}t} = 1 - r\omega\theta/L \tag{2}$$

It may be easily concluded from Eq. 2 is that during the stationary state ($\omega = 0$), θ becomes true time of contact (Marone 1998; Ruina 1983; Ranjith and Rice 1999). It is also obvious from Eq. (2) that θ reduces to the steady-state value θ_{ss}, under steady sliding, i.e. $\theta_{ss} = L/V_{ss}$ where $V_{ss} = R\omega_{ss}$ (Marone 1998; Ruina 1983; Ranjith and Rice 1999). Thus, θ_{ss} signifies average time to renew the contacts during steady sliding (Ruina 1983; Ranjith and Rice 1999). Notably, the conditions for steady-state sliding are $\mathrm{d}\theta/\mathrm{d}t = 0$ and $\mathrm{d}\tau/\mathrm{d}t = 0$ (Gu et al. 1984; Persson 2000; Ranjith and Rice 1999). The expression for steady dynamic stress τ_{ss} is given by (Gu et al. 1984; Ranjith and Rice 1999)

$$\tau_{ss} = \tau_* - (B - A)\ln\left(r\omega_{ss}/R\omega_*\right) + Cr\omega_{ss}/R\omega_* \tag{3}$$

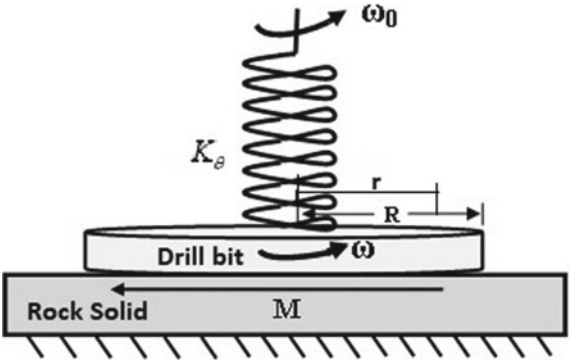

Fig. 1 A schematic sketch of the drill bit in the form of a solid disc is in contact with the rock surface

However, if steady frictional stress τ_{ss} decreases with steady velocity V_{ss}, it is known as the velocity-weakening (VW) process. On the other hand, if τ_{ss} increases with sliding velocity, this is called the velocity strengthening (VS) process (Gu et al. 1984; Ruina 1983; Ranjith and Rice 1999; Singh and Singh 2012).

Figure 1 presents a schematic sketch of a typical drill string modelled as a torsional pendulum having radius R and rotational stiffness K_θ (per unit area of contact surface). The free end of the spring is being rotated with a constant angular velocity ω_0, while the other end of the spring attached with the disc rotating with angular velocity ω. The drill bit is, in turn, in contact with the rock solid which causes frictional torque M per unit area of contact.

Further, frictional moment M in terms of frictional stress $\tau(r)$ is given by the following expression

$$M = 2\int_0^R \left(r/R\right)^2 \tau(r)\mathrm{d}r \tag{4}$$

Upon considering inertia I_z of the disc, the governing differential equation in view of Fig. 1 is given

$$I_z \frac{\mathrm{d}^2\omega}{\mathrm{d}t^2} = K_\theta(\omega_0 - \omega) - \pi\int_0^R \left(r/R\right)^2 \dot{\tau}(r)\mathrm{d}r \tag{5}$$

Using Eqs. (1, 2, 4 and 5), the final form of system of governing differential equations of the drill system in Fig. 1 is derived in dimensionless form as

$$\frac{\mathrm{d}\hat{\theta}}{\mathrm{d}T} = \mathrm{e}^{-\hat{\theta}} - \rho\mathrm{e}^{\phi}$$

$$\frac{\mathrm{d}\psi(\rho)}{\mathrm{d}T} = \left(1 + \hat{\gamma}\rho\mathrm{e}^{\phi}\right)\frac{\mathrm{d}\phi}{\mathrm{d}T} + \beta\left[\mathrm{e}^{\{\phi+\ln(\rho)+\hat{\gamma}\rho e^{\phi}+\psi_*-\psi(\rho)\}/\beta} - \rho\mathrm{e}^{\phi}\right]$$

$$\frac{\mathrm{d}\mu}{\mathrm{d}T} = \int_0^1 \frac{\mathrm{d}\psi(\rho)}{\mathrm{d}T}\rho^2 \mathrm{d}\rho$$

$$\frac{\mathrm{d}^2\phi}{\mathrm{d}T^2} = \frac{\mathrm{e}^{-\phi}}{r^2}\left\{k_\theta\left(\varphi_0 - \mathrm{e}^{\phi}\right) - \frac{\mathrm{d}\mu}{\mathrm{d}T}\right\} - \left(\frac{\mathrm{d}\phi}{\mathrm{d}T}\right)^2 \tag{6}$$

where dimensionless terms are defined as $\mu = M/2\pi AR$, $\psi_* = \tau_*/A$, $T = tV_*/L$, $\varphi_0 = \omega_0/\omega_*$, $V_* = R\omega_*$, $\rho = r/R$, $\phi = \ln(\omega_0/\omega_*)$, $\hat{\theta} = \ln(R\omega_*\theta/L)$, $\beta = B/A$, $k_\theta = K_\theta L/AR^2$, $r^2 = I_Z\omega_*^2/AL$. After further manipulating Eq. (6), one can get the following form of the solvable differential equation numerically as

$$\frac{\mathrm{d}\psi(\rho)}{\mathrm{d}T} = \left(1 + \gamma\rho\mathrm{e}^{\phi}\right)\frac{\mathrm{d}\phi}{\mathrm{d}T} + \beta\left[\mathrm{e}^{\{\phi+\ln(\rho)+\gamma\rho\mathrm{e}^{\phi}+\psi_*-\psi(\rho)\}/\beta} - \rho\mathrm{e}^{\phi}\right]$$

$$\frac{\mathrm{d}^2\phi}{\mathrm{d}T^2} = \frac{\mathrm{e}^{-\phi}}{r^2}\left\{k_\theta\left(\varphi_0 - \mathrm{e}^{\phi}\right) - \int_0^1 \left\{\left(1 + \gamma\rho\mathrm{e}^{\phi}\right)\frac{\mathrm{d}\phi}{\mathrm{d}T} + \beta\left[\mathrm{e}^{\{\phi+\ln(\rho)+\gamma\rho\mathrm{e}^{\phi}+\psi_*-\psi(\rho)\}/\beta} - \rho\mathrm{e}^{\phi}\right]\right\}\rho^2\mathrm{d}\rho\right\} - \left(\frac{\mathrm{d}\phi}{\mathrm{d}T}\right)^2 \tag{7}$$

The linear stability about steady sliding (ϕ_{ss}, ψ_{ss}) at $\rho = 1$ that is $(r = R)$ has shown that the critical stiffness $k_{\theta cr} = (\beta - 1)\left(1 + r^2\right) - \gamma\mathrm{e}^{\phi}$ where $\gamma = C/A$. The expression for steady frictional stress $\psi_{ss} = \psi_* - (\beta - 1)\phi_{ss} - (\beta - 1)\ln(\rho) + \gamma\rho\mathrm{e}^{\phi_{ss}}$. On the other hand, under the quasi-static conditions, upon neglecting inertial term r, $k_{\theta cr}$ now results in $k_{\theta cr} = (\beta - 1) - \gamma\mathrm{e}^{\phi}$. This expression also predicts a critical angular velocity $\phi_{cr} = \ln\left[(\beta - 1 - k_\theta)/\gamma\right]$ corresponding to that stick-slip motion disappears. These results are also confirmed with corresponding nonlinear solutions of Eq. (7) in the next section. The corresponding nonlinear solutions are discussed in the following sections.

2 Results and Discussion

2.1 Effect of Stiffness on Stick-Slip Vibration

Figure 2 presents the results concerning the effect of velocity-weakening parameter β on the stability of the drill string. It is seen that amplitudes of stick-slip vibration of the drill string increases with β. The drill string now experiences more vibration due to weakening of the interacting surfaces.

Note that β should decrease in the presence of slippery medium such as water or mud, which basically stabilizes the rotating system. Moreover, a decrease in β also results in strengthening of the rotating interface, thus the suppression of SS instability (Gu et al. 1984; Ruina 1983; Ranjith and Rice 1999).

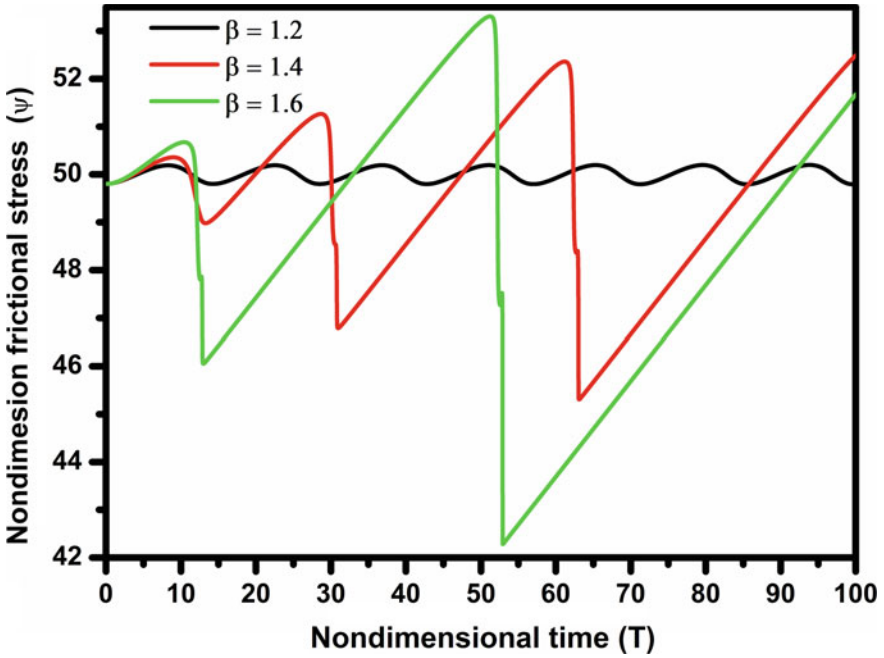

Fig. 2 Effect of stiffness of rotating system on stick-slip instability at a fixed value $\gamma = 0.001$, $\psi_* = 50$, $r = 0.1$, $\varphi_0 = 1.0$ and $k_\theta = 0.185$ and initial condition (0.001, 0.001, 49.8)

2.2 *Effect of Rotational Speed on Stick-Slip Vibration*

Figure 3 shows the effect of rotational speed of the drill on the stability of drill string. The drill string stabilizes with increase in rotational speed of the drill at a constant distance between the centre of drill and its outer perimeter. Initially, increase in rotational speed of the system goes to increase in amplitudes of the SS motion.

Further, if rotational speed exceeds a threshold value, then the drill string results in decrease of amplitudes of oscillation until at a constant amplitude.

2.3 *Effect of Viscous Damping on Stick-Slip Vibration*

Figure 4 indicates that viscous damping γ of the system such as lubricating fluid and drilling mud at the drilling interface on the stability. This always results in suppressing of SS with increase in γ.

This results again in prediction with the reported result in the literature (Gondane et al. 2017; Persson 2000; Sinha et al. 2018). The chaotic motion is intermediated stage at which system will be stable/unstable depending upon the condition.

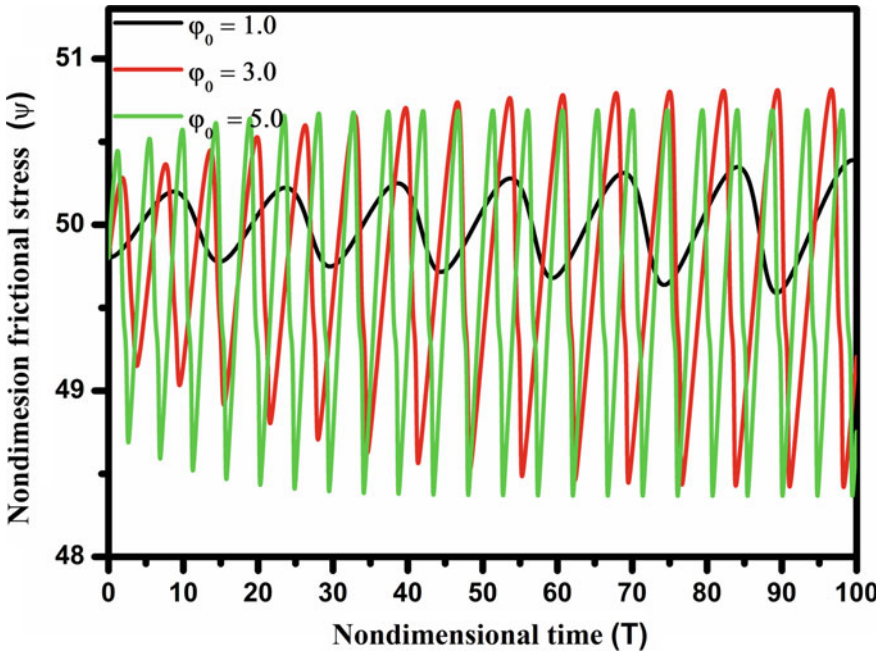

Fig. 3 Effect of rotational speed on stick-slip instability at a fixed value of $\gamma = 0.001$, $\psi_* = 50$, $r = 0.1$, $\beta = 1.2$ and $k_\theta = 0.185$ and initial condition (0.001, 0.001, 49.8)

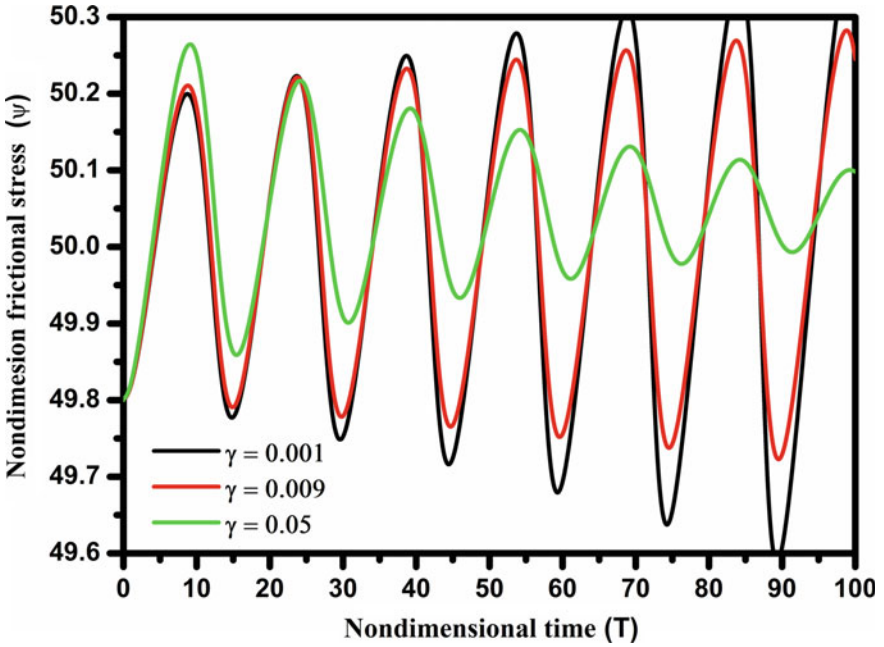

Fig. 4 Effect of viscous damping of system on stick-slip instability at a fixed value of $\psi_* = 50$, $r = 0.1$, $\beta = 1.2$, $\varphi_0 = 1$, $k_\theta = 0.185$

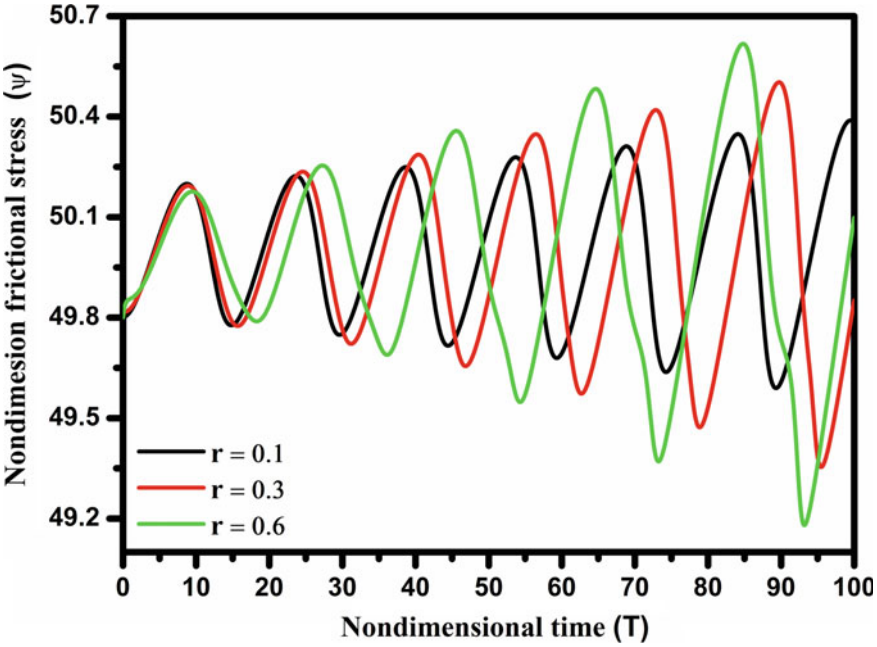

Fig. 5 Effect of inertia on stick-slip instability at a fixed value of friction parameters: $\gamma = 0.001$, $\psi_* = 50$, $\beta = 1.2$, $\varphi_0 = 1$ and $k_\theta = 0.185$

2.4 Effect of Inertia on Stick-Slip Vibration

Figure 5 shows the effect of inertia r on amplitudes of SS motion of the drill string. The system results in increased amplitudes of stick-slip vibration r.

As a result, the drill bit is now more prone to unstable motion. This is again consistent with the linear stability of the RSF model which predicts that critical stiffness increases with addition of inertia in the sliding system. The present numerical simulations will be more interesting if the present results are validated with experiments. It is also believed that the present study could also be useful for designing the control system of drill string in the light of stick-slip vibration.

3 Conclusions

The present numerical simulations show stick-slip vibration of a typical drill string due to drill bit in a wellbore. It is established that like linear motion, in rotation also, stiffness and rotational velocity are critical in controlling the rotational stick-slip. Inertia also enhances the tendency of stick-slip motion of the drill string. The presence of water or mud also affects the velocity-weakening parameter and thereby stick-slip motion as well.

References

Besaisow AA, Payne ML (1988) A study of excitation mechanisms and resonances inducing bottomhole-assembly vibrations. SPE Drilling Eng 3(01):93–101

Dareing DW, Livesay BJ (1968) Longitudinal and angular drill-string vibrations with damping. J Eng Ind 90(4):671–679

Dieterich JH (1978) Rock friction and mechanics of stick-slip. Pure Appl Geophys 116:790–805

Ghasemloonia A, Rideout DG, Butt SD (2015) A review of drill string vibration modelling and suppression methods. J Petrol Sci Eng 131:150–164

Gondane S, Singh AK, Vijayakumar RP, Sinha N (2017) The effect of carbon nanotubes based nanolubricant on stick-slip behaviour. Trans Indian Inst Met. https://doi.org/10.1007/s12666-017-1240-5

Gu JC, Rice JR, Ruina AL, Tse ST (1984) Slip motion and stability of a single degree of freedom elastic system with rate and state dependent friction. J Mech Phys Solids 32:167–196

Ibrahim RA (1994a) Friction-induced vibration, chatter, squeal, and chaos—part I: mechanics of contact and friction. Appl Mech Rev 47(7):209–226

Ibrahim RA (1994b) Friction-induced vibration, chatter, squeal, and chaos—part II: dynamics and modelling. Appl Mech Rev 47(7):227–253

Katsui T, Inoue T, Izutani K, Nagaishi Y, Rheem CK, Matsuo MY (2017) Considerations on numerical procedure for stick-slip analysis of drill string. In: American society of mechanical engineers 2017 36th international conference on ocean, offshore and arctic engineering, vol 8. https://doi.org/10.1115/omae2017-62158

Liao CM (2011) Experimental and numerical studies of drill-string dynamics. University of Maryland, MD, USA. https://drum.lib.umd.edu/handle/1903/12269. Accessed 22 Mar 2019

Lin YQ, Wang YH (1991) Stick-slip vibration of drill strings. J Eng Ind 113(1):38–43

Marone C (1998) Laboratory derived friction laws and their application to seismic faulting. Ann Rev Earth Plan Sci 26:643–696

Pasic B, Gaurina-Međimurec N, Matanovic D (2007) Wellbore instability: causes and consequences/Nestabilnost Kanala Busotine: Uzroci I Posljedice. Rudarsko-geolosko-naftni zbornik 19(1):87

Persson BNJ (2000) Sliding friction: physical principles and applications. Springer, Heidelberg

Plácido JCR, Santos HM, Galeano YD (2002) Drillstring vibration and wellbore instability. J Energy Res Technol 124(4):217–222

Ranjith K, Rice JR (1999) Stability of quasi-static slip in a single degree of freedom elastic system with rate and state dependent friction. J Mech Phys Solids 47:1207–1218

Ruina AL (1983) Slip instability and state variable friction law. J Geophys Res 88:10359–10370

Scholz CH (1990) The mechanics of earthquakes and faulting. Cambridge University Press, Cambridge

Singh AK, Singh TN (2012) Friction strength and steady relaxation using the rate and state dependent friction model. Pure appl Geophys 170(3):247–257

Sinha N, Singh AK, Singh TN (2018) The effect of inertia, viscous damping, temperature and normal stress on chaotic behavior of the rate and state friction model. J Earth Syst Sci 127:45. https://doi.org/10.1007/s12040-018-0935-2

Tian J, Wu C, Yang L, Yang Z, Liu G, Yuan C (2016) Mathematical modeling and analysis of drill string longitudinal vibration with lateral inertia effect. Shock Vib 2016. https://doi.org/10.1155/2016/6281264

Xue Q, Wang R, Sun F, Huang Z (2014) Chaotic vibration analysis of the bottom rotating drill string. Shock Vib 2014. https://doi.org/10.1155/2014/429164

Zoback MD (2007) Reservoir geomechanics. Cambridge University Press, Cambridge

Index

K. H. Singh and R. M. Joshi (eds.), *Petro-physics and Rock Physics of Carbonate Reservoirs*, https://doi.org/10.1007/978-981-13-1211-3

D